HAL
open science

Surface Distortion and Electrocatalysis : Structure-Activity Relationships for the Oxygen Reduction Reaction on PtNi/C Nanocatalysts
Raphaël Chattot

THÈSE

Pour obtenir le grade de

DOCTEUR DE LA COMMUNAUTE UNIVERSITE GRENOBLE ALPES

Spécialité : **Matériaux, Mécanique, Génie Civil, Electrochimie**

Arrêté ministériel : 25 mai 2016

Présentée par

Raphaël CHATTOT

Thèse dirigée par **Frédéric Maillard** et **Laetitia Dubau**

préparée au sein du **Laboratoire d'Electrochimie et de Physicochimie des Matériaux et des Interfaces**
dans l'**École Doctorale I-MEP2**

Surface Distortion and Electrocatalysis: Structure-Activity Relationships for the Oxygen Reduction Reaction on PtNi/C Nanocatalysts

Thèse soutenue publiquement le **5 Décembre 2017**
devant le jury composé de :

Dr. Ifan E. L. STEPHENS
Senior Lecturer, Imperial College London (Rapporteur)
Prof. Frédéric LEROY
Professeur, Université Aix-Marseille (Rapporteur)
Dr. Federico CALLE-VALLEJO
Ramón y Cajal Researcher, Université de Barcelone (Examinateur)
Prof. Marian CHATENET
Professeur, Université Grenoble-Alpes (Président du Jury)
Dr. Laetitia DUBAU
Chargée de Recherche, CNRS, Grenoble (Co-Directrice de Thèse)
Dr. Frédéric MAILLARD
Chargé de Recherche, CNRS, Grenoble (Directeur de Thèse)

*'What I am going to show you is not very Catho**d**ic'*

A (tired) speaker, GdR HySPàC, Corsica, 2015.

Because awesomeness does not have frontiers, I would like to warmly thank Vera, Henni, Steffi, Sissi, Ana Sofia, Fabio, Zarko, Thomas, Sören, Jorge and Prof. Dr. Peter Strasser from TU Berlin, Germany, for accepting me wandering inside their lab for 3 months (with officially no clear objective except curiosity!). I owe you so much, such as the presence of non-agglomerated catalysts in this manuscript! My only regret is to have missed the Kicker tournament! Thanks also to Juan, Sebastian and Prof. Dr. Thomas J. Schmidt from the Paul Scherrer Institute, Switzerland, for their share of material and knowledge. I hope our routes will cross again!

I would like to also thank Dr. Ifan E. L. Stephens, Prof. Frédéric Leroy, Dr. Federico Calle-Vallejo and Prof. Marian Chatenet for kindly accepting reviewing this manuscript.

To the so-called 'Team Hollow': Laetitia and Frédéric, I cannot find the words to express you my gratitude. On and far beyond the scientific aspect, you have been of a priceless support and wisdom. I may no longer be your Padawan, but I wish I could stay your friend (and colleague) forever! To Tristan and your infinite motivation, we share the same passion for this subject (and a lot of non-scientific ones) and I learnt a lot from you and our complementarity.

All the rest goes to my family and lifelong friends. Your unconditional support and understanding during these years are the major contribution to the accomplishment of this work. Whatever my silences (and I would like to apologize for them), you were always there and goodhearted. So, thank you. To my sister Chloé, I am afraid the figures of my Ph.D. cannot compete with yours ;) Thank you and Jason for the common redaction process, it was like vacations! To my mother, I know I can count on you in any time, I owe you my happiness. To François, Martine, my PBM, and Tom. To Coco, Roro and Panpan, my Rock'n'Roll buddies!

To Céline, my everything. They say the night is dark and full of terrors, but holding your hand does worth a million dawns.

To my father

R. Chattot, O. Le Bacq, V. Beermann, S. Kühl, J. Herranz, S. Henning, L. Kühn, T. Asset, L. Guétaz, G. Renou, J. Drnec, P. Bordet, A. Pasturel, A. Eychmüller, T. J. Schmidt, P. Strasser, L. Dubau, and F. Maillard, 'The Ineluctable Role of Surface Distortion in Oxygen Reduction Reaction Electrocatalysis', *To be submitted*, **2018**.

T. Asset, N. Job, Y. Busby, A. Crisci, V. Martin, V. Stergiopoulos, C. Bonnaud, A. Seyrov, P. Atanassov, **R. Chattot**, L. Dubau and F. Maillard, 'Porous Hollow PtNi/C Electrocatalysts: Carbon Support Considerations to Meet Performance and Stability Requirements', *ACS Catal.*, vol. 8, pp. 893-903, **2018**.

R. Chattot, **T. Asset**, J. Drnec, P. Bordet, J. Nelayah, L. Dubau, and F. Maillard, 'Atomic-Scale Snapshots of the Formation and Growth of Hollow PtNi/C Nanocatalysts,' *Nano Lett.*, vol. 17, no. 4, pp. 2447–2453, **2017**

R. Chattot, T. Asset, P. Bordet, J. Drnec, and L. Dubau, 'Beyond Strain and Ligand Effects: Microstrain-Induced Enhancement of the Oxygen Reduction Reaction Kinetics on Various PtNi/C Nanostructures,' *ACS Catal*., vol. 7, no. 1, pp. 398–408, **2017**.

O. Le Bacq, A. Pasturel, **R. Chattot**, B. Previdello, J. Nelayah, T. Asset, L. Dubau, and F. Maillard, 'Effect of Atomic Vacancies on the Structure and the Electrocatalytic Activity of Pt-rich/C Nanoparticles: A Combined Experimental and Density Functional Theory Study,' ChemCatChem, vol. 9, no. 12, pp. 2324–2338, **2017**.

L. Dubau, J. Nelayah, T. Asset, **R. Chattot**, and F. Maillard, 'Implementing Structural Disorder as a New Direction to Improve the Stability of PtNi/C Nanoparticles,' *ACS Catal*., vol. 7, pp. 3072–3081, **2017**.

T. Asset, **R. Chattot**, J. Drnec, P. Bordet, N. Job, F. Maillard, and L. Dubau, 'Elucidating the Mechanisms Driving the Aging of Porous Hollow PtNi/C Nanoparticles by Means of COads Stripping,' *ACS Appl. Mater. Interfaces*, vol. 9, no. 30, pp. 25298-25307, **2017**.

M. Lions, J.-B. Tommasino, **R. Chattot**, B. Abeykoon, N. Guillou, T. Devic, A. Demessence, L. Cardenas, F. Maillard, and A. Fateeva, 'Insights into the mechanism of electrocatalysis of the oxygen reduction reaction by a porphyrinic metal organic framework,' *Chem. Commun*., vol. 53, no. 48, pp. 6496–6499, **2017**.

G. Cognard, G. Ozouf, C. Beauger, G. Berthomé, D. Riassetto, L. Dubau, **R. Chattot**, M. Chatenet, and F. Maillard, 'Benefits and limitations of Pt nanoparticles supported on highly porous antimony-doped tin dioxide aerogel as alternative cathode material for proton-exchange membrane fuel cells,' *Appl. Catal. B Environ*., vol. 201, pp. 381–390, **2017**.

L. Dubau, J. Nelayah, S. Moldovan, O. Ersen, P. Bordet, J. Drnec, T. Asset, **R. Chattot**, and F. Maillard, 'Defects do Catalysis: CO Monolayer Oxidation and Oxygen Reduction Reaction on Hollow PtNi/C Nanoparticles,' *ACS Catal*., vol. 6, no. 7, p. 4673−4684, **2016**.

T. Asset, **R. Chattot**, J. Nelayah, N. Job, L. Dubau, and F. Maillard, 'Structure-Activity Relationships for the Oxygen Reduction Reaction in Porous Hollow PtNi/C Nanoparticles,' *ChemElectroChem*, vol. 3, pp. 1591–1600, Jul. **2016**.

L. Dubau, T. Asset, **R. Chattot**, C. Bonnaud, V. Vanpeene, J. Nelayah, and F. Maillard, 'Tuning the Performance and the Stability of Porous Hollow PtNi/C Nanostructures for the Oxygen Reduction Reaction,' *ACS Catal*., vol. 5, no 9, pp. 5333–5341, **2015**.

TABLE OF CONTENT

LIST OF ACRONYMS

AAS	Atomic Absorption Spectroscopy
AST	Accelerated Stress Test
AT	Acid Treated
BE	Benzyl Ether
CM	Corrected Microstrain
CNT	Carbon Nanotube
COP	Conference of the Parties
CV	Cyclic Voltammetry (Technique) or Cyclic Voltammogram (Plot)
DEMS	Differential Electrochemical Mass Spectroscopy
DFT	Density Functional Theory
DMFC	Direct Methanol Fuel Cell
DoE	American Department of Energy
ECSA	Electrochemically Active Surface Area
EELS	Energy Electron Loss Spectroscopy
E.F.	Enhancement Factor
EG	Ethylene Glycol
EIS	Electrochemical Impedance Spectroscopy
ESRF	European Synchrotron Radiation Facility
EV	Electric Vehicle
EVI	Electric Vehicle Initiative
FM	Frank-van der Merwe
FTIR	Fourier-Transform Infrared Spectroscopy
GA	Glycolic Acid
GHG	Green House Gas
GISS	Goddard Institute for Space Studies
GISTEMP	GISS Surface Temperature Analysis
HAADF	High Angle Annular Dark Field
HOR	Hydrogen Oxidation Reaction
HRSTEM	High Resolution Scanning Transmission Electron Microscopy
HRTEM	High Resolution Transmission Electron Microscopy
HSAC	High Surface Area Carbon

IEA	International Energy Agency
LSV	Linear Sweep Voltammetry
MA	Mass Activity
MEA	Membrane Electrode Assembly
MOF	Metal Organic Framework
NASA	National Aeronautics and Space Administration
NP	Nanoparticle
OCV	Open Circuit Potential
ORR	Oxygen Reduction Reaction
PDF	Pair Distribution Function
PEM	Proton-Exchange Membrane
PEMFC	Proton-Exchange Membrane Fuel Cell
PFSA	Perfluorosulfonic Acid
PGM	Platinum Group Metal
PSI	Paul Scherrer Institute
PVP	Poly(vinylpyrrolidone)
RDE	Rotating Disk Electrode
rpm	Rotation per Minute
RM	Raw Microstrain
RRDE	Rotating Ring-Disk Electrode
SA	Specific Activity
SAXS	Small Angle X-Ray Scattering
SD	Surface Distortion
SK	Stranski– Krastanov
SLD	Scattering Length Density
STEM	Scanning Transmission Electron Microscopy
TA	Thermally Annealed
TEM	Transmission Electron Microscopy
TDD	1, 2-tetradecanediol
TKK	Tanaka Kikinzoku Kogyo
TU	Technical University
UNFCCC	United Nations Framework Convention on Climate Change
UPD	Under Potential Deposition

UPS	Ultra-Violet Photoemission
USD	United State Dollar
VW	Volmer–Weber
WAXS	Wide Angle X-ray Scattering
X-EDS	Energy Dispersive X-ray Spectroscopy
XPS	X-ray Photoelectron Spectroscopy

A	Ampere
Ag	Silver
Au	Gold
Al	Aluminium
B	Boron
C	Carbon
Co	Cobalt
Cu	Copper
E vs. **Ref**	Potential relatively to Ref
F	Fluorine
F	Faraday constant
Fe	Iron (element) or Radiative Forcing (W m^{-2})
g	Gram
H	Hydrogen
Ir	Iridium
I	Electric Current (A) or scattering intensity (a.u.)
M	Early or late transition metal
m	Meter
Mg	Manganese
N	Nitrogen
Na	Sodium
Ni	Nickel
O	Oxygen
Pd	Palladium
Pt	Platinum
Rh	Rhodium
R	Universal gas constant
r	Radius
d	Diameter
S	Sulphur
s	Second

Sc	Scandium
S_{pt}	Pt specific surface area
$S_{Pt,CO}$	Pt specific surface area measured by CO_{ads} stripping experiment
Ti	Titanium
V	Volt
W	Tungsten (element) or Watt (unit)
Y	Yttrium
$E^0_{Ox/Red}$	Standard potential of the Ox/Red couple
°C	Degree Celsius
%	Percent
at. %)	Atomic fraction
wt. %	Weight fraction
e^-	Electron
eV	Electronvolt
η_i	Overpotential associated to reaction i
R_Ω	Cell electric resistance.
•X	Radical composed of element X
X_{ads}	Adsorbed X specie
ΔG	Free energy
ρ	Density
j	Current density
j_k	Kinetic current density
j_0	Exchange current density
θ	Angle (degree)
$G(r)$	Atomic PDF function
ε_d	d-band centre
μ_1^{CO}	Average CO_{ads} oxidation potential
Å	Ångström
D	Surface atoms ratio
N	Number of total atoms
N_s	Number of surface atoms
m	Number of atomic layers

H_{upd}	Under potentially deposited H
w	Electrode rotational speed (r.p.m.)
$U(E)$	Potential weight
γ_i	Catalytic site i
Q_{CO}	Coulometric charges during CO_{ads} oxidation
Q_H	Coulometric charges during H_{ads} desorption
$P(q)$	Form factor in SAXS analysis
$S(q)$	Structural factor in SAXS analysis
$\Delta\rho$	Scattering length density difference in SAXS analysis
ΔE	Electrode overpotential compared with the open circuit potential
α	Charge transfer coefficient
q	Length of the reciprocal lattice vector in WAXS and SAXS
Ω	Ohm
Hz	Hertz
LC	Local Ni composition in at. %

1 General Introduction

1.1 Energetic Context

1.1.1 Global Warming, is There Time for Scepticism?

The NASA's Goddard Institute for Space Studies Surface Temperature Analysis (GISTEMP) has unambiguously shown that, despite year-to-year fluctuations, the Earth's surface temperature has continuously raised for the last half century (see **Figure 1.1**). The question of the humankind responsibility in this trend is legitimate considering the expansion of the industrial activity in the very same period. However, if the current idea of Global Warming which bridges the Earth temperature increase to the high amount of Green House Gas (GHG) emissions released by human activities is generally admitted, a non-negligible portion of 'climate sceptic' (some with high governmental functions) prefers to see a natural temperature evolution cycle.
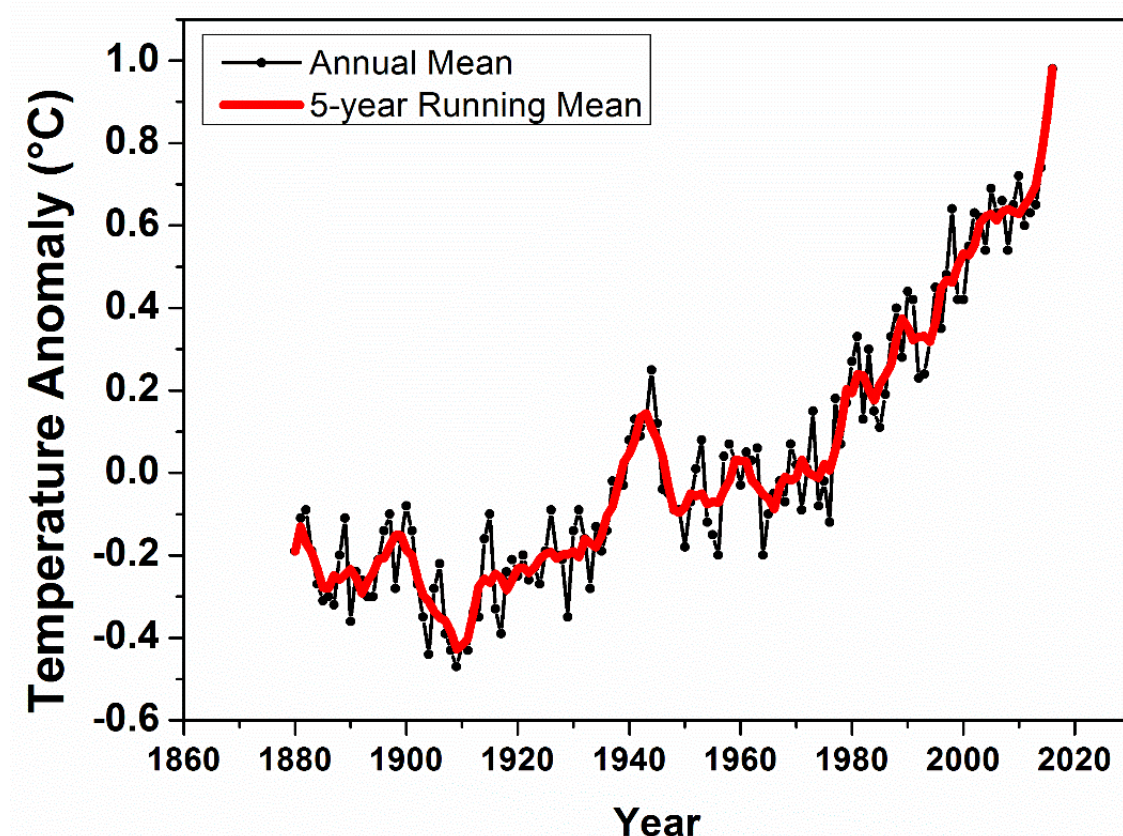
Figure 1.1: Global surface temperature anomalies mean estimates (based on land and ocean data) relative to 1951-1980 mean for annual (black) and 5 years running mean (red) through 2016. Adapted (and updated) from Ref. [1]

This brief introduction aims to humbly discuss, by providing simple and rationale evidence, this sensitive and complicated subject which is understood only by a selected scientific community and too often reduced to armchair debates by the uninitiated.

- *Humankind is responsible for the atmospheric CO_2 concentration increase.*

It is particularly striking to observe how the sharp increase of CO_2 content in the atmosphere after more than 1800 years of stability matches perfectly with the human's recent emissions since the industrial revolution. Despite the apparently obvious evidence provided by the **Figure 1.2**, the latter can still be (and is) contested because of some sub-decadal singular events where anthropogenic CO_2 emissions trend does not perfectly fit the atmospheric one [2]. How to be sure this extra atmospheric CO_2 is exactly the one from fossil fuel combustion and does not come from oceans degassing or ice melting?
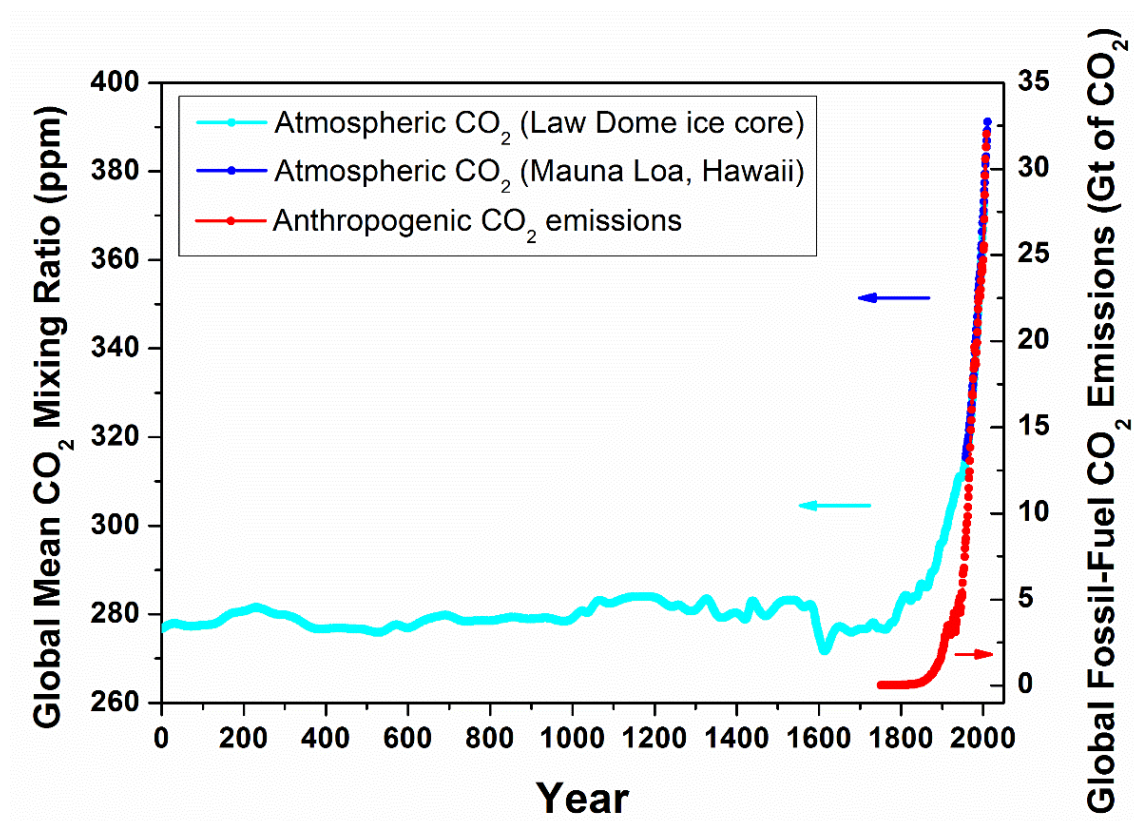
Figure 1.2: Correlation between increasing global CO_2 concentration in the atmosphere (from Law Dome ice core analysis [3] plotted in cyan, followed by direct atmospheric measurement in Mauna Loa, Hawaii [4] plotted in blue) and the anthropogenic CO_2 emissions from fossil fuel combustion estimates [5] plotted in red).

Fulfilling with their responsibility to inform government bodies and society about global warming, scientists found a further advanced route to address this issue by comparing the evolution of carbon isotopes proportions from various sources. Basically, CO_2 generated from fossil fuel and forest combustions has a different isotopic composition (about 2% lower $^{13}C/^{12}C$ ratio) compared to 'natural' atmospheric CO_2. The evolution record of the atmosphere $^{13}C/^{12}C$ ratio, via the study of corals and sea sponges by Böhm *et al.* in 2002 [6] shows an unequivocal decrease of the ^{13}C isotope content in the atmosphere, perfectly

matching with the increased global atmospheric CO_2 content (see **Figure 1.3**), proving the human-made interference with carbon content in atmosphere and oceans.
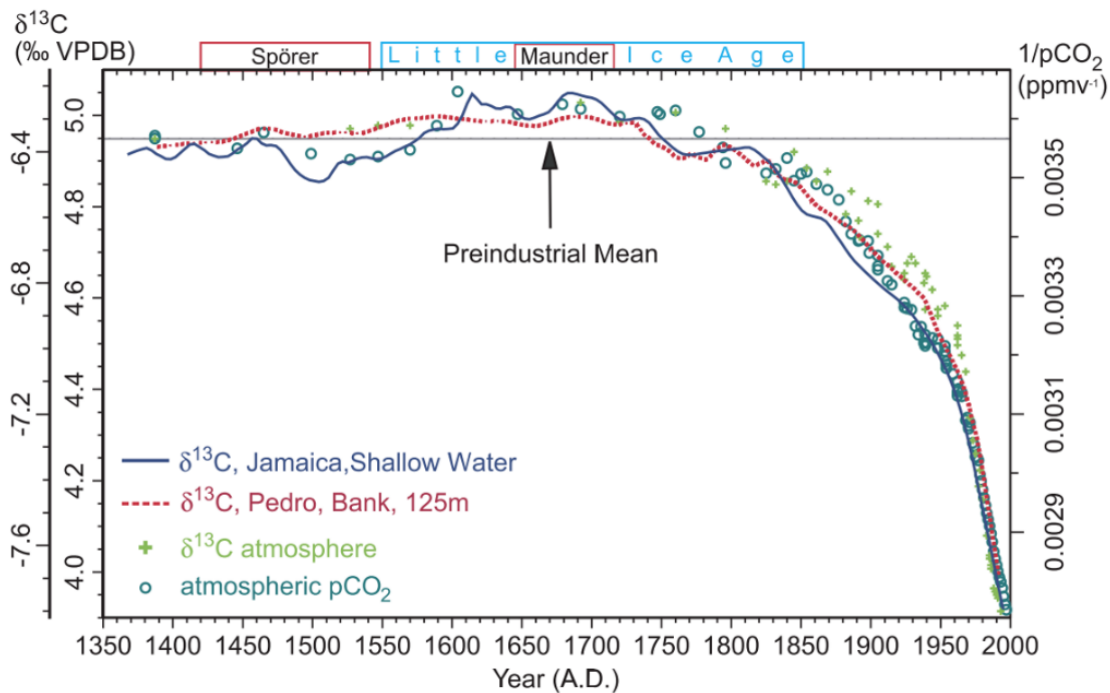
Figure 1.3: Comparison between Caribbean shallow (blue solid line) and deeper water sponge ^{13}C records (inner left *y* axis), ^{13}C of atmospheric CO_2 (green crosses, outer left *y* axis) and atmospheric *p*CO_2 (circles, right *y* axis, reciprocal scale). Figure from Böhm et al. [6]

- *Anthropogenic CO_2 is responsible for the global temperature increase*.

The greenhouse effect, the process by which for example the Earth's average surface temperature has for long been around 14°C instead -18°C, is a well-known phenomenon and cannot be contested. However, the influence of increased GHG in the atmosphere on the global warming via the greenhouse effect is recurrently minimized in climate sceptic's argumentations, in favour of natural cycles, such as variations in solar radiations (the latter being also a well-known phenomenon). To properly address this issue, it is important to recall that not only the incident solar radiations nor the atmospheric GHG content play a role in the greenhouse effect. Several parameters, such as ocean, snow, clouds or forest surface proportions influence the ability of Earth to reflect the Sun light (Albedo), while other parameters such as GHG contribute to the atmosphere warming by absorbing infrared thermal radiation from the underlying planet surface. Influence of each parameter can be expressed by its associated 'radiative forcing' (Fe) in W m^{-2} which express the associated increase (Fe > 0) or decrease (Fe < 0) of incident radiations received by the surface compared to a reference situation. Because of the multiplicity and

the high complexity of contributing phenomena (such as random volcanoes eruptions), the use of advanced climate simulations is required to the understanding of past and future climate events. The previously presented GISS evaluated the radiative forcing of the main contributing parameters to the greenhouse effect, and results are presented **Figure 1.4**.
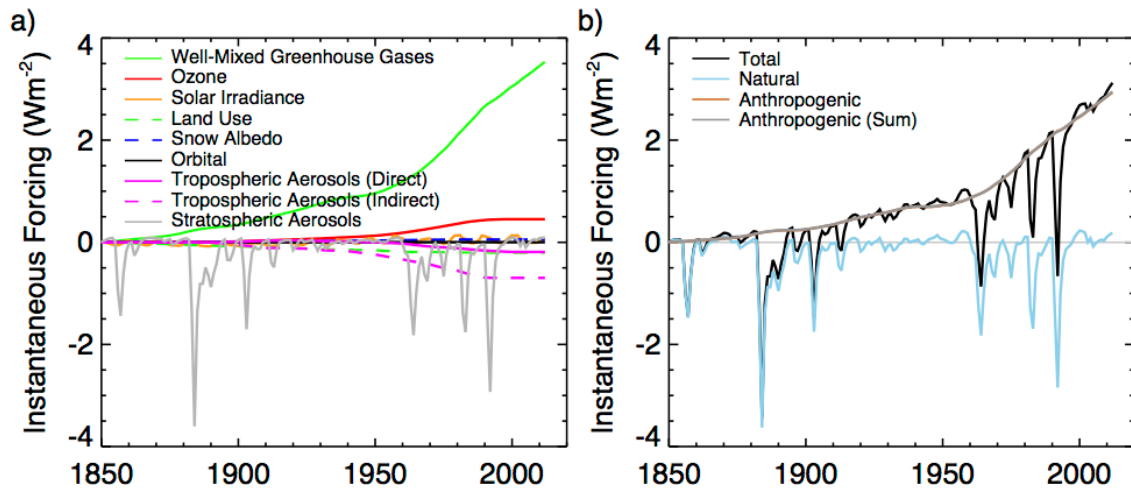
Figure 1.4: Instantaneous global climate forcing (Fe) employed in ref [7] for global climate simulations, relative to their values in 1880. Detailed contributions (a) and summarized contributions (b). Figure from Ref [7].

It is particularly striking to observe from **Figure 1.4 (a)** how much the radiative forcing of the GHG outweighs all other contributions, including solar irradiance variation by a factor of ~30 for the most recent values. As shown previously and in **Figure 1.4 (b)**, the anthropogenic contribution in GHG makes absolutely no doubt about human's direct responsibility in the sharp increase of the global temperature since the industrial revolution via the greenhouse effect.

- *What about the future?*

Estimations or predictions about climate are only possible via highly complex climate models, which by essence, are approximate and imperfect. It is worth mentioning that current models are nonetheless robust enough to perfectly describe past and present observations about global temperature variations as reported by the GISS (**Figure 1.5**).

Concerning the future, as described in **Figure 1.5** and with more details in ref [7], various scenario are possible, depending on human future GHG emissions and how ice sheets will actually respond to the evolving climate. However, conclusions provided by the authors are in all cases alarming. To the question 'can we avoid dangerous climate change?' based on the idea that 'dangerous' means different from the present climate which has existed for the last 12,000 years, the model shows it is already too late. The single increase in

temperature of 1°C (which is about to be reached around 2050 in the most optimistic scenario) will put the Earth in the conditions of half a million years back, where the stable water level was between 5 and 10 m above the current level (the most pessimist scenario gives about 25 m more). However even if the time for water level adjustment can be centuries, considering that more of a billion people live within 25 m above current sea level, societies will have to be prepared facing important climate refugees' migration movements, and deal with a massive ecosystem and wildlife disappearance. International cooperation to achieve a transition to clean carbon-free energy sources is of course absolutely needed before pushing the climate system beyond a level of irreversibility. However, the recent election of a climate sceptic at the head of the second CO_2 emissive country and the systematic rejection of modern ecologist parties in Europe is a waste of precious time.
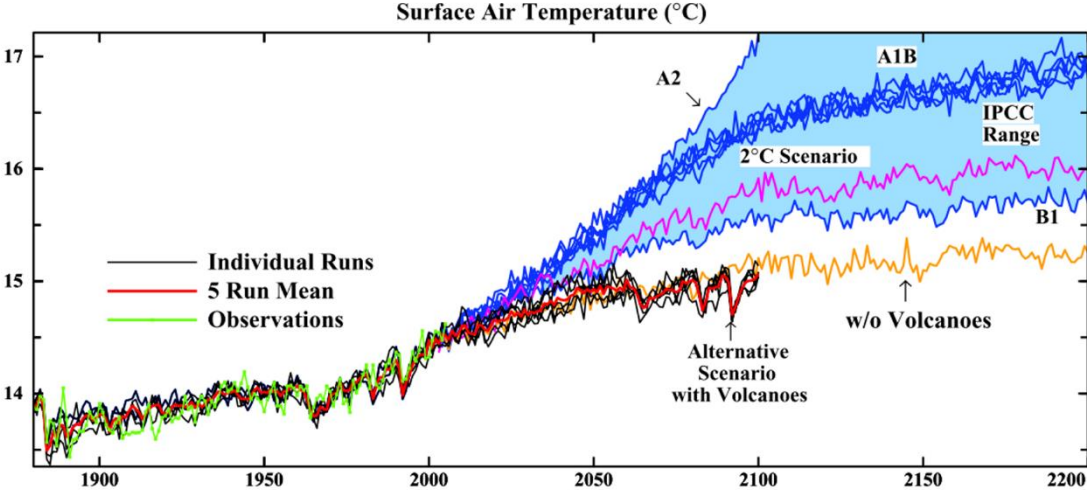
Figure 1.5: Global mean surface air temperature for several scenarios calculated according to the climate model used and presented in Ref [7].

1.1.2 The Energetic Transition

Nonetheless, reduction of greenhouse gas emissions (mostly carbon dioxide and methane) and the environmental damages caused by the depletion of fossil fuel resources are now of primary importance and raise international concerns. Agreements such as United Nations Framework Convention on Climate Change (UNFCCC) in May 1992, the Kyoto Protocol in December 1997 and more recently the United Nations Climate Change Conference (COP 21 or CMP 11) held in Paris in December 2015 have expressed the willingness of 195 states to increase their energy efficiency and the ratio of renewable

sources in their energy portfolio to limit the temperature increase below the value of 2°C above the pre-industrial period.
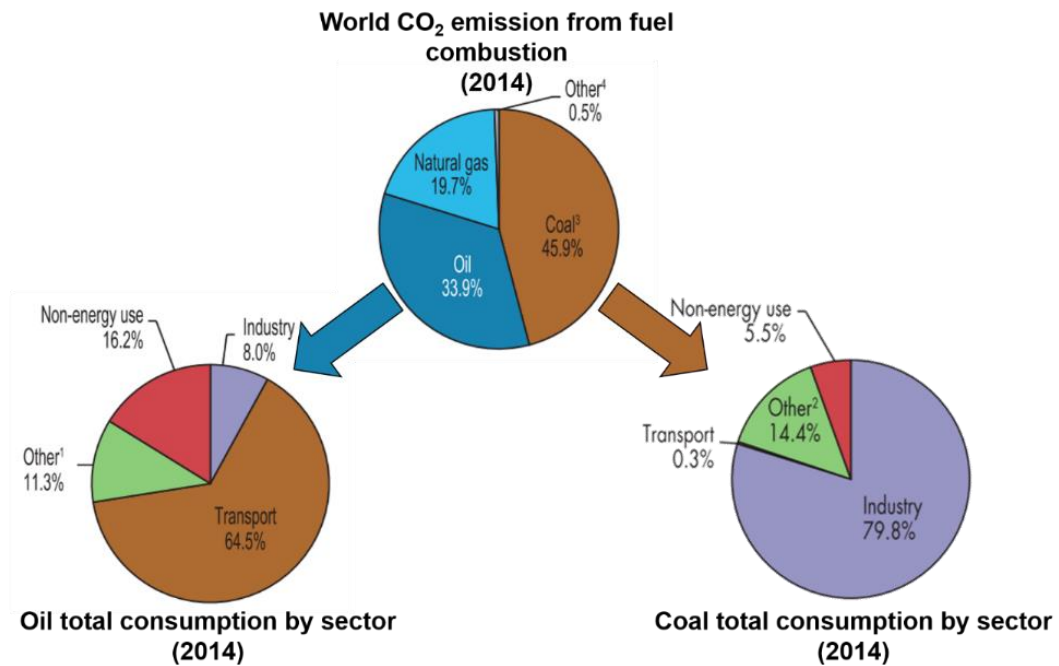
Figure 1.6: Origins of the CO_2 emissions from fuel combustion and their associated sectors. Adapted from Ref. [8].

To take appropriate governmental actions about how to decrease CO_2 emissions, it is essential to identify the critical sectors associated to massive GHG emissions. Statistics from the International Energy Agency (IEA, see **Figure 1.6**) revealed that in 2014, near 80% of the CO_2 emission originated from coal (45.9%) and oil (33.9%). Further studies clearly show that transportation sector is mainly responsible (64.5%) of the oil combustion while industry is by far the first coal consumer sector with a 79.8% part of the resource used principally for electricity production, but also steel and cement in lower proportions [9]. Mitigating greenhouse emission gas is unlikely to be achievable without deep technical revolutions in these sectors. Consequently, finding new routes for clean power generation and automotive engines has become the technological and scientific challenge of the 21st century.

- *Clean Power Production.*

Beyond ecological aspects, the rapid evolution of the economic and policy mechanisms toward energetic transition have made renewable energy systems (from renewable energy sources) a reality. The constant cost drops of solar, wind and hydro power systems associated with the fluctuations of oil and gas prices have finally caught financial markets

attention. This is well pictured by the fact that, since 1990, the renewable energy conversion has grown at an average annual rate higher than the world total primary energy source (2.2 % *vs*. 1.9 % respectively), with an especially high participation growth for solar photovoltaic and wind power (46.2 % and 24.3 % respectively) [10]. In 2014, renewables reached 22.3 % of the fuel shares in world electricity production. Because of the multiplicity and abundance of renewable energy sources all around the planet, the renewable energy-based transition is very likely to happen.

However, the intermittency of renewable sources (wind, sunlight etc.) makes this new form of electricity difficult to integrate in electrical grids, the latter being constantly maintained in the delicate equilibrium between power generation and demand. To address this issue, electricity produced after conversion of any renewable energy sources must be stored, to be later brought to its final conversion point by the consumer. In that context, clean and cheap energy storage systems development is of primary importance to the further expansion of decarbonised energy-based societies.

- *Towards Electric Vehicles*

Considerable efforts have also already been made to develop Electric Vehicles (EVs) worldwide. Indeed, as part of the actions taken by governments in favour of Electric Vehicle Initiative (EVI), United States, United Kingdom, China, Japan, Germany and France invested more than 16 billion USD between 2008 and 2014 in infrastructures, fiscal incentives and RD&D in favour of EVs. At the end of 2014, the global EV stock reached more than 665,000 unities which correspond to an increase of 370 % in a period of 2 years [11]. Beyond expectations, 2015 broke the threshold of the million electric cars, with 1.26 million EV on the road. If the EVI targets 20 million EVs deployed by 2020, this value still represent only 1.7 % of the global market share [12]. That means spread of EVs must goes with the decrease of the total number of vehicles, the latter can be achieved by the massive development of clean public transport. However, batteries costs and ranges are still key barriers for EV penetration to the mass market. Currently in France (May 2017), the average price of an EV produced by European main manufacturers is about 25,000-30,000 €, the latter being highly impacted by the lithium-ion based battery technology used.

- *Energy Storage and Hydrogen*.

Improving energy storage might be a convenient solution to reduce CO_2 emissions from the two first fossil fuel consumers (power production and transportation sectors). Many requirements are expected for suitable energy storage systems such as: (i) high energy and power densities (both gravimetric and volumetric), (ii) easy implementation in the existing energy network, (iii) high energy efficiency, (iv) economic viability, (v) sustainability and (vi) safety operation. As shown both in **Table 1.1** and **Figure 1.7**, each storage system device has its own application field, depending if high-power density, or long-term storage with high energy density is needed. If batteries are often chosen for short-term storage applications, their use as a long-term storage solution is compromised due to unavoidable self-discharge issues.

Table 1.1: Main properties comparison for several types of energy storage systems. From reference [13].

Technology	Capital cost ($/kWh)	Durability (Year)	Power density (W kg^{-1})	Gravimetric energy density (Wh kg^{-1})	Energy Efficiency (%)
Li-ion battery	600-2500	5-20	100-5000	75-250	85-90
Super-capacitor	300-2000	20+	500-5000	0.05-30	97
Pumped-hydro	5-100	40-100	-	0.5-1.5	70-87
Hydrogen	2-20	30	-	400-1000	-
Flywheel	1000-5000	15-20	400-1600	5-130	80-99
Pressurized air	2-50	20-100	-	30-60	40-80

The relative low-cost, sustainability and high energetic density (gravimetric) of hydrogen based systems make it one of the most interesting options for the long term storage and transportation applications. To be considered as a clean alternative to fossil fuels, all the branches of the energy chain relative to hydrogen must be further developed:

H₂ Production: If hydrogen is the most abundant element of the universe (75 wt. %), it can hardly be found in its pure dihydrogen form because of its highly reactive nature, but can be extracted from many natural compounds such as water, hydrocarbons and biomass [14]. Currently, 96 % of industrial hydrogen is produced from hydrocarbon reforming technique, which is a CO_2 emissive process known to produce a CO-polluted fuel [15] acooording to (using methane):

H₂ Production:

$$CH_4 + H_2O \leftrightarrow CO + 3H_2O \tag{1.1}$$

H₂ Purification:

$$CO + H_2O \leftrightarrow CO_2 + H_2 \tag{1.2}$$
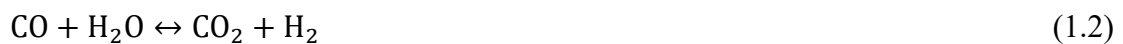
Only the last 4 % are produced via water electrolysis, which allows the conversion of electricity into high purity hydrogen (and oxygen) without any CO_2 emission. However, for the transportation application, according to the US Department of Energy (DoE), the transition toward hydrogen fuel would be economically viable if the hydrogen price of 1.3-2.5 € kg_{H2}^{-1} 'at the pump' could be reached. Large scale steam reforming production can compete with the final price of 1 € kg_{H2}^{-1}, while water electrolysis allows 50 € kg_{H2}^{-1} if renewable electricity is used.
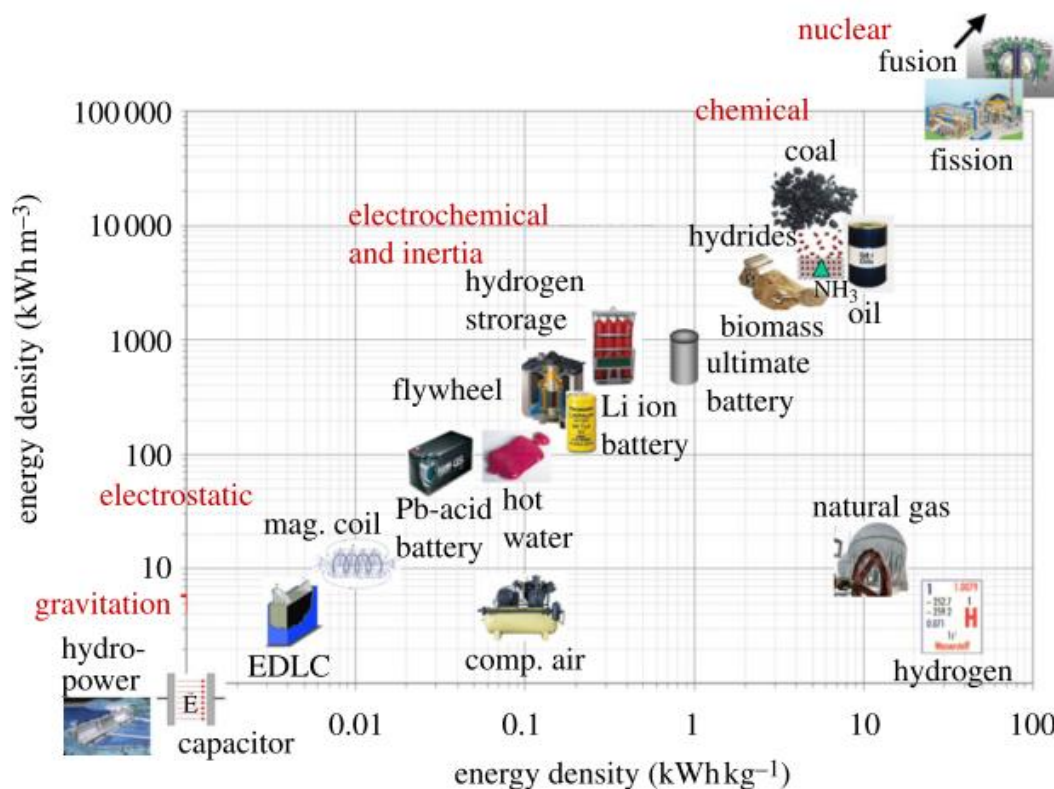
Figure 1.7: Volumetric versus gravimetric energy density of the most important energy carriers. From Ref [16].

H₂ Transport: Energetic transition is based on the idea that electricity (and so hydrogen through water electrolysis) will be produced in a de-centralized way, close to the renewable energy sources. The as-produced hydrogen energy vector has to be transported to its final place of consumption, or to hydrogen pump stations. Hydrogen can be transported after compression (1-2 MPa) via existing or new pipelines, but also by truck equiped with 20-35 MPa tank for short distances. Liquefied hydrogen offers a very interesting density improvement factor over gaseous hydrogen (about 800 times). However the liquefaction point of hydrogen (-253°C) requires the use of cryogenic tanks with their associated high energy consumption, making this alternative poorly attractive.

Table 1.2: Gravimetric and volumetric hydrogen densities in various materials and systems. The density in parenthesis is the theoretical limit of the given material. From Ref. [16]

	gravimetric hydrogen density ($kg\,H_2\,kg^{-1}$ system) (%)	volumetric hydrogen density ($kg\,H_2\,m^{-3}$ system)
pressure cylinder (500 bar, 25°C)	4	27
liquid hydrogen (1 bar, −253°C)	3 (100%)	40(71)
physisorbed hydrogen (70 bar, −200°C)	2(4%)	30
metal hydrides (1 bar, 25°C)	1.2 (1.85%)	50(110)
complex hydrides (1 bar, 150°C)	4 (13.5%)	50(120)
metals (1 bar, 25°C) Zn (H_2O)	3 (3.8%)	90
ammonia (1 bar, −33°C)	(17.6%)	(15)
hydrocarbons (1 bar, 25°C)	14 (14%)	10
water (1 bar, 25°C)	11	11

H₂ Storage: The very interesting high gravimetric energy density (39 kWh kg⁻¹) of hydrogen is however spoiled by its very low physical density of 11 m³ kg⁻¹ under ambiant conditions. Alternative routes to pressurized or liquid hydrogen are developped to increase its volumetric energy density and are presented **Table 1.2**. They include physisorbed hydrogen on high surface area materials (carbon nanotubes, metal organic frameworks (MOFs) etc.) or absorbed hydrogen in transition metal hydrides which can improve the volumetric density of hydrogen by three orders of magnitude (Mg_2FeH_6 and $Al(BH_4)_3$ can reach 150 kg m⁻³), without the risk of hydrogen leakage or tank explosion.

Finally, the further development of technologies for distribution, storage and use of hydrogen will be complementary to the development and widespread use of new CO_2-free production technologies, as briefly summarized **Figure 1.8**. However, if this concise and general introduction emphasized on the technical barriers to produce, store and transport hydrogen, there is still huge system improvements required for the electrochemical splitting (electrolysers) and recombination (fuel cells) of the water molecule. The next section is dedicated to the presentation of the proton exchange membrane fuel cell (PEMFC), as some problematics relative to this system are the purpose of this PhD thesis.
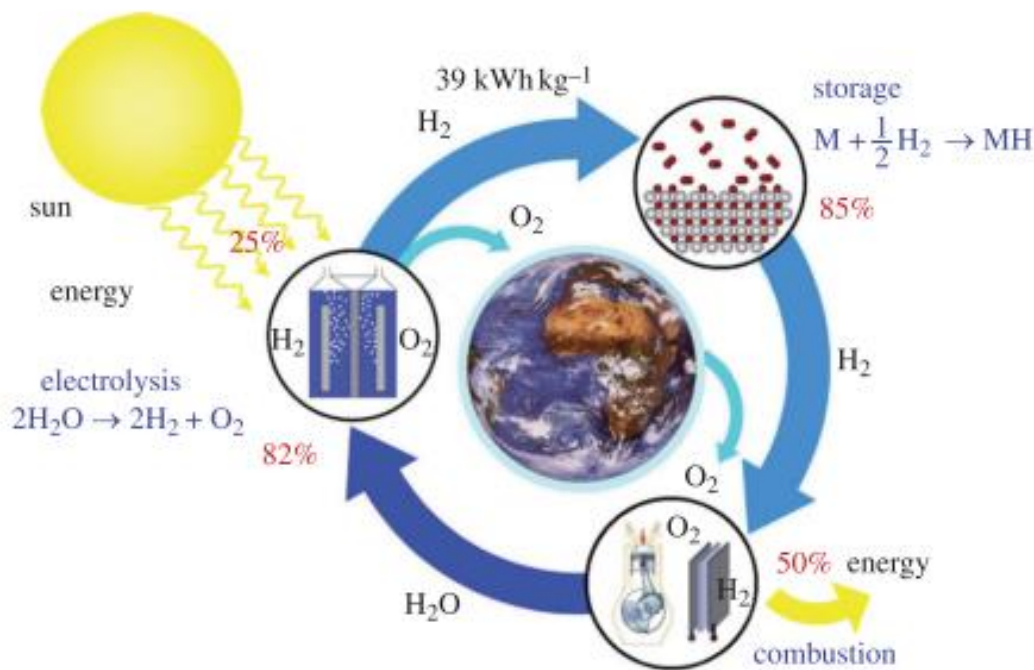
Figure 1.8: The hydrogen cycle: the energy from renewable sources (solar, hydro, wind etc.) is converted into electricity by means of photovoltaic cells or turbines. The electricity is used to dissociate water into hydrogen and oxygen. The latter is released in the atmosphere and hydrogen is stored, transported and distributed. Finally, hydrogen together with oxygen from the atmosphere are recombined to release electricity and heat, releasing water or steam in the atmosphere, closing the cycle. From Ref. [16].

1.2 PEMFC Overview

1.2.1 Principle

In batteries, electrochemical reactions are used to generate electricity, and the reacting materials, as well as the reaction products, are typically metals or other solid compounds (oxides, salts, etc.). In contrast, in fuel cells, both the reactants and the products are liquids or gases. This permits a continuous supply of reactants to the cell and a continuous removal of the reaction products. Thus, fuel cells generate electricity as long as the reactants are supplied and the reaction products removed. In contrast to batteries, they do not need to be refilled after complete discharge (exhaustion of the reactants). A variety of fuel cells exist, which differ in their constitutive materials, temperature range of use, electrolyte nature or electrochemical reactions. The technologically more-advanced fuel cell is the PEMFC, in which the hydrogen oxidation reaction (HOR) and the oxygen reduction reaction (ORR) take place at the anode and cathode, respectively. The membrane electrode assembly (MEA) is the core component of the PEM fuel cell. It is

28

an assembled stack of the proton exchange membrane, both anode and cathode catalyst layers and gas diffusion layers as shown on the scheme **Figure 1.9**.
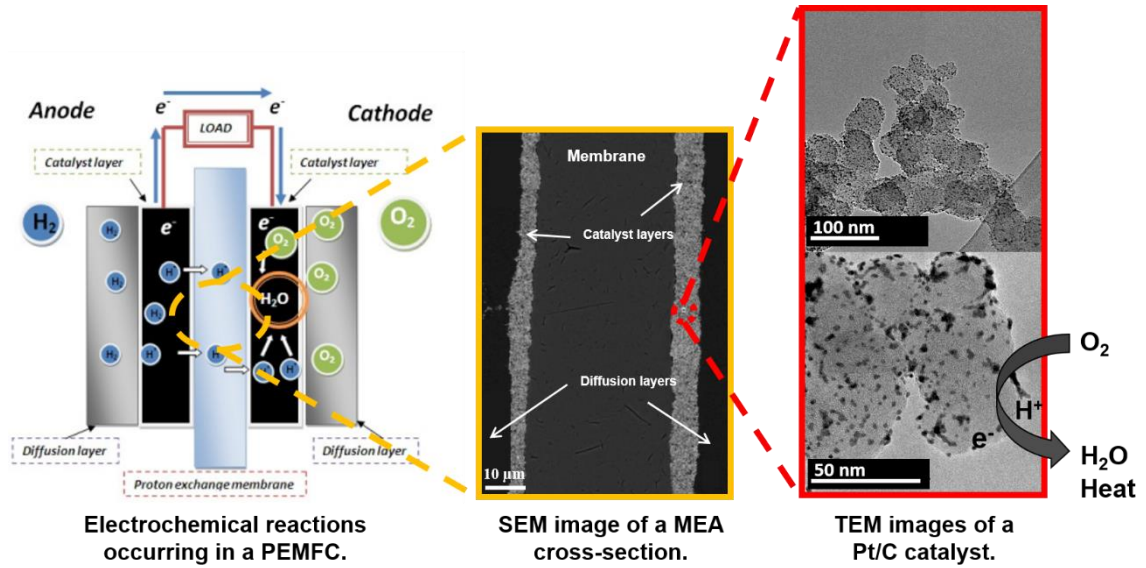
Figure 1.9: Components of a PEMFC single cell: schematic (left); scanning electron microscopy (SEM) image of the MEA (middle) and transmission electron microscopy (TEM) images of a commercial Pt/C catalyst (right).

At the anode, the HOR produces protons and electrons according to:

$$H_2 \rightarrow 2H^+ + 2e^- \qquad\qquad E^0_{H^+/H_2} = 0 \text{ V } vs. \text{ RHE} \qquad\qquad (1.3)$$

Where RHE is the Reversible Hydrogen Electrode. Those protons are forced to travel through the proton exchange membrane while electrons must take the external circuit to the cathode. At the cathode, protons recombine with electrons where oxygen is reduced according to:

$$O_2 + 4H^+ + 4e^- \rightarrow 2H_2O \qquad\qquad E^0_{O_2/H_2O} = 1.23 \text{ V } vs. \text{ RHE} \qquad\qquad (1.4)$$
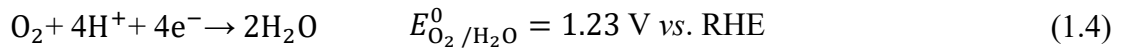
Finally, these exothermic reactions produce water and heat according to the overall reaction:

$$2H_2 + O_2 \rightarrow 2H_2O \qquad\qquad \begin{aligned} \Delta E^0 &= 1.23 \text{ V} \\ \Delta_r G^0 &= -237 \text{ kJ mol}^{-1}_{H_2} \end{aligned} \qquad\qquad (1.5)$$
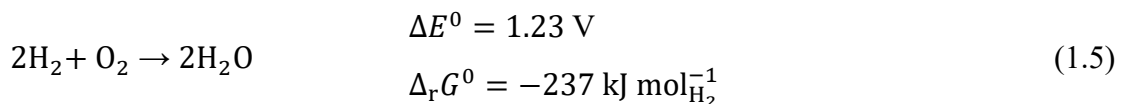
Thermodynamically, a single cell voltage is 1.23 V. Nevertheless, several factors can induce cell voltage drops:

Activation polarization: Mainly due to slow ORR kinetics and mixed potential caused by reactant permeation through the PEM.

Ohmic Polarization: Due to PEM and other components resistivity.

Concentration polarization: Reactants starvation at electrodes occurs for high current densities.

These factors are cumulative and affect the cell voltage on the global current range. However, it is possible to associate a region of the polarization curve to its dominant overpotential cause (note that others are also present) as shown **Figure 1.10**.
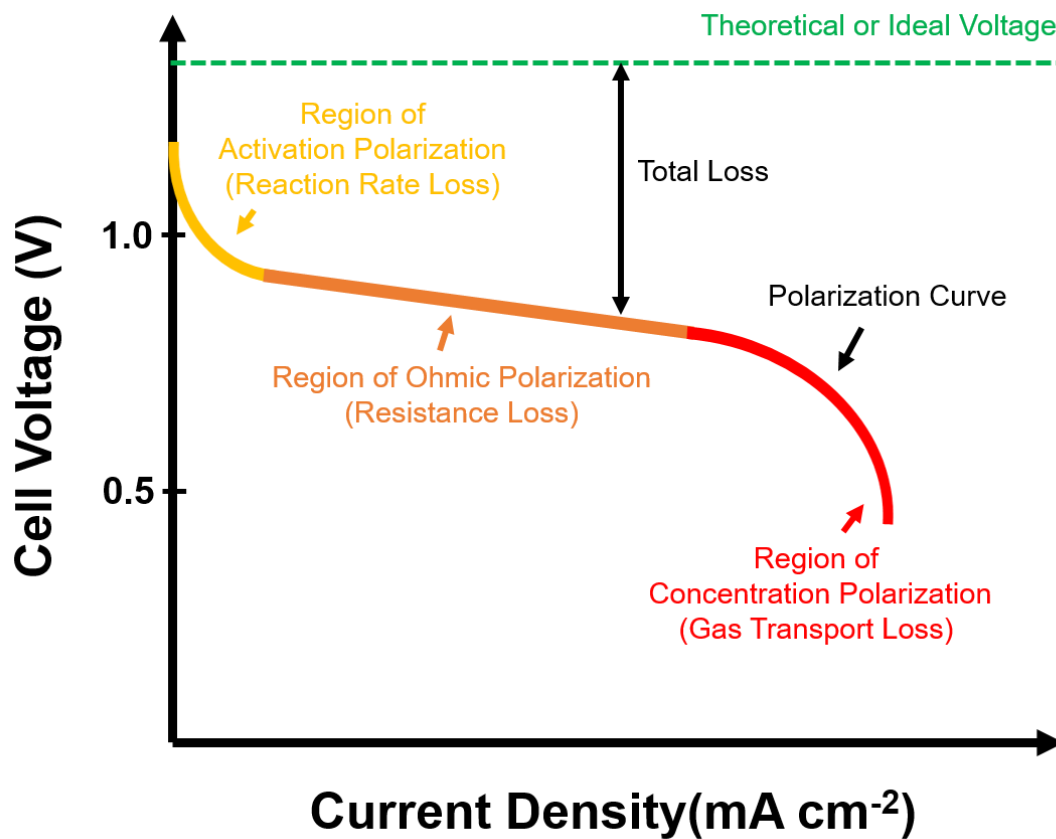
Figure 1.10: Ideal and practical fuel cell I-V (voltage *vs*. current) characteristics.

Usually, in first approximation, those overpotentials are simply added to obtain the cell voltage for an operating current *I*:

$$E(I) = E_{I=0} - \eta_{ORR}(I) - \eta_{HOR}(I) - \eta_{Conc}(I) - R_{\Omega}I \qquad (1.6)$$

Where η_i is the overpotential associated to reaction *i* and R_{Ω} the global electric resistance.

1.2.2 The Proton Exchange Membrane

The proton exchange membrane is the electrolyte of the PEM fuel cell. The three roles of the polymeric membrane in the PEM fuel cells are to:

- Provide an ionic path for protons to travel from the anode to the cathode,
- Separate the reactant gases,
- Be an electronic insulator.

In general, materials used in synthesis of the polymer electrolyte membranes are classified into three vast groups according to the literature [17]: perfluorinated ionomers (or partially perfluorinated), non-fluorinated hydrocarbons (including aliphatic or aromatic structures), and acid–base complexes. The most commonly used Nafion® membranes (**Figure 1.11**) developed by DuPont belong to the perfluorosulfonic acid (PFSA) membrane group.
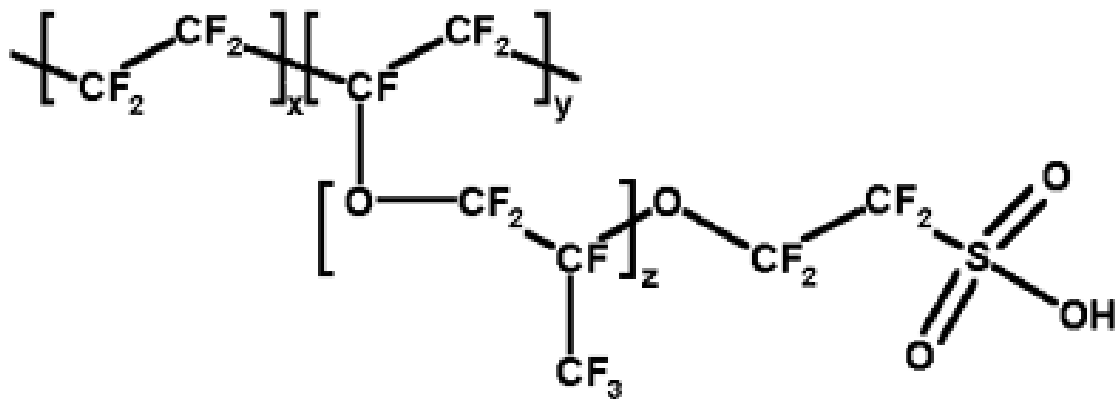
Figure 1.11: PFSA membrane structure. For Nafion ®: x = 6-10; y = z = 1.

Nafion® owes its mechanical integrity to the polytetrafluoethylene (PTFE) film structure and its ion exchange capacity from the perfluorinated side chain with terminal sulfonic acid groups. It can be underlined that the cost of such membrane technology (from \$400 to \$750 /m²) is currently one of the barriers for PEMFC development. For information, many promising researches based on radiation-grafted polymers [18,19] have been done recently to find alternative solutions to Nafion®. However, the polymer electrolyte membrane is currently still one of the components the most susceptible for failures. Three mechanisms can explain the membrane ageing [18] :

- Unzipping of polymer chains by radical attack. (Hydroxyl •OH or peroxy •OOH radicals) [19, 20].

- Mechanical degradation: crack and pinhole formation induced by temperature and humidity fluctuations [21].

- Thermal decomposition of the polymer.

A schematic of degradation mechanisms occurring into a PEMFC membrane has been proposed by de Bruijn *et al.* [22] and is shown on **Figure 1.12**:
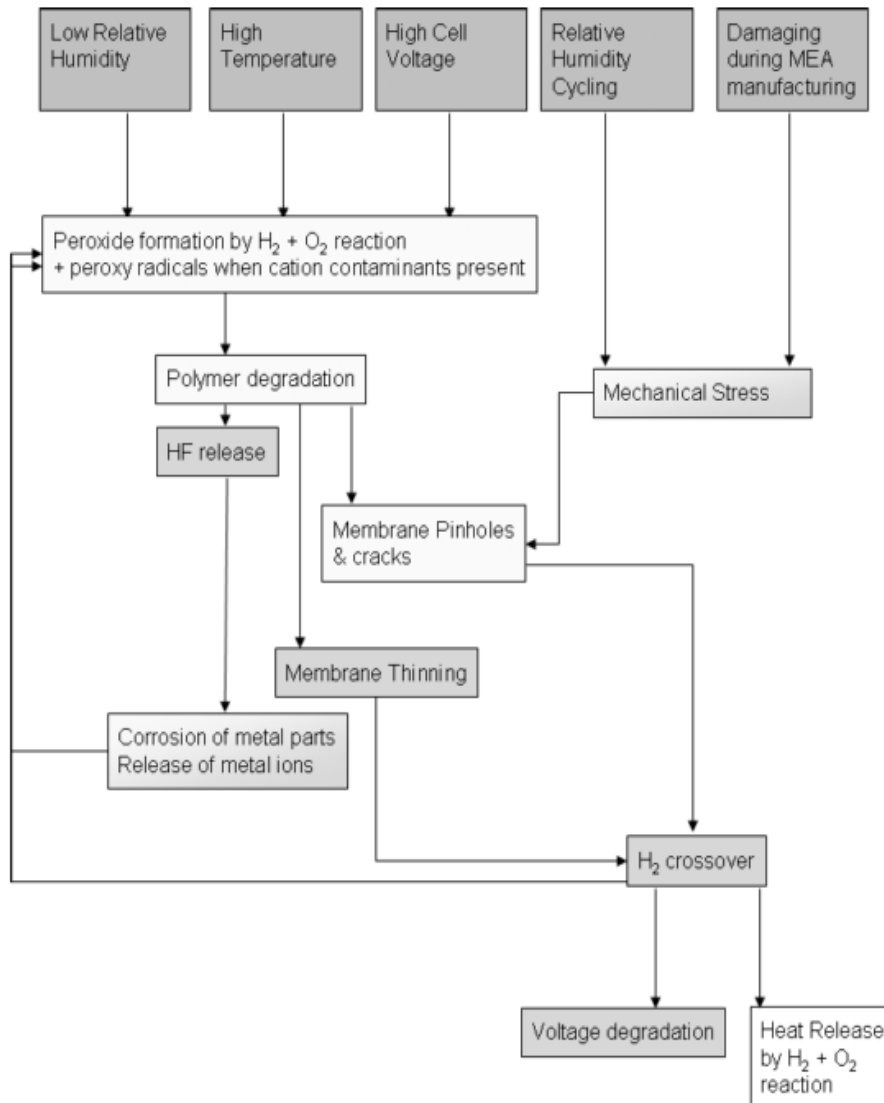
Figure 1.12: Degradation conditions, mechanisms and effects for perfluorinated membranes. Adapted from Ref. [22]

Many authors reported presence of fluorine ions, sulphate ions, and low-molecular weight perfluorosulfonic acid in drain water during PEMFC operation ([23], [24], [25] and [26]) which is believed to be an excellent indicator of membrane chemical degradation. Combined with studies of exhausted gas at cathode outlet by mass spectrometry where the formation of HF, CO_2, SO_x and H_2O_2 under open circuit potential (OCV) durability tests has been shown [27], a chemical degradation mechanism could be proposed. In this mechanism,

presence of oxygen at the anode side of the fuel cell because of cross-over, start/stop or air bleeding [28], leads, by reaction with hydrogen, to a production of H_2O_2 which can decompose to form the •OH or •OOH radicals. Even if they are not supposed to exist in currently chemically stabilized polymers according to **Figure 1.11**, polymer end groups with residual H-containing terminal bonds are believed to be formed during the polymer manufacturing process and may be present in the polymer in small quantities such as -CF_2X where $X = COOH$ for example [29]. These weak end groups are privileged sites for radical attacks, inducing 3 steps:

Abstraction of hydrogen from an acid end group (step 1):

$$R - CF_2COOH + \bullet OH \rightarrow R - CF_2 \bullet + CO_2 + H_2O \qquad (1.7)$$
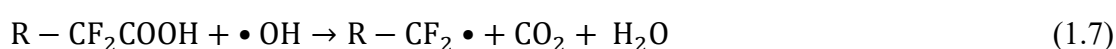
Perfluorocarbon radical reaction (step 2):

$$R - CF_2 \bullet + \bullet OH \rightarrow R - CF_2OH \rightarrow R - COF + HF \qquad (1.8)$$

Hydrolysis of the acid fluoride (step 3):

$$R - COF + H_2O \rightarrow R - COOH + HF \qquad (1.9)$$

At the end of step 3, weak H-containing terminal bounds are regenerated. This mechanism consequently '*unzips*' a complete PFSA unit into HF, CO_2 and other products. Besides, the reactant gas cross-over is believed to be a key factor in membrane degradation, but many other parameters can contribute to membrane ageing, particularly products from catalysts degradation as described in the following part.

1.2.3 The Catalyst Layers.

Currently in most PEM fuel cell systems, the most common catalysts used in both the anode and cathode are platinum (or platinum alloy) nanoparticles supported onto high surface carbon. The use of a precious metal for innovative technologies with wide applications is not without raising the thorny issue of Pt resources. The DoE has established in 2017 technical goals for reduction of the total Pt group metal (PGM) loading (metal mass per unit of surface electrode) to 0.125 mg cm^{-2}, targeting less than 10 g of precious metal per car by the year 2020 [30]. Strategies to reduce Pt loading in PEMFC catalysts will be further developed in a dedicated section.

1.2.3.1 Anode Catalyst.

Pure H_2:

The electrooxidation of hydrogen on platinum is well known to occur in two steps:

Dissociative adsorption of H_2 to form H_{ads} (Heyrovsky and/or Tafel mechanisms):

$$H_2 + Pt \leftrightarrow Pt\text{-}H_{ads} + H^+ + e^- \qquad \textit{Heyrovsky} \qquad\qquad (1.10)$$

$$H_2 + 2Pt \leftrightarrow Pt\text{-}H_{ads} + Pt\text{-}H_{ads} \qquad \textit{Tafel} \qquad\qquad (1.11)$$

Electrooxidation of H_{ads} into H^+(Volmer mechanism):

$$Pt\text{-}H_{ads} \leftrightarrow Pt + H^+ + e^- \qquad \textit{Volmer} \qquad\qquad (1.12)$$

This reaction is extremely fast, and is theoretically not a source of cell performance limitation (except in case of fuel starvation). But depending on the nature of the hydrogen, presence of pollutant (mainly CO) can strongly reduce anode reaction charges transfer as explained below.

CO poisoning:

The elimination of carbon monoxide is a current challenge in production of H_2 from decarbonized fossil fuels [15]. CO is very well known to decrease the performance of PEMFCs as it reduces the anode catalyst active surface area due to its strong adsorption onto the catalytic sites [31] depreciating the HOR kinetics, according to [32]:

$$CO + Pt = Pt\text{-}CO_{ads} \qquad\qquad (1.13)$$

This $Pt\text{-}CO_{ads}$ bond is much stronger than any Pt-H bond, nevertheless this adsorbed CO_{ads} can be electrooxidized at higher potential (0.6-0.9 V *vs.* RHE) according to the 'reactant pair' mechanism [33]:

$$Pt\text{-}CO_{ads} + H_2O \leftrightarrow Pt + CO_2 + 2H^+ + 2e^- \qquad\qquad (1.14)$$
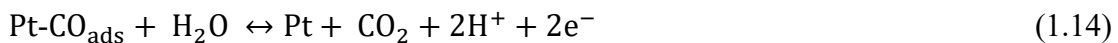
This mechanism needs the formation of oxygenated species from the water molecule dissociation on Pt. Then, these oxygenated species oxidize the adsorbed CO_{ads}. This poisoning issue is also occurring for Direct Methanol Fuel Cell (DMFC) where anodic methanol oxidation may lead to CO formation.

Pt-Ru anode catalyst:

It has been shown ([34–37]) that the use of alloyed or binary Pt-Ru as a catalyst at the anode strongly improves the PEMFC performance in presence of CO in the fuel. The enhancement of activity of Pt-Ru catalyst compared to Pt alone has been attributed to both:

- A bifunctional effect [38,39]: where the second (less noble) metal (here Ru) can generate OH_{ads} species from H_2O at lower potential than Pt. The OH_{ads} species oxidize adsorbed CO_{ads} on neighboring Pt catalytic sites (**Equations (1.15)** and **(1.16)**):

$$Ru + H_2O \leftrightarrow Ru\text{-}OH_{ads} + H^+ + e^- \tag{1.15}$$

$$Pt\text{-}CO_{ads} + Ru\text{-}OH_{ads} \rightarrow Pt + Ru + CO_2 + H^+ + e^- \tag{1.16}$$
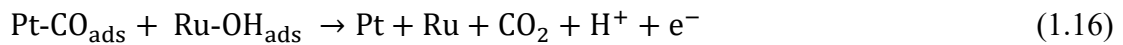
- A ligand effect (electronic interaction between Pt and Ru): where the presence of Ru reduces the strength of adsorption of CO on Pt, and so, facilitates the CO electrooxidation into CO_2 [34,40]. This effect will be further described in a following section.

Naturally, this catalyst is preferentially chosen for PEMFC system working with hydrogen from hydrocarbons based fuel and in DMFC devices.

1.2.3.2 Cathode Catalyst

At the cathode, the ORR (a relatively complex and slow reaction compared to HOR) occurs. Its low kinetics is mainly responsible for PEMFC overall performance limitation and remains since many years a challenging problem in electrocatalysis [41]. Several works in literature [41,42] highlighted two parallel mechanisms for oxygen reduction in acid environment as shown in **Figure 1.13** and **Equations (1.17)-(1.20)**:
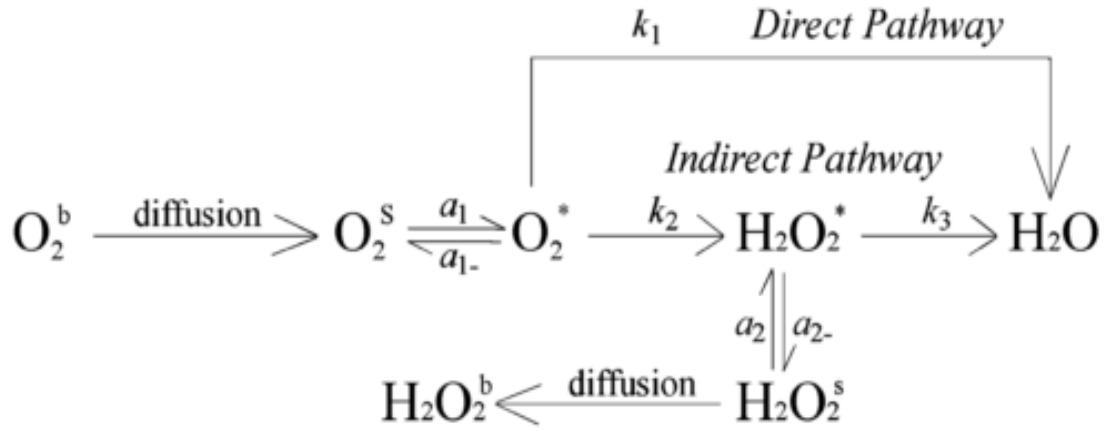
Figure 1.13: Simple scheme for the pathways of the oxygen reduction reaction. From Ref. [43].

4 electrons mechanism 'direct pathway':

$$O_2 + 4H^+ + 4\,e^- \rightarrow 2H_2O \qquad\qquad E^0_{O_2/H_2O} = 1.23 \text{ V } \textit{vs. } \text{RHE} \qquad (1.17)$$

2 electrons mechanism 'peroxide or indirect pathway' leading to H_2O_2 formation:

$$O_2 + 2H^+ + 2\,e^- \rightarrow H_2O_{2,ads} \qquad\qquad E^0_{O_2/H_2O_2} = 0.67 \text{ V } \textit{vs. } \text{RHE} \qquad (1.18)$$

Followed by either

$$H_2O_{2,ads} + 2H^+ + 2e^- \rightarrow 2H_2O \qquad\qquad E^0_{H_2O_2/H_2O} = 1.77 \text{ V } \textit{vs. } \text{RHE} \qquad (1.19)$$

Or

$$2H_2O_2 \rightarrow 2H_2O + O_2 \qquad\qquad (1.20)$$
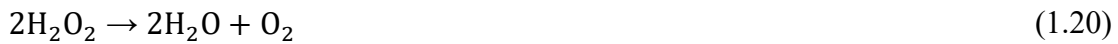
Based on rotating ring disk electrode experiments, several authors reported that the direct pathway on Pt is dominant, according to the small amount of H_2O_2 detected at the ring [41,42,44]. However according to the theoretical model developed by Nørskov and co-workers, the direct pathway on Pt is itself composed of several steps [45]:

$$O_2 + H^+ + e^- + Pt \rightarrow Pt\text{-}OOH_{ads} \qquad\qquad \textit{step 1} \qquad (1.21)$$

$$Pt\text{-}OOH_{ads} + H^+ + e^- \rightarrow Pt\text{-}O_{ads} + H_2O \qquad \textit{step 2} \qquad (1.22)$$

$$Pt\text{-}O_{ads} + H^+ + e^- \rightarrow Pt\text{-}OH_{ads} \qquad\qquad \textit{step 3} \qquad (1.23)$$

$$Pt\text{-}OH_{ads} + H^+ + e^- \rightarrow H_2O + Pt \qquad\qquad \textit{step 4} \qquad (1.24)$$

Changes in free energy compared to the final state for the different reaction steps (in the 'direct pathway') based on Density Functional Theory (DFT) calculations (from Rossmeisl *et al.* [46]) give further insights on the origin of the rather low ORR kinetics on Pt. One can observe **Figure 1.14**, that if the free energy for the overall reaction is globally diminished, there are two reaction steps (steps 1 and 4) where the change in free energy is positive. These two steps are limiting the reaction kinetics, and the one with the higher positive shift appears to be the decisive step. In case of Pt, the most positive ΔG is associated to step 4, meaning that OH_{ads} intermediates are strongly bound to the surface, block the surface and inhibit the reaction kinetics.
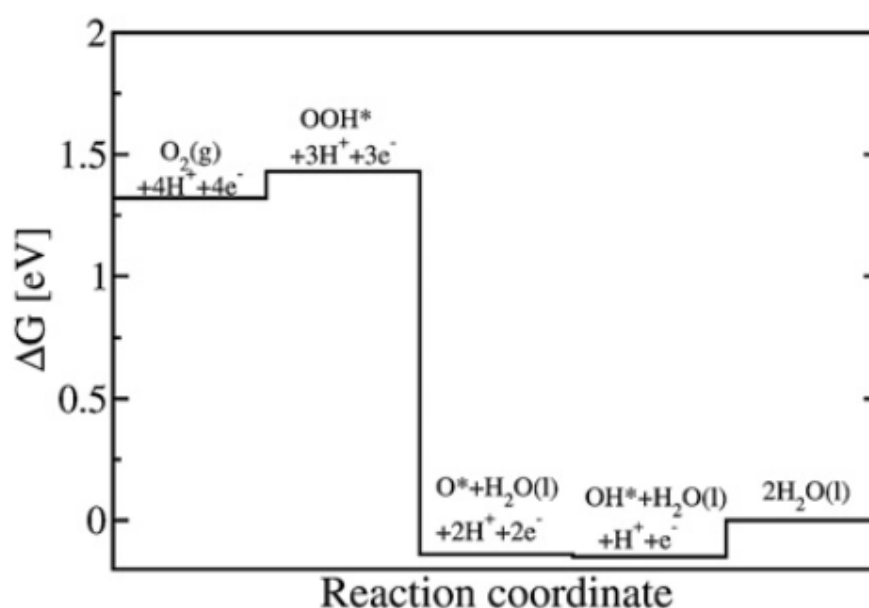
Figure 1.14: Free energy diagram for the 4 ORR 'direct pathway' steps at 0.9 V *vs.* RHE on Pt(111). The overall reaction decreases in free energy, but 1st and 4th steps show positive free energy changes. From Ref. [46].

Many efforts have been dedicated to tailor the structure and the atomic composition of the surface and near-surface layers of Pt-based catalysts to decrease the binding energy of $Pt\text{-}OH_{ads}$ intermediates, and a further detailed state-of-the-art on PEMFC cathode catalysts is proposed in the following chapter.

1.2.3.3 Carbon Support:

Carbon has been adopted for many years as widespread support for electrocatalyst because it's high electrical conductivity, low cost and relatively good chemical stability. Some of the key properties of high-surface area carbon (HSAC) supports commonly used in PEMFCs are referenced in **Table 1.3** [47].

Table 1.3: Carbon blacks commonly used as support for Pt catalysts in PEMFCs. From Ref. [47].

Carbon	Supplier	Type of carbon	BET surface area ($m^2\,g^{-1}$)[a]	DBP adsorption (units)[b]
Vulcan XC72	Cabot Corp.	Furnace black	250	190
Black Pearls 2000	Cabot Corp.	Furnace black	1500	330
Ketjen EC300J	Ketjen Black International	Furnace black	800	360
Ketjen EC600JD	Ketjen Black International	Furnace black	1270	495
Shawinigan	Chevron	Acetylene black	80	–
Denka black	Denka	Acetylene black	65	165

[a] BET: Brunauer–Emmett–Teller method.
[b] DBP: dibutyl phthalate number (measure of carbon void volume).

It may be seen that an 'ideal' electrocatalyst support must:

- Have a high specific surface area (m^2g^{-1}) to efficiently spread the metallic nanoparticles and avoid their agglomeration,
- Be chemically stable in the operating conditions of PEMFC anode and cathode,
- Have a high electronic conductivity.
- Be porous enough to allow reactant access to catalytic sites and products evacuation.

Because the cathode operates at the highest potential in a fuel cell (from 0.6 to 1.2 V *vs.* RHE), it is subject to severe corrosion phenomena. The electrochemical corrosion of the HSAC support is a major contributor to the catalyst degradation. As carbon is corroded, noble metal nanoparticles are detached or aggregate to form larger particles, which cause a loss of electrochemically active surface area (ECSA) and of catalyst mass activity. Note also that mild corrosion of the HSAC leads to changes in surface hydrophobicity that can cause gas transport limitations [47]. In the harsh operating conditions of a PEMFC (pH <1, 50-90°C) the following oxidation mechanism has been proposed: [48]

Oxidation of a carbon atom in the lattice:

$$C_s \rightarrow C_s^+ + e^- \tag{1.25}$$

Hydrolysis:

$$C_s^+ + H_2O \rightarrow C_sO + 2H^+ + e^- \tag{1.26}$$

Gasification of oxidized carbon to CO_2:

$$C_sO + H_2O \rightarrow CO_2(g) + 2H^+ + 2e^- \tag{1.27}$$

Roen *et al.* [49] showed that the corrosion rate of carbon catalyst support is accelerated in the presence of Pt-containing catalysts, due to the ability of Pt nanoparticles to more efficiently catalyse the oxidation of CO intermediate species (**Equation (1.27)**). Antolini

et al. and more recently Castanheira *et al.* showed that graphitized materials exhibit a better corrosion resistance [50–53] because of their more ordered structures,.

1.2.3.4 Pt Nanoparticles Degradation:

In addition to HSAC corrosion-induced nanoparticles loss or agglomeration, platinum corrosion is also thermodynamically possible in PEMFC cathode operating conditions (see Pourbaix diagram in **Figure 1.15**):

$$Pt + H_2O \rightarrow PtO + 2H^+ + 2e^- \tag{1.28}$$

$$PtO + 2H^+ \rightarrow Pt^{2+} + H_2O \tag{1.29}$$
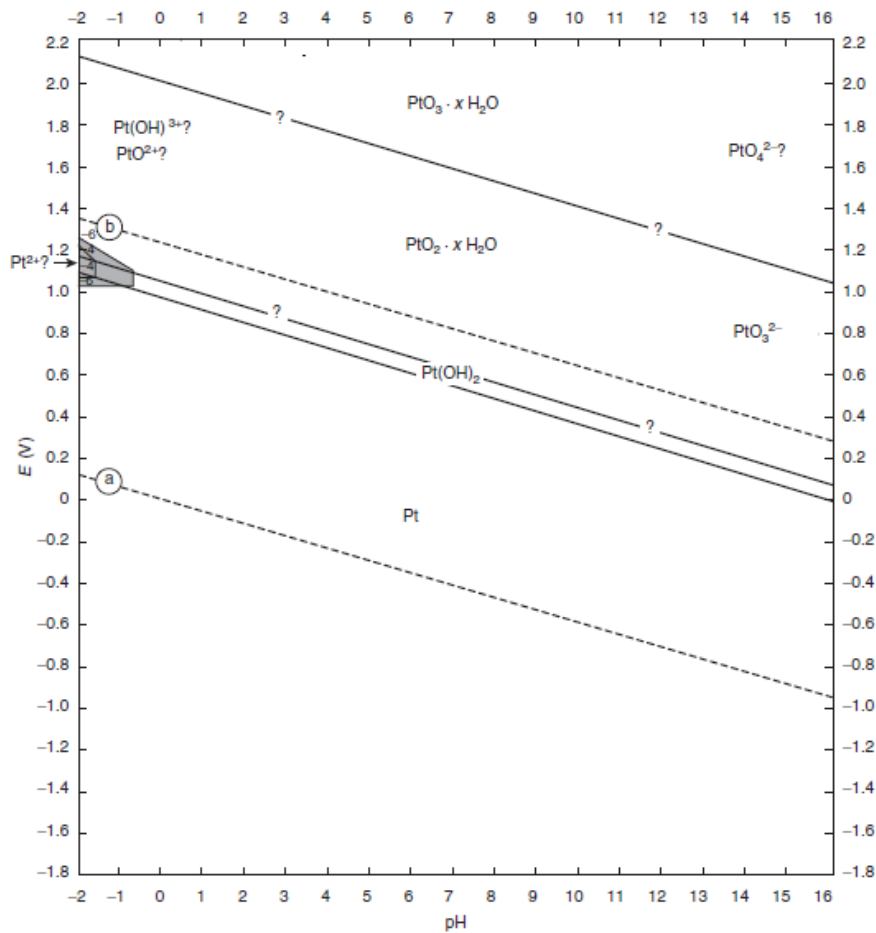
Figure 1.15: Pourbaix diagram of Platinum in water at 25°C. *E* (V *vs*. RHE) *vs*. pH

This phenomenon becomes thermodynamically more favourable with decreasing the size of the nanocrystallites, as the electrochemical potential of Pt atoms follows a Gibbs-Thomson relation (see **Figure 1.16**) [54]. This corrosion produces Pt^{2+} cations which can

spread all around the MEA and be electrochemically reduced on larger Pt particles (phenomenon known as Ostwald ripening as shown **Figure 1.16**) [54], or diffuse toward the anode side and be electrochemically reduced at this electrode or chemically reduced by H_2 molecules crossing-over from the anode to the cathode to form the so-called 'Pt band' in the polymeric membrane [55,56]. In any case, these degradation mechanisms yield lower catalyst specific surface area and consequently decrease of the PEMFC performance.

Chemical Potential

$$\mu_{Pt}(r) = \mu_{Pt}^o(\infty) + \frac{2\gamma V_m^{Pt}}{r}$$

$$\mu_{Pt}(r_o) > \mu_{Pt}(r_1)$$
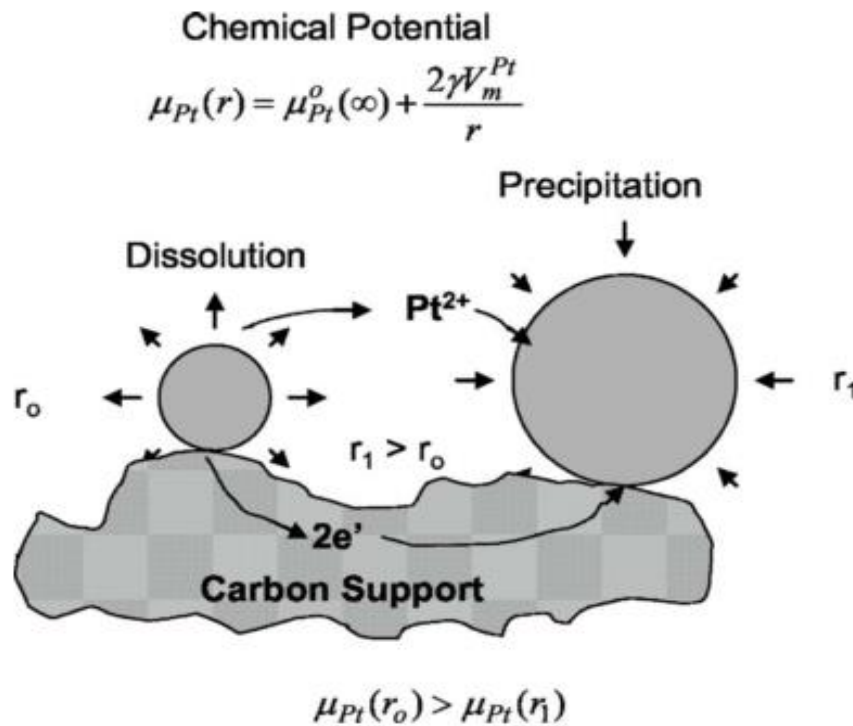
Figure 1.16: Ostwald ripening: dissolution of small particle with higher chemical potential, and precipitation on the larger ones. Cations transport occurs in liquid phase while electrons are transported by the conductive catalyst support (here carbon). From Reference [54].

In that context where the promising energetic alternative represented by the PEMFC is spoiled because of technical barriers having consequences on the system cost and durability, tremendous efforts have been made over the past decades to improve the cathodic catalytic layer. The next section of this PhD thesis is dedicated to a state-of-the-art of PEMFC precious metal-based cathode catalysts, presenting the main strategies to design material with reduced amount of precious metal and extended lifetime.

2 State-of-the-Art on ORR Electrocatalysis

2.1 The *d*-Band Theory for the ORR

2.1.1 Investigations on Extended Surfaces

As introduced in the previous section, Pt is the most active and stable electrocatalysts at a PEMFC cathode. **Figure 2.1** shows that metals having either stronger or weaker binding of oxygen than Pt poorly catalyse the ORR. In fact, this can be explained according to the Sabatier principle: if the interaction between the catalyst and the ORR intermediates (adsorbed O, OH and OOH species) is too weak (for example Au, Ag), no reaction takes place (right part of the volcano plot, the ORR kinetics is limited by the rate of electron and proton transfer). On the other hand, if the interaction is too strong (Fe, Ni), the catalyst surface gets blocked by adsorbed ORR intermediates (left part of the volcano, ORR rate is limited by oxide and anion removal). If it was established since the late 1980s-1990s, [57] that Pt alloyed with 3d transition metals (Co, Ni or Cu) better electrocatalyse the ORR, the DFT calculations from Nørskov *et al* [45].provided the reason why Pt better performs than other metals, and how its electrocatalytic activity can be improved (establish a delicate balance between OOH adsorption (step 1, **Equation (1.22)** and OH desorption (step 4 **Equation (1.24)**). Because the binding energies of OOH and OH species are proportional to each other, decreasing the binding energy of OH species (*i.e.* lowering ΔG_4) also results in decreased binding of OOH intermediates, and renders step 1 the limiting step: this is known as scaling relations and means that the two limiting steps of the Volcano plots cannot be optimized separately. Because of these relations, the optimal binding energy of oxygenated species is when $\Delta G_1 = \Delta G_4$. This optimal theoretical point may be reached for a surface binding oxygen about 0.2 eV weaker than Pt(111), and paves the way for ORR electrocatalysis optimization.

Following the work from Hammer *et al.* from 1995 [58] on the key parameters determining the reactivity of metal and alloy surfaces, Stamenkovic *et al.* investigated both experimentally and theoretically (DFT) the ORR activity of Pt$_3$M alloys with (111) crystallographic orientation (where M= Ni, Co, Fe, and Ti [59]). Alloying Pt with a transition metal is known to modify the surface reactivity according to the following effects:

Strain effect

Alloying Pt with smaller atomic size elements results in a contraction of the Pt lattice and a downshift of the Pt d-band centre. As the d-band centre of Pt surface atoms and the chemisorption energy of oxygen are correlated [59], enhanced ORR kinetics are observed on Pt_xM alloys $(0 < x < 1)$ relative to pure Pt. The degree of contraction of the Pt_xM lattice can be controlled by the nature of the alloying element, the chemical composition of the alloy, the degree of alloying, but also by post-treatments [60,61].
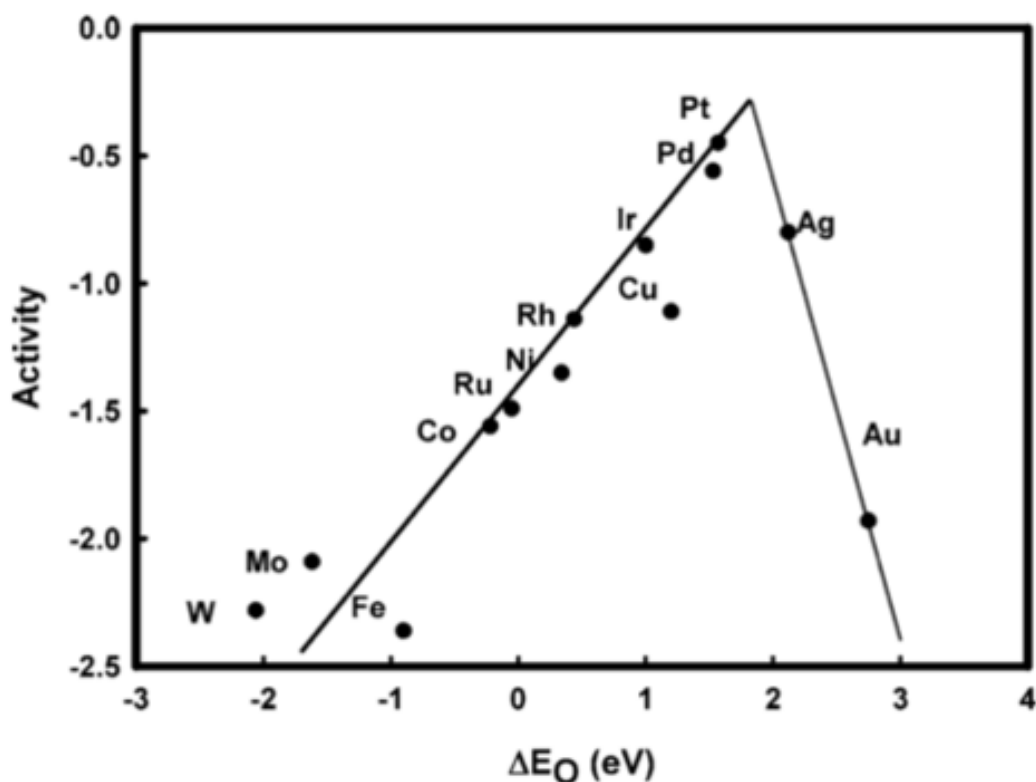
Figure 2.1: Trend in calculated oxygen reduction activity (arbitrary units) plotted as a function of the calculated oxygen binding energy for different metals. From Ref. [45]

Ligand effect

The ligand effect is due to the change in the electronic structure of the catalytic sites by the neighbouring M atoms. The strength of this interaction depends on the electro-negativity of the alloying element (the more electronegative, the more the Pt d-band vacancies increase due to a better affinity of electrons with the alloying element) [62].

In practice, because transition metals are easily leached out in acidic medium, Pt_3M single crystal surfaces from Ref. [59] consist of a pure Pt overlayer, with a M-enriched second layer on the top of the bulk Pt_3M composition ('Pt skin' structure). Both the computed

and physical Pt$_3$M surfaces resulted in a wide range of *d*-band centres and ORR activities. Surprisingly, while the Pt$_3$Ni alloy was predicted to feature the highest ORR activity according to DFT calculations, Pt$_3$Co was best performing for the ORR. However, one year later, Stamenkovic *et al.* reported that a Pt$_3$Ni(111)-skin surface performed 10 times and 90 times better compared to Pt(111) and a commercial Pt/C catalyst, respectively, in agreement with their previous theoretical work [59,63]. Although this surface has become the model surface for the ORR, the authors also reported the influence of the low-index surface orientation on the structure-sensitive adsorption of OH, establishing a hierarchy for Pt(*hkl*) (activities increasing in the order Pt(100) << Pt(111) < Pt(110)) or Pt$_3$Ni(*hkl*)-skin (Pt$_3$Ni(100)-skin < Pt$_3$Ni(110)-skin << Pt$_3$Ni(111)-skin) surfaces. Such effect is referred to as 'structural effect' or 'ensemble effect' in the literature, and interacts synergistically with the previously introduced 'strain' and 'ligand' effects.

It worth mentioning that late transition metals are not the only candidates for bimetallic PtM ORR catalyst. Using a computational screening, Greeley *et al.* identified various promising bimetallic alloys based on Pt and early transition metals [64]. In the screening process, the main parameters were the difference in O binding energy compared to Pt(111) (to reach higher ORR activity) but also the heat of formation of the PtM alloy. Indeed, since late transition metals rapidly interdiffuse in PtM alloys [65–67], more negative alloying energy and higher dissolution potential are believed to result in more stable alloys due to the slower interdiffusion of the M metal, and thus to enhance its durability under harsh electrochemical environment [68]. Among the identified alloys, Pt$_3$Sc and Pt$_3$Y featured heat of formation per atom about 0.9-1 eV more negative than the late transition metals such as Pt$_3$Ni, Pt$_3$Co or Pt$_3$Cu, and the electrochemical measurement revealed an excellent specific activity for the ORR on bulk polycrystalline Pt$_3$Y. This surface also performed 6 times better than polycrystalline Pt at 0.9 V *vs.* RHE. However the prepared extended surface were not designed according to the model used for the screening: instead of a Pt monolayer on the top of the alloy, the experimental surfaces were shown to feature a ~1 nm thick Pt overlayer, which suggested that the lattice strain more than the ligand effect indeed controlled the ORR activity [69–71]. More Pt$_x$M were also tested, notably derived from Pt$_5$Ln, where Ln is in the lanthanide series (Tb and Gb) and featured 5 to 6-fold enhancement of the ORR kinetics over pure Pt [72].
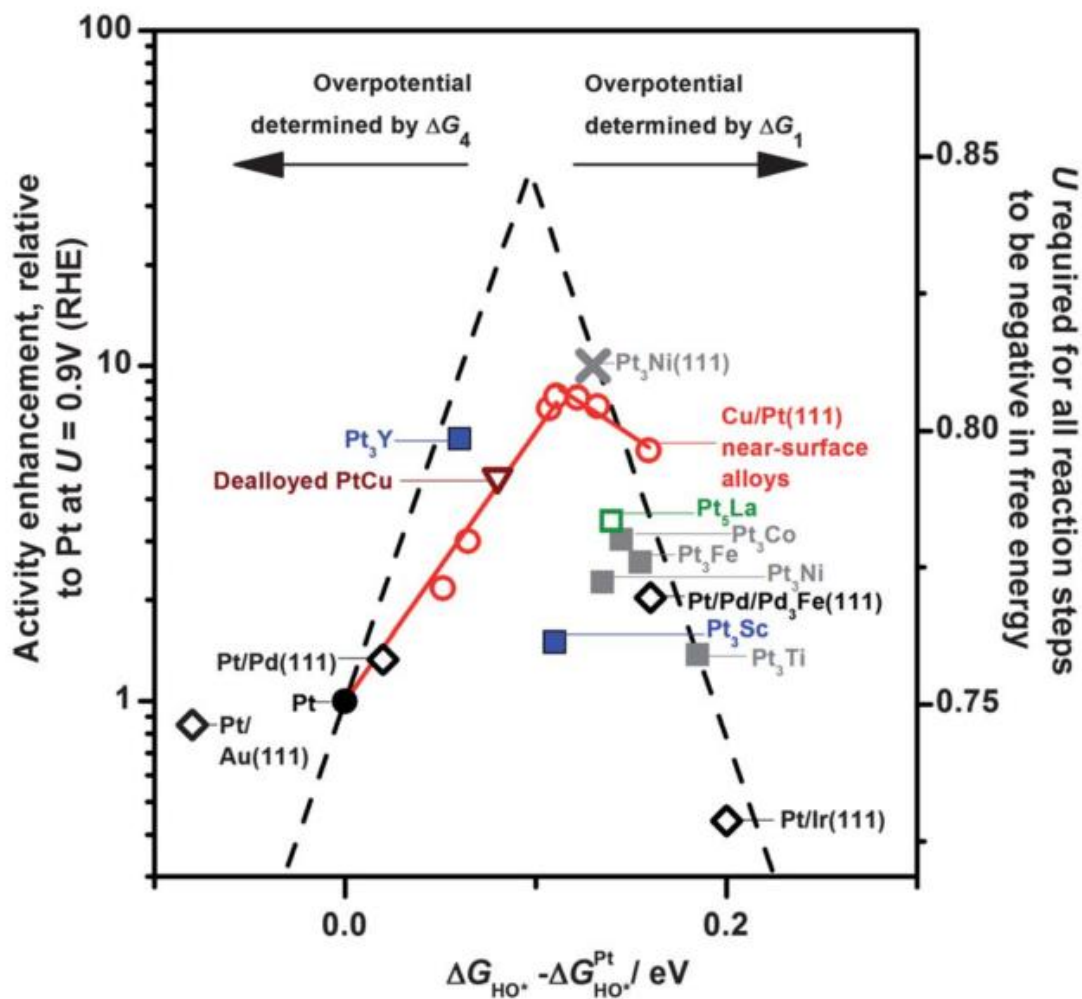
Figure 2.2: Volcano plot showing the rate of the oxygen reduction reaction on Pt-based alloys as a function of the calculated oxygen adsorption energy relative to Pt. From Ref. [69].

Finally, as represented in **Figure 2.2**, the intensive work on extended crystal surfaces has allowed the comprehension and further optimisation of Pt-based surfaces, leading to experimentally reach almost the optimal theoretical value in activity for the oxygen reduction reaction. However, in view of practical PEMFC systems, the findings obtained on extended surfaces must be transposed to nanomaterials: this is the aim of the following section.

2.1.2 From Single Crystals to Nanoparticles

Because ORR occurs at the surface (heterogeneous catalysis) of the rare and precious metal that is Pt, a catalyst with the highest possible surface / volume (*i.e.* mass) ratio is desirable. To take into account the high price of Pt, the efficiency of PGM catalyst is

usually expressed as the kinetic current associated to the reaction normalized by the mass of precious metal used:

$$MA\ [A\ g_{Pt}^{-1}] = S_{pt}[m_{Pt}^2\ g_{Pt}^{-1}] \cdot SA\ [A\ m_{Pt}^{-2}] \tag{2.1}$$

Where S_{pt} is the Pt specific surface area of the catalyst and MA and SA are its mass activity and specific activity for the reaction, respectively.

To maximize MA, both the S_{Pt} and the SA must be optimized. Whereas the most active surfaces (best SA values) for the ORR are extended surfaces presented in the previous section (**Figure 2.2**), a dramatic increase of S_{Pt} is observed on nanomaterials. In fact, for a spherical nanoparticle of radius r and density ρ, the surface to volume ratio and S_{Pt} are inversely proportional to its size according to:

$$S_{pt} = \frac{4\pi r^2}{\frac{4}{3}\pi r^3 \rho} = \frac{3}{r\rho} \propto \frac{1}{r} \tag{2.2}$$

As an example, Pt marbles (1.5 cm diameter) and 3 nm nanoparticles have specific surface areas of ~19 mm² g_{Pt}^{-1} and 93 m² g_{Pt}^{-1} respectively, meaning a ~5 million-fold enhancement of the specific surface area in favour of the nanoparticles.

Consequently, lot of efforts have been made over the past decade to transpose the optimized electrocatalytic properties for the ORR from single crystals to nanocatalysts in order to reach high mass activity values and thus increase the electrical performance of the PEMFC at a reduced cost. However, because of the small length scale in nanoparticles (quantum confinement), the usual energy band structure observed for bulk materials tends to disappear for discrete energy levels [73]. These changes in system energy have important consequences on its thermodynamic stability: nanoparticles can for example adopt a crystal structure different from that of the normal bulk materials. This modified electronic structure may also change the chemical reactivity of the particles, as well as their magnetic (supraparamagnetism), optical (plasmon resonance), thermal (diminution of the fusion point) or electrical (superconductivity) properties which all depend on the occupation of the outermost energy levels [74]. Additionally, surface atoms (in increased proportion in nanomaterials) feature a reduced number of nearest-neighbour atoms, which lead to differences in bounding and electronic structure, giving a rise in the surface energy and so chemical reactivity. The drawback of these metastable structures is their low

stability under variable potential and temperature conditions as exposed in the general introduction. The following sections will focus on the recent advances and challenges toward active and stable nanomaterials for the ORR.

2.2 Recent Advances in PEMFC Cathode Electrocatalysts

2.2.1 Shape-Controlled PtM Nanoparticles

The direct application of the conclusions obtained from single crystals studies leads to the idea that octahedral nanoparticles with a Pt_3Ni-skin composition would be the optimal catalyst for the ORR. Indeed, in the face centred cubic crystallographic system (which is the case for Pt_xNi_{1-x} alloys), the octahedral shape exhibits only (111) oriented facets, and so, this morphology is well-adapted to the maximal deployment of the ideal $Pt_3Ni(111)$-skin surface.

In 2010, Zhang *et al.* [75] reported the synthesis of very active Pt_3Ni nanoctahedra for the ORR, using oleylamine and oleic acid as both solvent and capping agents, and tungsten hexacarbonyl ($W(CO)_6$) as reducing agent. According to the authors, the presence of $W(CO)_6$ in the synthesis medium is key to reach high shape control of the nanocrystal, not because it stabilizes the (111) facets (that would be more the role of oleylamine and oleic acid, even if this facet orientation is naturally more stable) but because it facilitates fast Pt nucleation. By changing the order of addition of the synthesis precursors, nanocubes of same size and composition but exhibiting different surface orientation were produced. Surprisingly, the PtNi octahedra achieved 'only' 5 and 7-fold enhancement in specific activity (2.8 and 4-fold enhancement in mass activity) relative to the nanocubes and commercial Pt/C, respectively (where an enhancement of the ORR kinetics up to 90 *vs*. Pt/C could have been expected with resect to single crystal studies), as shown in **Figure 2.3**. Nevertheless, the significant difference of ORR kinetics on various particle shapes (octahedra *vs*. cubes *vs*. spheres) highlighted the viability of the approach.
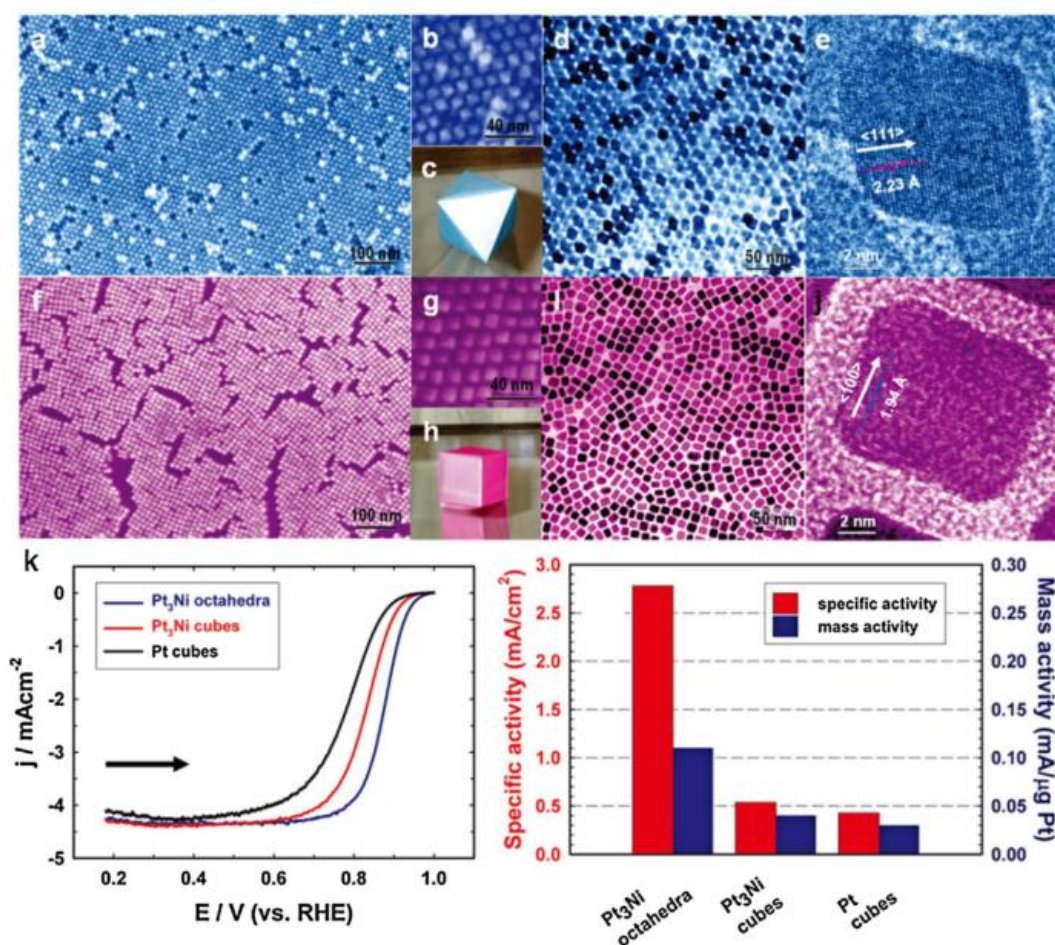
Figure 2.3: (a-e): Coloured TEM, HRTEM and physical images of Pt₃Ni nanoctahedra; (f-j): Coloured TEM, HRTEM and physical images of Pt₃Ni nanocubes; (k, left): polarization curves for ORR on Pt₃Ni octahedral, Pt₃Ni nanocubes and Pt nanocubes supported on a rotating GC disk electrode in O₂ saturated 0.1 M HClO₄ solution at 22 °C; scan rate, 20 mVs⁻¹; rotation rate, 900 rpm. Specific activity and mass activity were all measured at 0.9 V *vs.* RHE at 22 °C. From Ref. [75].

Two years later, using another synthesis route based on solvothermal reduction using *N,N*-dimethylformamide (DMF) as both solvent and reducing agent, Carpenter and co-workers prepared different alloyed Pt_xNi_{1-x} nanoctahedra with different nominal compositions. The Pt_1Ni_1 octahedra performed 15 and 5 times better than a commercial Pt/C reference in terms of specific and mass activity for the ORR, respectively [76]. The rationale for this enhancement was not discussed, but this was the first evidence that a fine tuning of the surface composition is also required to improve the ORR activity of bimetallic nanomaterials. Stability tests (20,000 potential cycles between 0.6 and 1.0 V *vs.* RHE at 25 °C) resulted in 50 % and 40 % decrease in specific activity and mass activity respectively, due to the massive loss of nickel and of the particle shape.

The same year, Cui *et al.* [77] opted for a better control of the near-surface composition of PtNi octahedral particles. Using also a solvothermal synthesis, the authors managed to

keep the nanoparticle bulk composition rather constant ($Pt_{46}Ni_{54}$) while enriching the first three atomic layers in Pt simply by increasing the duration of the synthesis. A 10-fold enhancement of both specific activity and mass activity was reported for catalysts featuring a Pt-enriched surface. In another study published in 2013 [78], using Scanning Transmission Electron Microscopy coupled with Electron Energy Loss Spectroscopy (STEM-EELS), the same authors reported that the corners and edges of the nanooctahedra are Pt-rich while the (111) facets are more Ni-rich due to anisotropic growth during the synthesis [79]. This elemental anisotropic growth is the reason for both high initial ORR activities, but also for the rapid decline in catalytic activity as Ni atoms are fastly leached out from the (111) facets, leading to a Pt-rich nanoframes exposing less active facets for the ORR (**Figure 2.4**). As discussed by the authors, a subtle equilibrium between Pt-rich shell thickness, subsurface Ni content and the ratio of stable (111) facets (during operation) are key factors for both ORR activity and stability.
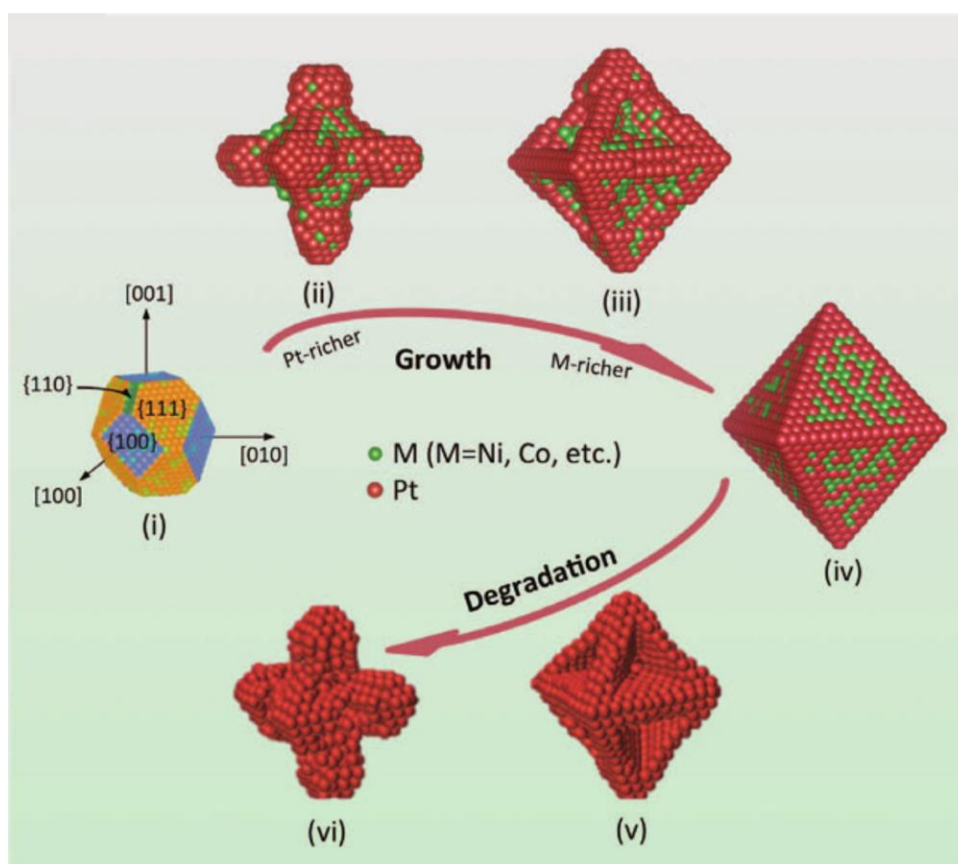
Figure 2.4: Atomic structural models of octahedral Pt bimetallic alloy NCs (Pt-M;M = Ni, Co, etc.) during the solution-phase co-reduction and during ORR electrocatalysis in acidic electrolyte. (i) Initially formed Pt-rich cuboctahedra. (ii) Rapid growth along the ⟨100⟩ directions, resulting in Pt-rich hexapods. (iii)A delayed, step-induced deposition of M-rich phase at the concave {111} surfaces. (iv) The complete formation of Pt-M octahedra with Pt-rich corners/edges and M-rich facets. (v) Selective etching of the M-rich {111} facets during ORR electrocatalysis in acidic electrolyte, leading to Pt-rich concave octahedra. (vi) Degradation of octahedra into Pt-rich hexapods after long-term electrode potential cycling. From Reference [79].

Since anisotropic elemental distribution seemed to be specific to solvothermal synthesis, in 2013, Xia's group modified the $W(CO)_6$-based synthesis first introduced by Zhang *et al.* [75] by using benzyl ether (BE) as a solvent and they treated the final particles with acetic acid in order to obtain a cleaner surface [80] (interestingly, the author attributed the shape control power to the $W(CO)_6$ due to preferential adsorption of CO on the (111) facets). A record 51-fold enhancement of the specific activity for the ORR compared to Pt/C was measured, approaching the theoretical value predicted on single crystal electrodes, while 40 % of mass activity was still lost after 5,000 potential cycles.

More recently, Beermann *et al.* tackled the stability issue by decorating the surface of PtNi nanooctahedra with 3 at.% of rhodium (Rh) [81]. Rh was believed to slow Pt surface diffusion under dynamic potential cycling, extending the octahedral shape conservation from 8,000 (undoped) to 30,000 (Rh-doped) potential cycles between 0.05-1.0 V *vs*. RHE. However, even if the shape and overall composition were longer maintained, the interdiffusion of Ni atoms and further leaching caused 65 % SA loss after the stability test.

2.2.2 Pt-Based Core-Shell Nanoparticles

Because of the lack of stability of shaped-controlled nanoparticles, Pt-based core@shell architectures have emerged as a promising paradigm to meet both activity and stability requirement of PEMFC cathode materials. A core@shell particle is characterized by a pure metal or alloyed core, surrounded by a Pt-rich shell, the latter providing high Pt utilization and preventing transition metal leaching. Besides, this structure offers Pt shell thickness, core composition, particle size and shape as tuneable parameters for catalytic properties improvement. Various synthesis routes have been reported in literature for the preparation of bimetallic core-shell catalysts. **Figure 2.5** shows an overview of the main approaches for the synthesis of bimetallic core@shell nanoparticles [82]. Surface segregation (case 1, route A-D) or deposition of Pt onto a pure M core (case 2, route E and F) are used as main strategies.

Routes A and B both use the difference between dissolution potential of the two metals composing the particle: by selectively dissolving the less noble metal, a Pt-shell is eventually formed and the process is stopped. In route A, an oxidative potential is applied to a Pt-poor alloy (electrochemical dealloying), while in route B a Pt-rich alloy is immersed in a corrosive environment (acid leaching). From this difference, original

structures can appear such as porous particles (route A) [83] or 'Pt skeleton' (route B) [84] and will be further discussed later. Another way to form a Pt-rich shell is to expose the PtM alloy to an atmosphere to which one of the alloy constituents has an affinity or in which it has a lower surface energy. Adsorbates such as CO, NO, O_2 or H_2 could be used [85], and possibly coupled with thermal annealing, with the risk of particle sintering [86].
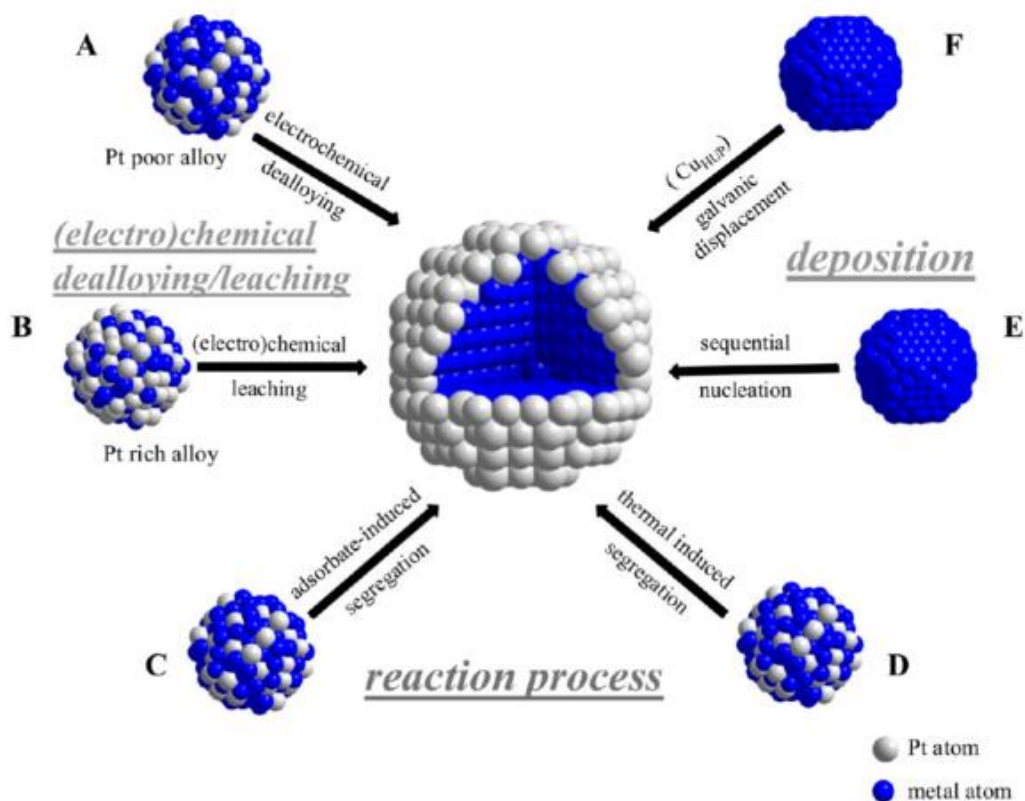
Figure 2.5: Illustration of basic synthesis approaches for the preparation of core@shell nanoparticle catalysts. Electrochemical (acid) dealloying/leaching results in (A) dealloyed Pt bimetallic core@shell nanoparticles and (B) Pt-skeleton core@shell nanoparticles, respectively. Reaction process routes generate segregated Pt skin core@shell nanoparticles induced either by (C) strong binding to adsorbates or (D) thermal annealing. The preparation of (E) heterogeneous colloidal core@shell nanoparticles and (F) Pt monolayer core@shell nanoparticles is via heterogeneous nucleation and UPD followed by galvanic displacement, respectively. Reprinted from [82]

In the second case (pre-formed non-noble metal M core), two deposition routes are possible depending on the origin of electrons used to reduce the Pt^{z+} ions ($z = 2, 4$). For route E, electrons are provided by an external reducing agent and the M core acts as a support for nucleation, while for route F electrons come directly from the sacrificial template core (galvanic replacement) until a protective Pt-shell is formed. In both case, the uniformity of the deposited Pt layer depends on the lattice mismatch between Pt and the substrate [87]. Briefly, depending on the energy balance between surface energies and

the interfacial energy of the lattice-matched system, three modes of nucleation and overgrowth have been observed and represented (**Figure 2.6 (a)).**
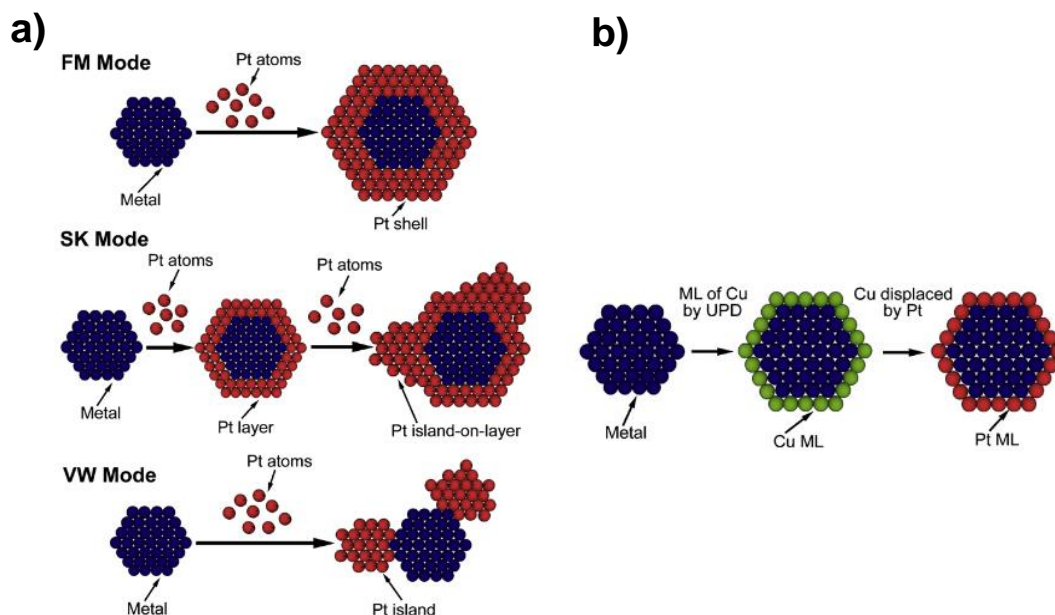
Figure 2.6: (a): schematic illustration of three different growth modes; (b): Schematic illustration of the synthesis of Pt mono-layer (ML) on metal nanoparticles using UPD followed by a redox replacement reaction. From Reference [87].

Under lattice-matched conditions with high interfacial bond energies, a Frank-van der Merwe (FM) mode or '2D layer-by-layer growth' occurs. On the contrary, if the lattice mismatch is high and the interfacial bond energy is low, a Volmer–Weber (VW) or '3D island growth' occurs to minimize the strain energy. An intermediate Stranski– Krastanov (SK) or 'island-on-wetting-layer growth' can also occurs in the case where the initial interfacial bond energy is sufficient to compensate the lattice mismatch and induce a temporary FM mode growth. But because of the progressive decrease of the interfacial bind energy with increasing number of Pt layers, the latter may become insufficient to compensate the lattice mismatch and a VW mode can take place. Of course, FM growth mode is required to obtained uniform core shell particles. It is however possible to obtain a Pt monolayer on a substrate with supposed SK or VW modes due to the lattice mismatch, by depositing *via* under potential deposition (UPD, route E) a sacrificial monolayer of another metal such as copper, followed by a galvanic displacement (route F) of the pre-deposited Cu layer by Pt cations (**Figure 2.6 (b)**), as shown by Adzic and co-workers [88].
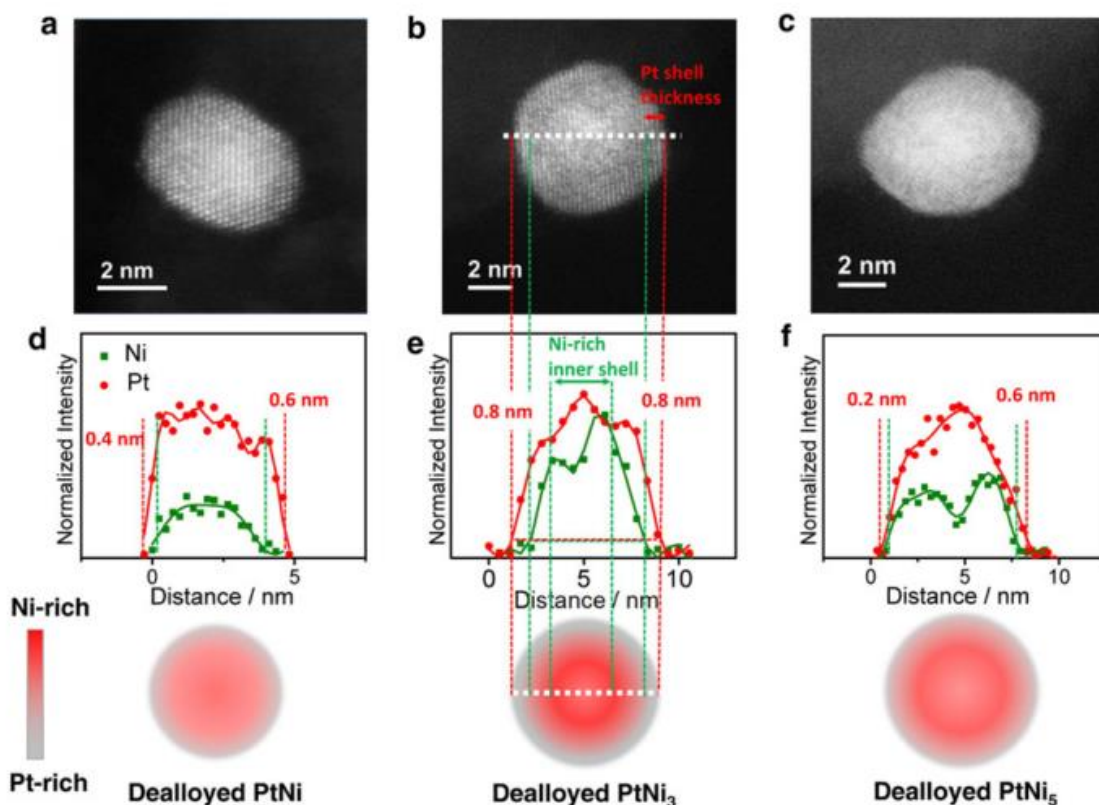
Figure 2.7: High resolution HAADF-STEM images of dealloyed PtNi (a), PtNi$_3$ (b) and PtNi$_5$ NPs (c), and EELS line compositional profiles (d– f) across the NPs, respectively. From Reference [89].

Using route A (dealloying), Strasser's group prepared various Pt$_x$Ni$_{1-x}$ core shell catalysts, among which the PtNi$_3$ displayed the highest enhancement factors of 5 and 10 times for mass activity and specific activity, respectively over a commercial 3 nm Pt/C catalyst. Interestingly, this PtNi$_3$ catalyst also showed the largest Pt shell thickness compared to other stoichiometries (**Figure 2.7**): this contrasts with literature beliefs that thick Pt-rich shell is associated to low ORR activity due to reduced compressive strain in the outermost Pt surface layer [90]. As presented on High Angle Annular Dark Field (HAADF) -STEM images and the associated EELS line-scan compositional profile in **Figure 2.7 (b and e)**, this catalyst seems to exhibit a Ni-enriched inner shell, believed to be responsible for high catalytic performance [91]. Such conclusion was confirmed by other studies which also suggested that a Ni-rich core protected by a Pt monolayer could lead to a decrease of performance and stability due to a too strong downshift of the Pt d-band centre and core instability [92,93]. This result shows that not only the near surface or shell thickness but the chemical composition of the first ~10 atomic layers control the ORR activity.

Further studies of the PtNi$_3$ core@shell nanoparticles (size comprised between 3 and 10 nm) revealed an enhanced stability during potential cycling compared to previously exposed complex shape-controlled metal alloy particles with only 24 % of mass activity loss after 30,000 potential cycles (0.6 – 1.0 V *vs*. RHE), thereby meeting the US DoE 2017 target for cathode ORR activity and durability in both Rotating Disk Electrode (RDE) and MEA tests [94], [95]. The same degradation protocol applied to a comparable catalyst but with broader size distribution (from 2 to 40 nm) revealed the formation of nanopores and voids during the initial electrochemical dealloying and/or further stability tests for particles exceeding a critical size (between 10 and 13 nm, see **Figure 2.8**), in agreement with former literature findings [83,96,97]. In fact, dissolution of non-noble metal (creation of vacancies) and surface diffusion of the noble metal (compensation of vacancies) are two competitive processes during dealloying according to Erlebacher *et al.* [98–101]. Increasing the particle size favours Rayleigh surface instabilities due to slower noble metal diffusion and thus formation of nanopores. In contrast, the increased mobility of noble metal uncoordinated atom at the surface of a smaller nanoparticle suppresses the formation of nanopores and leads to solid core@shell nanoparticles.
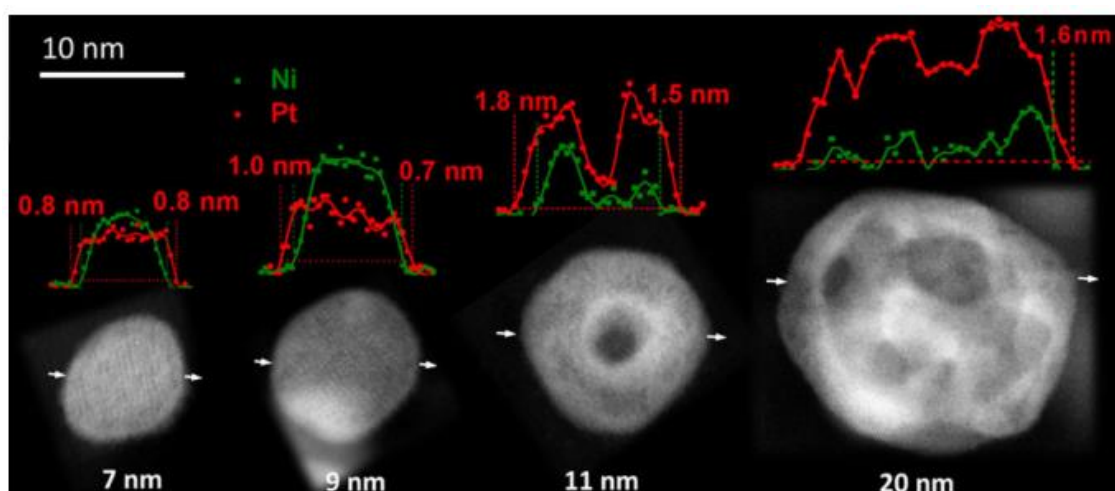
Figure 2.8: HAADF-STEM images and the corresponded EELS line-scan profiles of NPs with different sizes in air-dealloyed PtNi$_3$ catalyst after 10,000 cycles of stability test between 0.6 and 1 V *vs*. RHE. Particles larger than *ca*. 10 nm steadily showed the formation of nanoporosity and, consequently lower Ni content as well as larger Pt shell thickness after the accelerated stress test. From [94].

Although the porous hollow morphology may be desirable in electrocatalysis due to the increased specific surface area (see next section), the dealloyed nanoparticles owe their ORR activity to the compression of the Pt lattice induced by the high content of M (about 70 at. %) [102], and thus the gain in specific surface area due to nanopores hardly

compensates the dramatic drop in specific activity caused by the loss of lattice strain due to massive M dissolution [94]. To date, such size-controlled (below 10 nm) dealloyed PtM/C catalysts have shown the best compromise between initial activity (rather lower than shape-controlled nanoparticles) and stability (by far better than shape-controlled nanoparticles) under simulated and real PEMFC operating conditions [95]. However, the PEMFC stability tests mentioned in Ref. [95] were conducted under H_2/N_2 gas atmospheres (anode/cathode respectively), meaning that the impact of oxygen was not investigated.
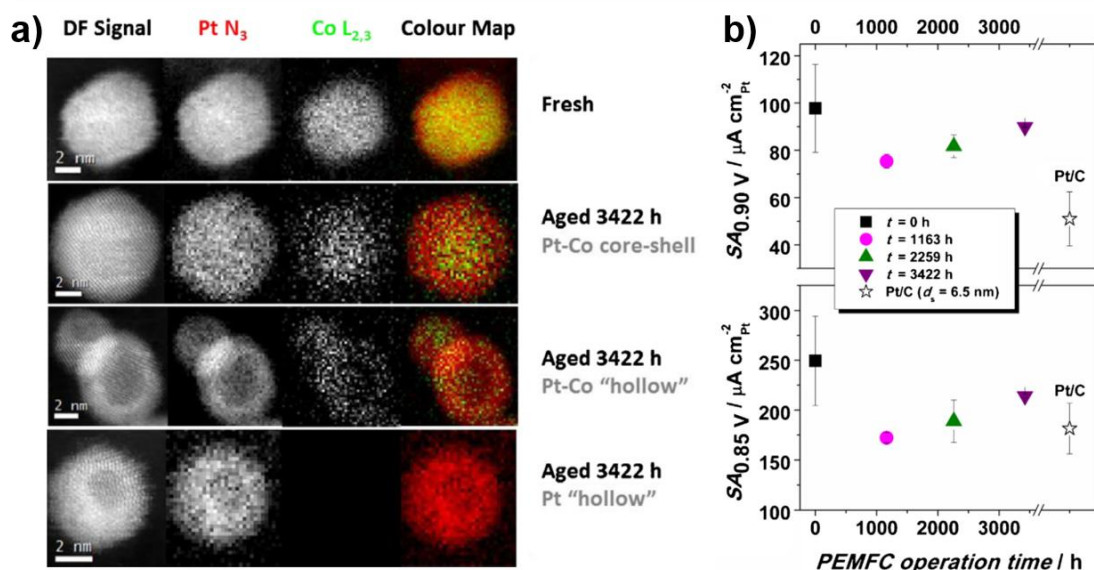
Figure 2.9: (a) HAADF-STEM and EELS elemental maps of a Pt₃Co catalyst before and after aging under PEMFC system, and (b) SA *vs.* cycling time of this Pt₃Co catalyst in comparison with a commercial Pt/C. Adapted from Ref [67].

In 2011, insights into the stability of Pt₃Co/C nanoparticles during real PEMFC operation (H_2/O_2) revealed the low stability of such catalyst, especially at low current density or during intermittent operation due to high cathode potential (> 0.6 V *vs*. RHE) [67]. The authors attributed the catalyst failure to particle agglomeration/detachment, 3D Ostwald ripening and compositional changes. Interestingly, despite a strong decrease in mass activity, the catalysts aged under such conditions featured an increase in specific activity for the ORR. HAADF-High Resolution STEM (HRTEM) and Energy Dispersive X-ray Spectroscopy (X-EDS) analyses shown **Figure 2.9** revealed the apparition of a Pt hollow nanostructure, formed by the leaching of Co atoms and the nanoscale Kirkendall effect. The Kirkendall effect is driven by the faster interdiffusion of non-noble metal atoms compared to noble metal atoms during thermsal annealing or upon strong adsorption. Consequently, the faster flux of the non-noble metal flux outwards cannot be compensated by noble metal motion inwards, leading to entrance of vacancies in the

nanoparticle. Ultimately, these atomic vacancies form nanoscale voids or a cavity located in the centre of the nanoparticle [103]. The authors attributed the catalytic activity gain to the formation of these hollow nanostructures (larger particle size, diminished concentration of under-coordinated atoms and lattice strain).

2.2.3 Hollow PtM Nanoparticles

Recently, due to facile tuning of their structure, shape and shell composition, surface to volume ratio, and their unique optic properties, hollow nanoparticles received much attention from medicine to catalysis applications. Unlike core@shell nanoparticles, the shell of a hollow nanoparticle surrounds one or several inner voids, and features nanoporosities which provide molecular accessibility. As previously discussed, hollow nanostructures can be prepared by dealloying core@shell nanoparticles (route A and B in **Figure 2.5**). The formation of nanopores depends on the initial particle size, dealloying method (nature of the electrolyte, temperature, atmosphere etc.), but the obtained particles were under poor morphology control. A method of choice to produce hollow, or hollow-porous structures combines galvanic replacement with other phenomena, which can be introduced or inhibited by adjusting a set of physico-chemical parameters [104–106]. This route consists in the sequential formation non-noble metal particle template onto which a noble metal alloy shell is deposited, followed by a selective removal of the non-noble particle core. Because galvanic replacement is a redox process, it is driven by the difference in the standard potential between the two metals involved. Basically, the metal core must have a lower standard potential to act as the anodic sacrificial template and provide electrons for the deposition of a metal with higher standard potential. **Table 2.1** shows examples of standard potentials of common template and deposited metals.

Table 2.1: Standard potentials of different metals in aqueous solution at 25 °C and 1 atm relative to the standard hydrogen electrode (SHE).

Redox Reaction	E^0 *vs.* SHE
$Co^{2+} + 2e^- \leftrightarrow Co_s$	-0.28
$Ni^{2+} + 2e^- \leftrightarrow Ni_s$	-0.25
$Cu^{2+} + 2e^- \leftrightarrow Cu_s$	0.34
$Ag^+ + e^- \leftrightarrow Ag_s$	0.80
$Pd^{2+} + 2e^- \leftrightarrow Pd_s$	0.95
$Ir^{3+} + 3e^- \leftrightarrow Ir_s$	1.16
$Pt^{2+} + 2e^- \leftrightarrow Pt_s$	1.18
$Au^{3+} + 3e^- \leftrightarrow Au_s$	1.52

Many parameters can be tuned to control the deposition of the noble metal. For example, galvanic displacement is known to occur preferentially on selected facets of the template (because each crystallographic orientation has different surface free energy) [107,108]. In case of a *fcc* crystal, the free energy of low index facets increases in the order (111) < (100) < (110), meaning that the dissolution of the atoms from the template should start on (110) facets while the atoms from the noble metal will be preferentially reduced on the (111) facets. However, the use of capping agent, such as poly(vinylpyrrolidone) (PVP), which preferentially binds to the (100) facets, makes the galvanic replacement possible first on (111) facets. Using this technique, Xia *et al.* could control the growth of cuboctaedral seeds to octahedra or cube with various truncation levels or (un)symmetry [109–111]. It is also possible to promote or prevent the galvanic replacement by using metal salt precursors with higher or lower solubility (*i.e.* changing the reduction potential of the metal) or by addition of ionic species to shift the equilibrium of the overall redox equation [112]. Alike to the discussion associated with **Figure 2.6**, the deposition of the noble metal onto its template is also depending on the lattice mismatch of the two metals, and may either lead to a smooth and monocrystalline shell in the shape of the substrate (FM mode) or to a polycrystalline one with irregular shape [112]. Finally, if the ions of the most noble metal are present in excess in the initial solution, the template core might be completely dissolved yielding pure hollow nanostructures of the noblest element. In case of a noble metal shell covering homogeneously the template core, the excess stoichiometry of the noble element can induce a driving force for the interdiffusion of the non-noble element outwards the nanoparticle, and the inner void is created through the nanoscale Kirkendall effect. These techniques are particularly mastered by Puntes *et al.* to synthesize nanoparticles with very complex architecture, as shown in **Figure 2.10** with their double-walled AuAg nanoboxes. However, such pieces of nanoart are obtained with an excessive use of capping agents and surfactants, which strongly adsorb on the nanoparticle surface and make their application in electrocatalysis compromised.
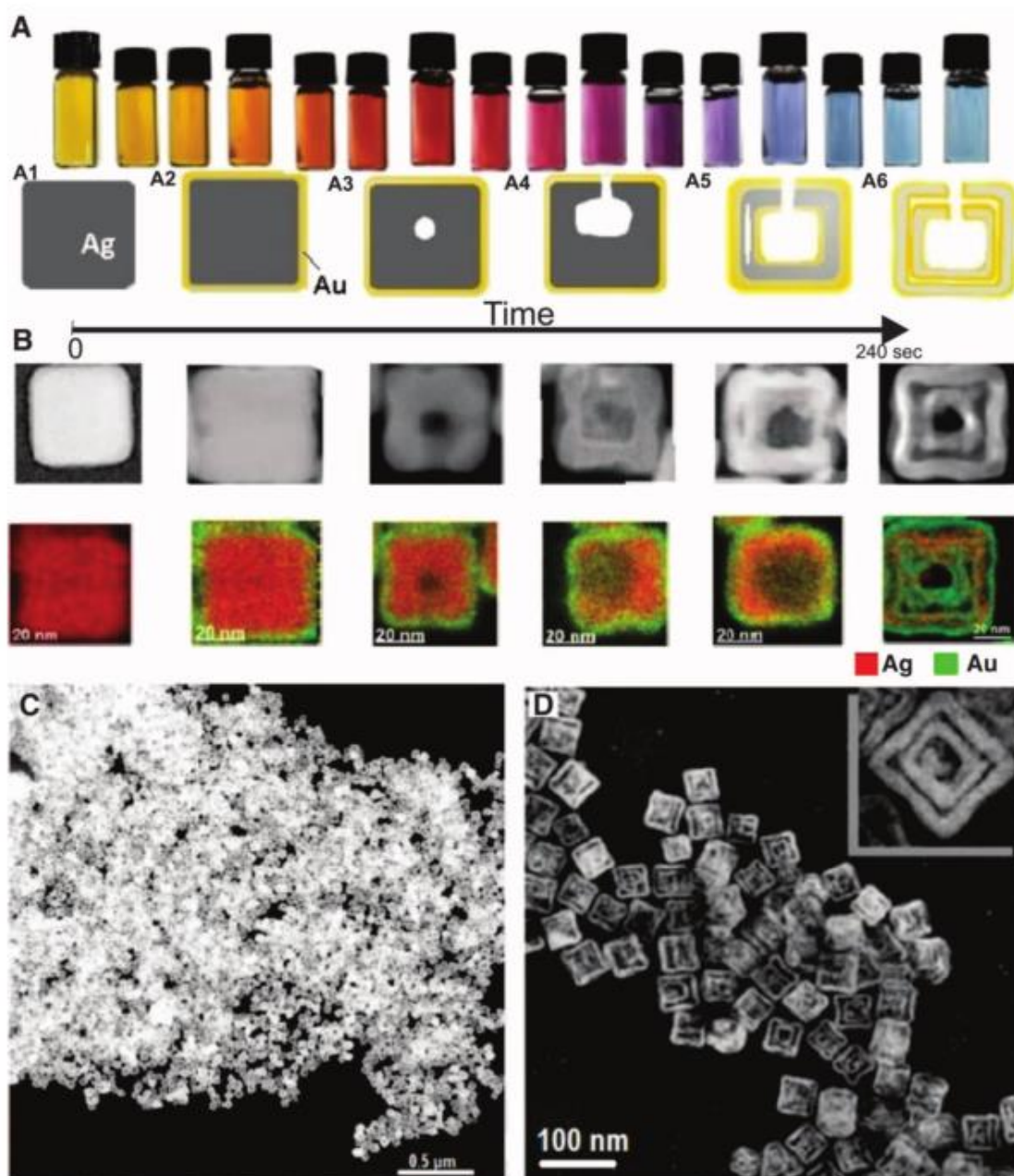
Figure 2.10: Optical and morphological evolution of AuAg double-walled nanoboxes (a); HAADF- STEM images and X-EDS maps for the different stages of evolution indicated in (a) (b); TEM images of AuAg double-walled nanoboxes, showing large yield production and the double-walled morphology. From Ref. [113].

In electrocatalysis, hollow nanostructures were first introduced for the methanol oxidation [114,115], and then applied to the ORR by several authors, introducing new materials such as carbon supported nanoporous PtNi [83,116], PtNi nanobowls [117], ultrathin PtNi hollow nanoparticles [118] or compositions, such as ultrathin Pt$_3$Co hollow nanoparticles [119], Pt-Ag nanoparticles [120], Pt-Ag featuring nanochannels [121] or Pd-Pt hollow nanocatalysts [122]. In 2012, Bae *et al*. reported on a facile surfactant-free one-pot synthesis of PtNi hollow nanoparticles which showed 3.3 and 7.8-fold enhancement of

mass and specific activity for the ORR relative to Pt/C, respectively [123]. This synthesis method was later adapted by Dubau *et al.* [124], who characterized hollow PtCo or PtNi nanoparticles with advanced physical and chemical techniques and reported promising ORR activity and stability under both liquid electrolyte and PEMFC ageing tests (PEMFC tests also on H_2/N_2 atmosphere). Probably one of the most famous 'success' of a hollow nanocatalyst for the ORR has been introduced by Stamenkovic *et al.* in 2014 [125] (see **Figure 2.11**). Starting from 20 nm large Pt_3Ni polyhedra obtained *via* co-reduction of Pt and Ni salts precursors, the authors used a slow and natural ageing process which selectively leached out the Ni atoms from the facets, leading to the formation of Pt-rich nanoframes. The very high mass activity for the ORR of this catalyst (~1 mA g_{Pt}^{-1} at 0.95 V *vs.* RHE) was attributed to the combination of an enhanced specific activity provided by its Pt(111)-skin surface and its high specific surface area due to its open architecture and access to reactants to its inner surface.
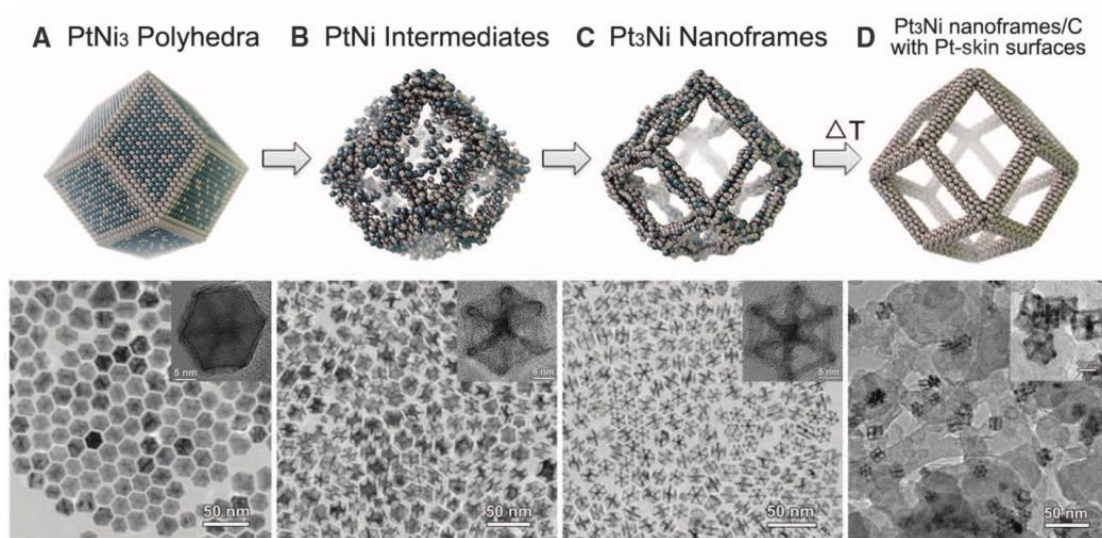
Figure 2.11: Schematic illustrations and corresponding TEM images of the samples obtained at four representative stages during the evolution process from polyhedra to nanoframes. Initial $PtNi_3$ polyhedra (a); PtNI intermediates (b); final hollow Pt_3Ni nanoframes with Pt(111)-skin-like surface dispersed on high surface carbon. From Ref. [125].

However, while enhancement factors > 15 in SA and > 20 in MA over commercial Pt/C were recorded in RDE experiments [125] (0.95 V *vs.* RHE), 'only' 6.5 and 3.5 were found respectively in real PEMFC cathode configuration as reported by the DoE [126].

2.3 PhD Thesis Outline

The first two chapters underlined the absolute necessity to reduce anthropogenic CO_2 emissions as even the more optimistic predictive scenarios for our future are alarming. Because CO_2 emissions are mainly due to fossil fuel combustion (energy production and transportation sector being the first oil consumer), solutions must be found for the widespread of electricity from clean energy sources, the latter being currently restricted by energy storage and transport (excessive cost and intrinsic limitations of batteries). Hydrogen as an energy vector between clean electricity production (wind, solar, hydro etc.) and demand (car, electric grid et.) is one of the most attractive opportunity to meet this energy paradigm. In that context, PEMFC are essential for clean conversion of hydrogen into electricity and its technology is currently in advance compared to other alternative approaches. However, the electrical performance of a PEMFC is still limited by the sluggish cathodic ORR kinetics and the high platinum content needed at the cathodic catalytic layer to compensate this poor kinetics creates a major cost barrier for massive commercialization of PEMFC systems. Along a non-exhaustive state-of-the-art on ORR electrocatalysis, we have documented that alloyed PtM/C or M-rich core@Pt-rich shell catalysts (where M is an early or late transition metal) feature tremendous ORR catalysis improvements compared to pure Pt/C, reaching higher performance at lower cost. Nonetheless, the use of high amount of non-noble metal and metastable nanoparticle shapes result in a poor stability of these new generation of catalysts.

This PhD thesis was initially motivated by the further understanding and development of hollow PtNi nanoparticles for the oxygen reduction, as their opened structure allows a better utilization of Pt atoms along with promising activity and stability. However, team work investigations on the formation and growth mechanism of hollow PtNi/C nanoparticles (especially those performed in collaboration with Dr. Jakub Drnec at ID31 of the European Synchrotron Radiation Facility (ESRF), see chapter 3) revealed that, beyond strain and ligand effects, structural disorder is key to boost the ORR kinetics. Chapter 4 was then dedicated to the quantification and extension of this hypothesis to various PtNi/C electrocatalysts featuring the same Pt:Ni composition (~85:15) but different nanostructures: solid, hollow and 'sea sponge' PtNi/C nanoalloys and Ni-core@Pt-shell nanoparticles. The extent of structural disorder in these nanostructures was monitored by Wide Angle X-ray Scattering (WAXS), and quantified by two independent

parameters: the microstrain derived from Rietveld analysis of WAXS spectra (a physical marker) and the average CO_{ads} oxidation potential (an electrochemical marker). Finally, in chapter 5, we tentatively integrate 'structurally-defective' nanomaterials into the ORR electrocatalysis landscape. To that goal, state-of-the-art nanocatalysts (bimetallic nanooctahedra, nanocubes and aerogels) have been synthesized thanks to a collaboration with the Electrochemistry Laboratory from the Paul Scherrer Institute (PSI), Switzerland, and to a 3-month stay in the Electrochemical Catalysis, Energy and Material Science Group of Prof. Dr. Peter Strasser at the TU Berlin, Germany. A generalization of the 'Defect do Catalysis' concept is also proposed and tools introduced to quantify structural disorder.

3 HOLLOW PTNI/C NANOPARTICLES AS ELECTROCATALYST FOR THE ORR

Associated Papers:

The results presented in this chapter have been partially or fully published in the following papers:

- R. Chattot, T. Asset, J. Drnec, P. Bordet, J. Nelayah, L. Dubau, and F. Maillard, 'Atomic-Scale Snapshots of the Formation and Growth of Hollow PtNi/C Nanocatalysts,' *Nano Lett.*, vol. 17, no. 4, pp. 2447–2453, 2017

Contribution: R.C. and T.A. equally contributed to the experimental work described in this paper. R.C. and T.A. conceived the experiments, synthesized the hollow PtNi/C nanoparticles *operando* and in classical conditions, performed the TEM, STEM-X-EDS and electrochemical measurements, analysed the physical, chemical and electrochemical data, discussed the results, drew conclusions, and approved the final version of the manuscript.

- L. Dubau, T. Asset, **R. Chattot**, C. Bonnaud, V. Vanpeene, J. Nelayah, and F. Maillard, 'Tuning the Performance and the Stability of Porous Hollow PtNi/C Nanostructures for the Oxygen Reduction Reaction,' ACS Catal., vol. 5, no 9, pp. 5333–5341, 2015.

Contribution: R.C. synthesized the hollow PtNi/C nanoparticles, performed electrochemical measurements, analysed the data, discussed the results, drew conclusions and approved the final version of the manuscript.

- L. Dubau, J. Nelayah, S. Moldovan, O. Ersen, P. Bordet, J. Drnec, T. Asset, **R. Chattot**, and F. Maillard, 'Defects do Catalysis: CO Monolayer Oxidation and Oxygen Reduction Reaction on Hollow PtNi/C Nanoparticles,' ACS Catal., vol. 6, no. 7, p. 4673−4684, 2016.

Contribution: R.C. helped for the experimental work and discussed the results.

3.1 Introduction

The electrocatalytic properties of bimetallic nanoparticles are strongly affected by their atomic arrangement. This holds especially true in PEMFC where enhanced ORR kinetics has been measured for specific chemical compositions and shapes of PtM alloys (M being an early or late transition metal) or M-rich core@Pt-rich shell nanoparticles (NPs) [63,80,125,127]. In that respect, a step-by-step characterization of the different nanostructures forming during the synthesis of bimetallic NPs are not only fundamental in terms of scientific knowledge but also provide a leverage for controlling the spatial distribution of the metal atoms and thus rationalizing their catalytic activity at the atomic-scale. Using this approach, Gan *et al.* [79] recently reported that, during the growth of PtNi octahedra, a branched Pt-rich structure forms first onto which Ni atoms are preferentially deposited, resulting into Pt-enriched apexes and Ni-rich facets.

Bimetallic hollow NPs, a class of highly active (electro)catalyst for the ORR [115,118,123,128,129], could benefit from the detailed knowledge of the synthesis steps. The nanoscale Kirkendall effect is an interdiffusion process into a bimetallic alloy or core@shell material driven by the difference in the interdiffusion coefficients of two elements and resulting into the entrance of atomic vacancies inside the metal lattice. It was first documented by Yin *et al.* [103] in nanomaterials. The authors have shown that this effect is responsible for the spontaneous formation of hollow Co_3S_4 or CoO NPs upon exposure to an elemental S or O_2 atmosphere. Combined sequentially or in series with galvanic replacement (a spontaneous electrochemical process in which the oxidation of a metal phase provides electrons to reduce the ions of another metal having a higher standard potential), the nanoscale Kirkendall effect has become a simple and versatile route to bimetallic hollow NPs composed of a noble element (typically gold - Au or platinum - Pt) and a less-noble element (typically silver - Ag, palladium - Pd, cobalt - Co or nickel - Ni), which acts as an anode during galvanic replacement (sacrificial template) [104,130,131]. Both (i) the nature of the sacrificial element, (ii) the stoichiometry between the more noble and the less noble elements, (iii) the temperature at which the synthesis is performed (the interdiffusion coefficient of the elements strongly depends on the temperature [132]) and (iv) the shape of the sacrificial template provide control over the chemical composition, the elemental distribution, the size and the shape of the final hollow NPs.

However, to date, the details and the kinetics of formation and growth of hollow nanocatalysts are still elusive. As physical methods have been reported powerful to monitor a growing film or particle [133–135], herein, using a unique combination of *operando* Synchrotron X-ray wide angle (WAXS) and small angle (SAXS) X-ray scattering, HRTEM, STEM and X-EDS we addressed these issues on hollow PtNi/C nanocatalysts prepared by the facile, surfactant-free and one-step synthesis route first introduced by Bae *et al.* [123]. Then, the fundamental knowledge the synthesis mechanism was used to optimize the preparation of the hollow PtNi/C nanoparticles. Various samples with varied sizes were synthesized, characterized and tested as ORR catalysts, allowing further comprehension of the origin of their enhanced electrocatalytic properties.

3.2 Unveiling the Synthesis of Hollow PtNi/C Nanoparticles

3.2.1 Methodology

Hollow PtNi/C NPs were synthesized by a one-pot process in which $Pt(NH_3)_4Cl_2.(H_2O)$, $NiCl_2.(6\ H_2O)$ were first dissolved in de-ionized water, mixed with Vulcan XC72 (a high surface carbon support), and reduced with dropwise addition of a sodium borohydride ($NaBH_4$) solution under vigorous magnetic stirring and air atmosphere [136]. Different electron or X-ray-based techniques were used to unravel the nature of the different nanostructures forming during the synthesis. For analyses with electron-based techniques, the synthesis was conducted in a glass reactor and a peristaltic pump was used to add the $NaBH_4$ solution in a dropwise manner. Sampling was performed in the reactor at $t = 0$ min, 1 min, 2 min, 3 min, 4 min, 5 min, 7 min, 10 min, 20 min, 40 min and 60 min after addition of the first drop of the $NaBH_4$ solution. The aliquots were then deposited onto TEM grids, and the chemical reactions at stake were stopped by drying as fast as possible with a heat gun. *Operando* WAXS and SAXS measurements were performed at ID31 beamline of the European Synchrotron Radiation Facility (ESRF). The synthesis was performed following the same protocol but a poly(methyl methacrylate) cuvette was used as reactor, and the $NaBH_4$ solution was added using a remote controlled syringe.

3.2.2 Atomic-Scale Morphological Changes Occurring During the Synthesis of Hollow PtNi/C NPs

Conventional TEM and STEM images as well as X-EDS elemental maps of the nanostructures formed after 1 min, 2 min, 3 min 4 min, 20 min, 40 min and 60 min are displayed in **Figure 3.1**. HRTEM images of the different synthesis intermediates are also provided in **Figure 3.2**. The X-EDS elemental maps show that the reduction of the metal salts by NaBH$_4$ is extremely fast, as ~ 12 nm large nanoparticles are already formed only 2 minutes after the first drop of NaBH$_4$ has been added to the solution containing the metal salt precursors.
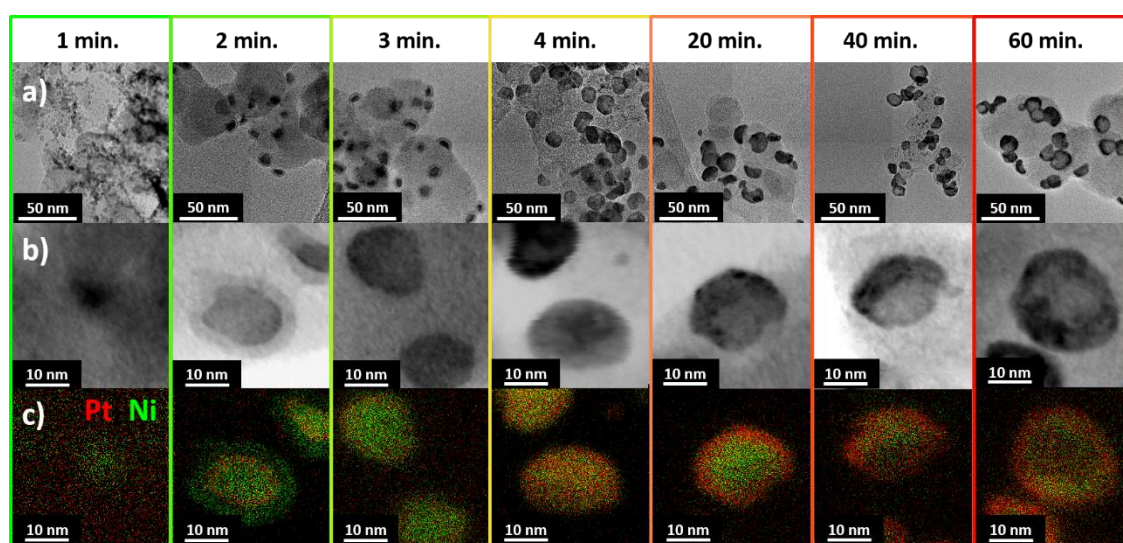
Figure 3.1: Time-sequenced formation and growth of hollow PtNi/C nanoparticles by electron and X-ray based techniques. (a) Conventional, (b) scanning transmission electron microscopy images and (c) X-EDS elemental maps of the different nanostructures forming during the synthesis of hollow PtNi/C NPs.

X-EDS elemental maps reveal the preferential reduction of Ni^{2+} ions by NaBH$_4$ during the early stage of the synthesis ($0 < t \leq 1$ min.). This is surprising in view of the more negative standard potential of Ni^{2+}/Ni ($E^0 = -0.26$ V $vs.$ SHE) relative to the Pt(NH$_3$)$_4$$^{2+}$/Pt ($E^0 = 0.62$ V $vs.$ SHE) and Pt^{2+}/Pt ($E^0 = 1.19$ V $vs.$ SHE) redox couples [137]. However, it may be rationalized by considering the nature of the Pt salt precursor. Indeed, [Pt(NH$_3$)$_4$]$^{2+}$ is inert (opposite to labile) $i.e.$ slowly decomposes in water, which allows for the sequential deposition of Ni atoms and then of Pt atoms. In contrast, due to faster decomposition kinetics in water, solid alloy PtNi/C NPs are formed when PtCl$_6$$^{2-}$ ions are used [138].
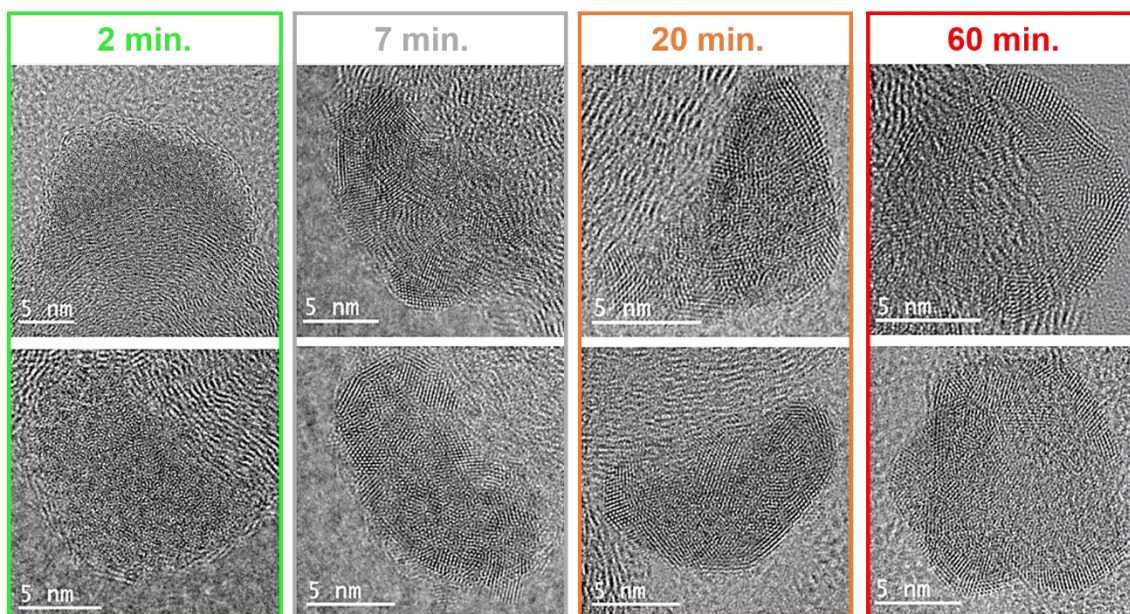
Figure 3.2: HRTEM images of the different nanostructures forming during the synthesis of hollow PtNi/C nanoparticles.

The Ni/C NPs are then rapidly ($1 < t \leq 2$ min) embedded into a matrix composed of Ni and one or several lighter element(s) as illustrated by the strong contrast between the core of the NPs and their surface and near-surface region in the STEM images (**Figure 3.1**). According to HRTEM images displayed in **Figure 3.2**, this matrix is poorly crystalline or amorphous. This result is in line with the affinity of boron (B) with most transition metal elements, and the associated spontaneous formation of transition metal borides as documented in literature [139]. Nickel borides (NiB, Ni_2B, Ni_3B and NiB_3 are the most common phases obtained via reduction of Ni in BH_4^--containing solution). Note that the Ni_xB_y shell may also contains oxygen (O) atoms as both the synthesis and the sequential sampling were performed under air atmosphere.

STEM-X-EDS images recorded between $2 < t \leq 20$ min show that the surface of the Ni-rich core@Ni_xB_y-shell/C nanostructures enriches in Pt, resulting in the formation of Ni-rich core@Pt-rich shell/C NPs after 20 min. Pt atoms are deposited at the surface of the growing NPs via galvanic replacement (the $Ni_xB_yO_z$ shell covering the Ni-rich cores is oxidized while $Pt(NH_3)_4^{2+}$ ions are reduced) and/or chemical reduction by hydrogen (H_2) molecules and/or BH_4^- ions present in solution. Note that the morphology of the Pt-rich shell is difficult to estimate due to the 2 dimensions projection provided by the TEM and STEM images combined with the different particles orientations and its superposition with the carbon support. However, one can see that the shell is most likely hemispherical,

as many particles appear more 'C'-shaped than perfectly spherical. This makes sense if one considers that galvanic replacement (and/or chemical reduction) does not occur on the Ni atoms at the interface with the carbon support. From a top (or bottom) view in electron microscopy, the PtNi shell 'dome' may looks spherical in transmission, the latter becoming more 'C'-shaped (or 'French beret'-shaped) for any other direction of the electron beam (particles located on an edge of the carbon support, *i.e.* observed from a side view are most likely 'C'-shaped in TEM or STEM images,).

Finally, a slow evolution of the solid Ni-rich core@Pt-rich shell nanoparticles into alloy hollow PtNi/C NPs is observed from $20 < t < 60$ min. This structural evolution may be rationalized by the progressive leaching of the Ni atoms either through nanopores present in the Pt-rich shell or any 'uncovered' Ni template surface. The dissolution of Ni is favoured as the reducing power of $NaBH_4$ decreases as it decomposes in water. Note also that the gradient in chemical potential between Pt and Ni atoms in the core@shell nanostructure formed after $t = 20$ min, and their different degrees of oxophilicity both act as strong driving forces for Ni atoms to interdiffuse into the Pt shell. Since Ni atoms interdiffuse outwards more rapidly than Pt atoms inwards, atomic vacancies enter the nanomaterial, and condensate into voids yielding ultimately hollow PtNi/C NPs. This phenomenon has already been introduced in the previous section and referred to as the Kirkendall effect.
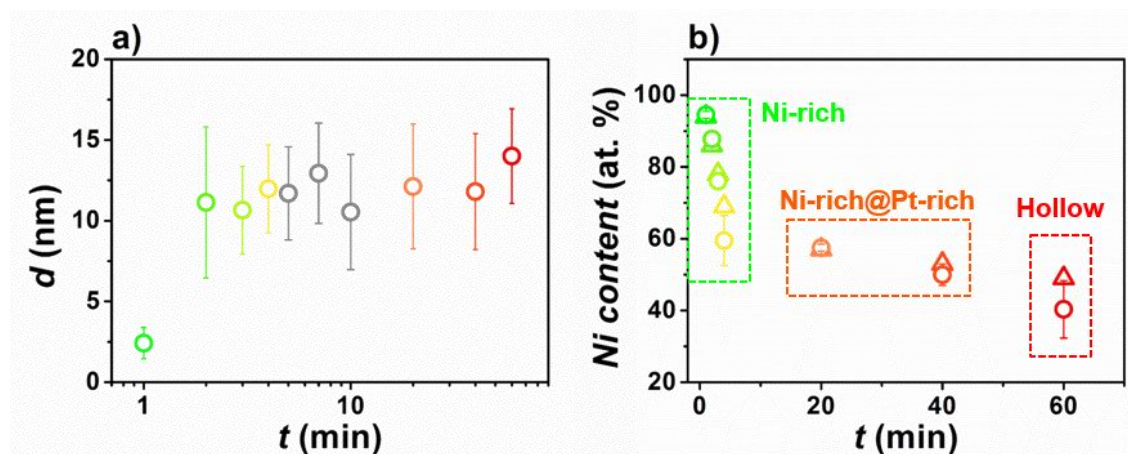
Figure 3.3: Structural and chemical changes occurring during the synthesis of the hollow PtNi/C nanoparticles. Variation of (a) the external diameter and (b) the Ni content of the NPs. The external diameter was approximated by counting *ca*. 200 nanoparticles at each stage. The triangles represent the Ni content measured on individual NPs by STEM-XEDS, and the circles the average chemical composition measured on hundreds of NPs (by X-EDS on low magnification TEM images). For both measurements, the error bar is the standard deviation.

The changes of the external diameter of the NPs and of their Ni content are represented in **Figure 3.3**. They suggest that galvanic displacement occurs mainly during the first 4 minutes of the synthesis (fast variation of the Ni concentration) while smoother variations of these two parameters at $t > 4$ min are caused by the progressive Ni dissolution and the nanoscale Kirkendall effect.

3.2.3 Structural Changes Occurring During the Synthesis of Hollow PtNi/C Nanoparticles

Complementary to electron-based techniques, *operando* WAXS measurements were carried out to probe the structure of the synthesis intermediates at a larger scale. Despite the strong H_2 evolution arising from the reduction of Ni^{2+} ions and the homogeneous hydrolysis of $NaBH_4$, the WAXS patterns of the growing PtNi/C nanocrystallites could be recorded (**Figure 3.4a**). The first reflections, observed at $2\theta \sim 4.5$ °, were ascribed to the formation of Ni_xB_y phases in agreement with Ref. [140]. For $3 < t < 5$ min, patterns typical of X-ray diffraction from Ni(111), Pt(111) and Pt(200) planes were observed at $2\theta \sim 6.0°$, $2\theta \sim 5.3°$ and $2\theta \sim 5.8°$, respectively. The reflections ascribed to Pt increased in intensity at longer times, indicating enrichment in Pt of the NPs in agreement with the STEM-X-EDS elemental maps displayed in **Figure 3.1**. The reflections also shifted to larger 2θ values, suggesting that the PtNi lattice parameter relaxed towards the value of pure Pt.

The experimental pair distribution functions (PDF) extracted from the WAXS patterns (**Figure 3.4b** and **Figure 3.4c**) provided insights into the structure of the growing hollow PtNi/C NPs. The first atomic coordination shells were distinguishable at $t \geq 3$ min (**Figure 3.4c**). The peak at 0.249 nm dominated the $G(r)$ signals between $3 \leq t < 4$ min, thereby suggesting the presence of Ni-rich NPs on the carbon support. However, assuming only Ni/C NPs was not sufficient to fully describe the extracted PDFs, most likely because Ni_xB_y and $Ni_xB_yO_z$ phases also formed in the experimental conditions of this study. At $t = 4$ min, the WAXS data were tentatively fitted with a mixture of Ni and Ni_3B. For $t \geq 4.5$ min, the peak at 0.271 nm became predominant in the PDF patterns, in line with the enrichment in Pt evidenced in **Figure 3.1**. For $t = 10$ min and 50 seconds the signal could be fitted with a single PtNi phase with a lattice parameter of 0.385 nm (not shown), indicating the disappearance of the $Ni_xB_yO_z$ phase. The lattice parameter relaxed at longer times, in agreement with the continuous loss of Ni atoms from the NPs monitored by X-

EDS (**Figure 3.1** and **Figure 3.3**). Last, a qualitative observation of the intensity of the Pt-Pt peaks allowed establishing that the maximum coherence length gradually increased from < 0.1 nm before 4.5 min to 2 nm at 60 min.
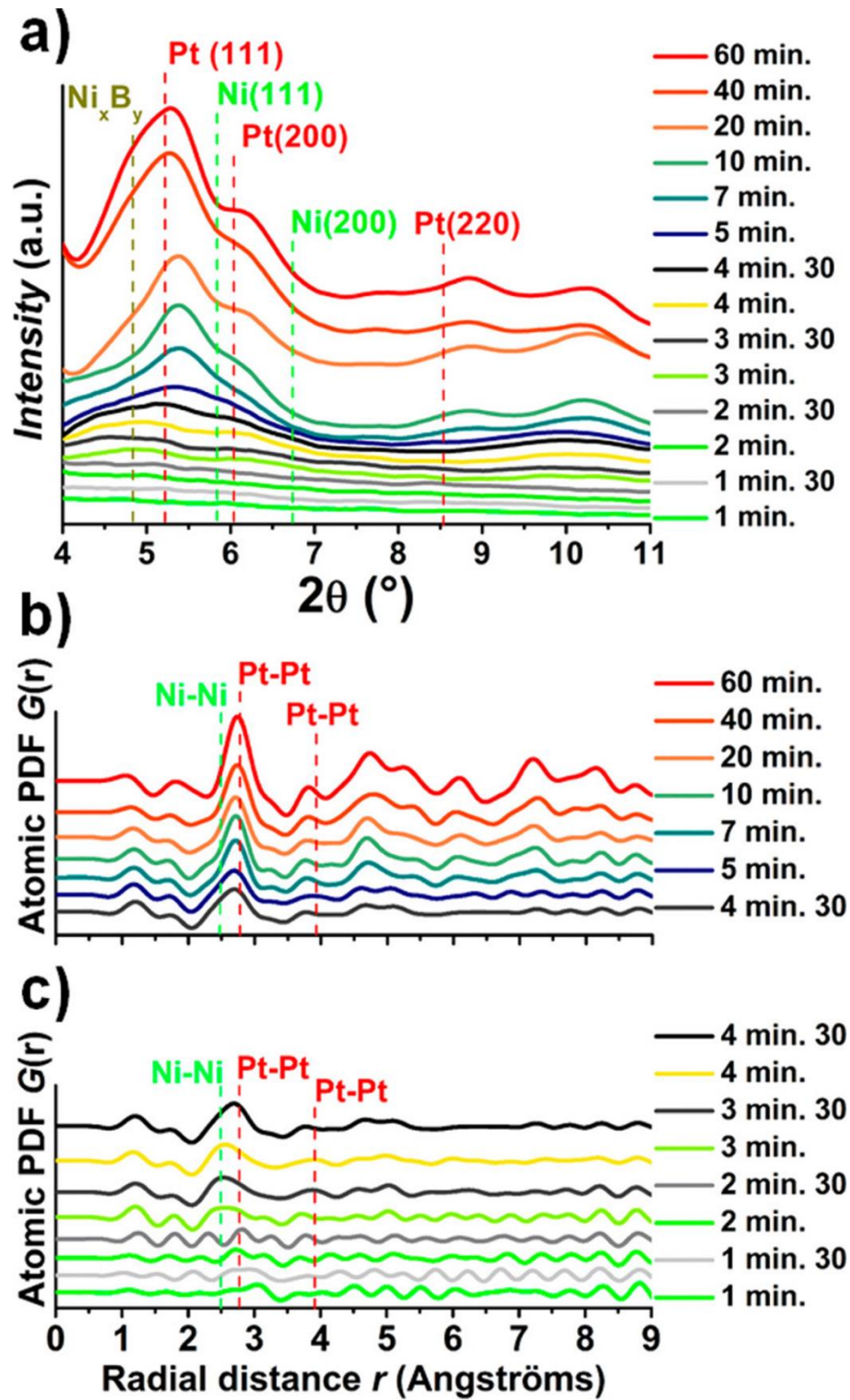

Figure 3.4: Structural characterization of the different nanostructures forming the synthesis of hollow PtNi/C nanoparticles. (a) High-energy WAXS patterns (the vertical dashed lines indicate the reflections of pure metallic Pt and Ni), (b, c) experimental atomic pair distribution functions.

The transformation of Ni-rich core@Pt-rich shell NPs into hollow PtNi/C NPs was confirmed by *operando* SAXS measurements. SAXS is a useful tool to probe the structure of the growing NPs in the size domain between several angströms and tens of nanometres. Moreover, as it provides information about the changes in morphology of the NPs during the synthesis. The *operando* SAXS experiments were performed in a separate run using the same experimental setup and synthesis protocol. The background due to the carbon support was eliminated by subtracting the SAXS pattern recorded before the addition of the first $NaBH_4$ solution droplet from the subsequent patterns.

The variations of the scattering length density (SLD) of the shell and of the core of the NPs (SLD_{shell} and SLD_{core}, respectively) as a function of time are displayed in **Figure 3.5a**. Slight changes of the carbon support morphology were observed in the course of the synthesis resulting in uncertainty about scaling factors and absolute values of SLDs. To compensate for these uncertainties, the SLD_{shell}/SLD_{core} ratio (the measurement of the X-ray contrast, and therefore the electron density contrast, between the shell and the core) was plotted in **Figure 3.5a**.

Figure 3.5b displays the changes of the shell thickness and of the core radius as a function of time. The morphological changes are then described starting from $t = 3$ min, which corresponds to the time when enough Pt is incorporated in the shell to develop sufficient X-ray contrast between the shell and the core in SAXS measurements. A slight decrease of the radius of the core was observed from $3 < t < 6$ min but it is believed not to be physically sound, rather an artefact resulting from the low SLD contrast between the Ni-rich core and the $Ni_xB_yO_z$-shell. For $6 \leq t < 25$ min, a non-monotonic variation of the shell thickness (from 1.3 nm to 2.8 nm) was observed in agreement with the enrichment of the surface of the NPs in Pt resulting from galvanic replacement. The core radius remained constant at a size *ca*. 2 nm during this period. Due to the variations of the individual SLD_{core} and SLD_{shell} values (**Figure 3.5a)**, the SLD_{shell}/SLD_{core} ratio increased during the first 20 min, flattened out at a value 3.2 ± 0.5 in the time period $20 < t < 35$ min, and steeply increased at $t \geq 35$ min (**Figure 3.5a**). This abrupt variation signs the dissolution of Ni atoms initially contained in the core of the NPs into the Pt-rich shell.
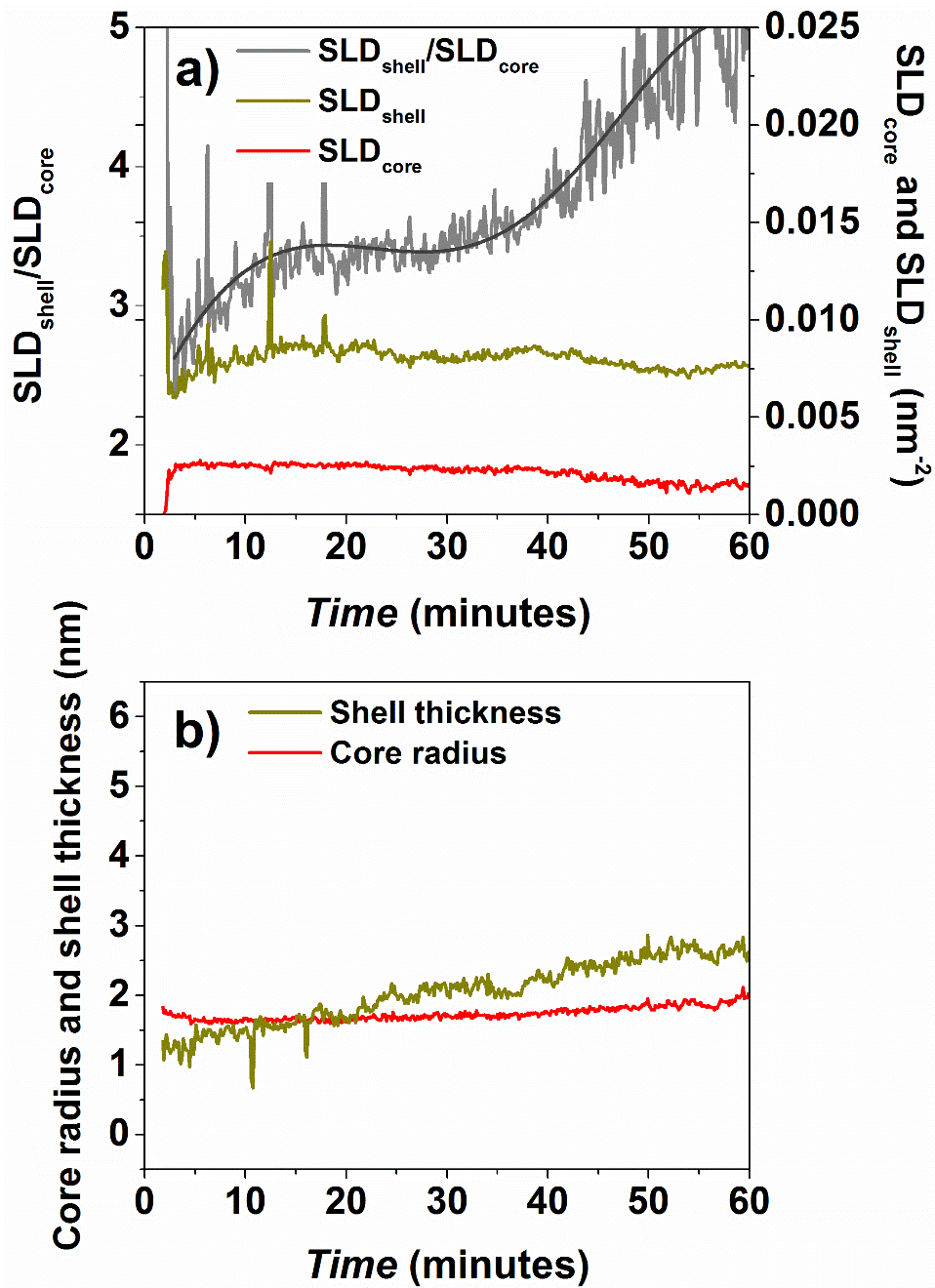
Figure 3.5: Morphological characterization of the different nanostructures forming the synthesis of hollow PtNi/C nanoparticles. Variation of the parameters extracted from the fitting of the SAXS data: (a) scattering light density of the core (SLD_{core}), of the shell ((SLD_{shell}) and their ratio, (b) core radius and shell thickness. The solid line in (a) is a 5th order polynomial fit of the SLD_{shell}/SLD_{core} ratio.

On the basis of the results of WAXS, SAXS and STEM-X-EDS measurements, a comprehensive formation and growth mechanism for hollow PtNi/C NPs is then proposed:

1. $0 < t \leq 1$ min: Ni^{2+} ions are preferentially reduced by $NaBH_4$ into solid Ni/C NPs;

2. $1 < t \leq 2$ min: Formation of Ni-rich core@$Ni_xB_yO_z$-shell/C nanostructures;

3. $2 < t \leq 4$ min: Deposition of Pt atoms onto the $Ni_xB_yO_z$-shell via galvanic replacement and/or chemical reduction by $NaBH_4$;

4. $4 < t \leq 20$ min: The metal shell enriches in Pt and thickens. Relaxation of the PtNi lattice parameter;

5. $20 < t \leq 60$ min: Depletion of the core in Ni. Formation of hollow PtNi/C NPs.

Based on these findings, the morphology of the final hollow PtNi/C NPs could be modified simply by adjusting parameters of the synthesis.

3.3 Electrocatalytic Performance of the Hollow PtNi/C Catalyst

3.3.1 Something More than Strain and Ligand Effects

Taking advantage of the sequential Ni-rich template and PtNi shell formation as shown in the previous section, we prepared hollow nanocatalysts with different morphologies by varying the initial Pt:Ni salts precursor ratios [136].

As shown in **Figure 3.6**, increasing Ni salt precursor stoichiometry while keeping the amount of Pt constant led to an increase of the overall particle size with thinner Pt-rich shell (see associated histograms). This makes sense considering that the increase of the initial concentration in Ni^{2+} cations favours the formation of more and larger Ni-rich NPs onto the carbon support. As shown in **Figure 3.1**, these Ni-rich NPs then act as sacrificial template for the deposition of Pt^{2+} ions leading to hollow PtNi/C NPs with larger inner cavity diameter and/or thinner PtNi shell. Note that the increased number of initial Ni template NPs (without size change) would also contribute to a decrease of the PtNi shell thickness without inner cavity size changes.
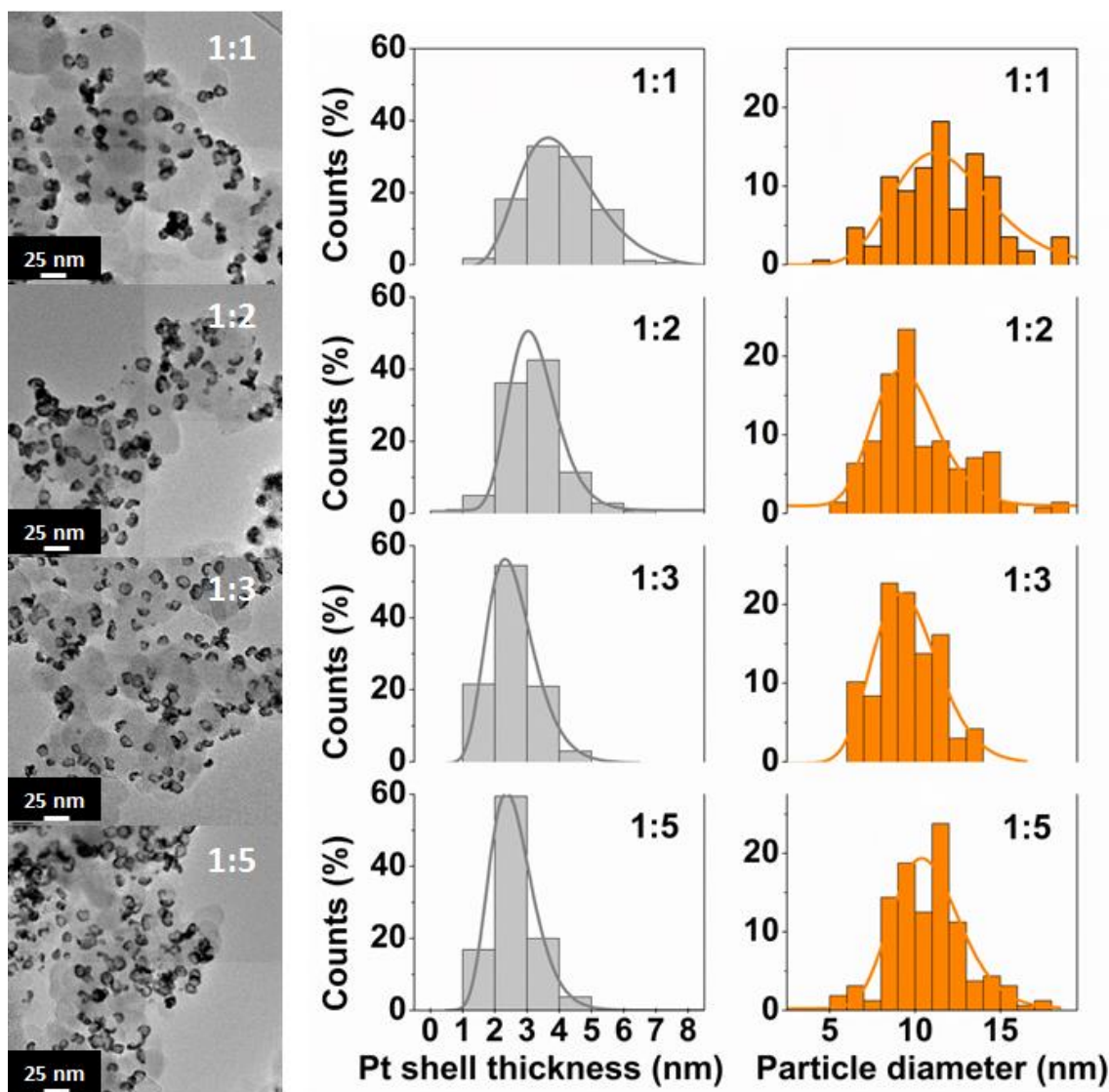
Figure 3.6: TEM images and histograms of the Pt-rich shell thickness and of the outer diameter of the hollow PtNi/C nanoparticles. The Pt:Ni stoichiometry in the initial metal salt precursor solution is indicated in the top right-hand side corner of individual histograms/images. From Ref. [136].

HRTEM images presented in **Figure 3.7** show the high degree of polycristallinity of the hollow nanocatalysts (here synthesized with an initial PtNi stoichiometry of 1:3). As also confirmed by X-ray Diffraction (XRD) (**Table 3.1**), the PtNi shell is composed of small nanocrystallites of ca. 2-3 nm interconnected by grain boundaries. Moreover, Fourier transform (FT) analysis of HRTEM images (here for a Pt:Ni stoichiometry of 1:3, see **Figure 3.7a**) revealed the presence of nanopores across the PtNi shell.

Table 3.1: Some chemical and structural parameters of the electrocatalysts evaluated in this work. Atomic composition determined by X-EDS, lattice parameter and crystallite size measured by XRD. Data from Ref. [136].

Electrocatalysts	at. % Ni (%)	Lattice parameter (nm)	Crystallite size (nm)
Solid Pt/C	0	0.393	2.2 ± 0.2
Solid PtNi/C	10 ± 4	0.386	2.9 ± 0.1
Hollow PtNi/C (1:1)	9 ± 2	0.388	3.0 ± 0.2
Hollow PtNi/C (1:2)	10 ± 2	0.387	2.5 ± 0.1
Hollow PtNi/C (1:3)	15 ± 2	0.386	2.4 ± 0.2
Hollow PtNi/C (1:5)	13 ± 2	0.386	2.3 ± 0.1

Surprisingly, X-EDS measurements performed on the various catalysts showed that, whatever the initial Ni precursor stoichiometry, the residual Ni content on the final nanoparticles (*i.e.* after acid-leaching in 0.1 M H_2SO_4 for $t = 22$ h) is ca. 10-15 at.%, resulting in only slight different Pt lattice parameters contractions (compared to pure Pt) for all the catalysts as displayed **Table 3.1**.
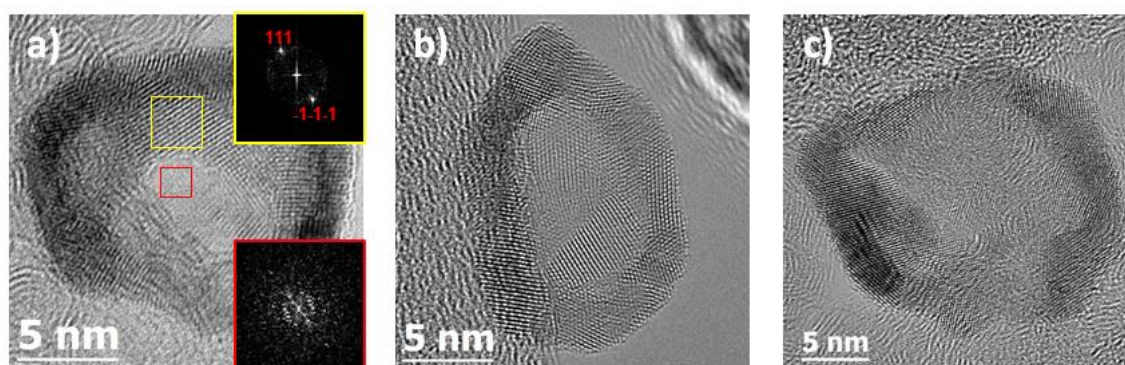
Figure 3.7: HRTEM images of hollow PtNi/C nanoparticles (initial Pt:Ni stoichiometry of 1:3). The FT patterns taken in different zones and showed in insert of picture (a) and confirm the presence of nanopores > 1 nm. From Ref. [136].

Various electrochemical measurements, partially represented in **Figure 3.8**, conducted on these various hollow nanocatalysts revealed that [136]: (i) according to the Pt specific surface areas calculated from CO_{ads} stripping experiments and theoretical calculations assuming an hemispherical shape for hollow PtNi/C catalysts, both the inner and the outer surface of the PtNi shell are accessible to gas reactants, in agreement with HRTEM images, (ii) the specific activity for the ORR on hollow PtNi/C NPs was between 6.7 and 8.3-fold that of a commercial Pt/C (purchased from E-TeK), (iii) a homemade reference PtNi/C catalyst of same crystallite size featuring the same degree of contraction of the PtNi lattice than the various hollow PtNi/C nanostructures performed only 2.2-fold better specific activity for the ORR than the reference Pt/C material.
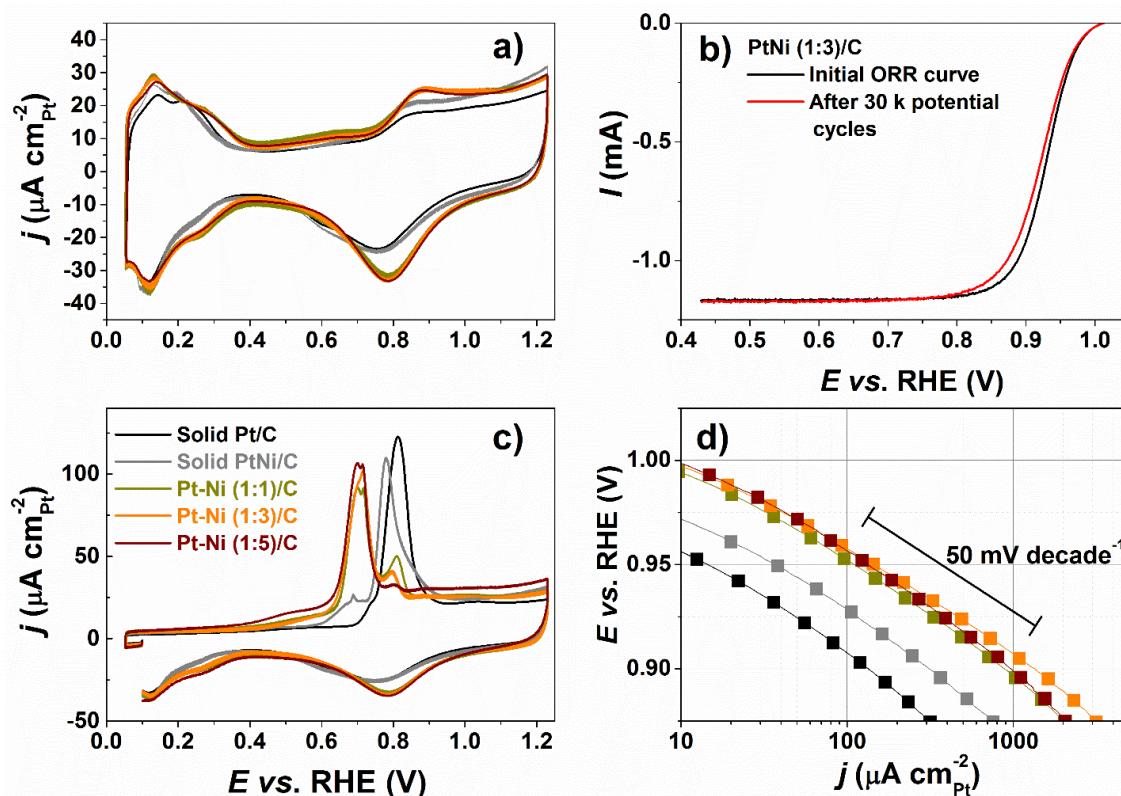
Figure 3.8: (a) Base and (c) CO$_{ads}$ stripping voltammograms measured on the porous hollow PtNi/C and the reference solid Pt/C and PtNi/C electrocatalysts, (b) positive-going potential sweep voltammograms recorded on the hollow PtNi (1:3)/C nanoparticles before and after the accelerated stress test (AST), and (d) Tafel plots of the mass-transport corrected kinetic current obtained from the steady-state I−E curves at ω = 1600 rpm for the electrocatalysts evaluated in this work. Parts a and c were conducted in Ar-saturated 0.1 M HClO$_4$ at v = 20 mV s^{-1} without rotation of the electrode. Parts b) and d) were conducted in O$_2$-saturated 0.1 M HClO$_4$ at a potential sweep rate v = 5 mV s^{-1}. Other conditions: T = 25 ± 1 °C, Pt loading = 8.0 μg. From Ref. [136].

This ORR kinetics improvement is particularly striking in the case of the hollow PtNi(1:1)/C NPs: indeed this catalyst features similar Ni content and crystallite size than the reference solid PtNi/C NPs (**Table 3.1**) but performs 3 times better for the ORR. As introduced earlier in Chapter 2, alloying Pt with a late transition metal positively impacts the ORR kinetics (lowering of the Pt d-band centre) via a direct compression of the Pt lattice parameter (strain effect), or indirectly through electronic interaction between the non-noble and the noble atoms (ligand effect). It is widely accepted in literature [102,141,142] (especially in this case, were the catalysts have been acid-treated and consequently feature a strong Ni depletion in the near surface region) that the strain effect is the predominant cause in the change of the electronic structure of Pt surface atoms . However, as evidenced in **Figure 3.9**, whatever the Pt lattice contraction (more or less contracted than the solid reference PtNi/C), hollow PtNi/C catalysts show dramatically improved ORR activity, in contradiction with the usual trends and theoretical expectations.
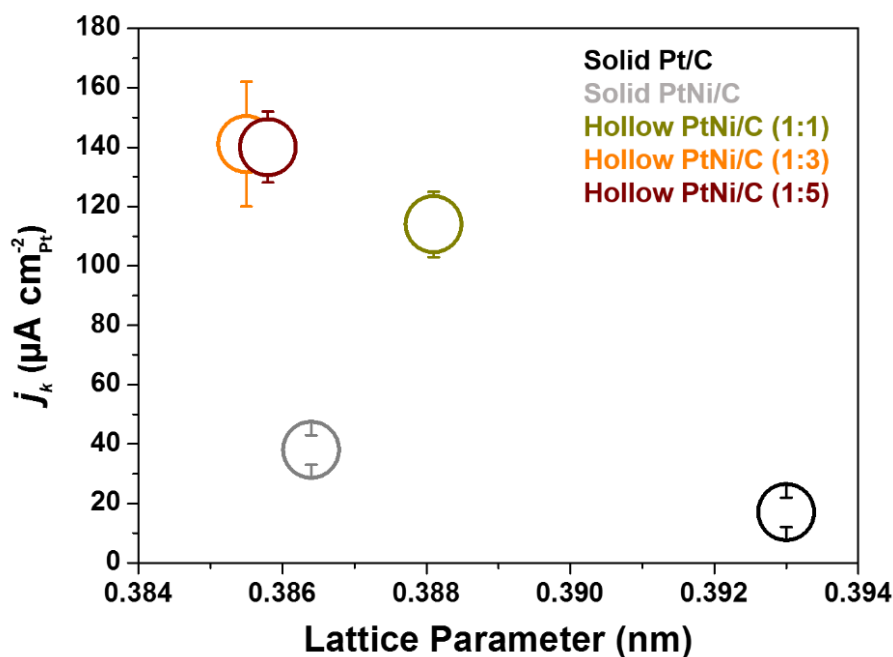
Figure 3.9: ORR kinetic current measured at $E = 0.95$ V *vs*. RHE *vs*. lattice parameter for the different electrocatalysts investigated in Ref. [136]. The measurements were conducted in O_2-saturated 0.1 M $HClO_4$ at a potential sweep rate $v = 0.005$ V s^{-1}. Other conditions: $T = 25 \pm 1$ °C, Pt loading = 8.0 µg. Lattice parameter extracted from XRD patterns.

3.3.2 Structure-ORR Activity Causal Relationship

Guided by these findings and the desire to unveil the reason of the enhanced ORR activity of the hollow PtNi/C nanoparticles, we thermally annealed hollow PtNi/C NPs (from 1:3 Pt:Ni initial stoichiometry) under different gas atmospheres (N_2, air or H_2) and synthesized a library of catalysts with modified structural properties but the same chemical composition [143]. As shown in **Figure 3.10**, the sample treated under N_2 atmosphere at $T = 400$ °C kept its polycrystalline and hollow nanostructure while the samples treated under air or H_2 atmosphere collapsed to form solid and near spherical nanoparticles containing eventually some grain boundaries. A Rietveld analysis of *ex situ* WAXS measurements performed on this library of nanomaterials provided more insights into the changes of the crystallite size and lattice parameter upon thermal annealing (see **Figure 3.11a-c**).

Beyond these 'classical' properties, Rietveld analysis of the WAXS patterns also provided a physical parameter usually largely neglected in the literature in the field of electrocatalysis: the microstrain. Microstrain, also referred as *local lattice strain,* [144] arises from the deviation of the atoms from their ideal positions due to the presence of structural

defects (stacking faults, twins, grain boundaries, and or dislocation arrays) [145], and produces a broadening of the WAXS peaks without any change in the peak position. But, since both crystallite size and microstrain contribute to broadening of the WAXS peaks, analytical methods are generally employed to separate the two contributions.
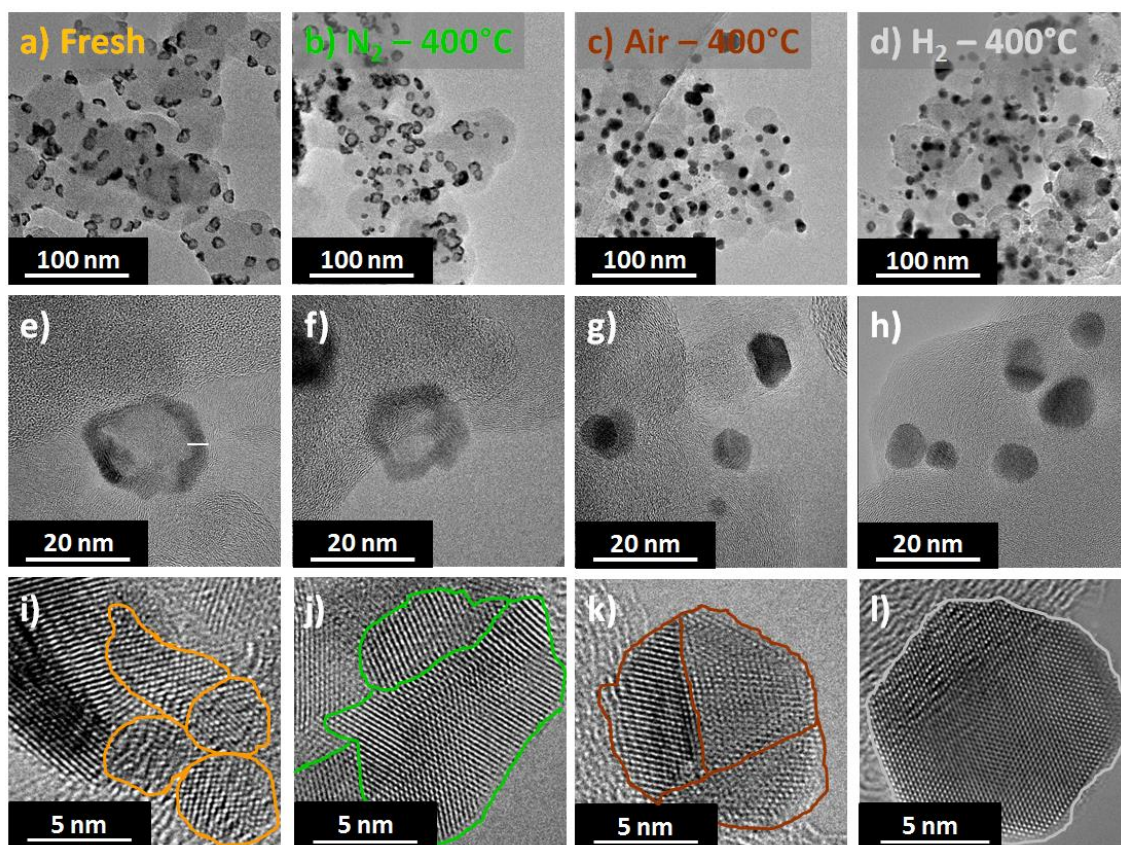
Figure 3.10: TEM (a-h) and HRTEM (i-l) images of the as-synthetized PtNi/C nanoparticles (a-d) and after thermal annealing at 400 °C under different gas atmospheres: (e-f). In (i-l), the boundaries between the individual PtNi nanocrystallites are highlighted in colour. From Ref. [143].

Note that the superiority of the Rietveld refinement method (used here) over others (such as the frequently employed Williamson-Hall analysis) was recently evidenced by Maniammal *et al.* [146] for ~3 nm crystallites. As shown in **Figure 3.11d**, the restructuring of the initial hollow catalysts into new nanomaterials dramatically changed the value of the microstrain, being small for solid and monocrystalline nanoparticles (air and H_2 treated samples) compared to the samples featuring a hollow nanostructure (as synthesized or thermally-annealed in N_2 atmosphere). Finally, a comparison of the ORR activity with the values of the microstrain for the different electrocatalysts showed that the structural defects (due to the peculiar structure of this catalyst) may play a significant role in ORR electrocatalysis.
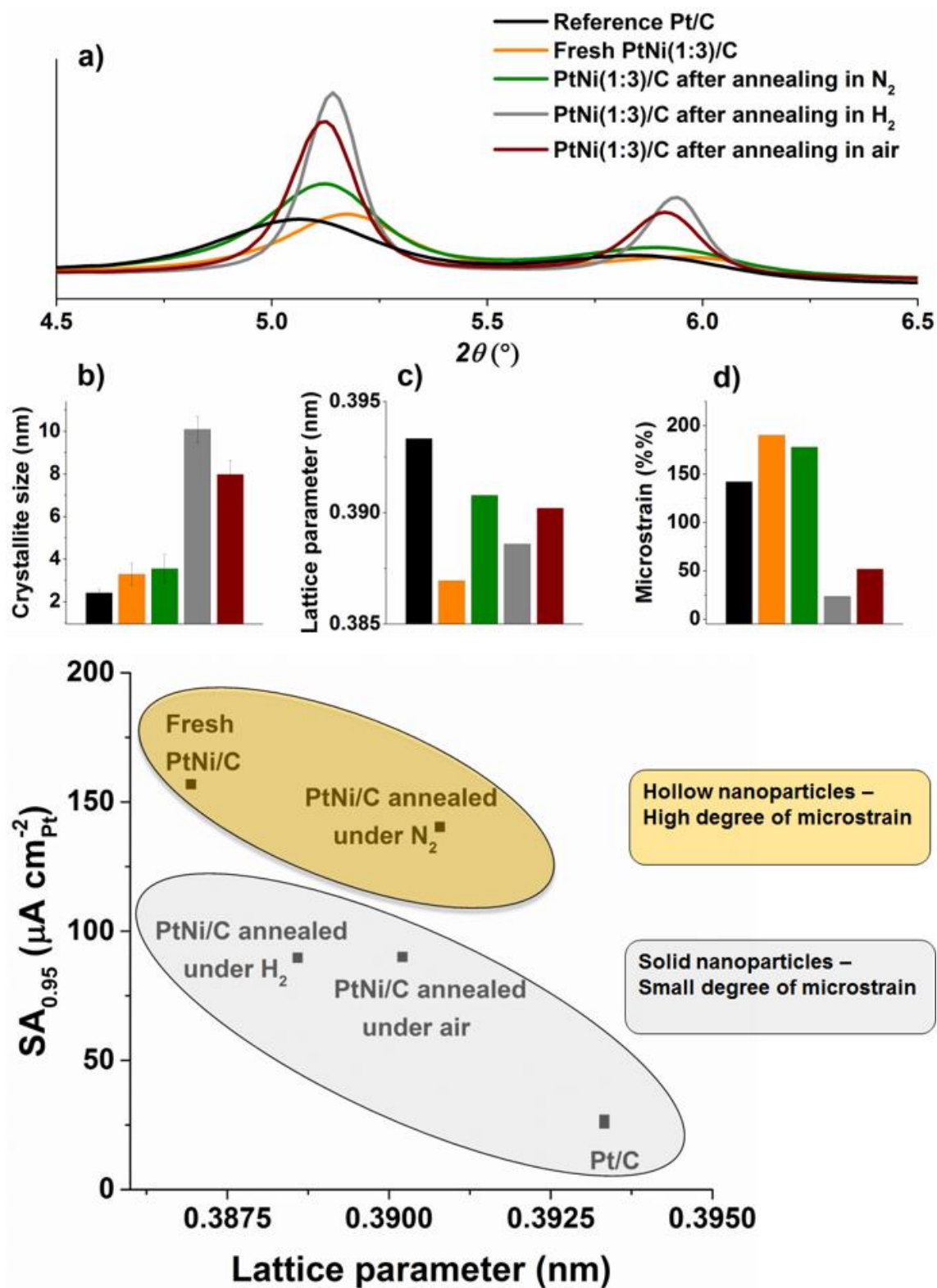
Figure 3.11: Structural parameters of the fresh and heat-treated hollow PtNi/C nanoparticles and the reference Pt/C material used in this study: (a) synchrotron XRD patterns; (b) average crystallite size; (c) lattice parameter; (d) microstrain estimated by Rietveld analysis of the WAXS patterns, and (e) ORR specific activity measured at 0.95 V *vs*. RHE compared with the lattice parameter for the different electrocatalysts. Adapted from Ref. [143].

3.4 Conclusion

This chapter was dedicated to the presentation of results obtained between researcher at LEPMI and other institutions such as the ESRF, Louis Néel Institute in Grenoble and the University of Paris Diderot. We first combined advanced X-ray and electron-based techniques, including (HR)TEM, STEM, X-EDS, WAXS, SAXS, Rietveld refinement and Pair Distribution Function (PDF) analysis which was used to unveil the formation of hollow PtNi/C nanoparticles, but that can also be easily transferred to any kind of nanomaterial. Because the 'one step' synthesis introduced by Bae *et al.* occurs trough sequential Ni-rich/C NPs formation, Pt-rich shell deposition and Ni-rich core dissolution, the synthesis could be modified to produce hollow PtNi/C NPs with various cavity size and shell thicknesses. The comparison of the ORR activity of hollow PtNi/C catalysts and of a solid PtNi/C reference material of similar composition and crystallite size indicated that, beyond the conventional *strain* and *ligand* effects usually associated to rationalize the enhancement of the ORR kinetics on PtM/C catalysts, an additional effect was at stake. Introduction and discussion of a physical parameter, the microstrain, derived from Rietveld refinement of WAXS patterns allowed establishing that the high concentration of structural defects in hollow PtNi/C NPs likely positively influence the ORR kinetics.

4 BEYOND ALLOYING EFFECTS: MICROSTRAIN-INDUCED ENHANCEMENT OF ELECTROCATALYTIC PROPERTIES ON VARIOUS PTNI/C NANOSTRUCTURES
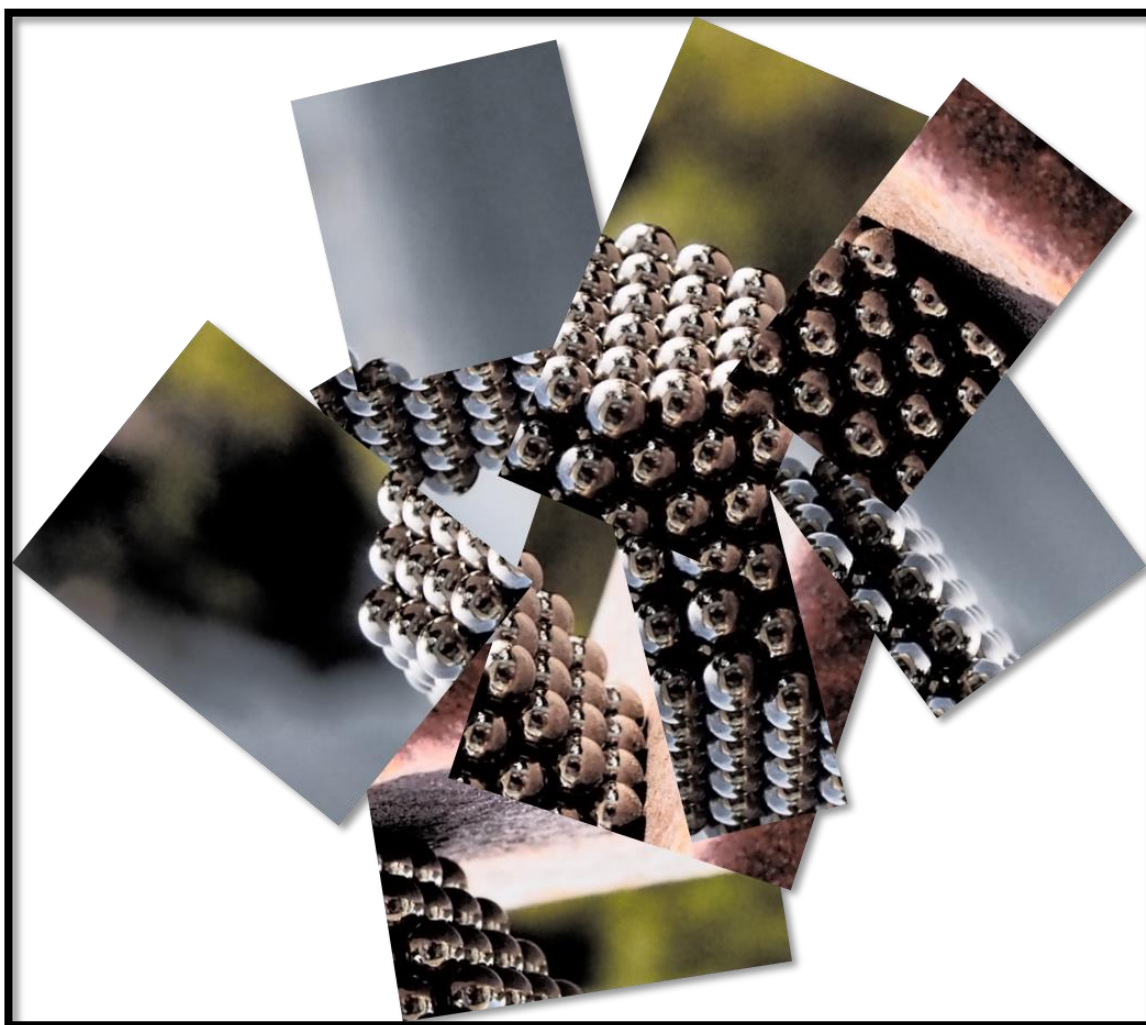
Associated Papers:

The results presented in this chapter have been partially or fully published in the following papers:

- R. Chattot, T. Asset, P. Bordet, J. Drnec, and L. Dubau, 'Beyond Strain and Ligand Effects: Microstrain-Induced Enhancement of the Oxygen Reduction Reaction Kinetics on Various PtNi/C Nanostructures,' ACS Catal., vol. 7, no. 1, pp. 398–408, 2017.

Contribution: R.C. synthesized and characterized the various PtNi/C nanostructures, performed electrochemical measurements, analysed the data, discussed the results, drew conclusions, and wrote the first version of the manuscript.

- O. Le Bacq, A. Pasturel, **R. Chattot**, B. Previdello, J. Nelayah, T. Asset, L. Dubau, and F. Maillard, 'Effect of Atomic Vacancies on the Structure and the Electrocatalytic Activity of Pt-rich/C Nanoparticles: A Combined Experimental and Density Functional Theory Study,' ChemCatChem, vol. 9, no. 12, pp. 2324–2338, 2017.

Contribution: R.C. synthesized and characterized the PtNi/C nanostructures used in this study, performed electrochemical measurements, analysed the data, discussed the results, drew conclusions and approved the final version of the manuscript.

4.1 Introduction

As detailed in Chapter 1 and Chapter 2, the high cost and the limited durability of PEMFC systems still hinder their widespread development [56,147]. The high cost of PEMFC electrodes is mainly due to the large quantity of platinum needed to activate the sluggish oxygen reduction reaction kinetics at the cathode [41]. The density functional theory calculations made by Nørskov *et al.* [45] on Pt(111) have shown that the origin of the large ORR overpotential is the strong adsorption of ORR intermediates, which block protons and electrons transfer. Since the interactions between a metal surface and oxygenated species depend on the *d*-band centre (ε_d) and of its degree of filling, an efficient strategy to tune their electronic structure and electrocatalytic activity of Pt surface atoms consists in alloying Pt with M atoms (M is an early or late transition metal), and benefit from the positive impact of strain [58,59,148–150] and ligand [151,152] effects on the ORR kinetics. A 10-fold and 90-fold enhancement of the ORR kinetics was reported on $Pt_3Ni(111)$ single crystal compared to Pt(111) and commercial nanometre-sized Pt/C, respectively [63]. Transposing this catalytic enhancement on nanomaterials is highly challenging and requires preferentially-shaped bimetallic nanocatalysts such as Pt_3Ni nanooctahedra (exhibiting exclusively (111) facets) [63,75–81,125,153].

Surface-segregated nanocatalysts featuring a Pt-enriched shell covering an alloy or a non-noble metal core hold promises to meet the electrocatalytic activity and stability requirement of PEMFC cathodes. Indeed, the Pt-rich shell prevents the leaching of the non-noble metal atoms in the PEMFC environment. Besides, their core composition, Pt shell thickness, particle size and shape are tuneable parameters for catalytic activity improvement. Using (electro)chemical dealloying, various surface segregated Pt_xNi_{1-x} nanocatalysts were recently prepared by the group of Prof. Dr. Strasser, [91] among which the dealloyed $PtNi_3$ displayed the highest ORR activity and stability, both in rotating disk electrode (RDE) experiments and PEMFC systems [95]. Intensive studies (see [89] and references therein) revealed that: (i) the compression of the Pt lattice induced by the M element controls the ORR activity [102], (ii) considerable surface strain is only possible via high M molar ratio (about 70 at. %) in the bulk of the nanomaterial, (iii) surface strain is controlled by the distribution of M in the 10 atomic near surface layers but that the first two-three monolayers are depleted in M as a result of M leaching in the acidic environment of a PEMFC [91,154], (iv) nanoparticles exceeding 10-13 nm in size are

ineluctably subjected to nanoporosity formation during the dealloying process or during PEMFC operation due to inability of the Pt-rich shell to prevent the dissolution of the underlying M atoms [83,94,96,97], (v) the loss of M atoms and the formation of nanopores increases the Pt specific surface area but is insufficient to compensate for the ORR activity drop due to Pt-lattice relaxation [94]. Similar to alloys or segregated nanostructures, a fine tuning of the electrocatalytic activity of Pt atoms is possible on core@shell nanoparticles [155]. Parameters such as the nature and the structure of the core material are critical for ORR electrocatalysis [156]. A maximal usage of Pt atoms is theoretically possible by decreasing the Pt shell to a monolayer but remains hardly feasible, [88] even when using the under potential deposition of Cu as an intermediate deposition step [157]. The incomplete final coverage of the underlying metal core M atoms by Pt atoms leads to corrosion and spontaneous evolution of PtM alloys into hollow nanoparticles under acidic conditions [121,124,136,143,158,159]. In that context, finding alternative routes to (metastable) shaped M-rich PtM/C particles is of primary importance to simultaneously meet ORR activity, stability and cost requirements of PEMFC cathode electrocatalysts.

Guided by the results presented in the previous chapter, we synthetized and characterized nanometre-sized PtNi/C electrocatalysts with similar crystallite size (~ 3 nm), Ni content (~15 at. %) but different nanostructure: solid, hollow or 'sea sponge' PtNi/C nanoalloys, and solid Ni-core@Pt-shell/C nanoparticles. These electrocatalysts were fully characterized and their electrocatalytic activity for the ORR correlated to two independent parameters: the microstrain determined from Rietveld analysis of Synchrotron WAXS patterns, and the average CO_{ads} electrooxidation potential (μ_1^{CO}) determined from CO_{ads} stripping measurements. Our experimental results, combined with DFT calculations, provide evidence for the first time that structural defects increase the electrocatalytic activity for both electroreduction and electrooxidation reactions.

4.2 Various Nanocatalysts from PtNi Nano-Bricks

Different experimental procedures were used to synthesize Ni core@Pt shell, solid or hollow alloy, and sea-sponge PtNi/C nanoparticles. A more complete description of the

various synthesis protocols can be found in the material and method section (see appendix).

4.2.1 Synthesis and Characterization of PtNi/C Nanoparticles

Solid PtNi/C Nanoparticles
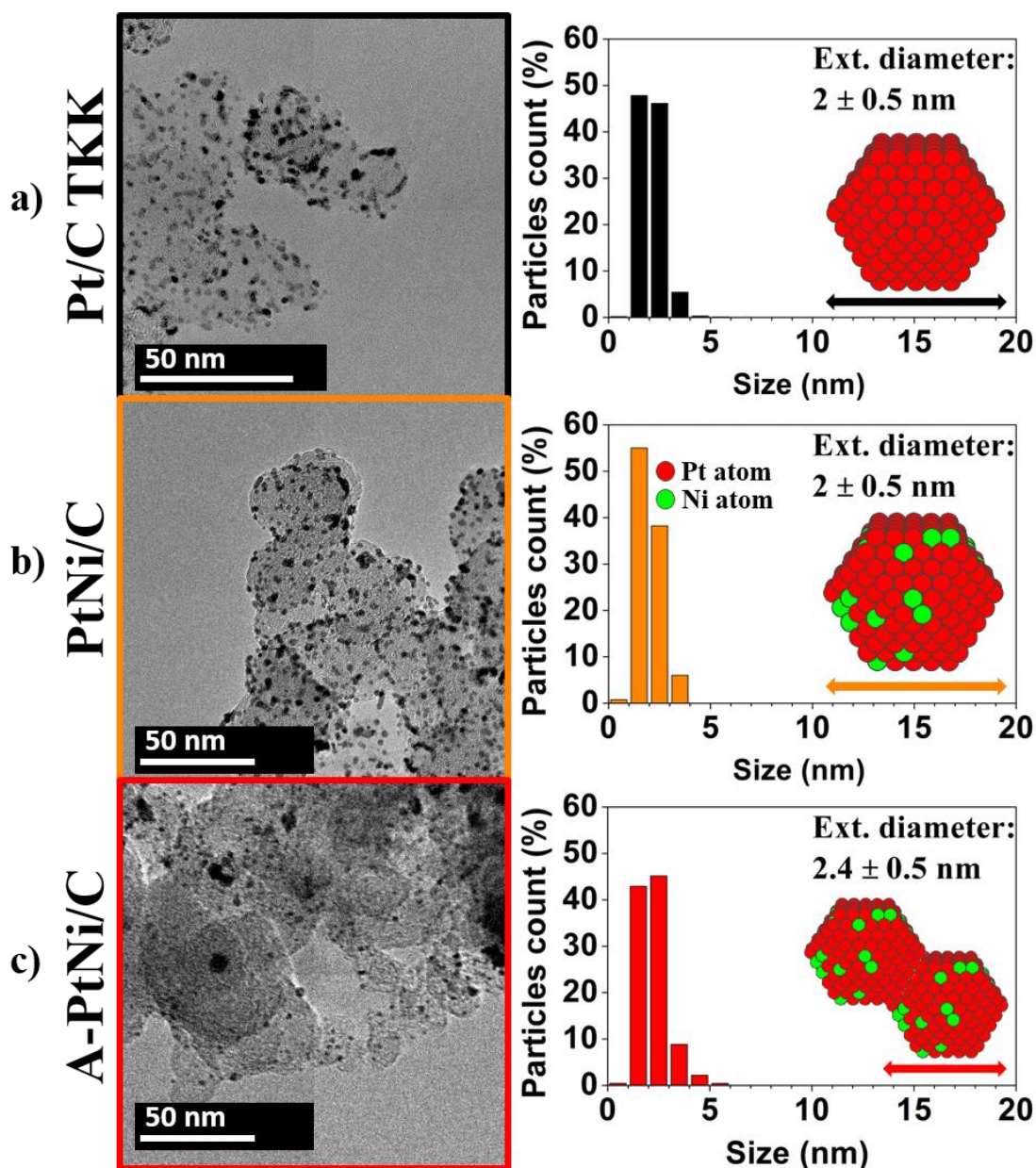
Figure 4.1: TEM images, particle size distributions and graphical representations (insert) of (a) the reference Pt/C TKK, (b) isolated alloy PtNi/C (PtNi/C) and (c) agglomerated alloy PtNi/C (A-PtNi/C) nanoparticles. The particle size distributions for each catalyst were built by measuring the diameter of more than 200 isolated (*i.e.* not-agglomerated) nanoparticles.

The polyol synthesis is a method of choice to prepare PtNi/C alloy nanoparticles with controlled size and chemical composition [160,161]. In this method, the PtNi/C nanoparticles are formed by the co-reduction of dissolved Pt and Ni salts in the presence of a high

surface area carbon support (here Vulcan XC72®) dispersed in ethylene glycol (EG). In the polyol synthesis, EG acts as solvent, stabilizer and reducing agent (the oxidation of EG into glycolic acid (GA) produces electrons, which are used to reduce the metal salt precursors). Fixing the pH at a value of 9-10 allows deprotonation of GA, formation of glycolate ions and CO molecules which prevent nanoparticle agglomeration [162]. Despite the stabilizing properties of glycolate ions, the co-reduction of Ni atoms and Pt atoms resulted into aggregated PtNi/C nanoparticles, in agreement with former literature reports [163]. Using mono-sodium citrate as surfactant in the initial EG solution, monodispersed PtNi/C particles could however be synthesized. **Figure 4.1** displays TEM images and particle size distribution for the isolated and agglomerated PtNi/C nanoparticles synthesized in this study and the reference Pt/C material (provided by Tanaka Kikinzoku, TKK), denoted as PtNi/C, A-PtNi/C, and Pt/C TKK, respectively.

Hollow PtNi/C Nanoparticles
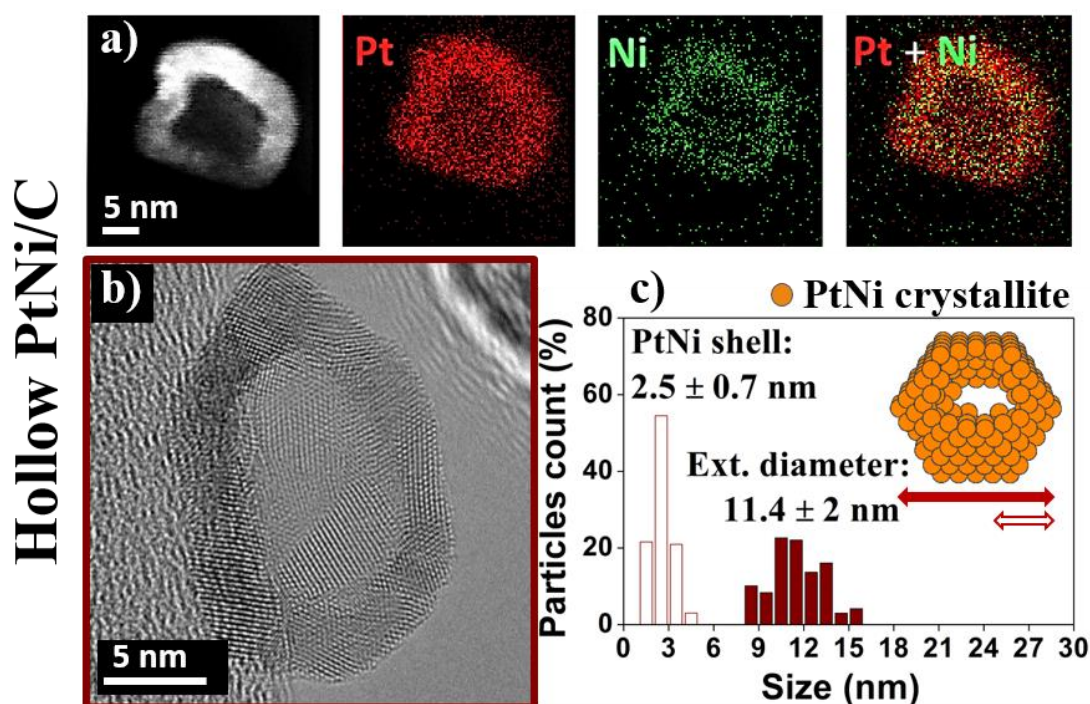
Figure 4.2. (a) High angle annular dark field scanning transmission electron microscopy (HAADF-STEM) image and X-EDS elemental maps, (b) TEM, particle size distribution and (c) graphical representation of hollow PtNi/C electrocatalysts. The particle size distribution was built by measuring the maximum Feret diameter of the outer metal shell and of the inner core on more than 200 isolated (*i.e.* not-agglomerated) nanoparticles.

Porous hollow PtNi/C nanoparticles were synthetized *via* the one-pot synthesis first reported by Bae *et al.* [164] (a step-by-step description of the synthesis and its elucidated mechanism are given in Chapter 3). During the last step of the synthesis, the Ni atoms

which were not alloyed with Pt were chemically dissolved *via* acid leaching in 1 M H_2SO_4 [124]. The final hollow PtNi/C nanoparticles are highly polycrystalline, as shown by high-resolution transmission electron microscopy (HR-TEM) images displayed in **Figure 4.2b**.

Sea Sponge PtNi/C Nanoparticles
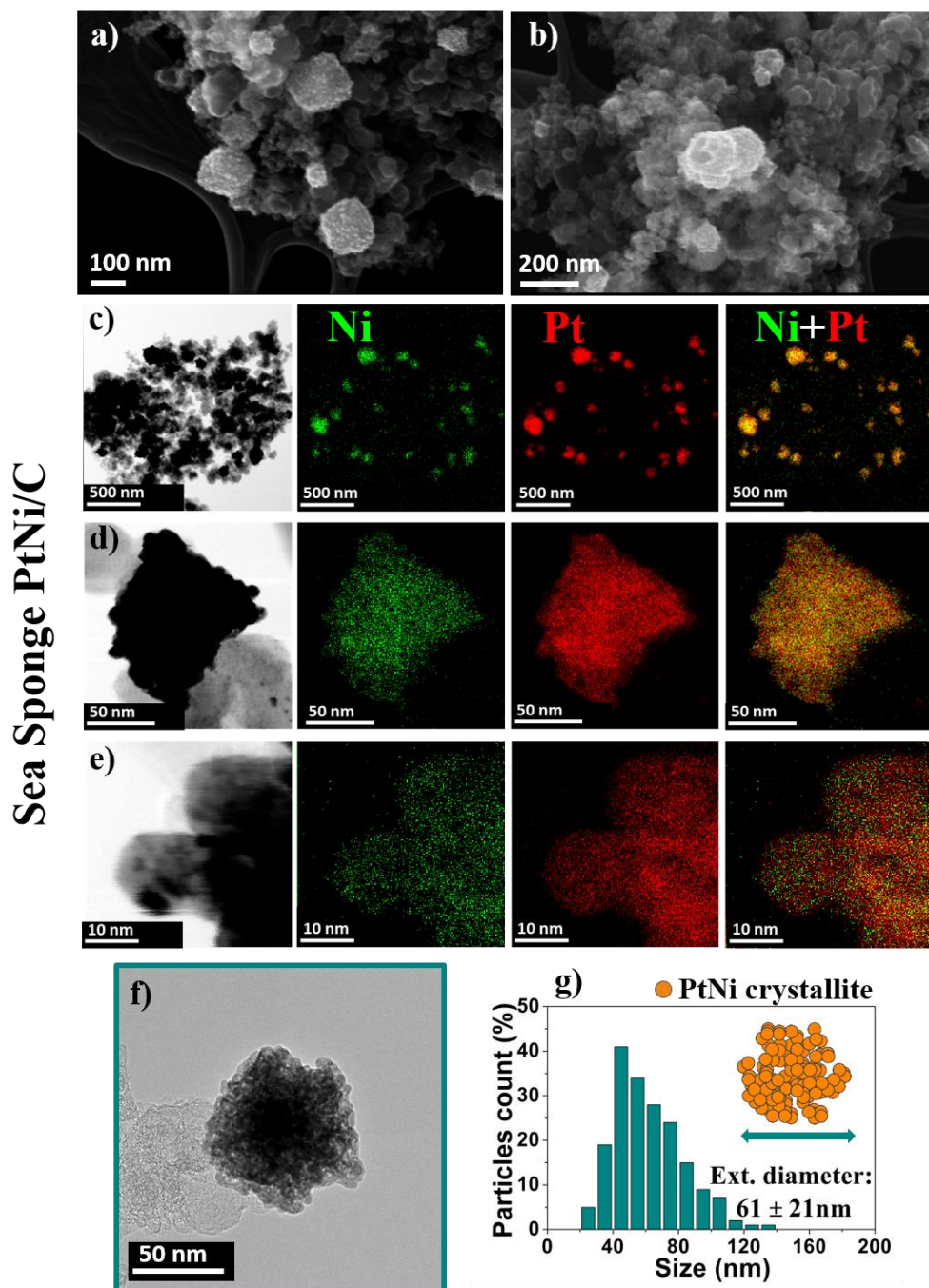
Figure 4.3: (a-b) SEM images; (c-e) STEM images and X-EDS elemental maps, (f) TEM; (g) particle size distribution and graphical representation of the 'sea sponge' PtNi/C electrocatalyst synthesized in this study. The particle size distribution was built by measuring the diameter of more than 200 aggregates. (b) shows the presence of opened porosities.

To produce 'sea sponge' PtNi/C nanostructures, the previously described polyol process was slightly modified: a Pt^{2+} rather than a Pt^{4+} precursor was chosen, and the initial Ni:Pt precursor ratio was 3:1. As shown by **Figure 4.3**, the resulting nanoparticles feature homogeneous Pt and Ni atomic distribution (**Figure 4.3c-e**) and open porosity (**Figure 4.3b**). This porous structure is believed to result from the massive dissolution of Ni atoms during the acidic post-treatment.

Ni@Pt Nanoparticles
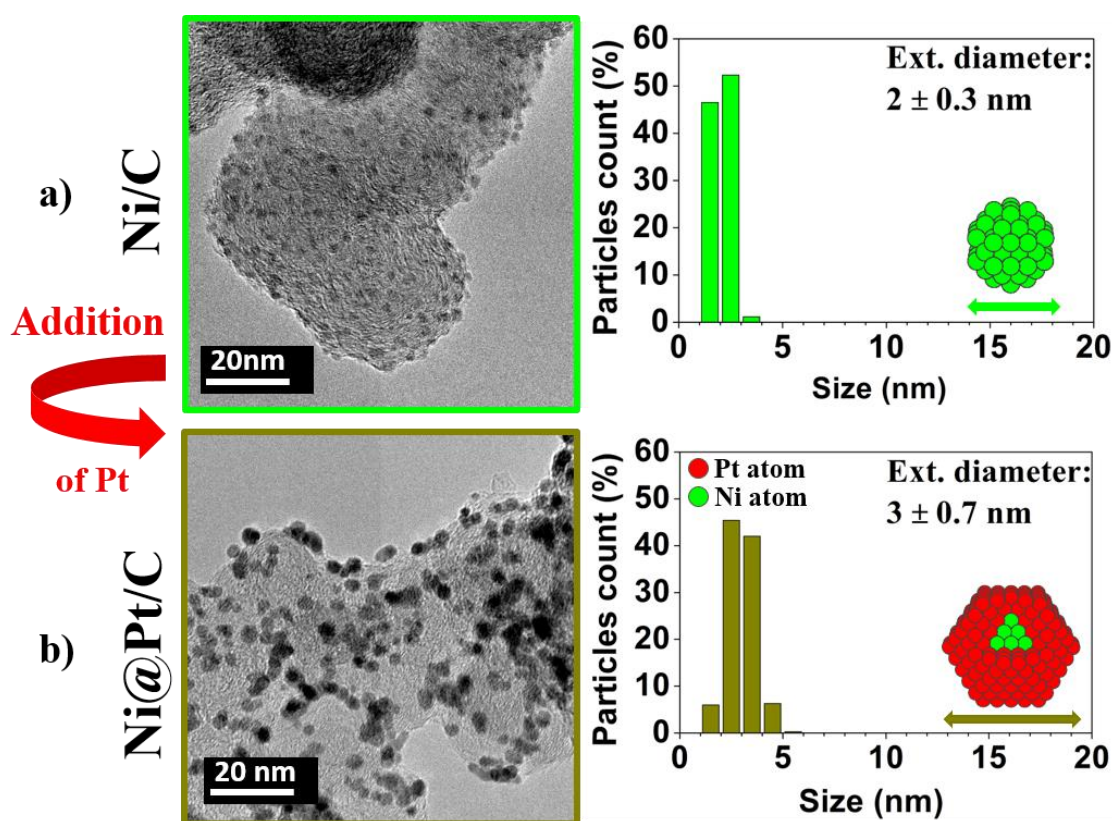
Figure 4.4: TEM images, particle size distributions and graphical representations (insert) of the (a) Ni/C template and (b) Ni-core@Pt-shell/C nanoparticles prepared *via* two sequential polyol syntheses. The particle size distributions of each catalyst were built by measuring the diameter of more than 200 isolated (*i.e.* not-agglomerated) nanoparticles.

Various synthesis routes have been developed to produce core@shell nanostructures [82]. However, most of them (including (electro)chemical dealloying, adsorbate-induced segregation and thermal induced segregation from a PtM alloy) produce M-rich core covered by a Pt-rich shell instead of two distinct phases. In this work, a sequential polyol method [165] was used to produce pure Ni-core@Pt-shell nanoparticles. Briefly, Ni nanoparticles supported on Vulcan XC72® were first prepared by the polyol method (in the presence of mono-sodium citrate). The Ni/C nanoparticles were then used as a

template for the deposition of Pt via the polyol route, resulting in the formation of Ni-core@Pt-shell nanoparticles.

The determination of the core@shell nature of a bimetallic catalyst is highly challenging [166]. However, we obtained convincing evidences that Ni-core@Pt-shell nanoparticles were synthesized. First, the increase in particle size from the initial Ni/C template to the final Ni@Pt/C nanoparticles (**Figure 4.4**) strongly suggested that Pt^{4+} ions were mainly chemically reduced on Ni/C. Second, X-EDS measurements revealed presence of both Ni and Pt atoms in the final Ni@Pt/C nanoparticles (**Table 4.1**). Finally, considering that the last step of the polyol synthesis was an acidification of the solvent for deposition of the nanoparticles on the carbon support (see material and method), any incompletely-covered Ni/C nanoparticles was likely dissolved. Note however that typical reflections of the small Ni cores could not be detected by WAXS with Synchrotron radiation. This is attributed to the fact that the scattering amplitude of X-rays increases with the product of the atomic numbers of the atoms constituting the pair. Hence, at a given Pt:Ni stoichiometry, the intensity of the Pt-Pt pairs is 7 times higher than that of the Ni-Ni pairs. Obviously, this trend was magnified by the low Ni content targeted in this study (*ca.* 15 at.%). In any case, despite their larger crystallite and particle sizes, the Ni@Pt/C nanoparticles exhibited a higher Pt specific surface area compared to Pt/C TKK (see **4.3.1 COads Stripping - ORR Catalytic Activity Relationships**): this is convincing evidence of the better utilization of Pt atoms in the Ni-core@Pt-shell nanostructure.

Because the chemical composition and the size of a bimetallic (two phases) core@shell particle are linked by the shell thickness, we could assess the number of deposited Pt monolayers on the template Ni/C cores. By combining the mean particle size determined by a statistical analysis of TEM images, the chemical composition provided by X-EDS measurements, and the geometric model introduced by Montejano-Carrizales, [167,168] the Pt shell was estimated to be *ca.* 0.9 ± 0.2 nm thick (*ca.* 4.5 ± 1 monolayers, see **Figure 4.5.**)
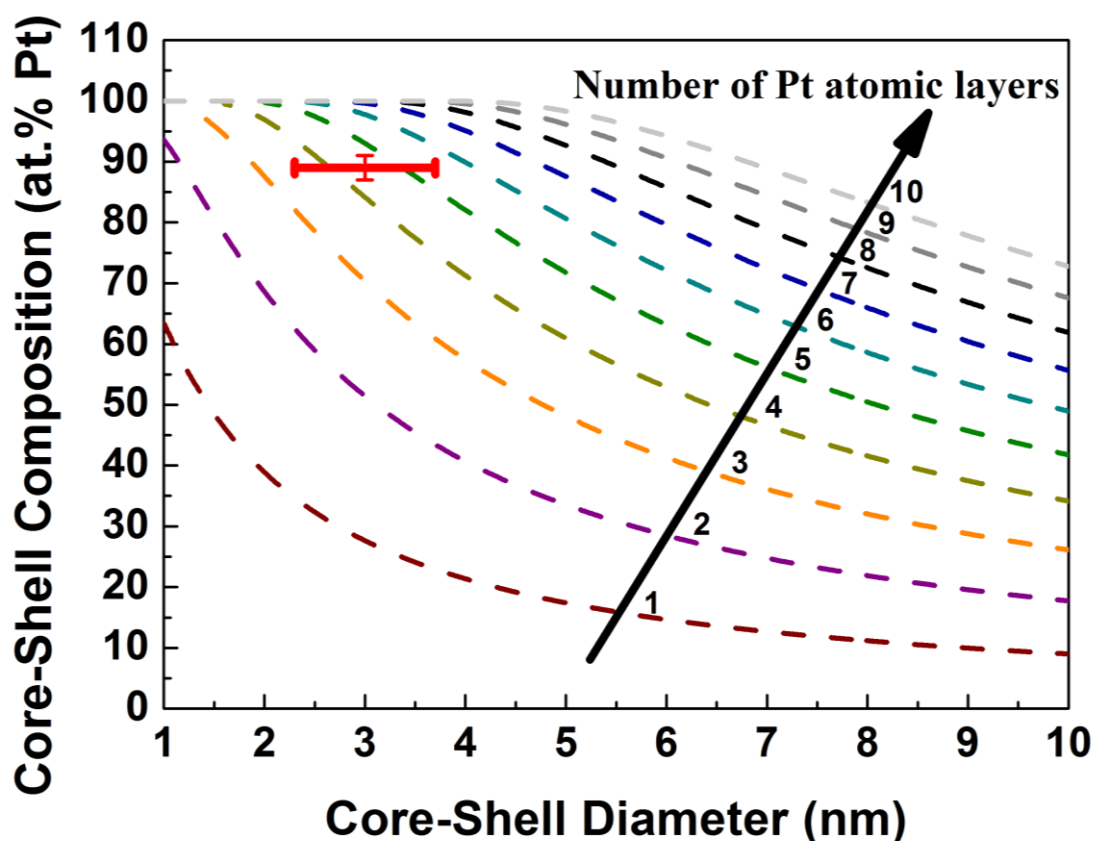
Figure 4.5: Relation between the chemical composition and the diameter of the core@shell nanoparticles established from the model of Montejano-Carrizales et al. [167,168]. The red symbol is the intersection of the composition of the core-shell catalyst measured by X-EDS and the particle size measured by TEM. According to the model, the Ni@Pt/C catalyst features a 4.5 ± 1 layers thick Pt shell.

4.2.2 Structure and Chemical Composition of the Different Electrocatalysts

The chemical composition of the synthesized bimetallic catalysts was determined by X-EDS and the Pt weight fraction by Atomic Absorption Spectroscopy (AAS). As shown by **Table 4.1**, all catalysts feature a Ni content *ca*. 15 ± 5 at. % and a Pt weight fraction close to 20 wt.%. The lattice parameter and the size of the PtNi/C nanocrystallites were obtained by Rietveld refinement of the WAXS patterns. The Synchrotron WAXS patterns measured on all catalysts are presented in **Figure 4.6a**. The shift of the Bragg peaks to higher 2θ values compared to Pt/C TKK is unambiguous evidence of Pt lattice contraction for the bimetallic catalysts. However, the degree of contraction of the Pt lattice (lattice strain) strongly depends on the fine arrangement of Pt and Ni atoms, being small for the

core@shell bimetallic nanostructure and large for alloyed nanostructures, as shown by **Figure 4.6b**.
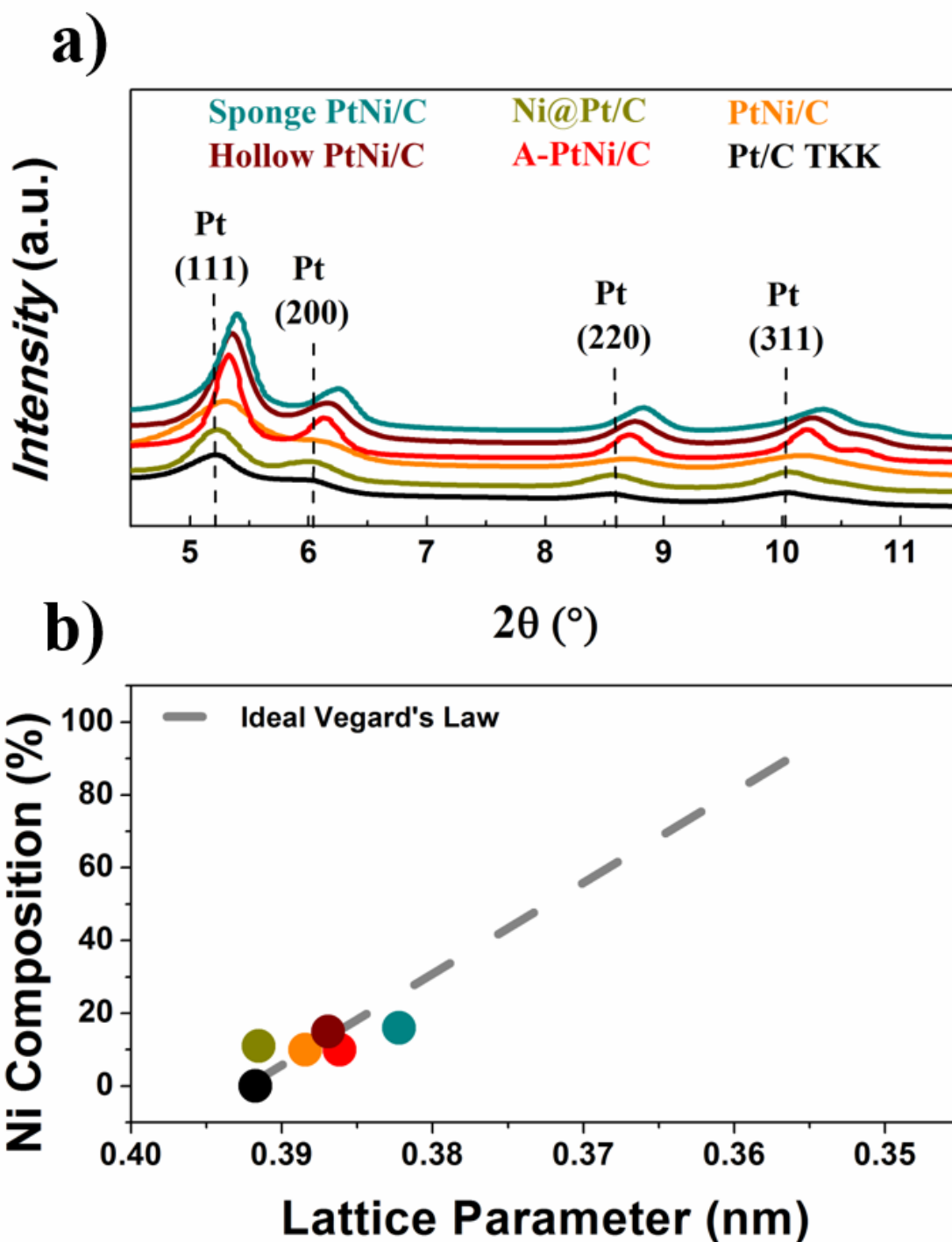
Figure 4.6: (a) Synchrotron WAXS patterns and (b) Ni composition measured by X-EDS *vs.* lattice parameter calculated from Rietveld refinement of the WAXS patterns for the synthetized bimetallic catalysts and of the reference Pt/C TKK material. The chemical composition predicted by the Vegard's law is represented as a dotted line in (b).

The crystallite sizes determined by Rietveld analysis of the WAXS patterns consistently agreed with the particle sizes or the Pt-rich shell thicknesses estimated by TEM or STEM on the Pt/C TKK, PtNi/C and Ni@Pt/C nanomaterials: 2 ± 0.5 nm, 2 ± 0.5 nm, 0.8 ± 0.2 nm, respectively. The marked difference between crystallite and particle sizes for the hollow and 'sea sponge' PtNi/C nanostructures illustrates the fact that these nanomaterials are composed of individual nanocrystallites interconnected with each other *via* grain boundaries.

Table 4.1: Structural and chemical parameters for the electrocatalysts evaluated in this study. Atomic composition determined by X-EDS, Pt weight fraction determined by AAS, lattice parameter and crystallite size determined from Rietveld refinement of the Synchrotron WAXS patterns.

	X-EDS	AAS	Synchrotron WAXS		
Electrocatalyst	**At. Comp (%)**	**Pt weight fraction (wt.%)**	**Lattice parameter (Å)**	**Contraction *vs*. Pt/C (%)**	**Crystallite size (nm)**
Pt/C TKK	$Pt_{100}Ni_0$	20.0*	3.918	0	1.3 ± 0.2
PtNi/C	$Pt_{90\pm3}Ni_{10\pm3}$	16.9 ± 0.2	3.885	0.8	1.2 ± 0.2
A-PtNi/C	$Pt_{90\pm4}Ni_{10\pm4}$	19.7 ± 0.1	3.862	1.4	4 ± 0.5
Ni@Pt/C	$Pt_{89\pm2}Ni_{11\pm2}$	19.4 ± 0.2	3.915	0.1	1.8 ± 0.2
Hollow PtNi/C	$Pt_{85\pm2}Ni_{15\pm2}$	22.6 ± 0.1	3.870	1.2	2.7 ± 0.4
Sponge PtNi/C	$Pt_{84\pm1}Ni_{16\pm1}$	16.9 ± 0.2	3.820	2.5	4.5 ± 0.9

* The weight fraction of the reference Pt/C material was guaranteed by TKK.

In addition to the lattice strain (that is the degree of contraction of the lattice parameter deduced from the shift in the position of the WAXS peaks relative to Pt/C), Rietveld analysis was also used to extract the microstrain (that is the spread of the lattice parameter values around the mean) [146]. The values of the microstrain (denoted as 'raw microstrain') are presented in **Figure 4.7** and **Table 4.2**. In general, higher microstrain values were found for alloyed and polycrystalline/aggregated nanoparticles (sea sponge PtNi/C, hollow PtNi/C and A-PtNi/C) compared to monodisperse and unalloyed nanoparticles (Pt/C and Ni@Pt/C). One exception was for the monodisperse PtNi/C catalyst, which exhibited a high raw microstrain value. However, this result is not surprising if one considers that microstrain depends on the crystallite size [169,170] (the microstrain increases with decreasing the crystallite size) and that the monodisperse PtNi/C catalyst features very small nanocrystallites (1.2 nm *vs*. 2.9 nm in average for other samples).
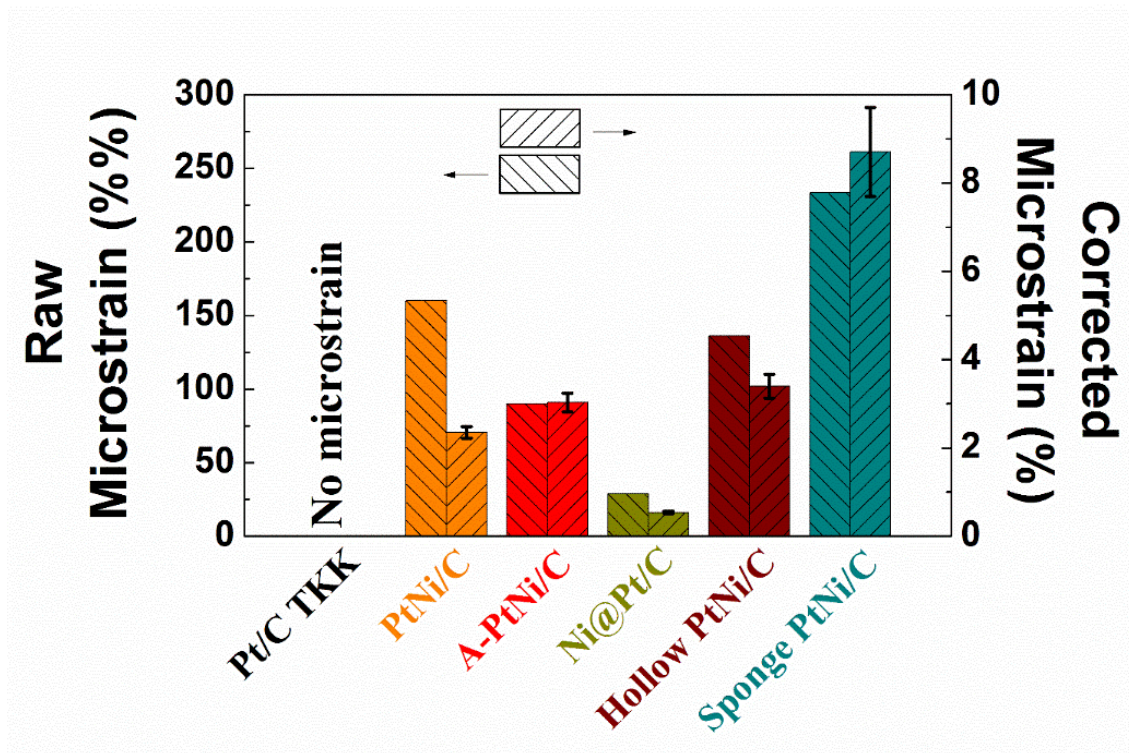
Figure 4.7. Values of raw microstrain (left scale) and microstrain corrected from surface effect ('Corrected Microstrain', see right scale) for the catalysts evaluated in this study.

The size dependence of the raw microstrain is problematic for catalytic aspects. Indeed, the raw microstrain (a bulk property) overestimates the atomic disorder caused by a structural defect present at the surface of a small crystallite simply because of the high atomic surface/volume ratio. On the contrary, the atomic disorder caused by a structural defect present at the surface of a large crystallite is compensated by a larger ordered core. To better consider the size dependency of the raw microstrain, a corrected microstrain was introduced using the dispersion (that is the ratio between surface and bulk atoms) as:

$$\text{Corrected microstrain (\%)} = \frac{\text{Raw Microstrain (\%\%)}}{D} \tag{4.4.1}$$

Where D is the dispersion or the 'Surface Atoms Ratio', as defined by Montejano-Carrizales *et al.* in their model [167,168]:

$$D = 100 \text{ x } \frac{N\text{s}}{N} \tag{4.2}$$

And N and Ns are the total number of atoms and the number of surface atoms, respectively:

$$N = 10\frac{m^3}{3} + 5m^2 + \frac{11}{3}m + 1 \tag{4.3}$$

$$Ns = 10m^2 + 2 \tag{4.4}$$

'*m*' corresponds to the number of atomic layers composing the crystallite in the Montejano-Carrizales model. The values of '*m*' are linked to the crystallite size '*d*' size by the relation:

$$m = \frac{d}{2\sqrt{3}r_{Pt}} \tag{4.5}$$

With 'r_{Pt}' the covalent radius of a Pt atom ($r_{Pt} = 0.135$ nm).

Both as-determined and corrected microstrain values are presented in **Figure 4.7** and **Table 4.2**.

Table 4.2: Structural parameters (as-determined and corrected microstrain values, dispersion calculated from the mean crystallite size) determined by Rietveld refinement of the WAXS patterns on the different PtNi nanocatalysts and the reference Pt/C TKK material.

Electrocatalyst	Microstrain (%%)	Dispersion (%)	Corrected Microstrain (%)
Pt/C TKK	0	65 ± 8	0
PtNi/C	160.0	68 ± 8	2.4 ± 0.1
A-PtNi/C	90.0	30 ± 4	3 ± 0.2
Ni@Pt/C	28.7	54 ± 6	0.5 ± 0.1
Hollow PtNi/C	136	40 ± 6	3.4 ± 0.3
Sponge PtNi/C	233.3	28 ± 6	8.7 ± 1

As shown in **Figure 4.7** and **Table 4.2**, even if the overall microstrain values decreased after correction, the only noticeable change resulting from this correction occurred for isolated and agglomerated PtNi/C nanoparticles. Hence, we argue that corrected microstrain values better reflect the fact that the A-PtNi/C catalyst is composed of individual PtNi/C nanocrystallites necking via grain boundaries. Note also that the values of the corrected microstrain estimated on nanostructures exhibiting pure Pt phases (Ni@Pt/C and Pt/C TKK) were by far smaller than those of alloyed nanostructures. The absence of microstrain for the reference Pt/C TKK was particularly striking. However, we stress that similar values were obtained on a Pt/C catalyst manufactured by E-TEK (raw microstrain: 17 %%; dispersion: 59 %; corrected microstrain: 0.29 %). *A contrario*, the nanostructures composed of aggregated crystallites feature the highest microstrain

values (A-PtNi/C < hollow PtNi/C < Sponge PtNi/C). This is believed to reflect the high density of structural defects (in particular of grain boundaries) contained in these nanostructures. Recently, a very good correlation has been established between microstrain measured from XRD and grain boundary density obtained from TEM images statistics of Cu nanoparticles [171]

4.3 Microstrain and Electrocatalysis

4.3.1 CO_{ads} Stripping - ORR Catalytic Activity Relationships

We then investigated the surface reactivity and the ORR activity of the different nanostructures. Prior to any catalytic activity measurement, all synthesized and reference nanocatalysts were introduced at $E = 0.1$ V *vs*. RHE in the electrochemical cell, and 'activated' by a procedure derived from the recommendations of Shinozaki *et al*. [172] (50 potential cycles at 500 mV s^{-1} between 0.05 and 1.23 V *vs*. RHE in Ar-saturated 0.1 M HClO$_4$, in order to obtain a stable surface state).

The first and the last 'activation' cycles in the potential region $0.05 < E < 0.50$ V *vs*. RHE measured on the different catalysts are shown in **Figure 4.8.** A strong dependence of the charge density associated with the desorption of under-potentially deposited H (H$_{upd}$) on the Ni content in the surface and near-surface region was found, in agreement with literature [173,174]. The presence of sharped H$_{upd}$ peaks before and after electrochemical activation **Figure 4.8a** and **Figure 4.8c** for Pt/C TKK and Ni@Pt/C confirms that they feature a pure Pt surface ('Pt to Pt'). In opposite **Figure 4.8b** and **Figure 4.8d**, sharp H$_{upd}$ peaks developed on PtNi/C and A-PtNi/C during electrochemical activation, which indicates that Ni atoms were leached out from the surface and near-surface region during this procedure resulting in the formation of a dealloyed surface ('PtNi to Pt'). Finally, on the hollow and 'sea sponge' PtNi/C nanoparticles, a small bump at $E = 0.3$ V *vs*. RHE usually attest to the presence of (100) type facets (**Figure 4.8e** and **Figure 4.8f**). As the presence of such low index facets is hardly probable in the case of such small, agglomerated and acid-leached nanocrystallites, this feature could however suggest a modification of surface Pt atoms electronic structure, for highly disordered nanocatalysts ('unconventional Pt').
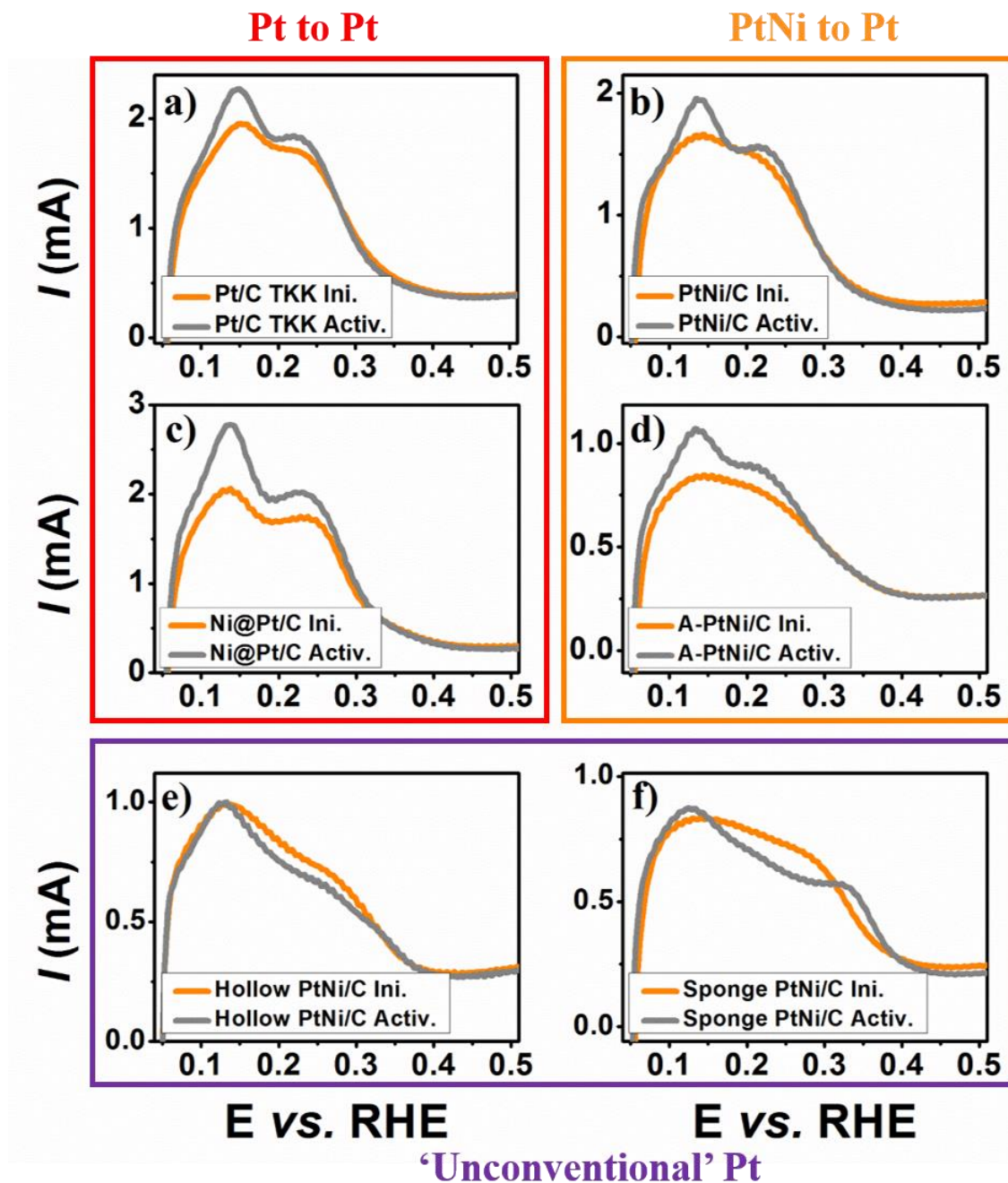
Figure 4.8. Comparison of the H_{upd} desorption region before (1st scan) and after (50th scan) electrochemical activation for (a) the reference Pt/C TKK, (b) PtNi/C, (c) Ni@Pt/C, (d) A-PtNi/C, (e) hollow PtNi/C, and (f) 'sea-sponge' PtNi/C (f) catalysts. Ar-saturated 0.1 M $HClO_4$; $v = 500$ mV s^{-1}; $T = 25 \pm 1$ °C; no rotation of the electrode; Pt loading: 20 µgPt cm$_{geo}^{-2}$.

CO_{ads} stripping measurements were performed to gain insights into the fine nanostructure of the synthesized nanomaterials. Indeed, the CO_{ads} electrooxidation is a highly structure sensitive reaction and many particle properties such as surface composition [38,175,176], particle size [177,178], particle agglomeration [178,179] and crystallographic orientation of the facets [180,181] influence the number, the position and the shape of the CO_{ads} stripping peaks.

The CO$_{ads}$ stripping voltammograms recorded on the synthesized materials featured two type of peaks (**Figure 4.9c**).

In agreement with former literature findings, [177–179,182–184] the first peak located between 0.40 < E < 0.73 V *vs.* RHE was ascribed to CO$_{ads}$ electrooxidation on individual nanocrystallites interconnected *via* grain boundaries, and the second peak located between 0.7 < E < 1.0 V *vs.* RHE was ascribed to CO$_{ads}$ stripping on isolated (*i.e.* non-agglomerated) nanocrystallites. This is unequivocally shown by **Figure 4.9c**: the CO$_{ads}$ stripping voltammograms are dominated by the high potential peak on monodispersed catalysts (Pt/C TKK, PtNi/C and Ni@Pt/C), and by the low potential peak on highly defective nanocatalysts (hollow and on 'sea sponge' PtNi/C). The catalyst A-PtNi/C, which contains both isolated and agglomerated nanocrystallites, represents an intermediate case. Note that the high potential peak contribution for the hollow catalyst may also be attributed to isolated nanoparticles that were observed in TEM images.
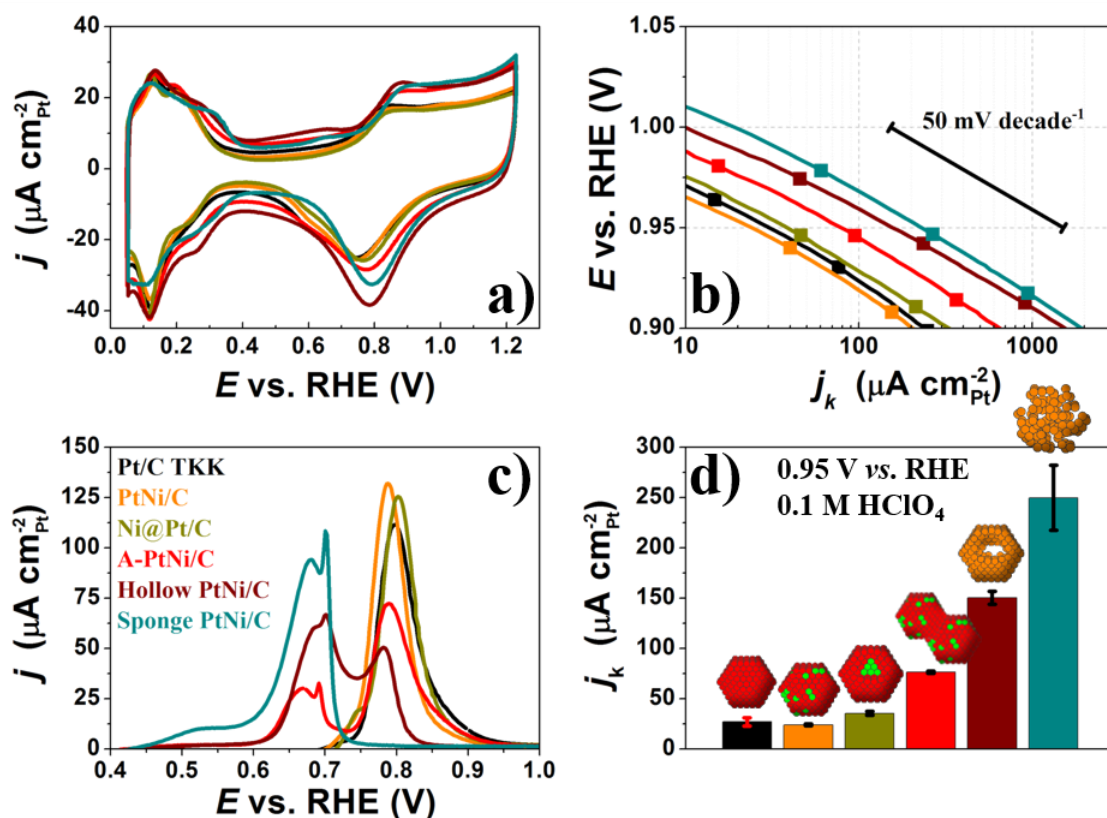
Figure 4.9. (a) Base and (c) background-subtracted CO$_{ads}$ stripping voltammograms measured on the nanomaterials evaluated in this work, (b) Tafel plots obtained from the steady-state $I-E$ curves measured at ω = 1600 rpm after correction for Ohmic losses and diffusion in solution and (d) ORR specific activity measured at E = 0.95 V *vs.* RHE for the electrocatalysts evaluated in this work. (a) and (c) were conducted in Ar-saturated 0.1 M HClO$_4$ at v = 20 mV s^{-1} without rotation of the electrode. (b) and (d) were conducted in O$_2$-saturated 0.1 M HClO$_4$ at a potential sweep rate v = 5 mV s^{-1}. Other conditions: T = 25 ± 1 °C, Pt loading = 3.92 μg, ω = 1600 rpm. The error bars are the standard deviation of at least three independent measurements.

It is striking that both CO$_{ads}$ stripping voltammograms (electrochemical measurement) and the corrected microstrain values derived from WAXS patterns (physical measurement) both suggested that the density of structural defects (such as grain boundaries) increased in the order: Pt/C TKK, PtNi/C, Ni@Pt/C < A-PtNi/C < hollow PtNi/C < sea sponge PtNi/C. To extract quantitative information from these electrochemical measurements, the CO$_{ads}$ electrooxidation voltammograms were statistically analysed. We introduce a new electrochemical parameter (the potential weight in CO$_{ads}$ stripping voltammograms $U(E)$ in V^{-1}) as:

$$\int_{0.4}^{1} U(E)dE = 1 \tag{4.6}$$

Yielding:

$$U(E) = \frac{j(E)}{\int_{0.4}^{1} j(E)dE} \tag{4.7}$$

Where $j(E)$ is the measured current density (µA cm$_{Pt}^{-2}$) at a given electrode potential E (here comprised between 0.4 – 1.0 V).

$$\mu_1^{CO} = \int_{0.4}^{1} E.U(E)dE \tag{4.8}$$

Therefore, the average CO$_{ads}$ oxidation potential μ_1^{CO} (in V) corresponds to the first moment of the potential weight:

The values of μ_1^{CO} determined for each nanostructure are displayed in **Table 4.3**. The relation between CO$_{ads}$ electrooxidation kinetics and the grain boundaries content [177–179] resulted into low μ_1^{CO} values on highly defective nanomaterials (hollow and sea-sponge PtNi/C nanoparticles). On the contrary, higher values of μ_1^{CO} were found for pure Pt phases (Pt/C TKK and Ni-core@Pt-shell).

The ORR activity of the various nanostructures was investigated according to the electrochemical protocol defined by Kocha *et al.* [172,185–189]. The Tafel plots and the ORR specific activity determined at E = 0.95 V *vs*. RHE are presented in **Figure 4.9**, and the ORR mass activity in **Table 4.3** (for the sake of comparison with other studies, the specific and the mass activity for the ORR were also calculated at E = 0.9 V *vs*. RHE (SA$_{0.90}$ and MA$_{0.90}$, respectively) and are displayed in appendix of this manuscript). A slight improvement of the ORR specific activity compared to pure Pt/C TKK was found

for the bimetallic nanostructures composed of monodispersed nanoparticles (PtNi/C and Ni@Pt/C). This slight improvement can be rationalized based on the mild Pt lattice compression, and the similar Pt-rich surface for Pt/C TKK, PtNi/C and Ni@Pt/C electrocatalysts (**Figure 4.8b, Figure 4.8c,** and **Figure 4.8d**).

Table 4.3. Pt specific surface area ($S_{Pt,CO}$), average CO_{ads} electrooxidation potential (μ_1^{CO}) and iR + mass transport corrected ORR specific activity ($SA_{0.95}$) and mass activity ($MA_{0.95}$) measured at $E = 0.95$ V *vs*. RHE on the PtNi/C nanostructures and the reference Pt/C TKK, and corresponding enhancement factor (E.F.). The ORR activity was determined in O_2-saturated 0.1 M $HClO_4$ at a potential sweep rate $v = 5$ mV s^{-1}. Other conditions: $T = 25 \pm 1$ °C, Pt loading = 3.92 μg, ω = 1600 rpm.

Electrocatalyst	$S_{Pt,CO}$ (m^2 g$_{Pt}^{-1}$)	μ_1^{CO} *vs.* RHE (V)	$SA_{0.95}$ (μA cm$_{Pt}^{-2}$)	E.F. SA	$MA_{0.95}$ (A g$_{Pt}^{-1}$)	E.F. MA
Pt/C TKK	78 ± 5	0.82	27 ± 4	1	21 ± 5	1
PtNi/C	104 ± 12	0.81	24 ± 1	0.9	25 ± 2	1.2
A-PtNi/C	39 ± 1	0.76	76 ± 1	2.8	30 ± 1	1.4
Ni@Pt/C	95 ± 6	0.82	36 ± 2	1.3	34 ± 2	1.6
Hollow PtNi/C	41 ± 4	0.72	151 ± 6	5.6	62 ± 8	3
Sponge PtNi/C	46 ± 4	0.66	250 ± 32	9.3	122 ± 19	5.8

The ORR specific activity was significantly enhanced on nanostructures composed of aggregated PtNi/C nanocrystallites: a 2.8, 5.8 and 9.3-fold enhancement of the ORR specific activity was monitored on A-PtNi/C, hollow PtNi/C and sea sponge PtNi/C respectively, compared to the reference Pt/C TKK material. This is unequivocal evidence that, at fixed Ni at. %, structural defects (such as grain boundaries) significantly enhance the ORR kinetics. To confirm our hypothesis, the ORR specific activity was plotted as a function of two parameters which are reflective of the fraction of structural defects: the corrected microstrain and the average CO_{ads} oxidation potential, μ_1^{CO}. The nearly linear structure – ORR activity relationships displayed in **Figure 4.10** unambiguously shows that, at low Ni at. %, structural properties outweigh alloying effects.

However, it can be noticed from **Figure 4.6b** that all the catalysts presented in this study do not feature the same lattice parameters. This difference can be explained by either slight variations of the Ni content from one catalyst to the other, or because the lattice parameter did not relax during dealloying, as previously reported in literature [90,142]. Because it is generally accepted that the lattice strain controls the activity on dealloyed PtNi nanoparticles [141], a direct comparison of lattice strain-ORR activity is presented in **Figure 4.11a**. This plot shows no direct correlation between lattice strain and ORR

activity for the catalysts of this study but it also reveals that, in the case of highly microstrained nanostructures, that the concept of lattice parameter must be considered carefully, as the dispersion around the mean lattice induced by the sum of local defects is non-negligible.
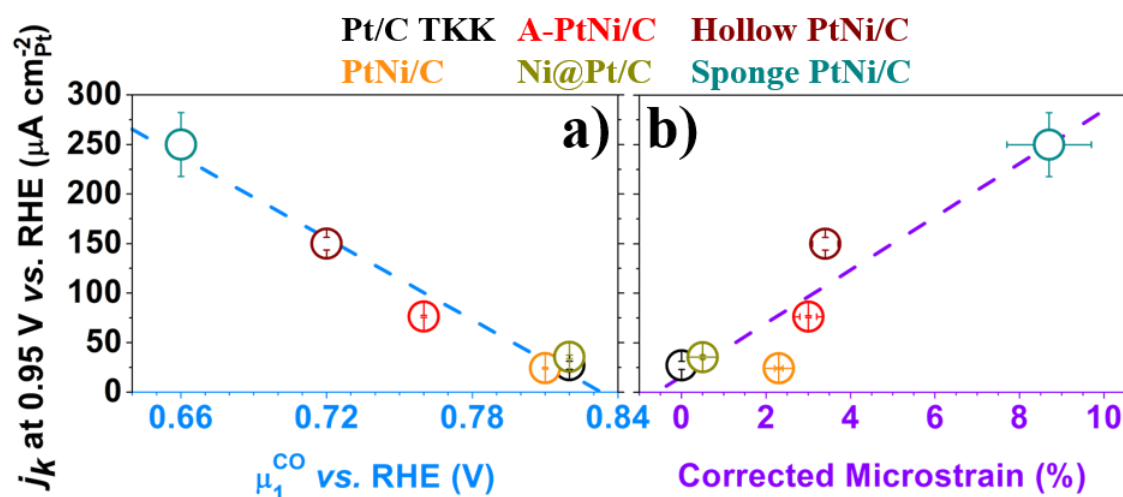
Figure 4.10. Relationships between the ORR specific activity measured at $E = 0.95$ V *vs.* RHE and the density of structural defects for the different nanostructures evaluated in this study. The density of structural defects was estimated by two independent parameters: (a) the average CO_{ads} oxidation potential and (b) the corrected microstrain. The ORR specific activities were extracted from ORR voltammograms conducted in O_2-saturated 0.1 M $HClO_4$ at a potential sweep rate $v = 5$ mV s^{-1} after correction from Ohmic losses and diffusion in solution. Other conditions: $T = 25 \pm 1$ °C, Pt loading = 3.92 μg, ω = 1600 rpm.

Then, based on these experimental insights, we postulate in **Figure 4.11b** a model on how microstrain can impact on CO oxidation reaction (COOR) and ORR. Basically, if the global lattice strain usually rules the ORR activity due to a decrease in oxygenated chemisorption energy (red point on the volcano plot), according to its definition, microstrain is the manifestation of highly contracted or relaxed lattice regions within the crystal, and, if located upon the surface such a region must also feature modified chemisorption energies (orange double arrow on the volcano plot). Consequently, a catalytic site located in a more contracted region features oxophobic properties (more positive OH adsorption energy relative to Pt(111), favouring the ORR) and one located in a more relaxed region features oxophilic (more negative OH adsorption energy relative to Pt(111), favouring the COOR as OH_{ads} species are needed for CO_{ads} oxidation). The duality of catalytic sites explains how both COOR and ORR are impacted by the increasing values of microstrain for the different electrocatalysts. Moreover, the positive impact for these two reactions (both COOR and ORR activities increase with increasing microstrain, see **Figure 4.10a**) suggests that if only few catalytic sites are impacted by

the structural disorder, their intrinsic catalytic activity (equivalent to turnover frequency in gas phase catalysis) is largely enhanced for the considered reaction, which in the end guarantees a better efficiency of the nanocatalyst.
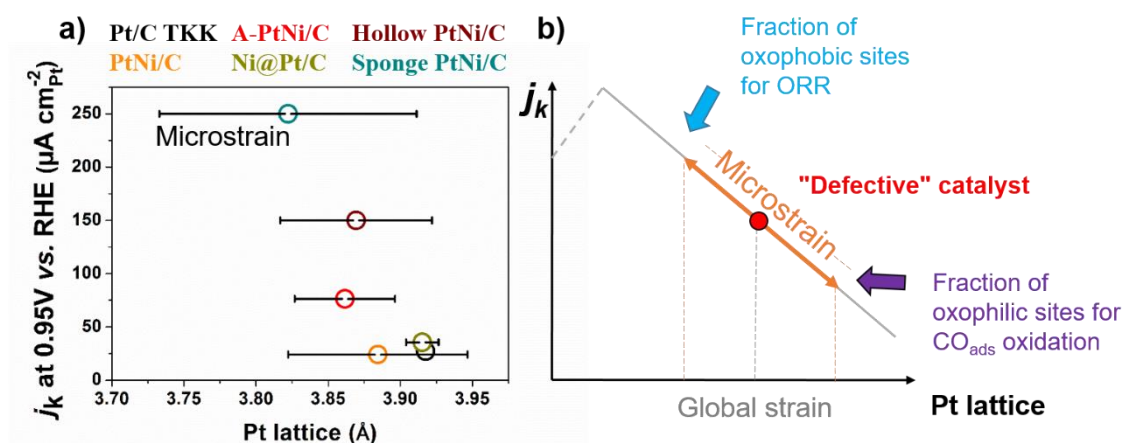
Figure 4.11: (a) Relationship between the ORR specific activity measured at $E = 0.95$ V *vs*. RHE and the Pt lattice parameter for the different electrocatalysts from this study. According to its definition, the microstrain is used as the error bar for the Pt lattice determination from Rietveld refinement of WAXS patterns; (b) schematic explaining the role of microstrain (compared to global strain) for both COOR and ORR in the admitted ORR activity-Pt lattice volcano plot.

These results confirm our former conclusions (see **Section 3.2.3** and Reference [143]) on the beneficial effect of structural defects on the ORR activity was first reported. However, they represent a significant step forward since the concept of microstrain-induced enhancement of the ORR activity is, for the first time, quantitatively extended to six different catalysts featuring different atomic arrangement (isolated or aggregated PtNi/C nanoparticles, solid or hollow alloy PtNi/C nanoparticles, Ni-core@Pt-shell nanoparticles). This catalytic trend is also in line with the recent *ab initio* calculations of Calle-Vallejo *et al*. [190]. Using DFT calculations and experiments on single crystal surfaces, the authors evidenced that catalytic sites with generalized coordination numbers greater than 7.5 feature superior ORR activity (the calculated optimum being 8.3). The results presented in this Chapter show that grain boundaries provide a proxy to implement catalytic sites with reduced atomic density and thus higher generalized coordination numbers. Combined with local strain provided by the Ni atoms, the ORR specific activity of structurally-defective nanocatalysts can be improved by a factor of more than 9 while keeping the PtNi stoichiometry identical. The results also suggest that the remarkable ORR activity measured on highly polycrystalline nanomaterials, such as PtM nanowires [191–193] or PtM aerogels [194,195] (which display a CO_{ads} electrooxidation peak comprised between 0.4-0.73 V *vs*. RHE in comparable experimental conditions of the present work)

likely arises from a combination of structural, strain and ligand effects. Our results are also in line with the remarkable ultrahigh ORR activity of the so called 'jagged platinum nanowires' recently reported by Li *et al.* [196]. Hence, implementing structural disorder in nanomaterials appears to be a promising route to enhance the ORR activity of bimetallic electrocatalysts.

4.3.2 DFT and Extension to Methanol and Ethanol Oxidation Reactions

To provide further evidence of the coexistence of oxophobic/oxophilic catalytic sites on a structurally defective surface, DFT calculations were performed by Le Bacq *et al.* [197]. We mimicked the leaching of Ni atoms from the surface and subsurface layers and the entrance of atomic vacancies inside PtNi materials (such as hollow or sea sponge nanoparticles) during their synthesis and acid-leaching steps by introducing atomic vacancies into slabs composed of pure Pt layers with (111) orientation. The slabs were then relaxed using the Vienna *ab initio* simulation package code until a stable configuration was obtained. The results of these calculations, partially summarized in **Figure 4.12**, unambiguously show severe residual distortion of the lattice after reconstruction.
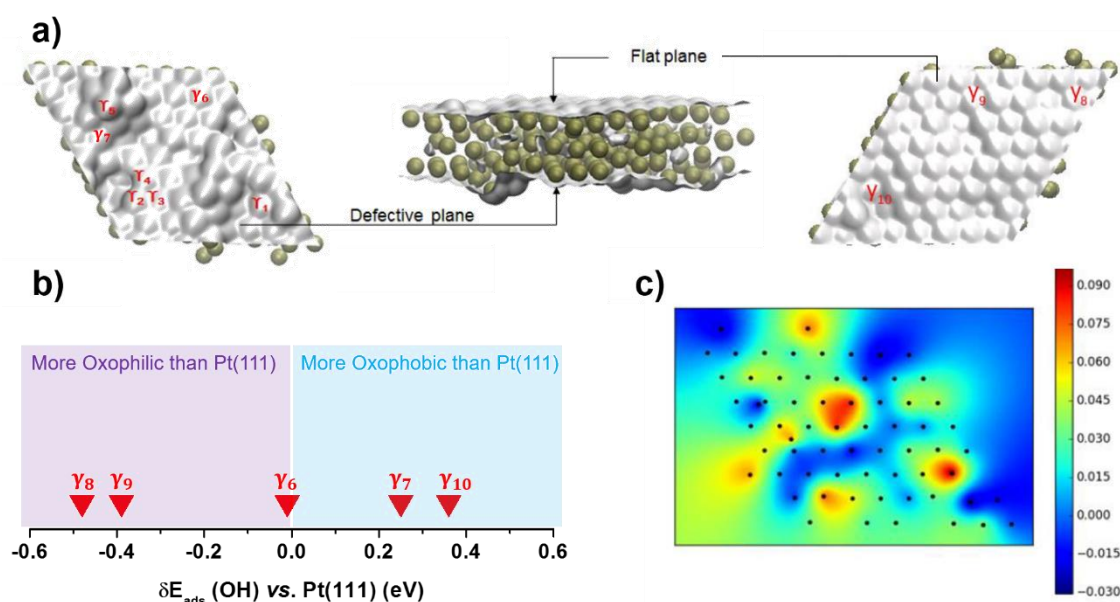
Figure 4.12: (a) views of the two surfaces formed on 5-layer Pt(111) slab after introduction of 40% atomic vacancies and relaxation using the VASP code; (b) OH adsorption energies relative to Pt(111) for selected catalytic sites and (c) map of the inner deformation of the surface. In b) purple and blue regions on the plot show the more oxophobic and less oxophobic catalytic sites than Pt(111) respectively. Adapted from [197].

Particularly, **Figure 4.12c** reveals the coexistence of both contracted and relaxed regions on the same surface, in perfect agreement with the notion of microstrain experimentally

measured on the real catalysts. Calculations of OH adsorption energies on randomly chosen catalytic sites (noted γ_6-γ_{10}) on both surface of the slab (one clearly distorted and the other flatter, see **Figure 4.12a**) showed that, whatever the surface chosen, each catalytic site features a singular OH adsorption energy, either higher or lower than 'perfect' Pt(111), providing further support to our hypotheses (**Figure 4.12b**).

Moreover, if more oxophilic catalytic sites than Pt(111) are present on a given surface, the latter should be more active for electrooxidation reactions. It is well-established, especially from Differential Electrochemical Mass Spectrometry (DEMS) [198], that CO_{ads} species are formed during dehydrogenation of adsorbed methanol species at low electrode potential (**Equations (4.9) and (4.10)**). The latter then poison the Pt catalytic sites before being oxidized into CO_2 (**Equations (4.12)**) via adsorbed oxygenated species (OH_{ads}) formed by water dissociation (**Equation (4.11)**).

$$CH_3OH + * \rightarrow CH_3OH_{ads} \tag{4.9}$$

$$CH_3OH_{ads} \rightarrow CO_{ads} + 4\ H^+ + 4e^- \tag{4.10}$$

$$H_2O + * \rightarrow OH_{ads} + H^+ + e^- \tag{4.11}$$

$$CO_{ads} + OH_{ads} \rightarrow 2\ * + CO_2 + H^+ + e^- \tag{4.12}$$
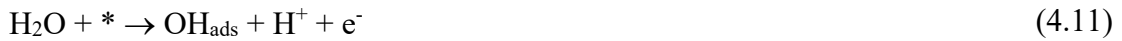
Where * denotes a Pt (or PtNi) catalytic site.

Similarly, the electrochemical oxidation of ethanol (EOR, ethanol oxidation reaction) on Pt surface occurs via adsorption and dehydrogenation of ethanol molecules, leading to the formation of acetaldehyde (**Equations (4.13) and (4.14)**). Further dissociation of acetaldehyde produces CO_{ads} and $C_xH_{2x+2,ads}$ species (carbohydrate fragments, such as methane and ethane [199] (**Equation (4.15)**) which can be further be transformed into CO_{ads} (**Equation (4.16)**). Note that direct dissociation of ethanol into CO_{ads} and $C_xH_{2x+2,ads}$ species is also possible (**Equation (4.17)**). In the final steps of the EOR, the dissociation of water molecules produces OH_{ads} groups (**Equation (4.11)**), which complete the electrooxidation of the adsorbed CO molecules (**Equations (4.12)**).

$$CH_3CH_2OH + * \rightarrow CH_3CH_2OH_{ads} \tag{4.13}$$

$$CH_3CH_2OH_{ads} \rightarrow CH_3CHO_{ads} + 2\ H^+ + 2\ e^- \tag{4.14}$$

$$CH_3CHO_{ads} \rightarrow CO_{ads} + CH_{2x+2,ads} + (4\text{-x})\ H^+ + (4\text{-x})\ e^- \tag{4.15}$$

$$CH_{2x+2,ads} + H_2O \rightarrow CO_{ads} + (2\text{+x})\ H^+ + (2\text{+x})\ e^- \tag{4.16}$$

$$CH_3CH_2OH_{ads} \rightarrow CO_{ads} + C_xH_{2x+2,ads} + (6\text{-}x)\,H^+ + (6\text{-}x)\,e^- \qquad (4.17)$$
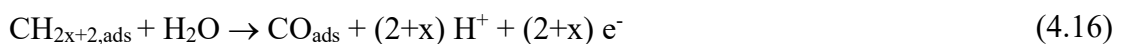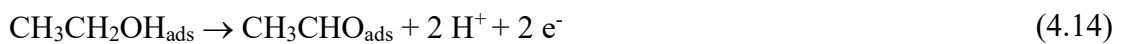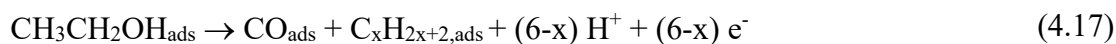
The electrocatalytic activity of the 'sea sponge', hollow, agglomerated and alloyed PtNi/C catalysts compared to Pt/C TKK for both MOR and EOR were determined in the following conditions: first, the potential of the electrode was maintained at $E = 0.1$ V $vs.$ RHE under alcohol containing electrolyte (0.1 M $HClO_4$ and 0.1 M methanol or ethanol) for $t = 15$ min (yielding a blockage of the catalyst surface with dehydrogenation products). To strip, these dehydrogenation products, 10 cycles between 0.05 and 0.1 V $vs.$ RHE were performed, and the 10th and stable voltammograms for each catalyst are plotted **Figure 4.13a** (MOR, methanol oxidation reaction) and **Figure 4.13b** (EOR). To take into account the eventual influence of Ni atoms, experiments were also performed on the solid PtNi/C and A-PtNi/C catalysts. The voltammograms displayed in **Figure 4.13** show a completely inhibited hydrogen adsorption and desorption region at low electrode potential (< 0.3 V $vs.$ RHE) for all the electrocatalysts in the two reactions media, in agreement with blocked Pt surfaces by the adsorbed alcohol molecules and dehydrogenation products.
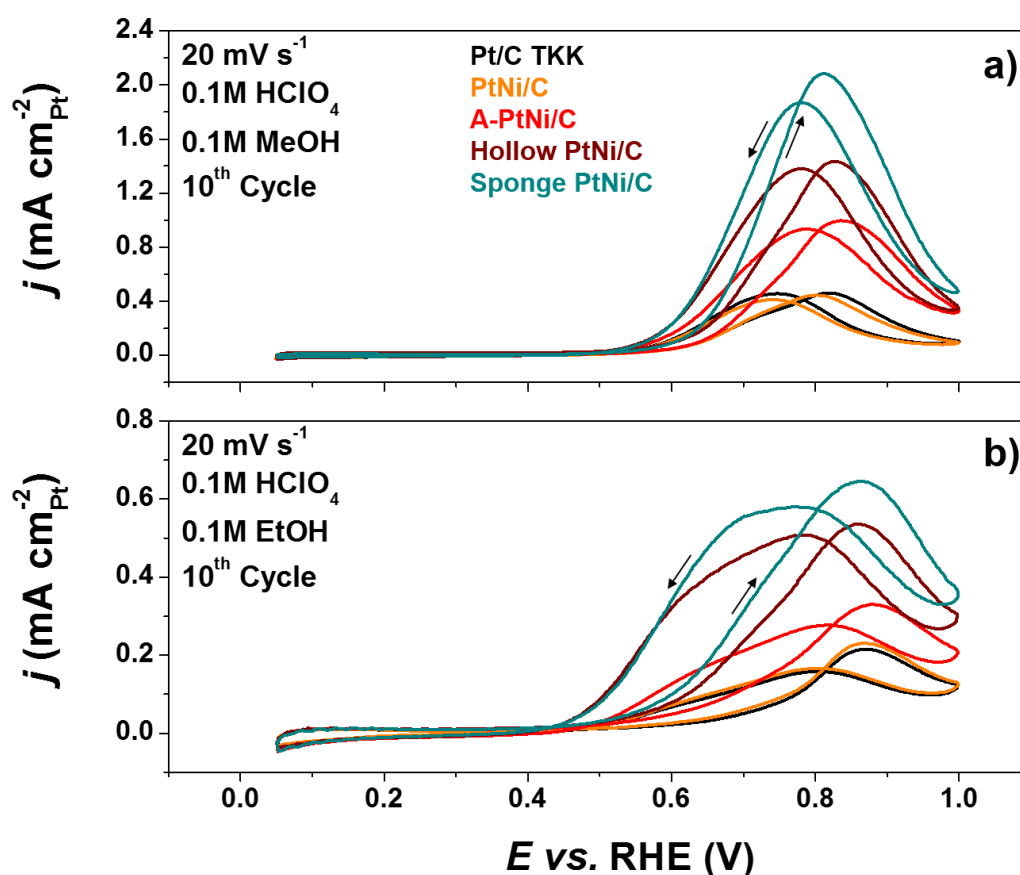
Figure 4.13: 10th cyclic voltammogram obtained in 0.1 M $HClO_4$ containing (a) 0.1 M methanol, (b) 0.1 M ethanol. Potential sweep rate: 20 mV s^{-1}, $T = 25 \pm 1$ °C and Pt loading: 20 µg$_{Pt}$ cm$^{-2}_{geo}$. The voltammograms were recorded after keeping the electrode potential 15 min at 0.1 V $vs.$ RHE. $T = 25 \pm 1$ °C.

As the electrode potential increased, a first oxidation peak appeared, with a far more negative onset potential for the defective materials: in case of the MOR, the current density of 200 $\mu A\ cm_{Pt}^{-2}$ was reached 12, 38 and 48 mV lower for A-PtNi/C, hollow PtNi/C and 'sea sponge' PtNi/C respectively compared to Pt/C TKK and PtNi/C, for the EOR and a current density of 50 $\mu A\ cm_{Pt}^{-2}$ the onsets decreased similarly (same catalysts order) but by 100, 140 and 160 mV. The oxidation currents then increased with the electrode potential, until a maximum was reached between 0.80 and 0.5 V *vs.* RHE. Because of the formation of surface oxides, the oxidation currents decreased above this potential for all catalysts. Note that the overall lower current density recorded for EOR compared to MOR is surprising considering the superior number of electrons available in the ethanol molecule compared to methanol (12 *vs.* 6), we however rationalize this observation by the probable limiting C-C bond breaking step, which is necessary in case of EOR (**Equation (4.15)**).

Table 4.4: Specific and mass activities for the MOR and EOR for the different electrocatalysts from this study. For each reaction, the currents were derived from the 10th cyclic voltammogram (0.7 V *vs.* RHE, positive-going potential sweep) in 0.1 M HClO₄ containing 0.1 M of the targeted alcohol molecule and normalized by either the ECSA measured via CO$_{ads}$ stripping experiment or the electrode loading (20 $\mu g_{Pt}\ cm^{-2}_{geo}$) for SA and MA respectively.

	MOR		EOR	
Electrocatalysts	$SA_{0.7}$ $(\mu A\ cm_{Pt}^{-2})$	$MA_{0.7}$ $(A\ g_{Pt}^{-1})$	$SA_{0.7}$ $(\mu A\ cm_{Pt}^{-2})$	$MA_{0.7}$ $(A\ g_{Pt}^{-1})$
Pt/C TKK	241	188	49	38
PtNi/C	245	255	60	62
A-PtNi/C	327	127	113	44
Hollow PtNi/C	536	220	233	96
Sponge PtNi/C	744	342	309	142

The superior activities of the defective materials toward both MOR and EOR are also obvious from specific and mass activity values displayed in **Table 4.4**. As expected from similar COOR activities (**Figure 4.9** and **Figure 4.10**), the simple addition of 15 at. % Ni did not show any improvement in MOR or EOR kinetics relative to Pt/C TKK. However, better MOR and EOR activities were measured on the defective catalysts, namely A-PtNi/C, hollow PtNi/C and 'sea sponge' PtNi/C compared to the isolated Pt/C TKK and PtNi/C.

In conclusion, the combination of theoretical and experimental results shows that implementing structural defects (such as grain boundaries and/or atomic vacancies) into nanocatalysts structure gives rise to local structural disorder (which can be physically quantified *via* a determination of the microstrain value), and, as this local disorder increases, the electrocatalysts surface develops a very interesting mix of oxophilic/oxophobic catalytic sites, which provides the possibility to speed up the kinetics of both electroreduction and electrooxidation reactions, as summarized in **Figure 4.14**.
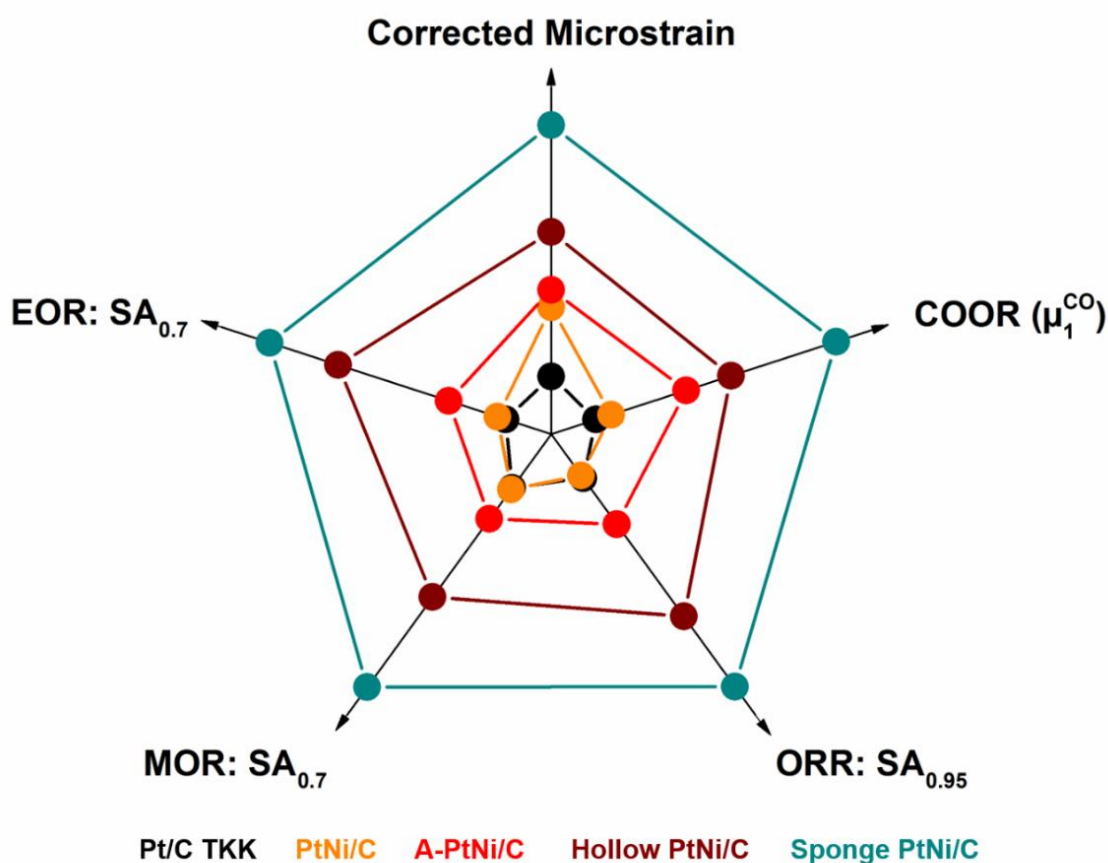
Figure 4.14: Spider graph summarizing the different key properties of the different electrocatalysts from this study, showing the similar trends between increasing defects content (corrected microstrain), COOR activity (μ_1^{CO}), ORR activity (SA measured at 0.95 V *vs.* RHE), MOR activity (SA measured at 0.7 V *vs.* RHE) and EOR activity (SA measured at 0.7 V *vs* RHE). All SAs corrected from ohmic drop, only the SA for ORR is corrected from diffusion.

4.4 Conclusion

In this chapter, PtNi nanoparticles with similar crystallite size and chemical composition (Pt:Ni stoichiometry *ca.* 85:15) but various nanostructures were synthetized and

characterized. By combining STEM-X-EDS elemental maps, Synchrotron WAXS and electrochemical characterizations, two independent structural parameters (corrected microstrain and average CO_{ads} oxidation potential, μ_1^{CO}) were extracted and used to quantitively bridge the ORR activity and the fraction of structural defects of a given catalytic nanomaterial (in particular its fraction of grain boundaries). A model presenting the microstrain as the fingerprint of locally contracted (oxophobic) and relaxed (oxophilic) catalytic site on the same surface was introduced and confirmed by DFT calculations. The duality of defective catalysts active sites was tested for electrooxidation reactions, and the results showed that, increasing structural disorder in Pt-rich-Ni nanocrystals simultaneously enhance its electrocatalytic activity for ORR, COOR, MOR and OER, as each adsorbate from these reactions may have access to electrocatalytic sites with optimal catalytic properties. This chapter then indicates that structural effects outweigh the strain and ligand effects at low Ni at. %, and suggests that targeting structural disorder is a promising approach to improve the electrocatalytic properties of bimetallic nanocatalysts.

5 FROM 'PERFECT' TO 'DEFECTIVE' PTNI ELECTROCATALYSTS: A MATTER OF TIME?

5.1 Introduction

Because catalytic activity for the ORR catalysts exhibit a volcano-type relation with the *d*-band centre and that *d*-band centre and chemisorption energies are related (the O 2p and the Pt 5d orbitals interact with each other), the main strategy over the past decade was to target a more oxophobic surface with increased site availability (as largely discussed in the first two chapters). Tacitly, researchers tried to transpose the conclusions obtained on extended surface to nanomaterials (the latter being the 'real-life' catalysts in PEMFC). Moreover, because it is difficult to reproduce structural disorder in a controlled manner in a nanomaterial, investigations on the effect of structural defects have also been restricted to extended stepped surfaces [200–205]. These studies have nevertheless shown that terrace and/or steps sizes and/or crystallographic orientations, electrolyte media (acid or alkaline) and surface preparation are varying and influent parameters. To the best of our knowledge, only a few groups, including us [143,206–209] but also others [171,196,210], have tackled the question of structural defects directly at the nanoparticle level, or tried to bridge the findings obtained on extended surfaces to nanoparticles [197,211]. In the previous chapters, physical and electrochemical tools (corrected microstrain (CM) and the average CO_{ads} oxidation potential, (μ_1^{CO}) were introduced to quantitatively bridge structural defects density and ORR activity first on one class of catalyst [143] and then on various PtNi nanostructures [206] Our experimental results showed a near linear raise of the ORR activity on PtNi catalysts with increasing the concentration of structural defects, and no maximum was identified so far.

However, these descriptive tools were used for electrocatalysts with low Ni stoichiometry (~15 at. %), small crystallite size (< 5 nm) and no preferentially oriented facets. Note also that these tools were introduced for hollow or 'spongy' PtNi/C nanoparticles developed by our group, hence their interest for other types of electrocatalysts might remain limited for the electrocatalysis community. In this chapter, we then aim to know if our hypotheses can be extended to other types of nanomaterials, among the most active for the ORR, including PtNi/C spheres, PtNi/C cubes, PtNi nanooctahedra (collaboration with Electrochemical Catalysis, Energy and Material Science group from TU Berlin, Germany) and PtNi aerogels (collaboration with the Electrochemistry Laboratory from the Paul Scherrer Institute, Switzerland and Physical Chemistry group from TU Dresden,

Germany). In contrast to the electrocatalyst used in **Chapter 4**, these feature different Ni content, shape, and crystallographic orientation.

5.2 PtNi Materials Sampling from the ORR Electrocatalysis Landscape

5.2.1 PtNi Materials Introduction and Synthesis

Different protocols were used to synthesize shape controlled and structurally defective PtNi materials. A more complete description of the various syntheses can be found in the materials and methods section. Six 'key' materials were prepared.

PtNi/C Spheres

PtNi/C nanoparticles with high Ni content have recently received a lot of interest since they are the precursor of highly active dealloyed PtNi catalysts (see state-of-the-art section). So far, only these electrocatalysts were successfully transferred from laboratory to industry, and met ORR activity, stability and cost requirements [95]. A fine control of the particle size (below ~10 nm) was demonstrated to be the key parameter to obtain ORR active and stable dealloyed nanoparticles [91,102,212]. In TU Berlin, we prepared sub-10 nm PtNi nanoparticles according to a protocol adapted from Gan *et al.* [213], also referred at the 'hot injection' method. Briefly, Ni 2, 4- pentanedionate (Ni(acac)$_2$) metal precursor and 1, 2-tetradecanediol (TDD) reducing agent were dissolved in dibenzylether solvent in the presence of oleylamine and oleic acid (which act as capping agents). The solution was then heated to 200 °C, a preparation of Pt 2, 4- pentanedionate (Pt(acac)$_2$) in 1, 2-dichlorobenzene was quickly introduced in the reactor, leading to the reduction of the metal salts precursors by the TDD and the formation of spherical PtNi nanoparticles. In fact, introducing the Pt precursor at such a high temperature and under such a reducing solvent (just not reducing enough to reduce Ni atoms alone) leads to a sharp separation of PtNi nanoparticles nucleation and growth steps: this has been reported to be essential to obtain monodisperse nanoparticles according to the well-known LaMer's mechanism describing nanocrystal formation [214]. The as-synthetized particles were collected by centrifugation, supported on Vulcan XC-72R, washed, dried *via* the freeze-drying

technique and then thermally treated at 400°C. As shown by **Figure 5.1a**, the spherical PtNi/C nanoparticles are homogeneously distributed on the carbon support and the particle size distribution is monodisperse with an average size estimated to 9.3 ± 0.8 nm. In what follows, this sample will be referred to as 'Sphere PtNi/C'.

PtNi/C Octahedra

Although various preparations routes for shape-controlled PtNi nanoparticles have been developed (see state-of-the-art section), we chose the method originally introduced by Zhang *et al.* [75] because it does not imply the element-specific anisotropic growth reported for the solvothermal method (the final PtNi nanooctahedra feature Pt-rich apexes and Ni-rich facets) [79], and is also a versatile method to produce pure Pt or PtNi cubic particles [75]. Note however that this synthesis method has been reported to produce 'polluted' octahedra by Xia's group, which recently proposed a more complex adaptation [80]. We followed the protocol recently described by Beermann *et al.* [215]. Briefly, $Pt(acac)_2$ and $Ni(acac)_2$ salts precursors were dissolved in oleylamine and oleic acid, the solution was then deaerated with N_2 and heated. When the temperature of the solution reached 130 °C, $W(CO)_6$ powder (reducing agent) was quickly introduced, the N_2 flow stopped, and the solution was further heated to 230 °C and stirred for 45 min at this temperature. The nucleation and growth mechanism occurring at this stage leading to the octahedral shape was intensively discussed by Zhang *et al.* [75] and Xia *et al.* [80]. In particular, it was argued that W^0 atoms (which have a far lower redox-potential compared to Pt) arising from $W(CO)_6$ can act as seeds and favor a fast Pt cations nucleation in the early stage of the synthesis, while the increasing amount of as-produced W^{n+} cations may decelerate the particle growth in a second step. Also, CO species produced by decomposition of $W(CO)_6$ molecules are believed to influence the final particle shape (together with oleylamine and oleic acid cosurfactants) by preferentially poisoning specific facets (Pt(100) or Pt(111) in the absence or presence of Ni atoms in the solution, respectively). The growth of the nanoparticles is consequently blocked in these specified direction, leading to either cubic or octahedral shape in the absence or presence of Ni atoms at the early stage of the synthesis, respectively. When both Pt and Ni precursors are initially introduced, this synthesis protocol produced 8.3 ± 1 nm octahedra, which were collected by centrifugation, deposited on Vulcan XC-72R, washed with ethanol and finally freeze-

dried. **Figure 5.1c** shows TEM and particle size distribution of the as-prepared catalyst, which will be referred to as 'Octahedron PtNi/C' in what follows.

Figure 5.1: TEM images, associated symbol and particle size distributions of the main catalysts of this study (a) Sphere PtNi/C; (b) Cube PtNi/C; (c) Octahedron PtNi/C; (d) Hollow PtNi/C; (e) Aerogel PtNi and (f) Sponge PtNi/C.

Cube PtNi/C

While a Pt₃Ni(111) with a skin nanostructure (Pt₃Ni(111)-skin *i.e.* a 1-2 atomic layer of Pt covering the underlying Pt₃Ni core with the second surface layer being enriched in Ni) is particularly desirable for ORR electrocatalysis, a comparison with Pt₃Ni(100)-skin has revealed an interesting hierarchy: Pt₃Ni(111)-skin >> Pt₃Ni(100)-skin > Pt(111) > Pt(100) [63]. Consequently, PtNi/C nanocubes were synthetized at TU Berlin according to the protocol introduced by Zhang *et al.* [75] (basically, a slightly-modified of the protocol described for the synthesis of PtNi octahedra). As mentioned above, the same experimental protocol but without introduction of Ni atoms in the early stages of the synthesis, leads to cubic PtNi nanocrystals, however, by slowly injecting the Ni precursor after the addition of $W(CO)_6$, the lack of Ni stoichiometry still allows the formation of the cubic shape, while interlayer Ni diffusion ensures the formation of the PtNi phase. Due to the subtlety of this mechanism, the as-prepared material does not feature a perfect shape selectivity, as showed by TEM image and particle size distribution (**Figure 5.1b**), but still represent an intermediate case between spherical and octahedral shapes, with a main contribution of cubic nanoparticles. This sample will be referred as 'Cube PtNi/C'.

Hollow PtNi/C

Hollow PtNi/C were synthetized as described in Chapter 3 and Chapter 4 of this manuscript, and referred to as 'Hollow PtNi/C' in what follows.

Unsupported PtNi Aerogel

As mentioned in Chapter 4 we believe that structural effects, particularly structural defects may contribute to enhance the ORR activity of bimetallic nanoparticles. Especially, we mentioned the very promising unsupported PtNi aerogels first introduced by the common work of TU Dresden, Germany and the Paul Scherrer Institute (PSI), Switzerland [194,216]. In fact, these aerogels are composed of PtNi nanocrystallites interconnected to form a porous structure that is structurally similar to the hollow and sponge PtNi/C catalysts presented above. In response to our invitation to collaborate, both institutions kindly accepted to provide a sample of this material and its electrochemical fingerprints, to confront this original structure to our previously established structure-ORR and COOR activity relationships. The PtNi aerogel was prepared through a co-reduction of Pt and Ni precursors in aqueous media, using $NaBH_4$ as a reducing agent.

While the reduction of Pt and Ni occurs rapidly in such conditions (very close to the synthesis of the hollow PtNi nanoparticles, except the absence of the carbon support), the colloidal suspension was maintained in room conditions for four days, resulting in the formation of a black hydrogel in the bottom of the flask. To recover the hydrogel, the supernatant was sequentially, and cautiously replaced by fresh water and then acetone. The resulting anhydrous gel was transferred to a critical point dryer operating in CO_2 to preserve its highly porous and 3D structure. More details about this material are presented in Ref. [194]. As shown by **Figure 5.1e**, the PtNi aerogel consists of a 3D structure of nanochains that are composed of aggregated 5.6 ± 1.2 nm crystallites. This sample will be referred to as 'Aerogel PtNi' in what follows.

Sponge PtNi/C

The Sponge PtNi/C catalyst was prepared as presented in the previous chapter and will be referred to as 'Sponge PtNi/C' in what follows.

To allow a better understanding of the different synergetic effects (crystallographic orientation, chemical composition or defectiveness) on the electrocatalytic properties for the ORR, four supplementary materials were synthetized and/or characterized.

Reference Isolated Pt/C TKK

A Pt/Vulcan XC72 catalyst with a Pt weight fraction of 20% (TEC10V20E) was purchased from TKK and used as reference material without any treatment.

Aggregated Pt/C

Aggregated Pt/C nanoparticles were synthetized and characterized to measure the effect of agglomeration (*i.e.* of grain boundaries) on the electrocatalytic activity for the ORR without the influence of alloying effects. Such catalyst was prepared by diluting an aqueous Pt(II) stock solution in presence of sodium citrate, and $NaBH_4$ as reducing agent. The relatively low amount of sodium citrate used allowed partial agglomeration of nanoparticles, and led to a high surface area catalyst with isolated particles of size $\sim 3.4 \pm 1.1$ nm according to TEM images (**Figure 5.2b**). This sample will be referred to as 'A-Pt/C' in what follows.

Aggregated PtNi/C

Aggregated PtNi/C catalyst was prepared as presented in the previous chapter and will be referred to as 'A-PtNi/C'. As shown in **Figure 5.2b** and **Figure 5.2c**, aggregated Pt/C and PtNi/C look similar in terms of particle size, degree of agglomeration and distribution on the carbon support.
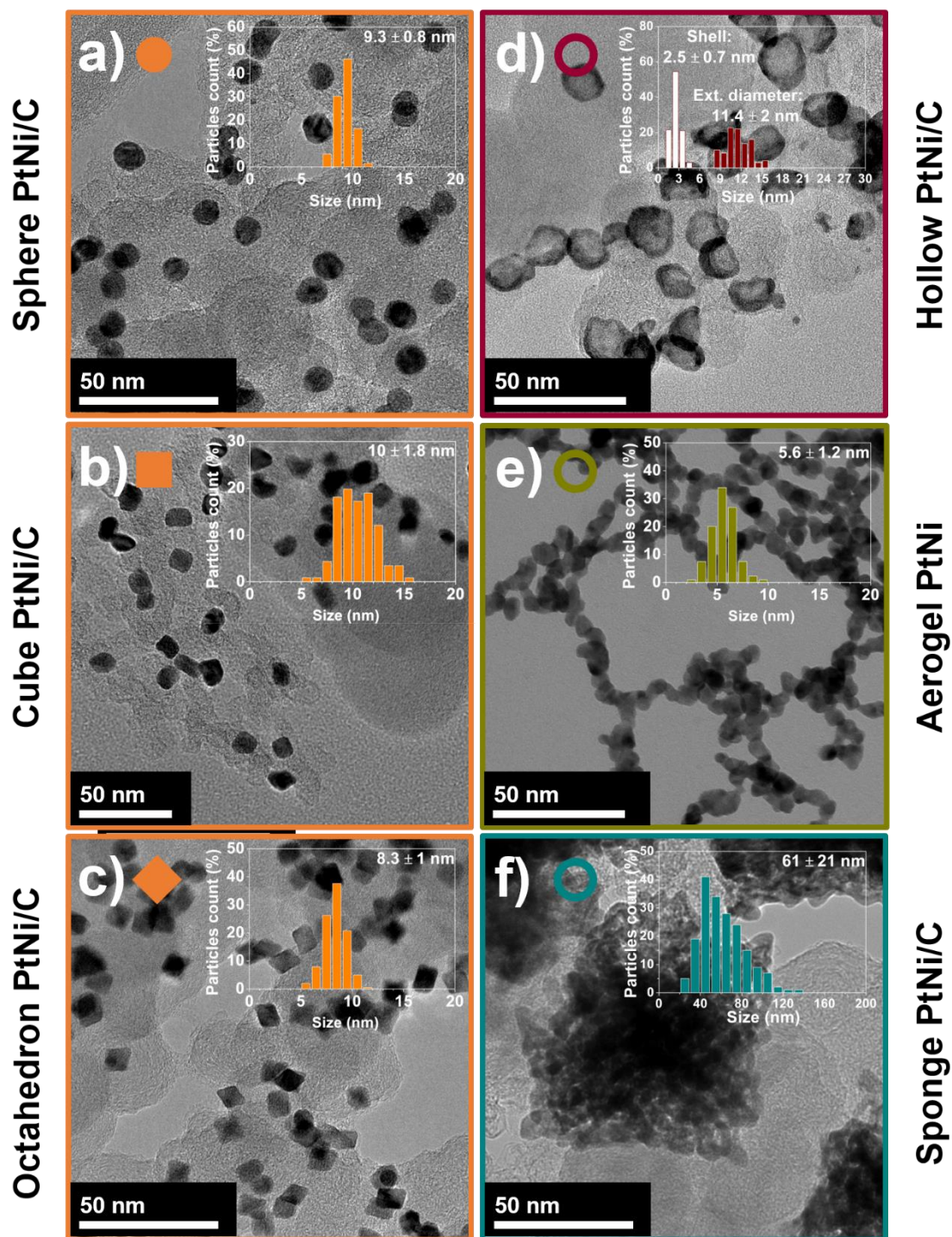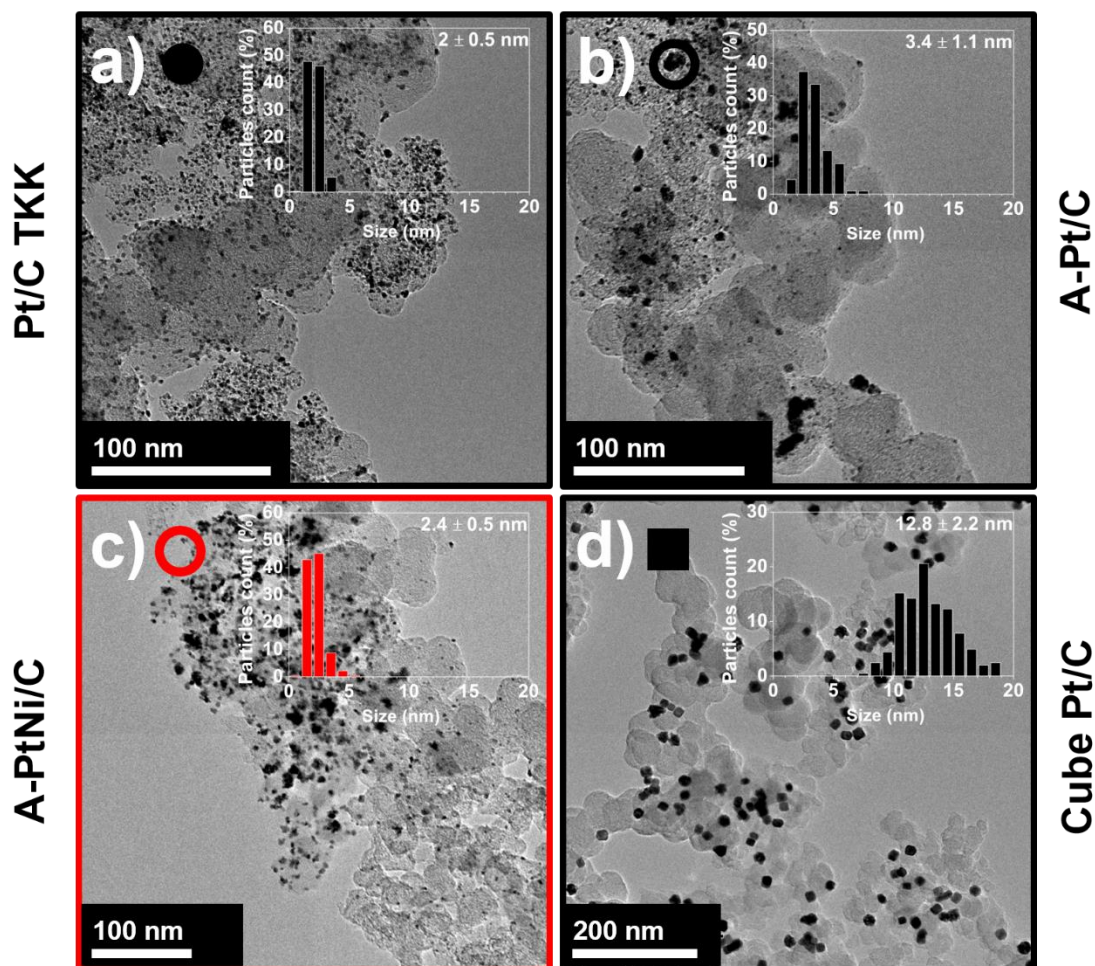

Figure 5.2: TEM images, associated symbol and particle size distributions of the reference catalysts of this study (a) Pt/C TKK; (b) A-Pt/C; (c) A-PtNi/C and (d) Cube Pt/C.

Pt/C Cubes

To investigate the effect of (100) preferential orientation without the contribution of Ni, pure Pt/C cube were prepared by following exactly the same protocol used for the synthesis of PtNi/C octahedra, except no Ni precursor was introduced [75]. Cubic nanoparticles of ~12.8 ± 2.2 nm, that is slightly larger than the PtNi/C catalyst, were obtained as shown in **Figure 5.1b** and **Figure 5.2d**.

5.2.2 Materials Characterization

Table 5.1: Structural and chemical parameters for the main electrocatalysts evaluated in this study.

Electrocatalysts	X-EDS	Synchrotron WAXS + Rietveld Refinement				Average Ni content (at. %)
	Ni content (at. %)	Ni content (at. %)	Lattice parameter (Å)	Crystallite size (nm)	Microstrain (%%)	
Sphere PtNi/C	56 ± 1	56	3.711	8.6 ± 0.4	72	56 ± 1
Cube PtNi/C	25 ± 2	18	3.853	12.9 ± 0.6	32	22 ± 5
Octahedron PtNi/C	31 ± 1	26	3.822	9.2 ± 0.3	53	29 ± 3
Hollow PtNi/C	11 ± 3	10	3.884	3.3 ± 0.5	173	11 ± 1
Aerogel PtNi	17 ± 2	18	3.853	4.8 ± 0.6	198	18 ± 1
Sponge PtNi/C	16 ± 1	26	3.820	4.5 ± 0.9	233	21 ± 5

Chemical and structural properties of the different electrocatalysts were investigated using TEM, STEM, HRSTEM, X-EDS and WAXS. Rietveld refinement of the WAXS patterns allowed extracting key physical parameters such as the Pt or PtNi lattice parameter, crystallite size and degree of microstrain of the various samples. It can be seen from **Table 5.1** and **Figure 5.3** that the main catalysts can be divided in two families: on the one hand, the 'single crystal inspired' materials, namely Sphere PtNi/C, Cube PtNi/C and Octahedron PtNi/C which are composed of large (~10 nm) crystallites with similar nanoparticle size (as determined by statistical analysis of TEM images), suggesting monocrystalline nanoparticles. Also, 'single-crystals' inspired catalysts feature relatively high Ni content (> 25 at. %) and low microstrain values.

Table 5.2: Structural and chemical parameters for the references electrocatalysts evaluated in this study.

Electrocatalysts	X-EDS	Synchrotron WAXS + Rietveld Refinement				Average Ni content (at. %)
	Ni content (at. %)	Ni content (at. %)	Lattice parameter (Å)	Crystallite size (nm)	Microstrain (%%)	
Pt/C TKK	0	0	3.918	1.3 ± 0.2	0	0
A-Pt/C	0	0	3.921	7.4 ± 0.6	70	0
A-PtNi/C	10 ± 4	15	3.862	4 ± 0.5	90	13 ± 5
Cube Pt/C	0	0	3.921	9.5 ± 0.2	21	0
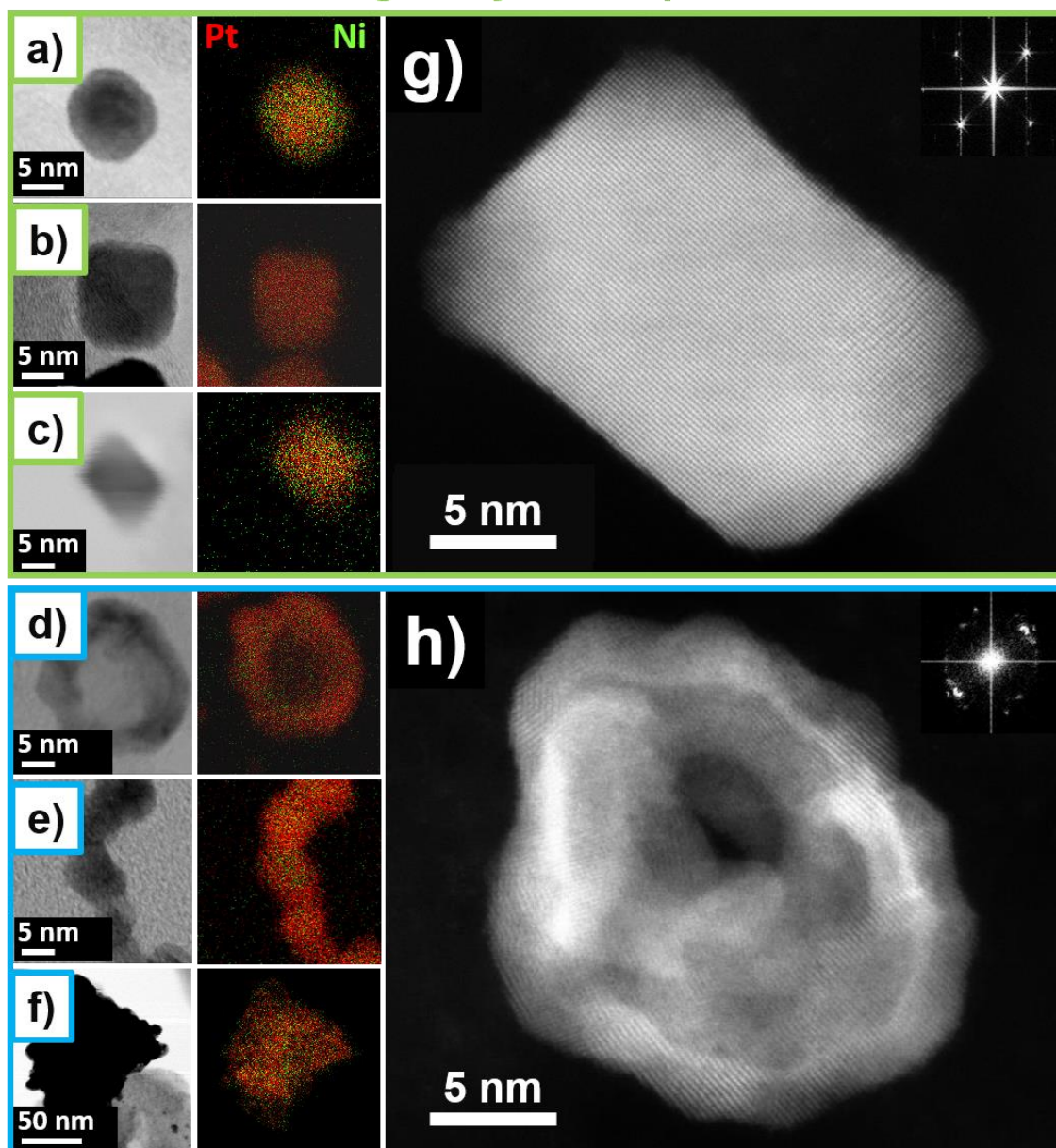
Figure 5.3: STEM images and X-EDS elemental maps (Pt: red, Ni: green) of the main electrocatalysts evaluated in this study. (a) Sphere PtNi/C; (b) Cube PtNi/C; (c) Octahedron PtNi/C; (d) Hollow PtNi/C; (e) Aerogel PtNi and (f) Sponge PtNi/C. The catalysts have been divided in two families, the 'single crystal inspired' materials composed of monocrystalline, Ni-rich and potentially facetted nanoparticles (a-c) and the 'nanostructured' catalysts composed of polycrystalline and Ni-poor nanoparticles (d-f). HAADF-HRSTEM images with their associated fast Fourier transform of Pt/C Cube (g) and Hollow PtNi/C (h)) highlighting the properties of the two different 'families'.

On the other hand, the 'nanostructured' catalysts, namely Hollow PtNi/C, Aerogel PtNi and Sponge PtNi/C show small crystallite sizes (< 5 nm), low Ni content and high microstrain values. In fact, in the first case high Ni content is required for both the strain and ligand effects to occur (as for extended single crystal), however, in the second case,

Ni is essentially used as a sacrificial element to achieve nanoscale carving (removal of excess Ni atoms is ensured by post-synthesis acid leaching).

A non-negligible mismatch can be seen **Table 5.1** between Ni contents measured from X-EDS and refinement of XRD patterns (especially for the 'single crystal' inspired materials). This can be rationalized by the presence of a pure Ni phase as already reported in the case of the Zhang's synthesis for PtNi octahedra and cubes [75,80]. This extra Ni phase can either be in the form of independent and isolated particles (that may not be observed in STEM-X-EDS), or in the form of Ni oxides covering the surface of the nanoparticles (that cannot be ignored in STEM-X-EDS), as observed in HAADF-HRSTEM images and the associated elemental map (**Figure 5.4**). Consequently, the Ni amount determined from the Pt lattice parameter using the Vegard's law (*i.e.* the Ni atoms really alloyed with Pt) is likely to be inferior to that derived from X-EDS analysis.

However, this does not make results from XRD a more absolute truth: in the case of acid-treated samples, the two methods may give more consistent values, but it is known that residual lattice strain can be obtained after non-noble metal leaching [102,142], leading to an opposite trend where XRD estimations overtake X-EDS values (Aerogel PtNi and Sponge PtNi/C **Table 5.1** and A-PtNi/C **Table 5.2**). To face this doubt about the catalysts compositions, averaged values from both techniques were calculated and will be considered for the following discussions (**Table 5.1** and **Table 5.2**). Note that the surprising low Ni at. content obtained by X-EDS compared to XRD for the Sponge PtNi/C sample was also confirmed by XPS analysis (not shown).

These preliminary characterization results confirm our thought from the previous Chapter: dealloyed catalysts composed of aggregated nanocrystallites (Sponge PtNi/C, Aerogel PtNi, Hollow PtNi/C, A-PtNi/C and A-Pt/C) generally feature higher microstrain values compared with monocrystalline nanoparticles (except for the Sphere PtNi/C, as discussed later). It is also noteworthy that the Aerogel PtNi from TU Dresden gave the second highest microstrain value after the Sponge PtNi/C catalyst. This demonstrates that key materials from the literature may feature unrevealed microstrain. We also measured the apparition of microstrain in pure Pt catalyst in the case of the agglomerated A-Pt/C (**Table 5.2**) sample, in agreement with our predictions and conclusions about structural disorder and grain boundaries.
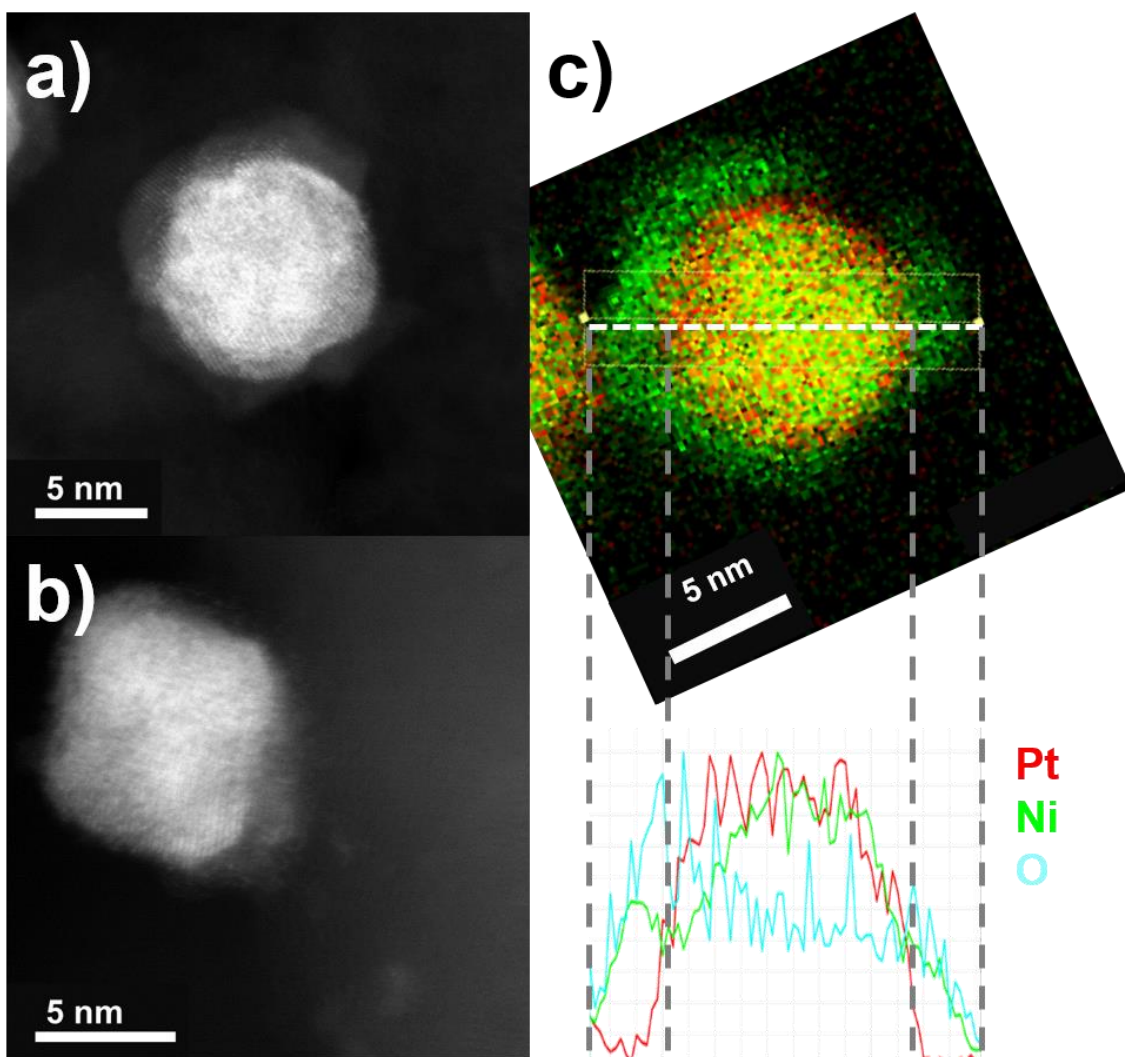
Figure 5.4: Evidence of a Ni oxides phase. HRSTEM-HAADF images of (a) Sphere PtNi/C; (b) Octahedron PtNi/C showing the presence of a lighter (than PtNi) phase on the surface of the nanoparticles composing these samples. (c) X-EDS elemental map and linear scan crossing a spherical PtNi nanoparticle, the extra surface phase is composed of Ni and O.

5.3 Toward Unprecedented Electrocatalytic Trends

5.3.1 From Microstrain to Surface Distortion

The microstrain values determined from Rietveld refinement of WAXS data are displayed in **Table 5.1** and **Table 5.2**. It may appear surprising that microstrain values comprised between 32 and 118 were determined on supposedly 'defect-free' catalysts (Sphere, Cube and Octahedron PtNi/C). Indeed, even if these values are two times less important than

those determined on 'nanostructured' NPs', they are not negligible amounts. It is even more surprising that low microstrain values were reported only on isolated, monocrystalline and Ni-free nanoparticles (Cube and TKK Pt/C), which suggests a possible contribution of the Ni content to the value of microstrain. To check this hypothesis, the microstrain values determined from Rietveld refinement of WAXS data were plotted as a function of the Ni at. % (**Figure 5.5**).
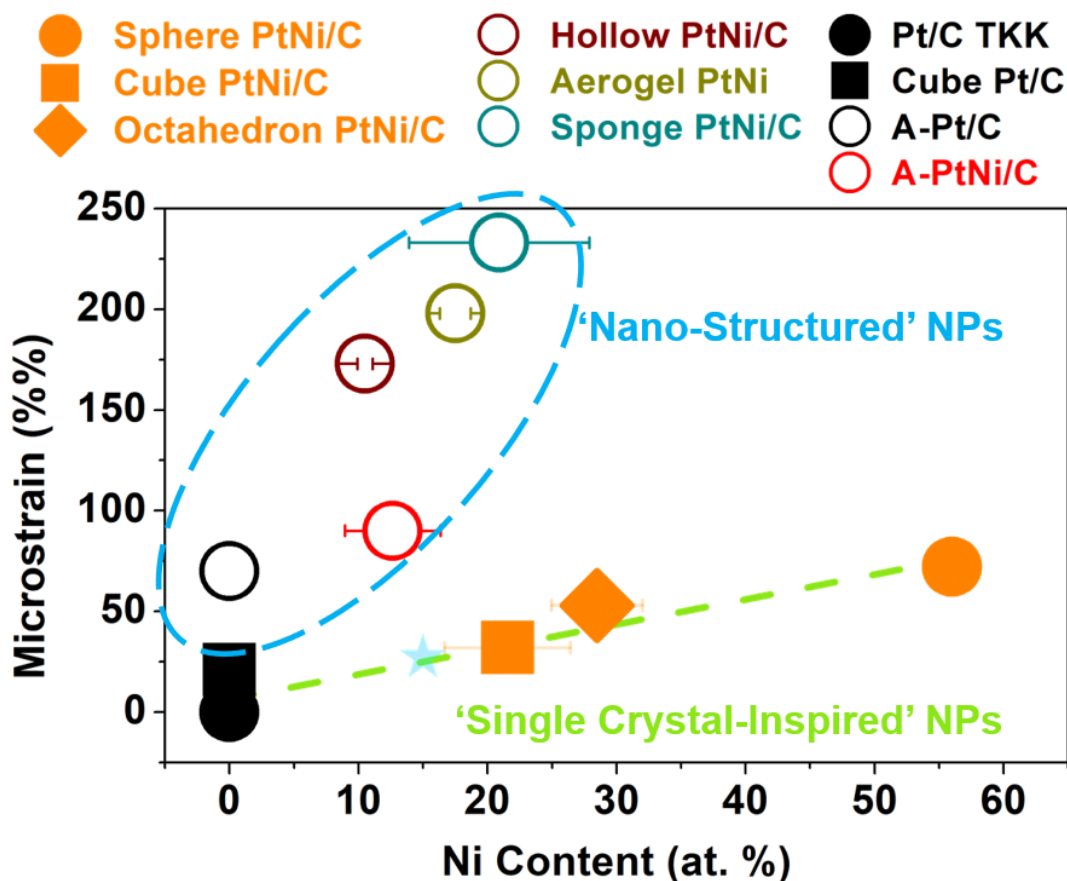
Figure 5.5: Microstrain *vs*. Ni content for the electrocatalysts evaluated in this study. The plot shows an almost linear variation for the'single crystal' inspire nanoparticles, indicating a contribution of Ni atoms to the microstrain. The cyan star symbol represents the theoretical position of an isolated monocrystalline PtNi nanoparticle featuring 15 at. % Ni, based on the microstrain-Ni content relationship revealed by this plot.

An almost linear microstrain-Ni content evolution in the range of 0-55 at. % Ni was observed for the isolated and monocrystalline nanoparticles, while a more complex trend is observed for the defect-containing materials. This means, if increasing Ni content contributes to the overall contraction of the Pt lattice through the insertion of foreign and smaller atoms inside the Pt cell, there are limits to the theoretical Vegard's law describing the Pt lattice-alloy composition relationship, as this theory is based on a homogenous alloy solution. If rising microstrain with increasing the at. % of one of the element has

already been reported in case of supersaturated α-uranium phase by Kimmel *et al.* on extended flat surfaces [217], from the best of our knowledge this is the first time that such local fluctuations in the concentration of the alloying element is described for strategic bimetallic nanoparticles obtained from commonly used synthesis. The detection of Pt-richer regions has had certainly been possible in case of dealloyed or anisotropic particles via X-EDS linear scan technique, but we emphasize that microstrain analysis provides much more fine insights in term of detection sensibility (note that the localization of such local defects cannot however be extracted).

In **Figure 5.6**, we summarize the possible sources of microstrain in bimetallic PtM nanoparticles according to our findings:
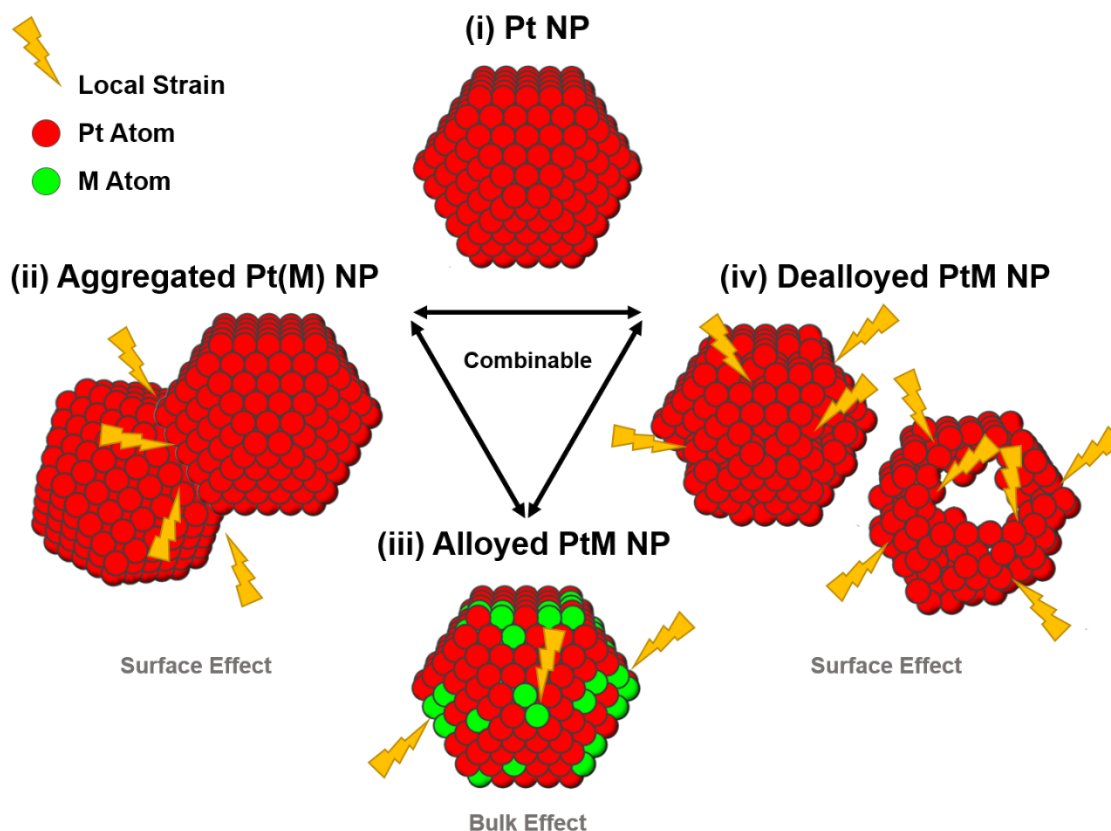
Figure 5.6: Possible sources of microstrain in bimetallic PtM nanoparticles (NPs). While slight or no microstrain can be found in monocrystalline pure Pt NPs, (i) the value of microstrain can rise due to NP aggregation in the presence of grain boundaries, (ii) inhomogeneous PtM alloy solution, (iii) catalysts produced by dealloying (iv). Unlike aggregation and dealloying which occur on the surface of the crystallites, inhomogeneous PtM solid solution affects the whole nanoparticle bulk.

Based on our experimental data, monocrystalline pure Pt/C exhibits slight or no microstrain whatever the crystallite size: case (i), see Cube Pt and TKK Pt/C.

Introducing grain boundaries *via* particle agglomeration (*i.e.* going from monocrystalline to polycrystalline) leads to higher values of microstrain, most probably in the region of the grain boundary itself (see case (ii), A-Pt/C and also possibly slightly agglomerated Cube Pt/C catalysts). Consequently, and as already discussed in the previous chapter, because the atomic arrangement is perturbed by the presence of grain boundaries (surface effect), their contribution to the microstrain values is directly linked to the crystallite size.

As previously discussed, the addition of a foreign element into the bimetallic lattice gives also rise to microstrain due to the ineluctable inhomogeneity of the formed alloy: case (iii), see all monocrystalline catalysts: TKK Pt/C and Cube Pt/C, Sphere, Cube and Octahedron PtNi/C. As shown in **Figure 5.5**, **Table 5.1** and **Table 5.2**, the contribution of the transition metal element to the microstrain value is nearly linear and independent of the crystallite size, suggesting a bulk effect (in agreement with the bulk distribution of the transition metal).

Finally, as discussed on the basis of DFT calculations in the previous chapter [197], the introduction of atomic vacancies in the surface and near surface region (for example *via* electrochemical or chemical dealloying) leads to a highly distorted surface featuring microstrain [197] : case (iv). The contribution of this surface effect to the microstrain must also be dependent on the crystallite size, especially as porosity may be formed during this process, leading to an even more increased surface/volume atomic ratio (or apparent decrease of the crystallite size).

It must now be emphasized that the effects described above (NPs aggregation, alloying and dealloying) can act in synergy. In fact, Hollow, Sponge, and A-PtNi/C catalysts are composed of dealloyed (acid treated) PtNi crystallites of ~15 Ni at. % bulk composition, interconnected to each other by grain boundaries, in which the three effects are likely combined.

Because we want to establish general structure-electrocatalytic activity relations, this extra source of microstrain (originating from the nanoparticle bulk) is problematic as it interferes with the contribution of structural defects arising from the surface (the latter being of primary interest for electrocatalytic aspects). Consequently, a descriptor of the surface defectiveness must be found. In the previous chapter, where all the catalysts featured a similar composition of ~15 at. % Ni, the corrected microstrain (raw microstrain corrected from the crystallite size) was appropriately accounting for the effect of both

grain boundaries and dealloying (two 'surface' effects). However, the introduction of various Ni content requires to better take account of the effect of microstrain and of its ability to control the surface reactivity. Guided by the preliminary trends plotted in **Figure 5.5**, suggesting independent contributions of the Ni content and grain boundaries on the value of microstrain (see Pt/C TKK, A-Pt/C and A-PtNi/C), we propose the following relation:

$$\text{Microstrain} = f(\%\text{Ni}) + \text{Surface Distorsion} * \text{D} \qquad (5.1)$$

Where the microstrain (RM, in %%) is the raw microstrain value derived from the Rietveld refinement of the WAXS patterns, *%*Ni the average Ni at. % in the catalyst (expressed in %) and Surface Distortion (SD, in %) is a parameter that takes into account the effects of grain boundaries and/or dealloying. *D* is the dispersion or the 'Surface Atoms Ratio', as defined by Montejano-Carrizales *et al.* in their model [167,168], and previously described by **Equations (4.2)-(4.5)**.

Note that for catalysts featuring similar Ni at. %, the effect of "Surface Distortion" on the reaction kinetics is directly related to the 'Corrected Microstrain' value (CM) *i.e.* the value of Raw Microstrain (RM) value divided by the dispersion (*D*): this is the approach we have used in **Chapter 4**. Now, for a set of catalysts composed of alloyed and monocrystalline nanoparticles (*i.e.* without surface distortion), SD = 0 and **Equation (5.1)** can be simplified into:

$$\text{Microstrain} = f(\%\text{Ni}) \qquad (5.2)$$

Considering that Pt/C TKK, Cube PtNi/C, Octahedron PtNi/C and Sphere PtNi/C satisfy the conditions of **Equation (5.2),** the type of function *f* can be determined from a fit of **Figure 5.5** with only these 4 points.

If *f* may be quite well approximated by an affine function as shown by **Figure 5.5** and **Figure 5.7**, we nonetheless choose a polynomial function. As presented in **Figure 5.7**, using a third order polynomial function that naturally features inflexions points, suggests the presence of a maximum Ni contribution to the microstrain value (reached for a Ni composition around 50 at.%), which makes physical sense. Indeed, one may expect this maximum when considering that in a solid solution the role of 'foreign' and 'host' elements reverse at the 50 at. %-50 at. % composition. In our case, a pure Ni crystallite should not exhibit more disorder that a pure Pt crystallite. The existence of this maximum

was also observed by an 'in house' 2D computational simulation presented in appendix of this manuscript.
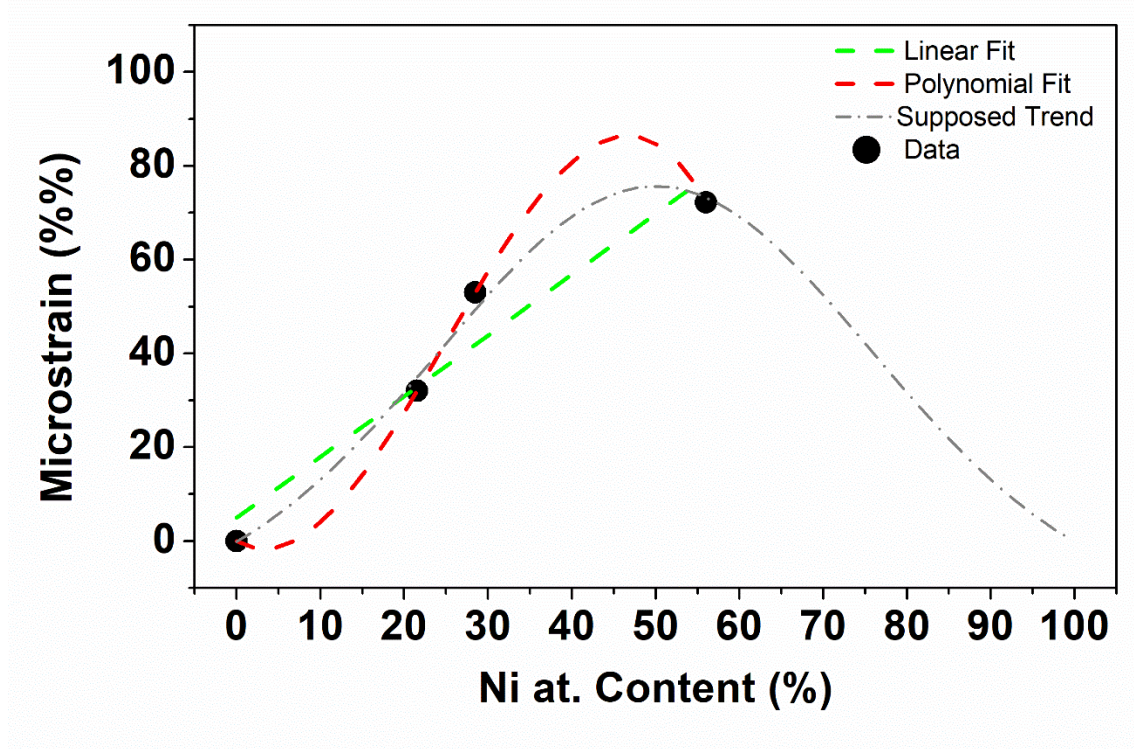
Figure 5.7: Possible descriptions of the effect of the Ni at. % on the value of microstrain. Both the linear and the polynomial fit give reasonable agreement but the polynomial fit was chosen as it naturally suggests the existence a maximal Ni contribution to the microstrain (around 50 at. %, supposed trend), which makes physical sense.

Our polynomial fit in the region of the experimental data gave:

$$f(\%Ni) = \sum_{i=0}^{3} \alpha_i (\%Ni)^i \qquad (5.3)$$

With:

$$\alpha_0 = 0 \qquad (5.4)$$

$$\alpha_1 = -1 \qquad (5.5)$$

$$\alpha_2 = 0.16 \qquad (5.6)$$

$$\alpha_3 = -2.2 * 10^{-3} \qquad (5.7)$$

Finally, the estimation of f allows the expression of the Surface Distortion free from the Ni contribution for all the electrocatalysts:

$$SD = \frac{RM - f(\%Ni)}{D} = CM - \frac{f(Ni)}{D} \qquad (5.8)$$

Where CM is the corrected microstrain introduced in the previous Chapter. **Equation (5.8)** shows that SD and CM values are equivalent in case of Ni-poor and small

nanocrystallites, as confirmed by **Table 5.3** and **Table 5.4**. However, CM tends to overestimate the structural disorder induced by the Ni content, as it normalizes the bulk disorder by the surface dispersion.

Table 5.3: Structural parameters derived from the Rietveld analysis of the WAXS patterns for the main PtNi/C electrocatalysts.

Electrocatalysts	*D* (%)	*CM* (%)	*SD* (%)
Sphere PtNi/C	15 ± 1	4.8 ± 0.1	0.1 ± 0.1
Cube PtNi/C	10.4 ± 0.6	3.1 ± 0.1	0.0 ± 1.0
Octahedron PtNi/C	14.1 ± 0.6	3.7 ± 0.1	0.0 ± 0.5
Hollow PtNi/C	35.0 ± 6	5 ± 0.4	4.8 ± 0.4
Aerogel PtNi	25.7 ± 4	7.8 ± 0.4	7.0 ± 0.6
Sponge PtNi/C	28 ± 6.0	8.7 ± 1.0	7.6 ± 1.4

Table 5.4: Structural parameters derived from the Rietveld analysis of the WAXS patterns for the reference Pt/C and PtNi/C electrocatalysts.

Electrocatalysts	*D* (%)	*CM* (%)	*SD* (%)
Pt/C TKK	65 ± 8	0.0	0.0
A-Pt/C	17.4 ± 2	4 .0 ± 0.2	4 .0 ± 0.2
A-PtNi/C	30 ± 4	3.0 ± 0.2	2.7 ± 0.4
Cube Pt/C	13.5 ± 0.6	1.6 ± 0.1	1.6 ± 0.1

A comparison of the microstrain values before or after correction from the contributions of chemical composition and crystallite size is displayed in **Figure 5.8**. Interestingly, an increasing microstrain value does not necessarily implies surface disorder. Based on our data, increasing microstrain by nanostructuring indeed leads to much more surface distortion. Transfer of microstrain, a bulk parameter, to surface distortion strongly depends on the chemical composition of the catalyst, being efficient for pure Pt and less straightforward for Ni-rich nanoparticles. Ni-poor nanoparticles combining aggregation and dealloyed surface provide the highest values of both microstrain and surface distortion, the maximum being obtained by the Sponge and Aerogel nanostructures.
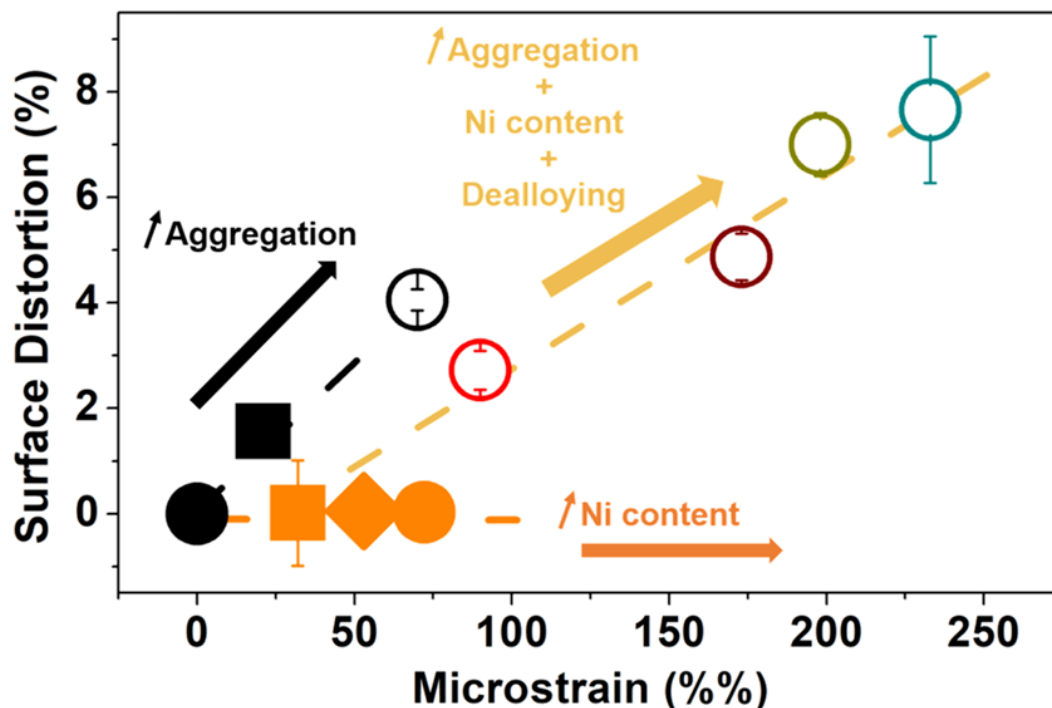
Figure 5.8: Surface distortion *vs*. microstrain for the different electrocatalysts used in this study. After deconvolution from the Ni contribution and crystallite size, it may be observed that high microstrain values do not necessarily imply surface distortion (this strongly depends on the structure and the chemical composition of the electrocatalysts).

5.3.2 Facing the CO$_{ads}$ Stripping Puzzle

As previously discussed (see previous Chapter), the structure sensitivity of the CO$_{ads}$ electrooxidation reaction makes the CO molecule a convenient probe to investigate the fine structure of the surface of disordered catalysts. Because particle's composition [35,38,175,176], size [177–179,218], agglomeration [178,179], and crystallographic facets orientation [180,181] influence the CO$_{ads}$ stripping voltammograms, we introduced previously the 'average CO$_{ads}$ oxidation potential' (μ_1^{CO}) to directly quantify the degree of agglomeration. In the present case however, this direct grain boundary quantification is no longer possible as larger, shape controlled and Ni-rich nanoparticles are being used. Disentangling the contributions of these physico-chemical parameters to the electrocatalytic activity for the COOR is an arduous, if not impossible, task as the literature is still debating on fundamental questions such as the nature of preferential adsorption sites and modes of binding (linear, bridge, multi-bonded) and their dependence

on the CO_{ads} coverage, the mobility of CO_{ads} molecules on the surface, or the nature of active sites [180,202,219–222]. These aspects are reinforced by the fact that the reactivity of low-coordination sites is very different on single crystals (steps, adatoms positively influence the COOR kinetics) and on nanomaterials (where the COOR kinetics is depreciated when the nanoparticle size decreases *i.e.* when the concentration of low-coordinated sites increases) [223,224]. In this context, one must be extremely cautious to not reach hasty conclusions.

Figure 5.9: Background-subtracted CO_{ads} stripping voltammograms recorded in Ar-dearated 0.1 M $HClO_4$ electrolyte at a potential sweep rate of 20 mV s^{-1} on (a) 'single crystal' inspired and (b) 'nanostructured' electrocatalysts evaluated in this study. Dotted lines represent CO_{ads} stripping of extended Pt surfaces, Pt(111) in (a) and Pt-poly in (b). (c) Position of the average μ_1^{CO} for each catalyst.

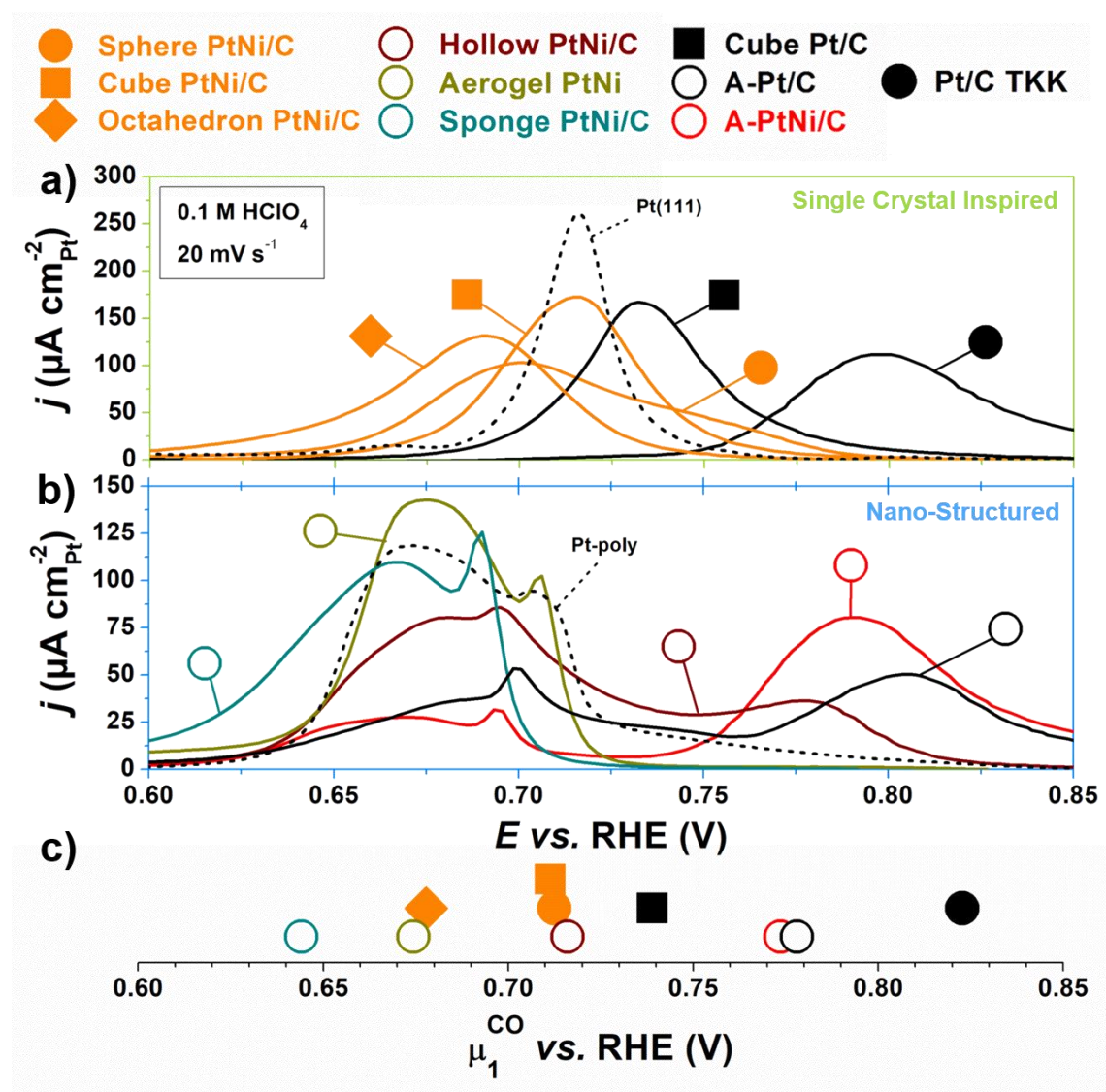**Figure 5.9** shows the background-subtracted CO_{ads} stripping voltammograms recorded for all the electrocatalysts presented in this section. For clarity, the voltammograms have been plotted separately according to the two materials families: 'single crystal inspired' (**Figure 5.9a**) and 'nanostructured' (**Figure 5.9b**) catalysts. It can be seen from **Figure 5.9a** that a variation of the shape and the composition of the monocrystalline samples results in pronounced negative shift of the CO_{ads} stripping voltammograms. At fixed chemical composition, it can be seen that controlling the facets orientation decreases the CO_{ads} oxidation onset potential in the order Pt(111) < Pt(100) << Pt(poly-oriented) for pure Pt and PtNi(111) < PtNi(100) $\cong$ PtNi(poly-oriented) for PtNi nanoparticles. Similarly, at fixed facet orientation, the introduction of a transition metal into the Pt lattice also results in a negative shift of the onset potential (due to a decrease of the CO binding energy), in agreement with other studies [225,226]. Note that, despite the fact that our results are likely biased by the varying crystallite sizes and PtNi compositions of the different samples, the results of our experiments on pure Pt/C nanocrystallites somehow confirm the findings reported by Urchaga *et al.* [180].

A striking point is the different CO_{ads} stripping voltammograms recorded on monocrystalline (single CO_{ads} electrooxidation peak) and polycrystalline (multiple CO_{ads} electrooxidation peaks) nanomaterials (**Figure 5.9b**). On partially agglomerated catalysts, *i.e.* presenting only a fraction of monocrystalline particles (A-Pt/C, A-PtNi/C), two CO_{ads} stripping peaks are noticed: the first at low potential ($0.6 < E < 0.73$ V *vs.* RHE) itself composed of a broad peak featuring a 'spike' in the region of $E = 0.7$ V *vs.* RHE, associated with aggregated crystallites (grain boundaries) [177–179,182–184] followed by a high potential peak ($E > 0.73$ V *vs.* RHE) associated with monocrystalline isolated particles, and so, whatever the composition of the catalyst (with or without Ni). The electrical charge under the low potential peak is low for only partially agglomerated catalysts (A-Pt/C and A-PtNi/C), predominant for the Hollow PtNi/C catalyst (low proportion of isolated nanocrystallites) and totally dominant in case of Aerogel PtNi, Sponge PtNi/C and extended poly-Pt surface.

We then calculated the average CO_{ads} oxidation potential μ_1^{CO} according to **Equations (4.7)-(4.8)**. The results, presented in **Figure 5.9b and Figure 5.9c**, **Table 5.5** and **Table 5.6**, show no hierarchy between single crystals and nanostructured catalysts. In fact, the values of μ_1^{CO} and of microstrain depend on the same parameters (particle size, chemical

composition and degree of defectiveness) except that μ_1^{CO} values are also sensible to the orientation of the crystallographic facets. Not surprisingly, the comparison of the microstrain *vs.* μ_1^{CO} plots (**Figure 5.10**) highlights two separate trends: one for shape-controlled particles due to their ability to efficiently oxidize CO_{ads} at low microstrain and another one for polycrystalline nanocatalysts of different chemical composition and structure. Note that the Sphere PtNi/C, which exhibits poly-oriented but large facets seems to represent an intermediate case.
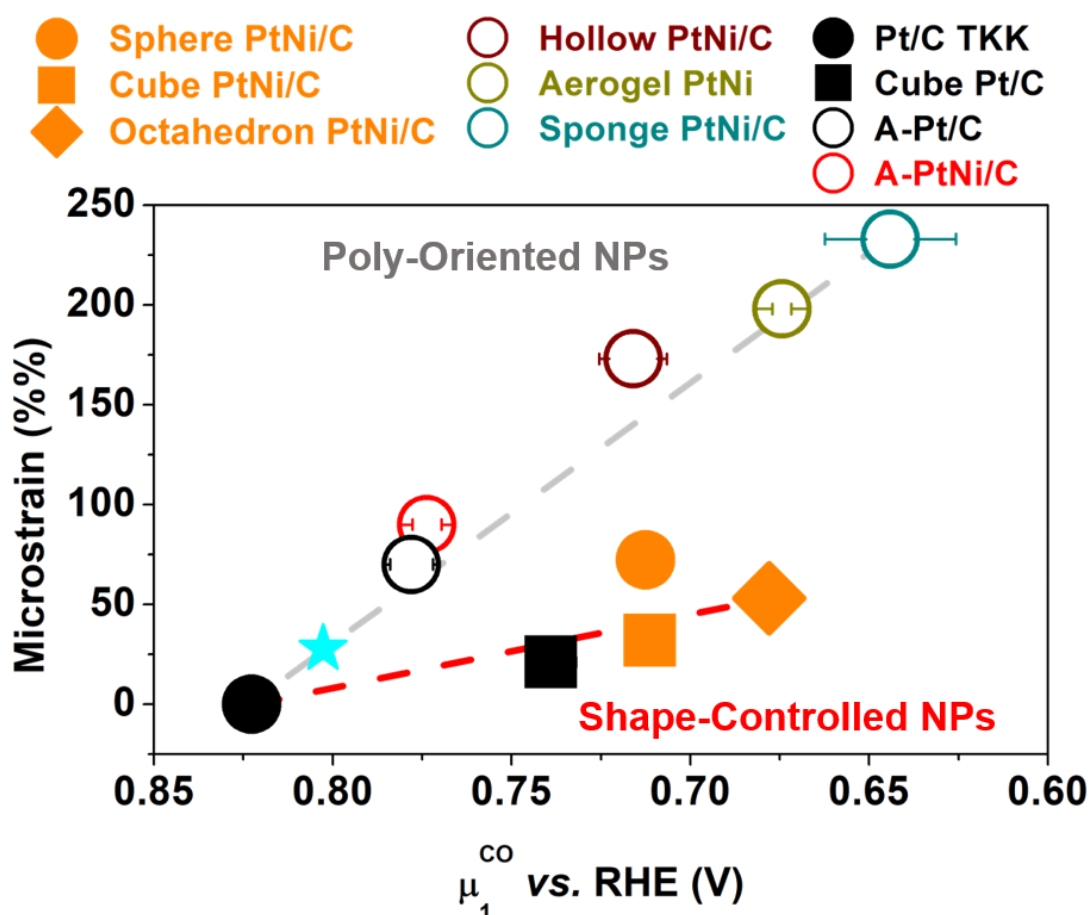
Figure 5.10: Microstrain *vs.* μ_1^{CO} plot for all electrocatalysts evaluated in this study. As μ_1^{CO} and microstrain depend on the same parameters except that μ_1^{CO} is also sensible to the orientation of the crystallographic facets, two different slopes are obtained for shape-controlled and nanostructured electrocatalysts. The cyan star symbol represents the theoretical position for an isolated monocrystalline PtNi nanoparticle (featuring 15 at. % of Ni) based on the theoretical value of microstrain extracted from **Figure 5.5** and the trend observed for the polycrystalline nanocatalysts.

If **Figure 5.10** allows isolating the structure sensitivity (effect of different crystallographic facets on monocrystalline nanoparticles) of the CO_{ads} stripping voltammograms, the contributions of structural defects and of Ni content are still entangled (defective catalysts and Sphere PtNi/C on the same trend). By using the

previously introduced Surface Distortion parameter, disentangling their respective contributions becomes possible. **Figure 5.11** displays the Surface Distortion *vs.* μ_1^{CO} and almost the same trend as **Figure 5.10** can be observed, except that pure Pt and Ni-rich particles exit the general 'poly-oriented' trend, revealing the contribution of surface disorder in case of A-Pt/C or alloying effects for Sphere PtNi/C.
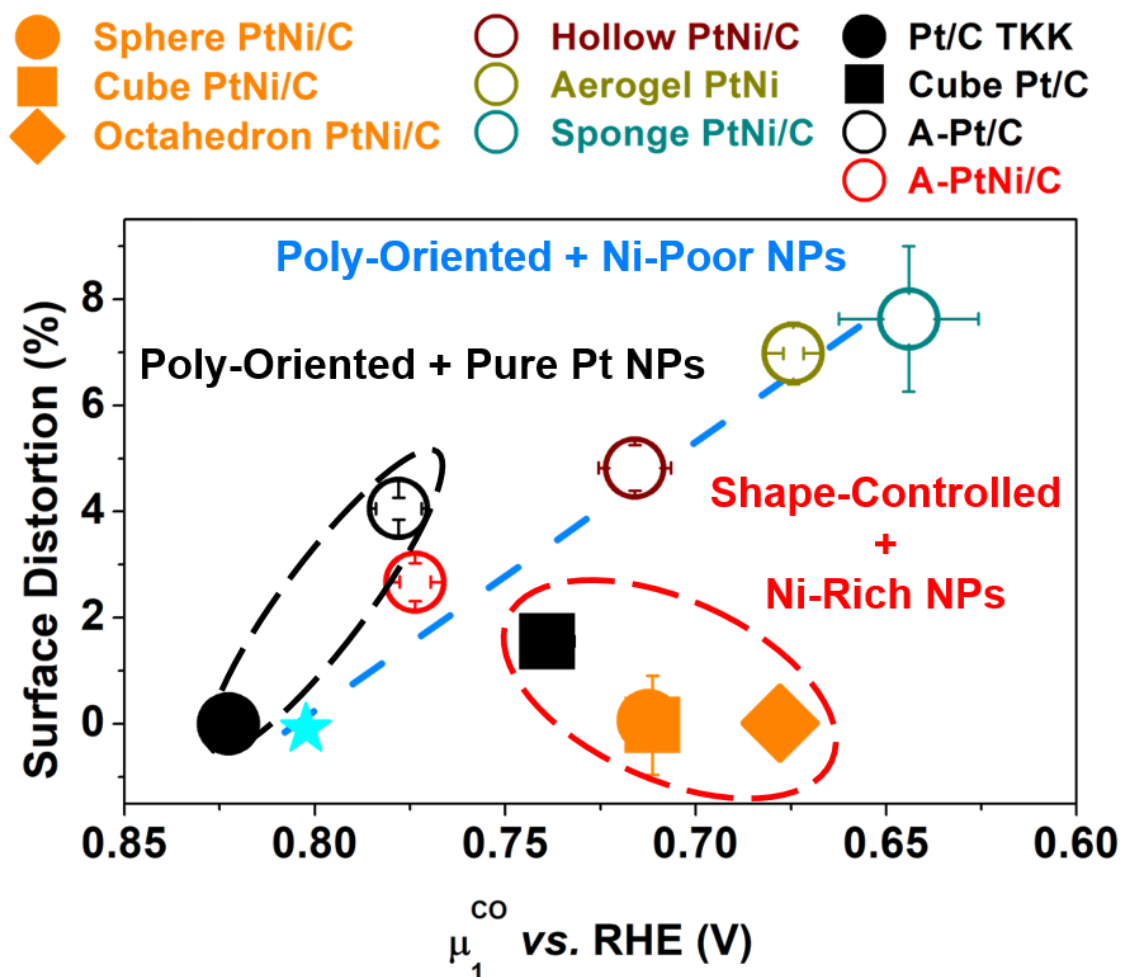
Figure 5.11: Surface Distortion *vs.* μ_1^{CO} for the electrocatalysts evaluated in this study. As the SD does not take account the bulk Ni content, this plot allows isolating the contribution from the surface disorder. The cyan star symbol represents the theoretical position of an isolated monocrystalline 15 at. % Ni PtNi nanoparticle based on the theoretical value of μ_1^{CO} extracted from **Figure 5.10**.

Through the introduction of physical parameters such as the microstrain and its derived surface distortion, we proposed a method to efficiently decorrelate the different catalyst structural and chemical effects contributions to the CO$_{ads}$ stripping reaction, the latter being robust enough to be applied to a wide range of particle morphologies.

5.3.3 Apprehending ORR Catalysis Differently

The ORR activity of the different electrocatalysts was then investigated using rotating disk electrode in O_2-saturated 0.1 M $HClO_4$ at a potential sweep rate of 5 mV s^{-1}. **Figure 5.12** displays the Ohmic drop and mass-transport corrected voltammograms whereas the specific and mass activities are listed in **Table 5.5** and **Table 5.6**. Among the various nanostructures evaluated in this section, the highest specific activity was obtained on the PtNi/C octahedra with the impressive value of 567 ± 118 µA cm$_{Pt}^{-2}$ measured at 0.95 V *vs*. RHE, reaching an enhancement factor of 21 compared to the reference Pt/C TKK. Such value is by far higher than the value (7) reported by Zhang *et al*. [75] for the same material prepared *via* the same synthesis route.

Table 5.5: Pt specific surface area ($S_{Pt,CO}$), average CO_{ads} oxidation potential (μ_1^{CO}), iR + mass transport corrected ORR specific activity ($SA_{0.95}$) and mass activity ($MA_{0.95}$) measured at E=0.95 V *vs*. RHE on the main electrocatalyst evaluated in this section, and corresponding enhancement factors (E.F.) compared to the reference Pt/C TKK.

Electrocatalyst	$S_{Pt,CO}$ (m^2 g$_{Pt}^{-1}$)	μ_1^{CO} *vs*. RHE (mV)	$SA_{0.95}$ (µA cm$_{Pt}^{-2}$)	E.F. SA	$MA_{0.95}$ (A g$_{Pt}^{-1}$)	E.F. MA
Sphere PtNi/C	47 ± 1	713 ± 8	207 ± 45	7.7	97 ± 2	4.6
Cube PtNi/C	24 ± 2	711 ± 3	274 ± 46	10.1	67 ± 5	3.2
Octahedron PtNi/C	28 ± 3	678 ± 5	567 ± 118	21	157 ± 19	7.5
Hollow PtNi/C	45 ± 7	716 ± 9	176 ± 10	6.5	79 ± 12	3.7
Aerogel PtNi	34 ± 2	674 ± 3	220 ± 30	8.1	76 ± 3	3.6
Sponge PtNi/C	46 ± 2	644 ± 18	317 ± 11	11.7	146 ± 4	6.9

Table 5.6: Pt specific surface area ($S_{Pt,CO}$), average CO_{ads} oxidation potential (μ_1^{CO}), iR + mass transport corrected ORR specific activity ($SA_{0.95}$) and mass activity ($MA_{0.95}$) measured at E=0.95 V *vs*. RHE on the reference electrocatalyst evaluated in this section, and corresponding enhancement factors (E.F.) compared to the reference Pt/C TKK.

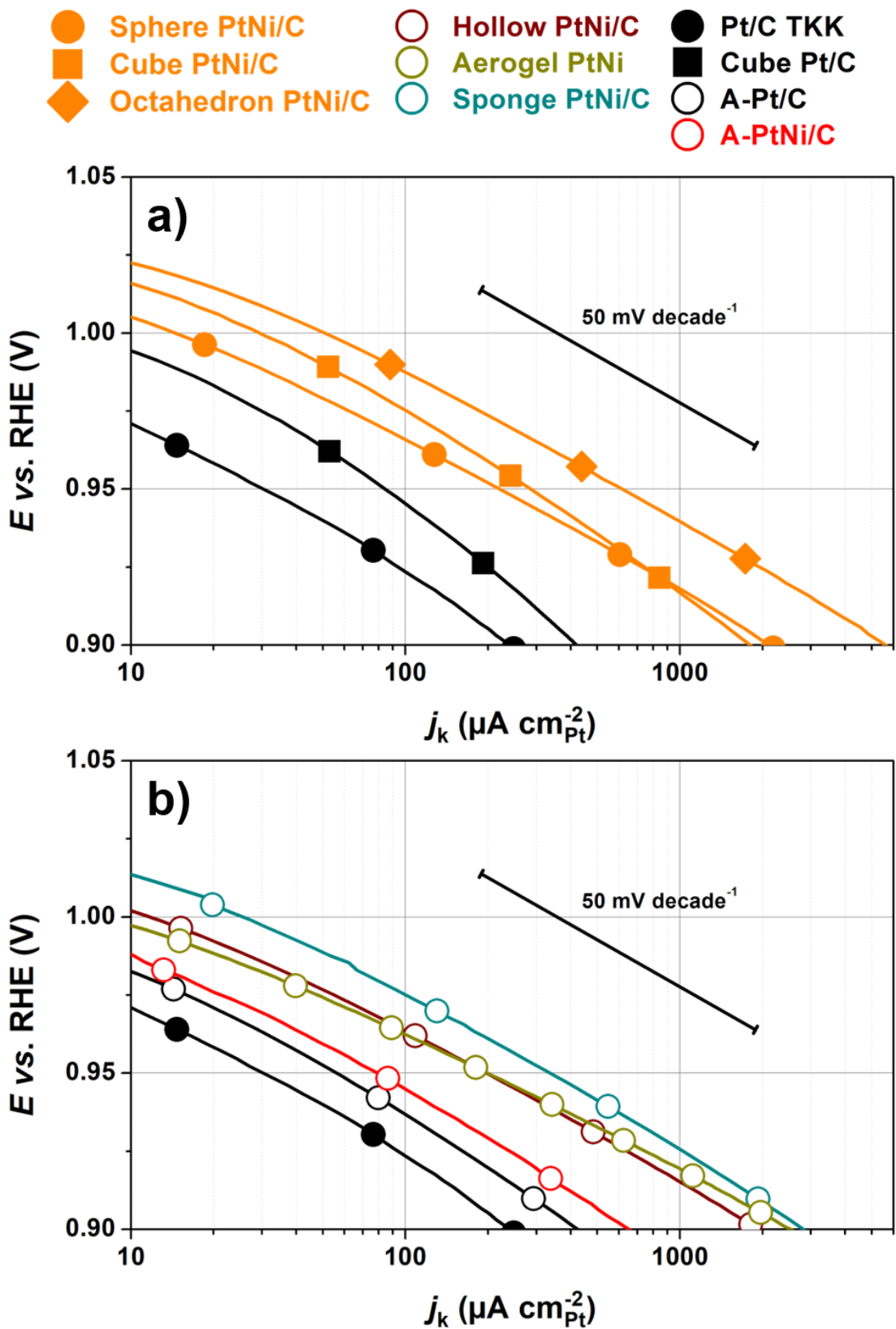| Electrocatalysts	$S_{Pt,CO}$ (m^2 g$_{Pt}^{-1}$)	μ_1^{CO} *vs*. RHE (mV)	$SA_{0.95}$ (µA cm$_{Pt}^{-2}$)	E.F. SA	$MA_{0.95}$ (A g$_{Pt}^{-1}$)	E.F. MA
Pt/C TKK	78 ± 5	823 ± 4	27 ± 4	1.0	21 ± 1	1.0
A-Pt/C	36 ± 1	778 ± 6	53 ± 5	2.0	19	0.9
A-PtNi/C	39 ± 1	774 ± 4	76 ± 1	2.8	30 ± 1	1.4
Cube Pt/C	12 ± 1	739 ± 7	97 ± 30	3.6	11 ± 1	0.5

Figure 5.12: Tafel plots obtained from the steady-state $I-E$ curves measured at $\omega = 1600$ rpm after correction for ohmic losses and diffusion in O_2-saturated 0.1 M $HClO_4$ at a potential sweep rate of 5 mV s^{-1}.

Because it is of primary importance, we would like to firstly rationalize this substantial activity measurement difference between our group and Zhang *et al*: **Figure 5.13** presents a short literature overview of the mass activities (and associated enhancement factors compared to commercial Pt/C) reported by several groups for a selection of PtNi/C octahedra.
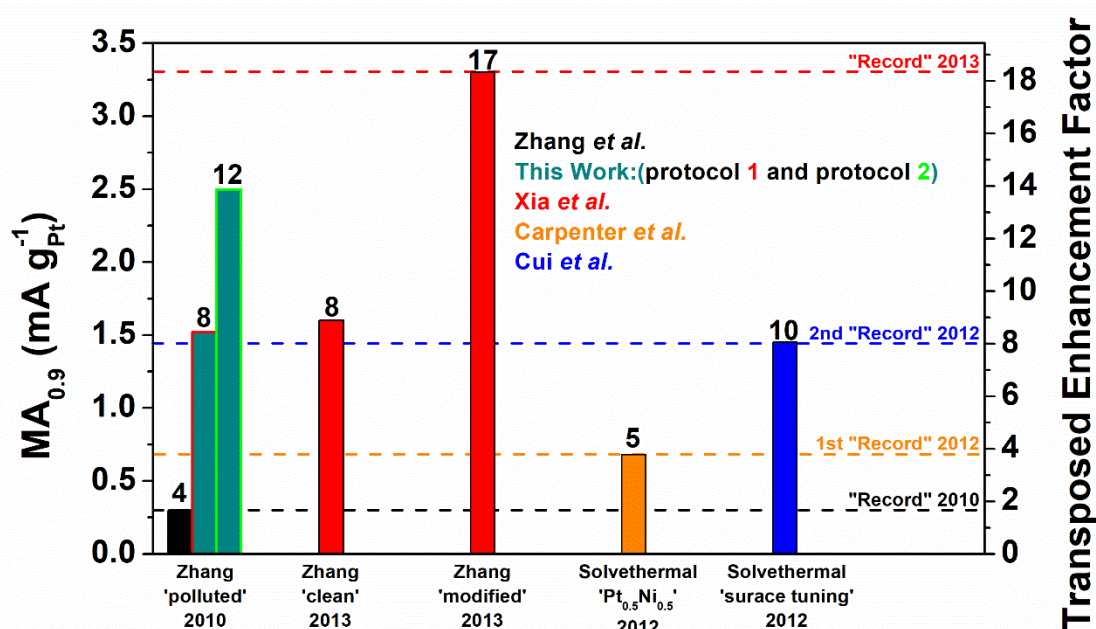
Figure 5.13: Short literature overview on the improvements reported for the synthesis of highly active PtNi/C octahedra for the oxygen reduction. Mass activity recorded for the original PtNi/C octahedra firstly introduced by Zhang *et al*. in 2010 [75] referred as 'polluted' due to remaining surfactants, which was later removed by post synthesis treatment under acetic acid (Zhang 'clean' [80]). In 2013, another solvent was introduced to reach an even better controlled and clean surface, leading to the best activity ever recorded for these regular octahedra [80]. In the meantime, a solvothermal synthesis method was developed [76] and improved [77]. The black numbers on tops of bars represent the original enhancement factors reported by the various authors compared to a reference Pt/C catalyst while the right y-scale shows a transposition of the left y-axis into enhancement factor compared to our Pt/C TKK reference catalyst. In this work, we evaluated the electrochemical activity of the 'dirty' octahedra according to 2 different electrochemical protocols.

Surprisingly, we measured a 5-fold higher current on the original Zhang's material (Zhang 'polluted') simply by applying our standard electrochemical characterization protocol (described in the material and method section, and referred as 'protocol 1' in **Figure 5.13**). Note that this value overcomes or equals in term of absolute and enhancement factor the values reported for the further improvements of the original synthesis: cleaning step [80], or alternative approaches (solvothermal [76]) with or without fine surface composition tuning [77]). Even more striking, by adapting our electrochemical characterization to a 'soft measurement' (lowering the Cyclic Voltammetry (CV)s upper potential limit from 1.23 to 1 V *vs*. RHE and recording the ORR activity from the first positive-going Linear Sweep Voltammetry (LSV) under oxygen-saturated electrolyte

(see material and method), protocol 2 in **Figure 5.13**) we almost doubled the measured activity value and overcome approached the actual activity 'record' obtained *via* the most recent update of the Zhang's synthesis reported by Xia *et al* [80]. Note that, adapting this protocol to the reference Pt/C still results in an increase of the enhancement factor (12 *vs.* 8). This is evidence that, claiming catalytic activity 'world record' makes absolutely no sense neither in absolute (MA or SA) nor in relative (enhancement factor) values considering the impact of the electrochemical measurement protocol, in perfect agreement with previous studies from Kocha *et al.* [172], and raises doubts about the trends of this 'race for the highest ORR activity'.

In this Chapter, through the employment of a unique electrochemical protocol, the fair comparison between different shape controlled PtNi materials **Figure 5.12a** showed a shape-dependent increase of the specific activity in the order Cube Pt/C << Cube PtNi/C < Octahedron PtNi/C, in agreement with the results from single extended crystal surfaces (Pt(100) < PtNi(100) << PtNi(111)) [63]. However, the pronounced activity enhancement of the Cube PtNi suggests the presence of a high fraction of PtNi(111) facets in the sample, as suggested by STEM and TEM images. Interestingly, the Tafel slopes from **Figure 5.12** seems to vary significantly between electrocatalysts, being generally lower (down to 44 mV decade^{-1}) for highly active materials (Octahedron PtNi/C, Sponge PtNi/C, Hollow PtNi/C and Sphere PtNi/C) and higher (up to 77 mV decade $^{-1}$) for poorly active materials (Pt/C TKK and Cube Pt/C), around in agreement with literature for pure Pt surface [172] . Assuming the expression of the Tafel relation:

$$\Delta E = \frac{RT}{\alpha F} \log(\frac{j_k}{j_0}) \tag{5.9}$$

 where ΔE is the electrode overpotential compared with the open circuit potential, R the universal gas constant, T the temperature, j_k the kinetic current density (corrected from Ohmic drop and O_2 mass transport in solution and j_0 the so-called exchange current density, we tried to quantitatively bridge the enhanced ORR activity of the various electrocatalysts with either the Tafel slope **Figure 5.14a** or the exchange current density j_0 **Figure 5.14b** but quite unsuccessfully as the determination of the Tafel slope is a delicate process in our case (some electrocatalysts do not exhibit linear region in their Tafel plot) which is also problematic for the determination of the exchange current density. Also, even at similar Pt loadings on the electrode, the particle morphology (size,

shape) influence the amount ECSA (being smaller for large particles) and so the number of electrocatalytic sites, which is known to impact the Tafel slope [227].
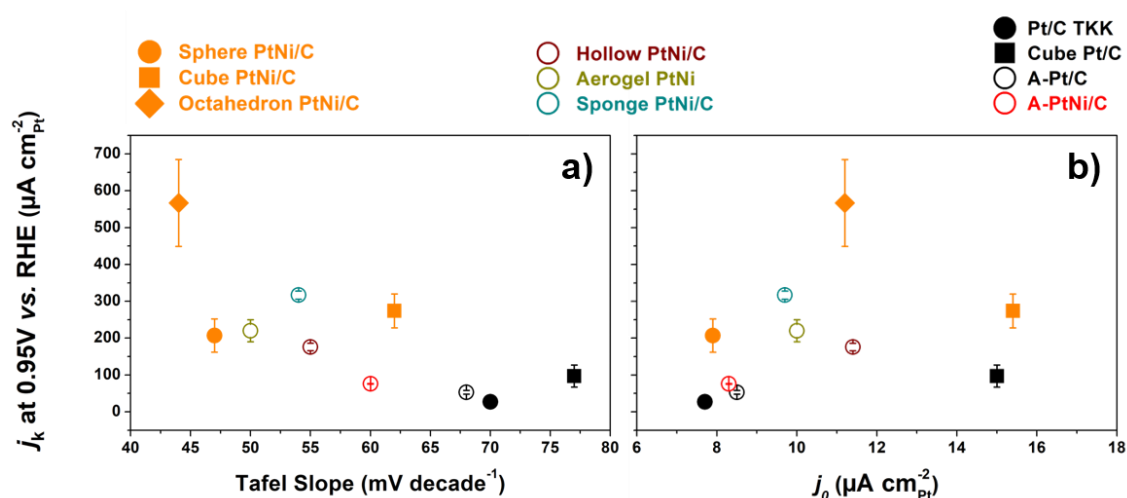
Figure 5.14: Relationship between the ORR specific activity measured at *E*= 0.95 V *vs*. RHE and the Tafel slope (a) or the exchange current density *j₀* for the different electrocatalysts from this study.

However, in the case of the Aerogel PtNi, one can see that despite its slightly lower onset potential and Pt specific surface area compared to the Hollow and Sponge PtNi/C catalyst (probably due to its combined higher crystallite size and agglomeration), its Tafel slope is significantly lower, allowing a positive evolution of its enhancement factor compared to Pt/C TKK with decreasing electrode potential. This may be attributed to its unsupported nature, which makes (at constant Pt loading electrodes) a thinner electrocatalytic film (but still porous) leading to increased catalytic site availability. The possibility to achieve active and unsupported catalyst structure *via* nanostructuring is a very promising approach in real PEM fuel cell application, as recently reported by Henning *et al.* [216].

We then tried to rationalize the different ORR activities in the frame of the *d*-band theory. We concede that a direct measurement of the *d*-band centre through integration of low energy X-ray photoelectron spectroscopy (ultra-violet photoemission (UPS) or synchrotron radiations) spectra in the valence band region is the method of choice usually adopted in literature [228], but attempts to derive physical parameters from UPS in collaboration with CEA Grenoble revealed unsuccessful. Instead we focused on an easier but indirect detection of the possibly altered electronic properties of the catalyst's surfaces by cyclic voltammetry in support electrolyte. It has been widely reported, that modified adsorption behaviour is expected for PtM catalysts, especially a shift of surface-oxide

formation to higher electrode potential, which is believed to sign less oxophilic surface and be the origin of their high activity for the ORR [63,225].
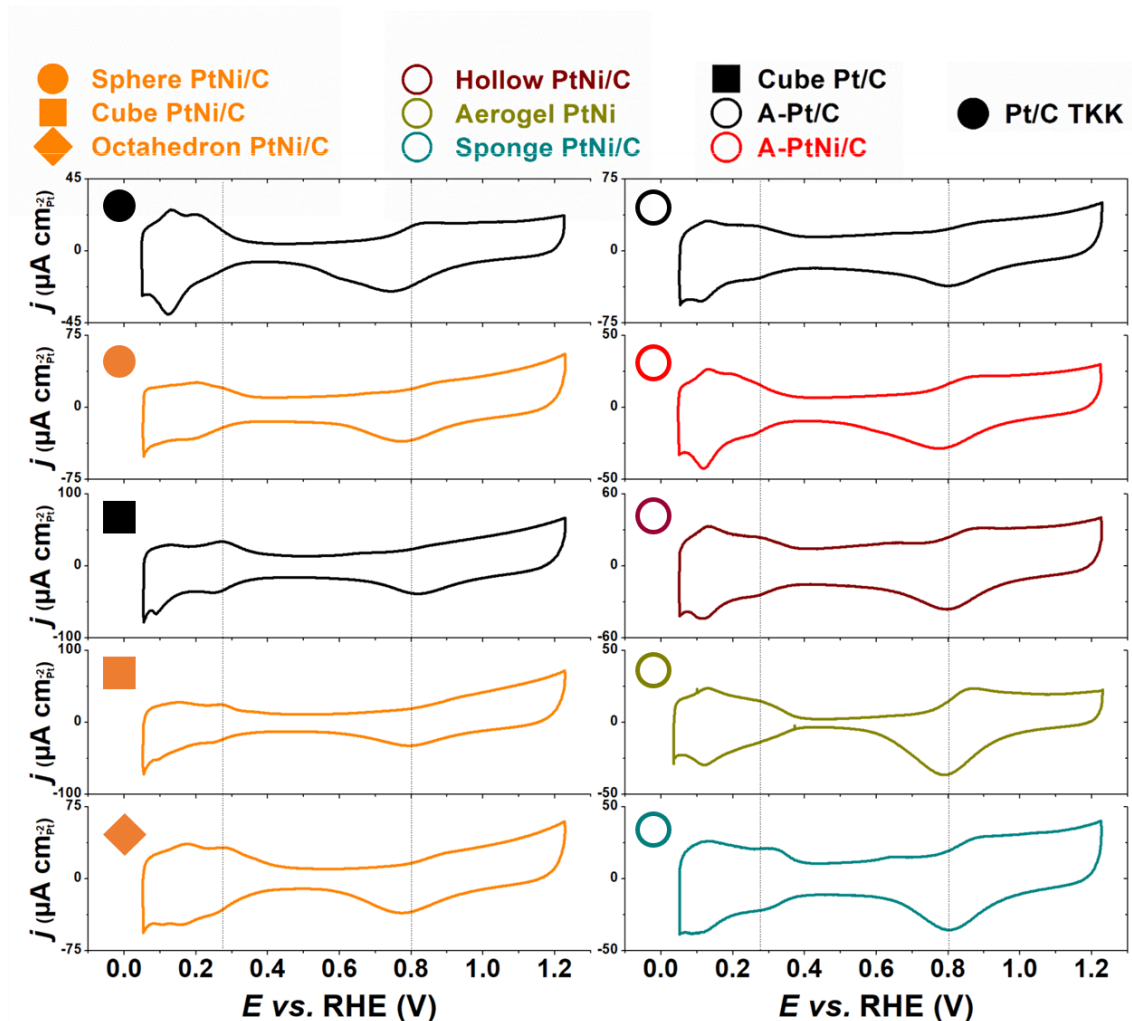
Figure 5.15: Base voltammograms measured on the electrocatalysts evaluated in this Chapter. The measurements were conducted in Ar-saturated 0.1 M HClO₄ at a potential sweep rate of 20 mV s⁻¹. The currents were normalized by the ECSA measured *via* CO$_{ads}$ stripping experiments.

Figure 5.15 shows the base voltammograms recorded in Ar-saturated 0.1 M HClO₄ electrolyte, after 'electrochemical activation' (50 cycles at 500 mV s⁻¹ between 0.05-1.23 V *vs*. RHE) was performed. It is well-established that the shape of the H$_{upd}$ region provides a lot of information about the crystallographic orientation of the nanoparticle facets. For example, model studies on single crystals [201] attributed the current between 0.2 < E *vs*. RHE < 0.3 to H$_{upd}$ desorption from the (100) facets (which is particularly developed for the Pt/C and PtNi/C Cubes samples, in agreement with their observed shapes), while the feature at lower potential (0.1 < E *vs*. RHE < 0.2) is generally attributed to (110)-oriented steps on a (111) surface, the latter being observable for almost all the

catalysts except the Sphere PtNi/C where the especially high Ni content is known to inhibits usual observations [174]. All the defective catalysts (right part of **Figure 5.15**) present similar H_{upd} general shape, featuring the low potential (110)-steps contribution also with a bump at high electrode potential, whch is more pronounced in the case of the Sponge catalyst. It must be stressed out, that this high potential contribution also appears after simple partial agglomeration of a Pt/C catalyst (see Pt/C TKK compared to A-Pt/C), hence it is very unlikely that this current is related to H_{upd} desorption from (100)-oriented surfaces.

As expected, the adsorption and the desorption of oxygenated species coming from water dissociation occur at lower potential (at 0.8 and below 0.8 V *vs*. RHE respectively) for commercial Pt/C TKK compared to other (and more active) catalysts, confirming its more oxophilic surface. Nevertheless, several striking points must be discussed. First, for isolated nanoparticles, the introduction of Ni atoms in the Pt lattice is not the only reason for this potential shift, as observed for the Cube Pt/C which presents an impressive shift of 77 mV toward more positive potential (this is the maximum shift among all the catalysts). This is particularly surprising considering that the origin of the low activity of Pt(100) compared to other low-index surfaces has been attributed to the too strong adsorption of OH intermediates by Stamenkovic *et al.* and Panchenko *et al.* [63,229]. A possible explanation for this contradictory experimental observation could be the increased crystallite size of Pt cube compared to TKK (9.5 nm *vs*. 1.3 nm), as previously documented [177]. Second (still for isolated NPs), the potential shift induced by the addition of Ni (Sphere PtNi/C (23 mV) < Octahedron PtNi/C (33 mV) < Cube PtNi/C (49 mV)) is not related neither to the Ni concentration (Cube PtNi/C (22 at. %) < Octahedron PtNi/C (28 at. %) < Sphere PtNi/C (55 at. %)) nor to the ORR measured activity (Sphere PtNi/C < Cube PtNi/C < Octahedron PtNi/C) whereas the crystallites size is rather identical. These two points are for us unambiguous experimental evidence that the conclusions from single crystals do not apply for nanomaterials, as already suggested by Calle-Vallejo *et al.* [211]. In fact, isolated nanoparticles of common shapes (spheres, cuboctahedra, truncated octahedra cubes, octahedra etc.) generally feature convex surfaces, which can be in the better case atomically flat but are necessarily surrounded by low coordination atoms at the vertexes and edges. These undercoordinated atoms are known to be responsible for the overall decrease of nanoparticle ORR activity due to very strong oxygen binding energies at these sites [230,231]. This site heterogeneity must be the reason for the

inconsistency between the apparent catalysts surfaces affinity with oxygenated species in the base voltammograms and their overall ORR activities: in adsorption-desorption phenomena such as in base voltammograms, supposing one motionless adsorbate per catalytic site, each site contributes equally to the observed current by interacting with its adsorbate. This response is unique and depends on the site local configuration. However, under steady-state and continuous heterogeneous reaction (ORR polarization curve), the contribution of a catalytic site directly depends on its proper turnover frequency, being negligible for an inactive site or higher than the average for an active site. If the extended single crystal science has conducted to the most active catalyst of this study (Octahedron PtNi/C, targeting the $Pt_3Ni(111)$-skin surface), it is striking to observe that according to its base voltammogram dominated by a rather oxophilic surface response, the really active sites may be in minor number.

However, if the heterogeneity of catalytic sites explains the possible observation of an oxophilic behaviour for an overall active catalyst, it is surprising that all the highly defective catalysts (right part of **Figure 5.15**) show an apparent oxophobic nature (the potential for surface-oxide formation is globally increased by 40-50 mV and 10-20 mV compared to less active Pt/C TKK and more active Octahedron PtNi/C respectively), whereas one would have expected an even more pronounced contribution of oxophilic sites. Two hypotheses are then possible: first, the defects generated by nanostructuring only created highly-coordinated catalytic sites featuring decreased affinity with oxygenated species (*i.e.* oxophilic sites do not exist). This assumption is hardly probable considering DFT predictions from the previous studies [197] and the enhanced activity of the defective catalysts toward CO_{ads} oxidation discussed in former Chapters. Another possibility would be that, for some reasons, the fraction of oxophilic sites does not contribute to the current measured during the base voltammograms in the region $E > 0.6$ V *vs*. RHE. This second hypothesis will now be discussed based on the comparison of the coulometric charges during CO_{ads} oxidation and H_{ads} desorption.

It has been discussed by Dubau *et al.* [65] and Stamenkovic *et al.* [225] that the alteration of electronic properties on bimetallic PtM surfaces creates a decrease in the magnitude of the H_{upd} region (due to a weaker H adsorption), leading to an inferior H_{ads} surface coverage while CO_{ads} surface coverage remains unchanged. Accordingly, an integrated charge ratio $Q_{CO}/2Q_H > 1$ (usually in the range of 1.3-1.5) is evidence of a Pt-skin surface

and is supposed to be ~1 in case of a surface alloy or Pt-skeleton type surface. We extracted both Q_{CO} and Q_H values out from CO_{ads} stripping experiments, as it has been reported to be more accurate for the estimation of Q_H [232]. The results presented **Table 5.7** are particularly striking: all the defective catalysts revealed unprecedented $Q_{CO}/2Q_H$ ratios < 1, in the range of 0.8-0.9 suggesting that the Pt specific surface areas estimated from the Q_{CO} charge were less pronounced than those determined using the method involving $2Q_H$. This result is particularly disturbing since all the specific surface areas discussed in this manuscript were derived from the Q_{CO} charge. However, instead of an unexplained diminished CO_{ads} surface coverage, $Q_{CO}/2Q_H$ ratios < 1 may also be rationalized by and extra charge Q_H in the H_{upd} region for the defective catalysts.

Table 5.7: Integrated charges for H_{upd} (Q_H) and CO_{ads} stripping (Q_{CO}) obtained from CO_{ads} stripping experiments for the catalysts evaluated in this section. The ratio between these two charges show unprecedented small values for the defective catalysts.

Electrocatalysts	$Q_{CO}/2Q_H$	Electrocatalysts	$Q_{CO}/2Q_H$
Sphere PtNi/C	0.98 ± 0.04	**Sponge PtNi/C**	0.81 ± 0.02
Cube PtNi/C	1.04 ± 0.08	**Pt/C TKK**	0.96 ± 0.07
Octahedron PtNi/C	1.04 ± 0.1	**A-Pt/C**	0.85 ± 0.03
Hollow PtNi/C	0.83 ± 0.03	**A-PtNi/C**	0.90 ± 0.03
Aerogel PtNi	0.79 ± 0.05	**Cube Pt/C**	0.93 ± 0.03

Note that the monocrystalline materials exhibited $Q_{CO}/2Q_H$ ratios comprised in the range 0.97-1.05 (except for the Cube Pt/C), in agreement with the literature [177,225]. We believe this is experimental evidence of a controversial model introduced in 2008 by Marichev *et al.* [233], further developed by Koper et al. [201] in 2013 and also discussed by Calle Vallejo *et al.* [224] in 2017 suggesting a possible replacement of H_{ads} species by OH_{ads} (and *vice versa*) in the potential region $E < 0.4$ V *vs.* RHE due to water dissociation on specific catalytic sites on Pt. Briefly, these authors provide answers to previously deserted questions, such as: (i) why H_{ads} adsorption/desorption are sensible to facets orientation (and may feature several peaks) while OH adsorption/desorption are not? (ii) Why the H_{upd} adsorption/desorption peak depend on pH (in alkaline media, the H_{upd} region is shifted toward positive potential *vs.* RHE [201])? (ii) Why *in situ* Fourier-Transform Infrared Spectroscopy (FTIR) during CO_{ads} stripping experiment on PtNi/C materials band associated to CO_2 production can be detected at a potential as low as ~0.4 V *vs.* RHE or even lower (~0.3 V *vs.* RHE) in case of Hollow PtNi/C [197] ? Using single crystals experiments and DFT calculations, Koper *et al.* suggested that the introduction of steps

of specific surface orientations (such as (100) and (110) steps on Pt(111)) leads to specific features: first, while the maximum H_{ads} surface coverage on (111) terrace is known to be 1, their calculations predicted a maximum coverage of 0.5 on the step sites (both (100) and (110)) while no maximum value was found for OH_{ads}, but its binding energy dramatically increases on these sites. Second, the Q_H charge from the H_{upd} region did not vary with the predicted decrease of surface coverage of H species when steps were introduced, suggesting a contribution from one or several other adsorbates. They consequently proposed OH_{ads} species as the most probable candidate, which could replace adsorbed H species in the region of the steps following an equation of the type:

$$H_{ads} + H_2O \leftrightarrow OH_{ads} + 2H^+ + 2e^- \tag{5.10}$$

This simplistic equation must be considered carefully as it predicts an increase of the Q_H charge due to the 2e⁻ involved in the process and a pH dependency which does not match experimental values from Ref. [201]. It remains nonetheless still probable considering the unknown initial surface coverage of H species on the steps, the occurrence of such replacement by OH_{ads} on the steps and the proportion of steps on the surface.

Whereas the term 'step' might be inappropriate for nanostructured electrocatalysts, we have shown previously that dealloying or aggregation of nanoparticles creates such a disorder that the proportion of defective sites makes the notion of lattice parameter more an approximation considering the high dispersion (microstrain) around its mean value (global strain). Accordingly, because they were working on stepped extended single crystal surfaces, we believe Koper *et al.* did not observe significant changes in the Q_H charge due to the lack of defective sites (*i.e.* regions featuring decreased H_{upd} coverage and electronic configuration allowing **Equation (5.10)**). A simple experimental proof of the presence of OH_{ads} species in the H_{upd} region is presented in **Figure 5.16**, where it can clearly be seen on Sponge PtNi/C, that the CO_{ads} oxidation peak and the end of the H_{upd} desorption region overlap in a short potential window ~0.3-0.5 V *vs.* RHE). Note that the case presented here represents an extreme and unambiguous evidence of H_{upd} and OH co-adsorption below 0.4 V *vs.* RHE, but a CO_{ads} oxidation onset potential higher than 0.4 V *vs.* RHE (without overlap with the H_{upd}) does not exclude pre-adsorbed OH_{ads} from the H_{upd}.
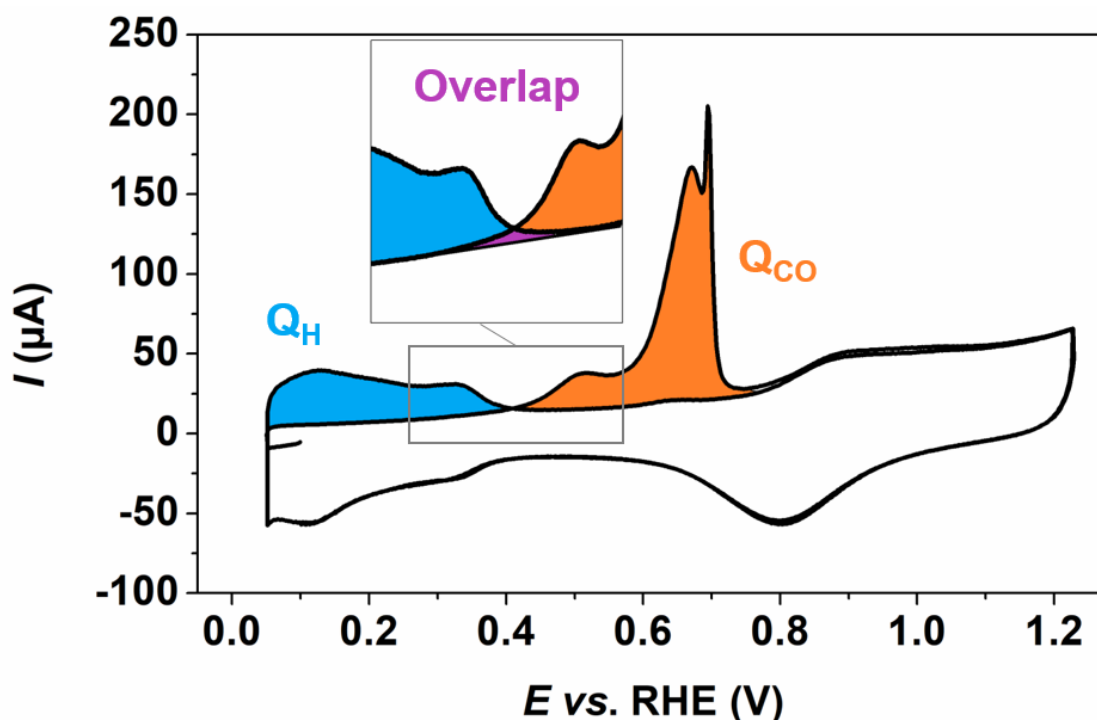
Figure 5.16: The first two cycles of a CO_{ads} stripping experiment for the Sponge PtNi/C catalyst. Regions considered for the Q_H and Q_{CO} have been coloured in blue and orange, respectively. This catalyst has been chosen to highlight the overlapping of H_{upd} desorption and CO_{ads} electrooxidation regions, which means that H and OH species are co-adsorbed in the potential region of the overlap. 0.1 M $HClO_4$, potential sweep rate 20 mV s^{-1}, $T = 298K$.

More than answering to long-term inconsistencies from literature as listed above, this replacement of H_{ads} by OH_{ads} in the H_{upd} region (which makes absolutely no doubt according to our experimental evidence) is likely to produce the extra Q_H charge observed only for defective materials and quantifiable through the $Q_{CO}/2Q_H$ ratio. Also, the unexpected oxophobic behaviour of defective catalysts in the oxide-surface adsorption/desorption region can now be rationalized by the contribution of highly oxophilic shifted toward negative potential, *i.e.* in the H_{upd} region.

To give more credit to this hypothesis, a comparison between the $Q_{CO}/2Q_H$ ratios determined for all the electrocatalysts and their associated Surface Disorder extracted from XRD patterns is presented in **Figure 5.17a.** The good matching of these two parameters, the first being directly a signature of the surface due to modified adsorption properties and the second associated to the surface from correction of a bulk parameter (the Raw Microstrain) is a sign of the validity of our approach. Note that the Raw Microstrain free from correction does not predict the surface adsorption properties that well (**Figure 5.17b**).
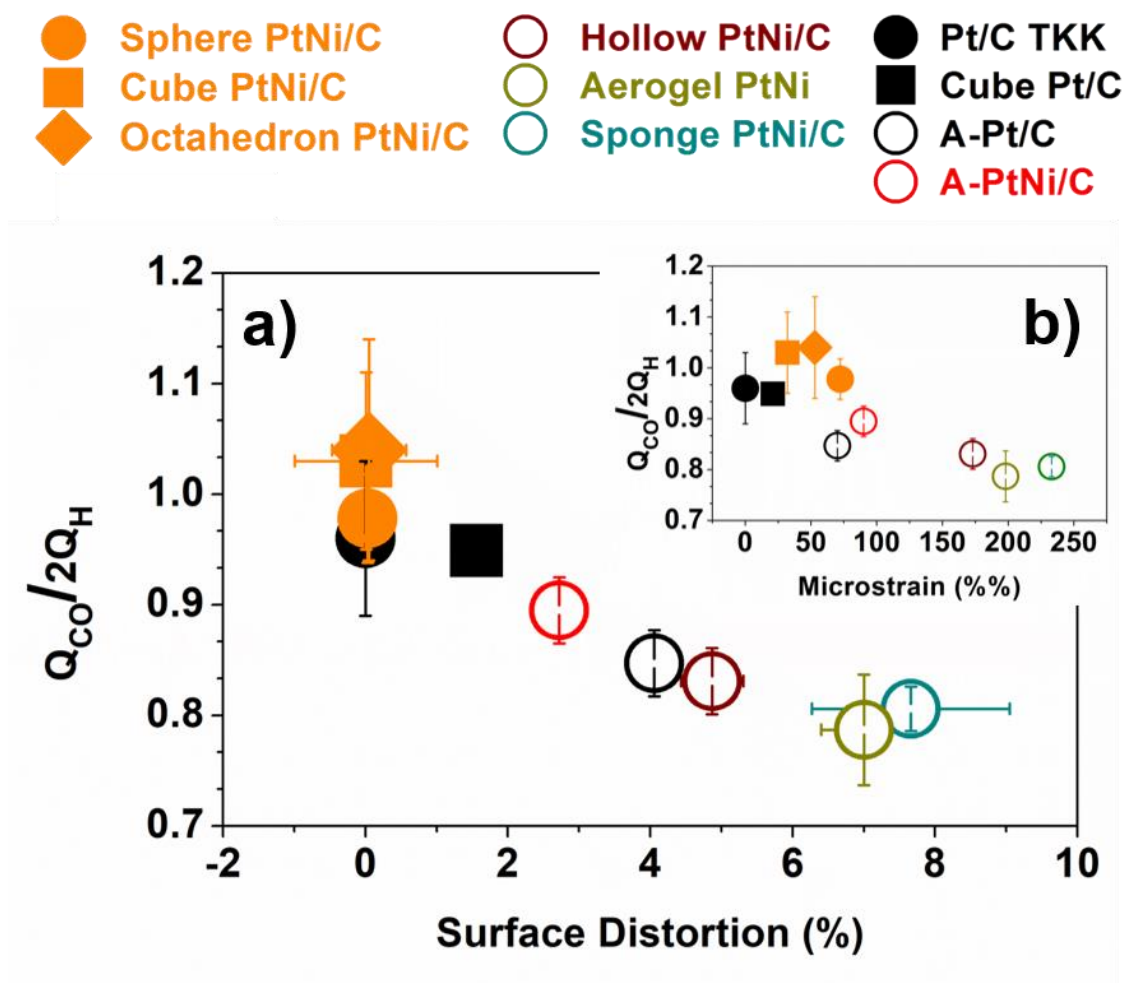
Figure 5.17: Surface disorder determined *via* the $Q_{CO}/2Q_H$ ratio *vs.* structural disorder derived from XRD via the Microstrain, with correction from the Ni content and crystallite size 'Surface Distortion' (a); and without correction (b).

We must however emphasize that, if both $Q_{CO}/2Q_H$ and the SD may be two quantifiers of the same physical phenomenon (the surface disorder) they both suffer from approximations, as the SD cumulates errors from the microstrain and crystallite size measurement (XRD, Rietveld analysis hypothesis etc.), the Ni content estimation (X-EDS and/ or XRD) also with the determination of the dispersion D via a mathematical model. The approximations concerning $Q_{CO}/2Q_H$ are those related to the CO_{ads} stripping technique, *i.e.* the proper correction of the background, right choice for the integration potential limits, or any undesired adsorption phenomena [232]. Also, as shown by **Figure 5.16** the integration regions for Q_H and Q_{CO} tend to overlap with increasing defects content, which induces an overestimation of the charges ratio (which can explain the relatively high $Q_{CO}/2Q_H$ for Sponge PtNi/C compared with its SD). However, despite all the approximations, it is striking to observe that in the case of the Cube Pt/C, the slight

aggregation deduced from the positive SD (which may have been an artefact) is confirmed by the $Q_{CO}/2Q_H$, showing a good sensibility for both parameters.

Figure 5.18: Relationship between the ORR specific activity measured at *E*= 0.95 V *vs*. RHE and both electrochemical (a) and physical (b) markers for the density of structural defects for the different electrocatalysts evaluated in this study.

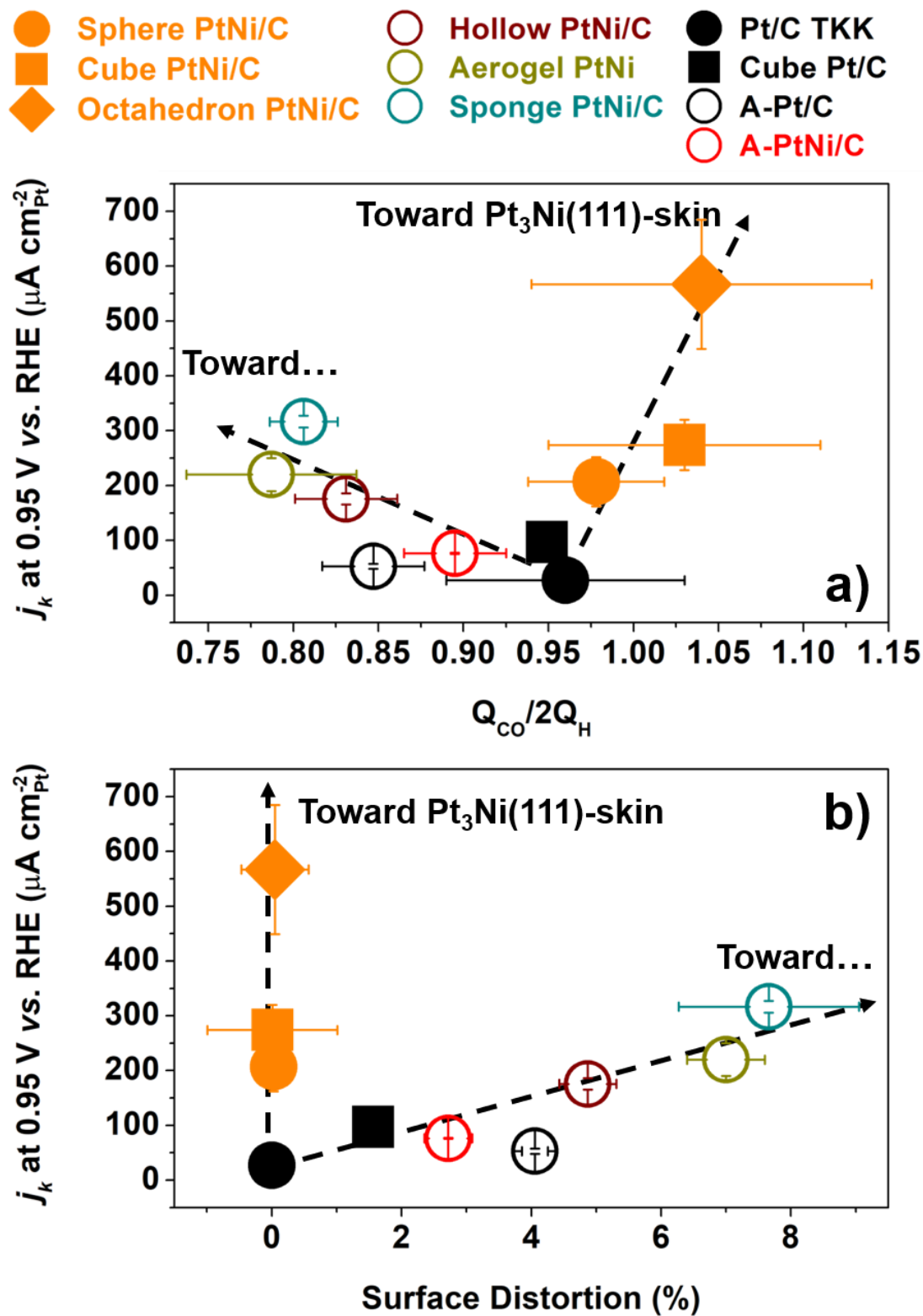Finally, in **Figure 5.18**, the ORR activity of all electrocatalysts evaluated in this study is plotted as a function of $Q_{CO}/2Q_H$ (**Figure 5.18a**) and the Surface Distortion (**Figure 5.18b**). Note that $Q_{CO}/2Q_H$ provides a convenient route to estimate the surface disorder relative to SD (it only requires CO instead of a Synchrotron radiation facility), but similar trend is observed for both parameters. Beyond the overall comparison of the ORR activity for the different structures, the two of these plots show again two different branches. On one branch of the 'reverse volcanoes' (to which belongs the Sphere, Cube and Octahedron PtNi/C catalysts, right part in **Figure 5.18a** and left part **Figure 5.18b**), the ORR activity dramatically increases with $Q_{CO}/2Q_H$ or low Surface Distortion. An increase of the $Q_{CO}/2Q_H$ or a decrease of the Surface Distortion are a fingerprint of homogeneously high-coordinated surface atoms with progressive and uniform disappearance of oxophilic catalytic site, the ideal surface pointed by this trend would be the $Pt_3Ni(111)$-skin surface owing to its low affinity for oxygenated species [63].

On the other branch for each plot, the ORR activity increases much more slowly with decreasing $Q_{CO}/2Q_H$ or increasing Surface Distortion. This branch is composed of defective catalysts where the philosophy is, through the insertion of structural disorder, to randomly implement highly-coordinated surface atoms in specific concave sites [211]. The price to produce such sites is however to 'scarify' catalytic sites to a low-coordination configuration, resulting in a poor contribution to the ORR catalysis but enhanced electrocatalytic activity for oxidation reactions [197]. This original approach may never compete with the uniformly optimized surface in terms of initial specific activity, but it allows promising possibilities for ORR mass activity improvements, the latter being possibly achieved by the use of small crystallite and porous structures, as recently demonstrated by the 'jagged' ultrafine Pt nanowire [196] (note that the MA of Octahedron PtNi/C and Sponge PtNi/C catalysts are not that far from each other). Extrapolation of this trend is unknown and difficult to predict; but it may represent a pathway to break the scaling relations between O_{ads}, HO_{ads} and HOO_{ads} species that impose a minimum ~0.4 V overpotential to make each reaction step downhill in free energy on classical Pt-based catalysts [69], or to involve a different ORR mechanism.

5.4 Initial Trends *vs.* (Electro)chemical Ageing.

In this section, we confront the structure-activity relations presented above to the harsh chemical and/or electrochemical environment of a PEMFC cathode. Both acidic treatment and potential cycling were used to simulate the degradation of the electrocatalysts under real PEMFC operating conditions, and thus get insights on the long-term viability of the 'perfect' *vs.* 'defective' catalysts approaches. More details about the ageing procedures are provided in the materials and methods section in appendix of this manuscript.

5.4.1 Acidic Treatment

We first emphasize that the protocols used for the preparation of the Ni-rich and/or shape-controlled nanoparticles (Sphere, Cube and Octahedron PtNi/C) protect the surface from any corrosive atmosphere, starting from the synthesis to their characterization (water-free organic solvent syntheses, centrifugation and freeze-drying techniques to collect the as-prepared catalysts from the synthesis medium, see materials and methods section). This is in total contrast with the defective catalysts, which were synthetized in pure water (or mixture of water and polyol), filtered in water and then acid-treated to ensure dissolution of Ni nanoparticles possibly remaining post-synthesis and formation of a Pt-rich topmost surface. However, it is unrealistic to believe that octahedral or cubic shapes will be preserved in the long-term because they are thermodynamically 'out-of-equilibrium' and because the harsh operating conditions in a real PEMFC cathode (highly acidic pH due to Nafion®, oxidizing electrochemical potential and atmosphere, and high temperature) are strong driving forces to return to the thermodynamically stable equilibrium shape ('cuboctahedron'). Therefore, to better take into account the combined effects of pH, oxidising atmosphere and electrode potential, the Sphere, Cube and Octahedron PtNi/C samples were acid-treated in 1 M H_2SO_4 for 22 h at room temperature under air atmosphere (open circuit potential close to 1.0 V *vs.* RHE). The acid-treated samples are referred as Sphere PtNi/C-AT, Cube PtNi/C-AT and Octahedron PtNi/C-AT in what follows.

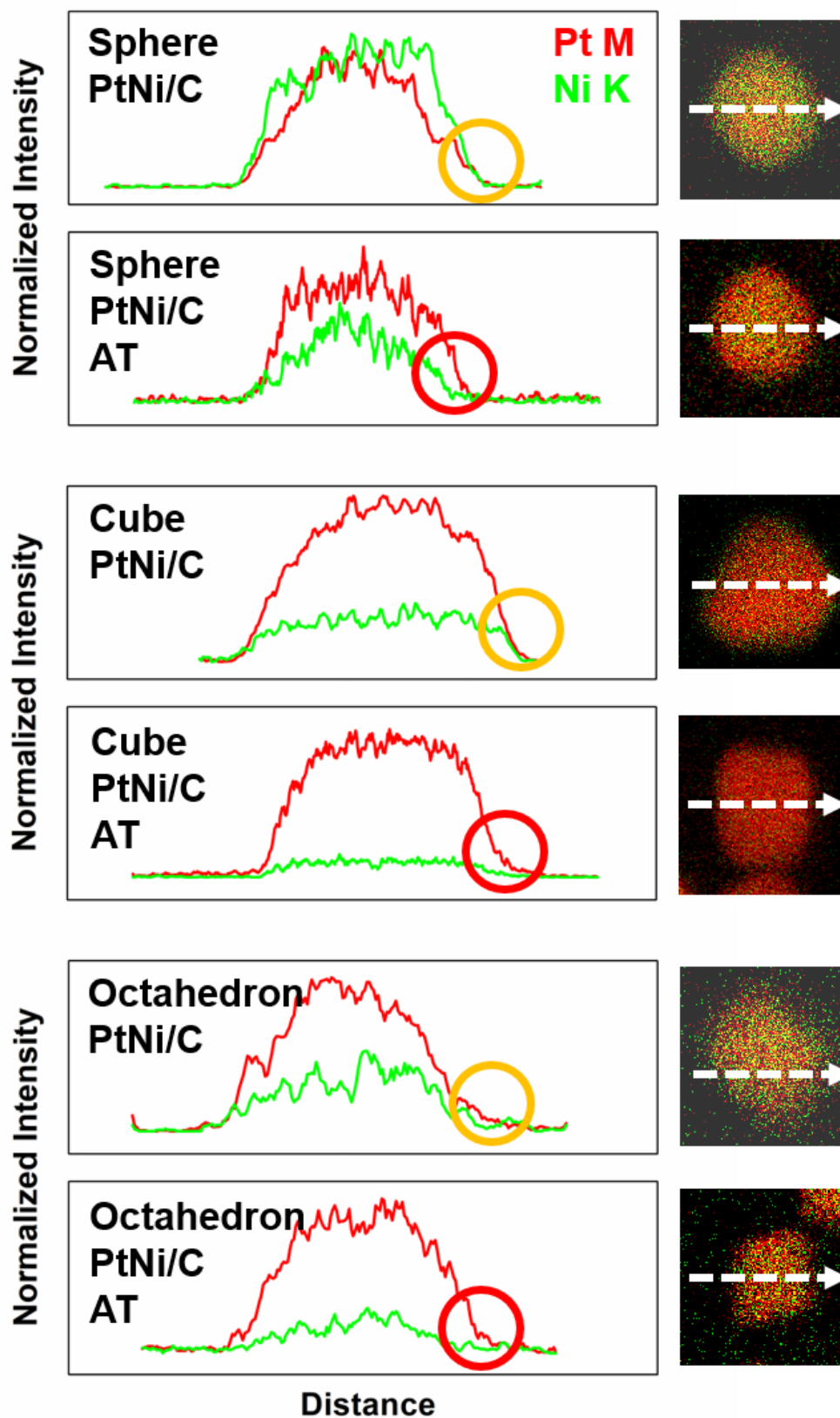**Figure 5.19**: STEM-X-EDS compositional line profiles and elemental maps of the 'single crystal inspired' samples before and after acidic treatment in 1M H_2SO_4. The STEM-X-EDS profiles are normalized to the elemental scattering factors, allowing a direct reading of the thickness -projected composition through the intensity ratios. The circles highlight the surface Pt:Ni stoichiometry changes during the acidic treatments.

Table 5.8: Structural and chemical parameters for the acid-treated 'single crystal inspired' electrocatalysts evaluated in this study.

Electrocatalysts	X-EDS	Synchrotron WAXS + Rietveld Refinement				Average Ni content (at. %)
	Ni content (at. %)	Ni content (at. %)	Lattice parameter (Å)	Crystallite size (nm)	Microstrain (‰)	
Sphere PtNi/C-AT	34 ± 1	44	3.750	11.6 ± 1.8	130	39 ± 6
Cube PtNi/C-AT	11 ± 1	9	3.890	10.1 ± 0.2	14	10.2 ± 2
Octahedron PtNi/C-AT	19 ± 1	25	3.830	8.3 ± 0.4	45	22 ± 4

Table 5.8 shows the structural and chemical parameters of the 'single crystal inspired' acid-treated samples derived from STEM-X-EDS and XRD measurements. The initial Ni content decreased by *ca.* 40-50 % (according to X-EDS measurements), and by 3, 20 and 50 % (according to XRD patterns and the Vegard's law) for the Octahedron, Sphere and Cube respectively. The STEM-X-EDS elemental maps displayed in **Figure 5.19** reveal that the Ni content decrease is associated with the formation of PtNi-core@Pt-rich-shell-like nanoparticles (*i.e.* Ni atoms were dissolved mostly from the surface and near-surface region of the catalysts). The almost constant lattice parameter for the raw and acid-treated Octahedron PtNi/C is striking, but is believed to provide evidence of the lattice contraction (strain) remaining after removal of Ni atoms from the near-surface region. Note that any pure Ni (or Ni oxides) phase covering the particle surface was likely dissolved during the acidic treatment, as shown for the Sphere PtNi/C-AT nanoparticles, the surface and near-surface layers of which were initially Ni-rich.

We now focus on the microstrain values extracted from the diffraction patterns and presented in **Table 5.8**. As previously discussed in **Figure 5.5** and presented in **Figure 5.6**, where the diverse sources of microstrain had been highlighted, a decrease in Ni content can either (i) lower the microstrain value (chemical term in **Figure 5.6**) or (ii) enhance the microstrain value if the initial atomic arrangement is destroyed and pores are forming [197]. **Figure 5.20** displays the microstrain values plotted as a function of the Ni at. % for the 'single crystal inspired' nanoparticles before and after acidic treatment, superposed with the initial trend presented in **Figure 5.5** (transparent data points). For the facetted nanoparticles (Cube PtNi/C and Octahedron PtNi/C), the diminution of Ni

content goes along a decrease of the microstrain, in agreement with the microstrain-Ni at. % relationship presented in **Figure 5.7** (fitted curve, reproduced in green dashed line in **Figure 5.20**), suggesting conservation of the initial atomic arrangement.
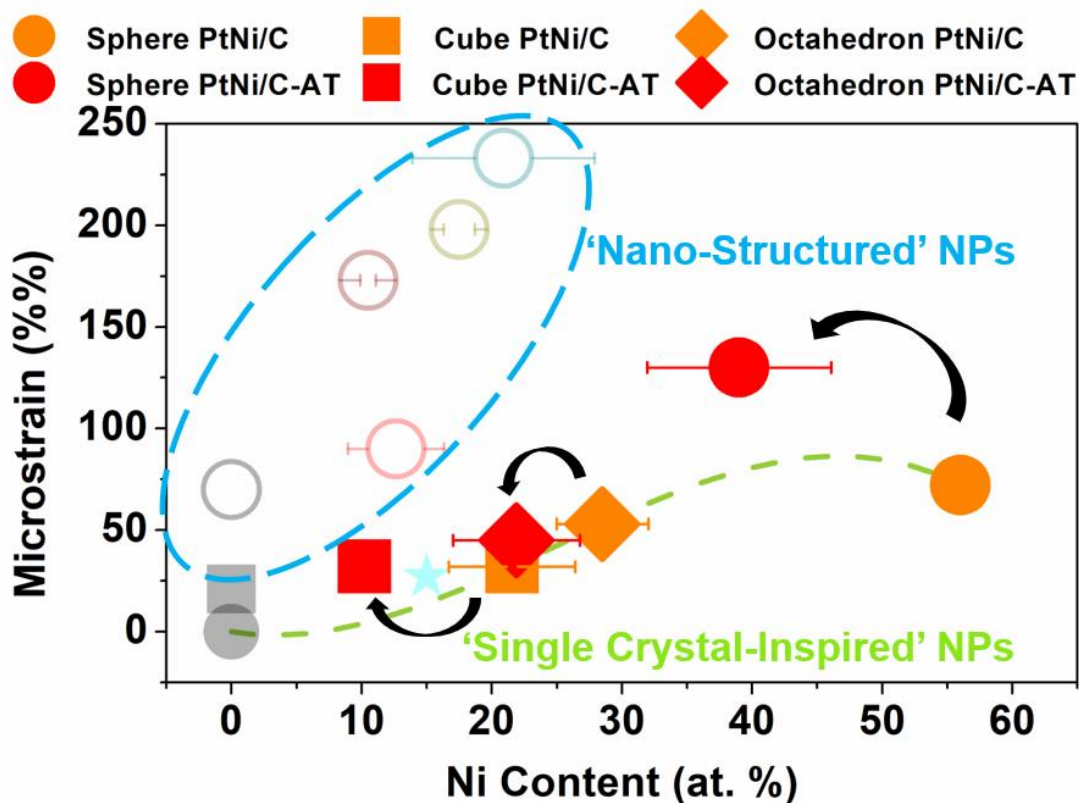
Figure 5.20: Microstrain *vs*. Ni content for the electrocatalysts evaluated in this section superposed on the initial trend introduced **Figure 5.5**. Transparent data points correspond to **Figure 5.5**, while opaque symbols are related to the 'single crystal inspired' catalysts before (orange) and after (red) acidic treatment. The green dashed line corresponds to the microstrain-Ni at. % relationship as fitted **Figure 5.7** and considered in this study.

However, a drastic increase of the microstrain value manifested for the Sphere PtNi/C sample after acidic treatment. This increase is in contrast with the diminishing Ni content, suggesting an extra source of microstrain, such as a modification of the nanoparticle shape and/or the apparition of structural defects at the surface of the nanoparticles.
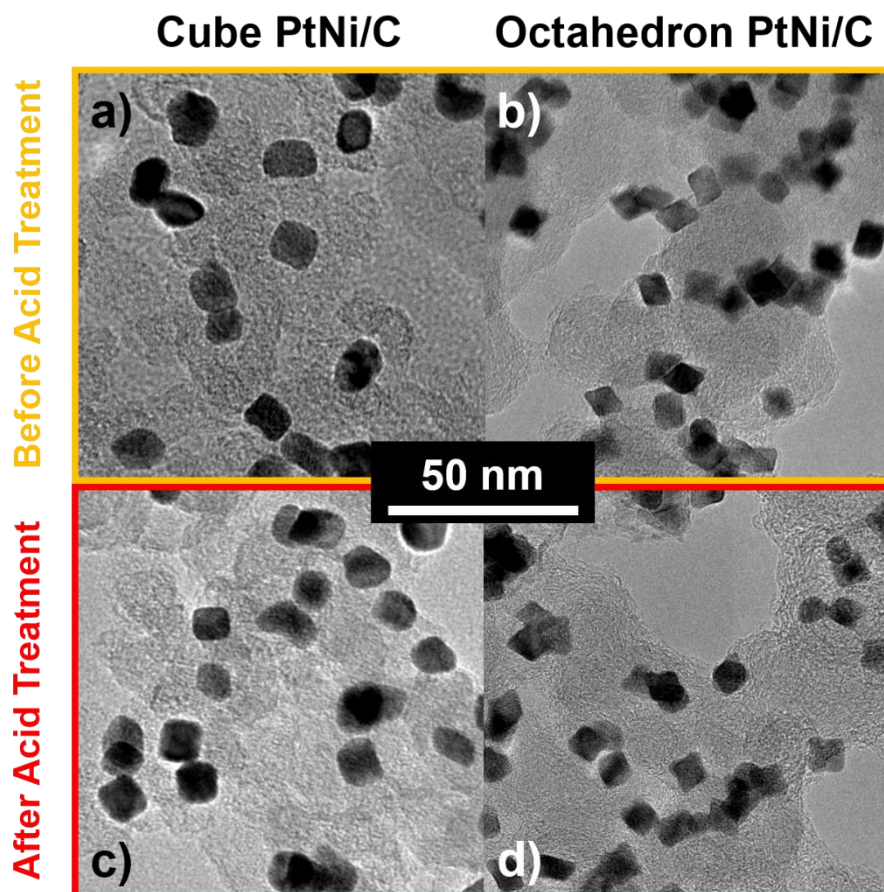
Figure 5.21: TEM images of the facetted nanoparticles (Cube PtNi/C and Octahedron PtNi/C) before and after acidic treatment, showing an overall conservation of the particle shape.

The TEM images of the samples before and after acidic treatment, displayed in **Figure 5.21**, are perfectly in line with the predictions made from physical and chemical characterizations. Indeed, for facetted nanoparticles (Cube PtNi/C and Octahedron PtNi/C), the acidic treatment did not induce drastic changes in the nanoparticle shape (even if a slight concavity of the facets may be noticed in case of the Octahedron PtNi/C-AT **Figure 5.21c)**, at least, no porosity formation could be noticed. Note that the stability of the facets may also explain the non-negligible difference in Ni retention after acidic treatment between the cubic (*ca.* 10 at. %) and octahedral (*ca.* 22 at. %) particles, due to the superior atomic density of (111)-oriented facets relative to (100)-oriented facets for the octahedra and cubes respectively.
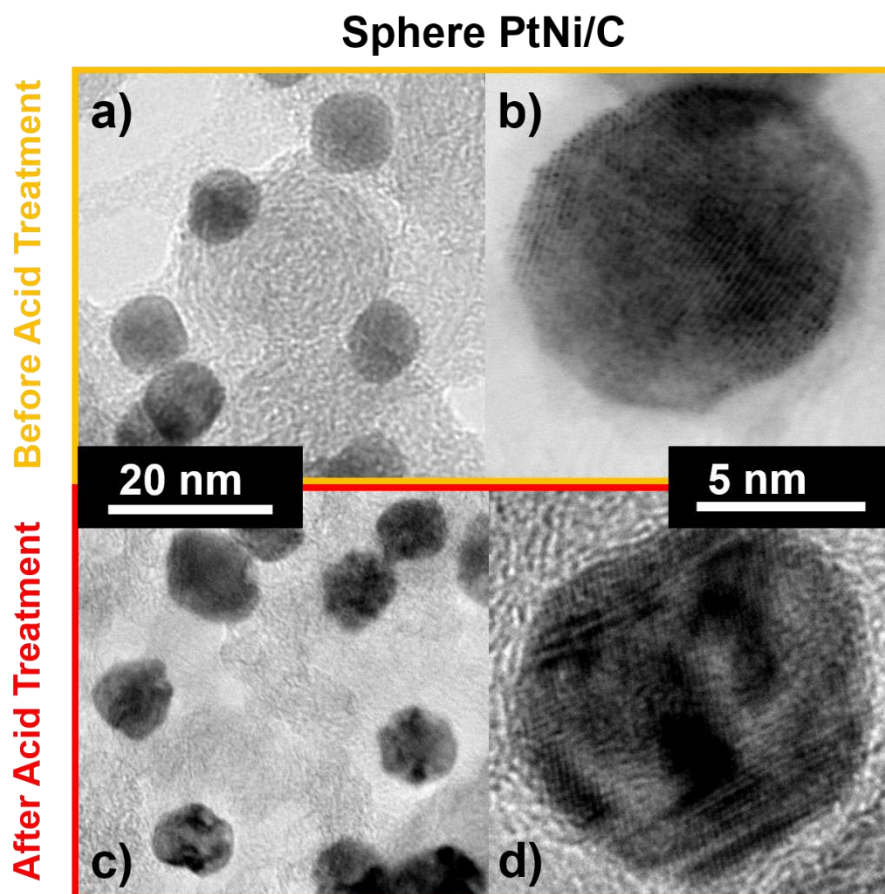
Figure 5.22: TEM (a, c) and HRTEM (b, d) images of the Sphere PtNi/C nanoparticles before and after acidic treatment showing the apparition of porosity.

However, and as already reported in literature [83,94,96,97,213], nanoparticles exceeding 10 nm in size are likely subject to nanoporosity formation when exposed to acidic environment. The size of the nanoparticles synthesized in this work is located at the borderline, which is supposed to guarantee the morphological stability. As shown in **Figure 5.22**, the 8-11 nm Sphere PtNi/C catalyst sample unambiguously turns porous (or at least partially) when treated in 1 M H_2SO_4 for 22 h under air, in agreement with literature [97]. This coherency between the predicted and observed chemical composition-microstrain-structure relationship is a further evidence of the viability of the approach introduced in this work.

We then calculated the values of Surface Distortion parameter for the acid-treated catalysts, following the exact same methodology as introduced in **Section 5.3.1**. Without much surprise, a very large Surface distortion value in case of the porous Sphere PtNi/C-AT catalyst (with a SD close to our defective Hollow PtNi/C catalyst), while the remaining solid Cube and Octahedron PtNi/C-AT samples keep a relatively high surface

order (**Table 5.9**). These surface properties evolution will now be discussed in the light of CO_{ads} oxidation and O_2 reduction.

Table 5.9: Structural parameters derived from the Rietveld analysis of the WAXS patterns for the acid-treated PtNi/C electrocatalysts.

Electrocatalysts	*D* (%)	*SD* (%)
Sphere PtNi/C-AT	11.6 ± 2	5.1 ± 1
Cube PtNi/C-AT	13.4 ± 0.3	0.8 ± 0.2
Octahedron PtNi/C-AT	15.6 ± 1	0.8 ± 0.6

Figure 5.23 shows the CO_{ads} stripping voltammograms recorded for the 'single crystal inspired' catalysts before and after acidic treatment. Slight shifts toward positive potential of the CO_{ads} stripping peaks are observed for Cube and Octahedron PtNi/C-AT after acidic treatment (probably related from depletion of Ni atoms from their surface) [226]. In contrast, the CO_{ads} stripping voltammogram of the Sphere PtNi/C is quite similar before and after acidic treatment. One might therefore be tempted, on the basis of electrochemical characterizations alone, to conclude that the Ni content of these catalysts has remained unchanged, which is in complete contrast to the results of the physical and chemical characterizations presented above. In fact, this contradictory observation points towards a limit of structure-electrocatalytic activity-stability relationships, as physical and chemical parameters are often determined *ex-situ* and could be completely different in electrochemical environment. However, a simple TEM image of the raw Sphere PtNi/C (*i.e.* without acidic treatment) after electrochemical characterization (see **Figure 5.24**) clearly shows that pores were already formed at this stage.
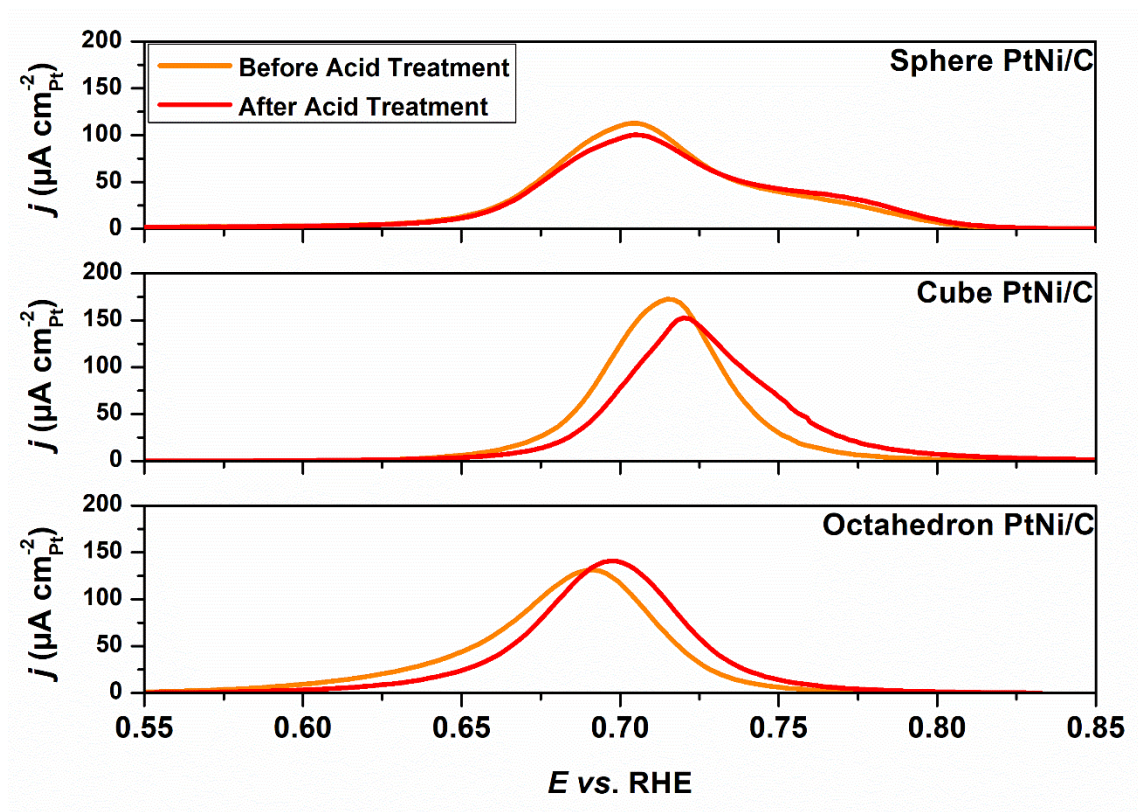
Figure 5.23: CO$_{ads}$ stripping voltammograms recorded under Ar-saturated 0.1 M HClO$_4$ electrolyte at v = 20 mV s^{-1} for the 'single crystal inspired' electrocatalysts before and after acidic treatment.

Consequently, the nearly-identical CO$_{ads}$ stripping voltammograms are actually a manifestation of their extreme instability and, as their initial atomic arrangement vanishes after a few potential cycles, the 'initial' CO$_{ads}$ stripping voltammogram presented in **Figure 5.23** is likely that of porous (and not solid) spherical PtNi/C nanoparticles.
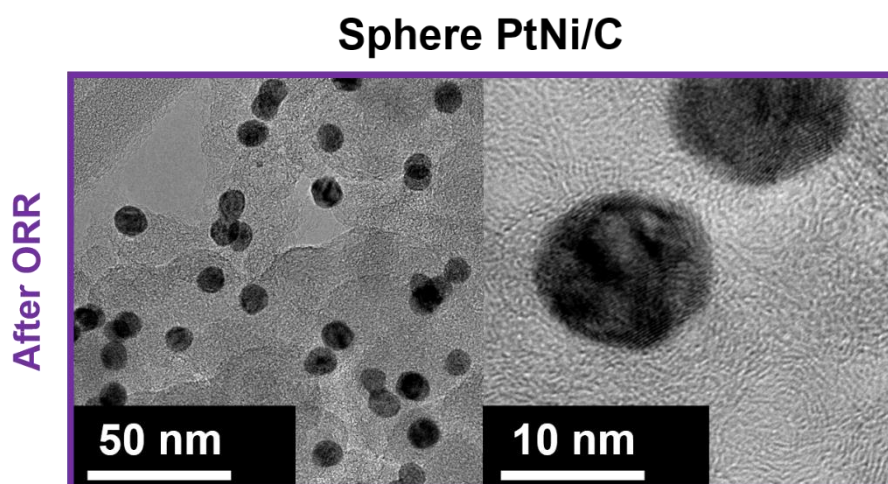
Figure 5.24: TEM images of the Sphere PtNi/C nanoparticles after electrochemical characterization, showing the apparition of porosity, even in the absence of the acidic treatment.

Fortunately, this example likely represents an extreme case, as the acidic treatment greatly affects the electrocatalytic properties of the Cube and Octahedron PtNi/C, providing evidence that a simple electrochemical characterization does not cause systematically major structural and acidic damages to the surface.
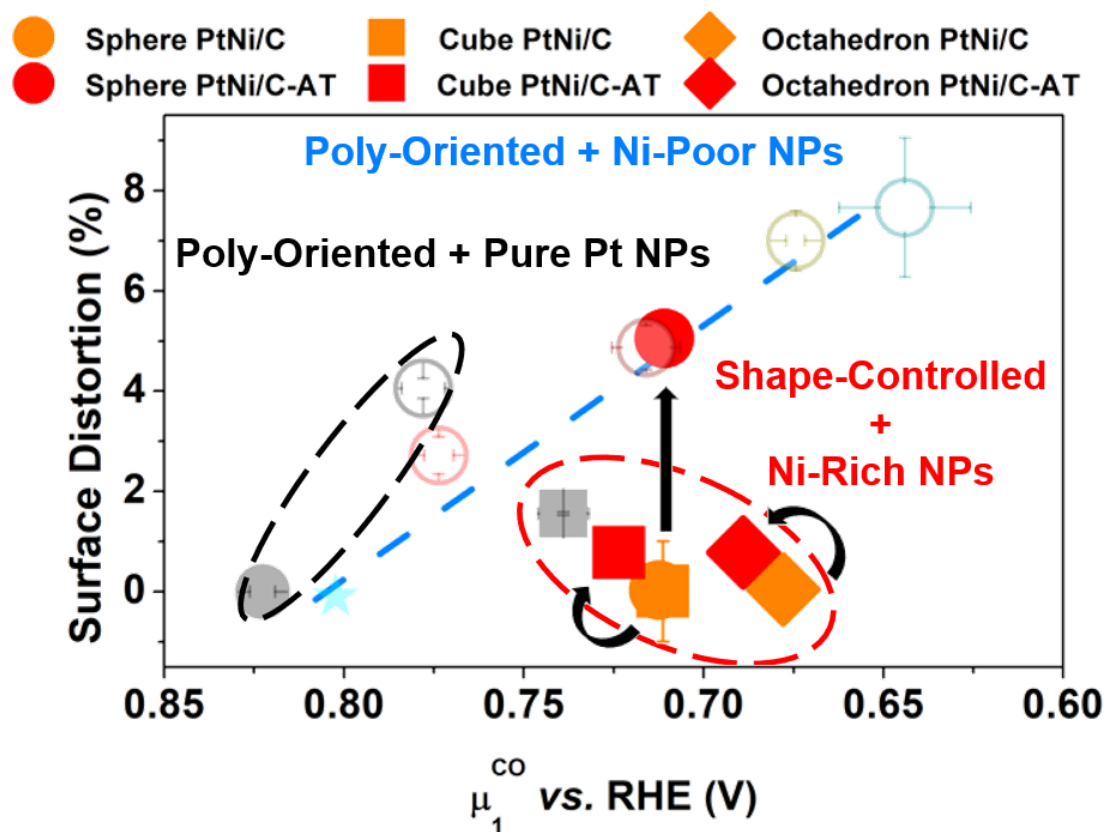
Figure 5.25: Surface Distortion *vs*. μ_1^{CO} for the electrocatalysts evaluated in this section. The initial trend introduced in **Figure 5.10** is superposed for the sake of comparison. Transparent data points correspond to **Figure 5.10** while opaque symbols are related to the 'single crystal inspired' catalysts before (orange) and after (red) acidic treatment.

It is now interesting to compare the μ_1^{CO} (listed in **Table 5.10**) and the Surface Distortion values. As shown in **Figure 5.25**, the slight changes of the average CO_{ads} electrooxidation potential and Surface Distortion values suggest a conservation of the initial atomic arrangement (structural order) in case of facetted particles (Cube and Octahedron PtNi/C-AT). However, despite similar μ_1^{CO} value before and after acidic treatment, the porous Sphere PtNi/C-AT catalyst now belongs to the 'poly-oriented + Ni-poor nanoparticles' branch, in agreement with the destruction of the crystalline facets associated with the formation of pores. Note that the 'real' μ_1^{CO} value of the untreated Sphere PtNi/C is actually unknown because inaccessible at the non-porous state.

Finally, the ORR activity of the acid-treated electrocatalysts was determined. As presented in **Table 5.10**, a *ca.* 50-55 % decline of the specific activity at 0.95 V *vs.* RHE was observed after acid leaching in case of facetted nanoparticles, in agreement with the massive Ni depletion from the near surface region, whereas 'only' 30 % of the initial $SA_{0.95}$ value was lost for the Sphere PtNi/C after acid-leaching.

Table 5.10: Average CO_{ads} oxidation potential (μ_1^{CO}), iR + mass transport corrected ORR specific activity ($SA_{0.95}$) measured at $E = 0.95$ V *vs.* RHE on the acid-treated electrocatalysts evaluated in this section, and corresponding enhancement factors (E.F.) relative to the reference Pt/C TKK.

Electrocatalyst	μ_1^{CO} *vs.* RHE (mV)	$Q_{CO}/2Q_H$	$SA_{0.95}$ ($\mu A\ cm_{Pt}^{-2}$)	E.F. SA
Sphere PtNi/C-AT	711 ± 3	0.88 ± 0.03	147 ± 5	5.4
Cube PtNi/C-AT	724 ± 3	0.93 ± 0.04	124 ± 6	4.6
Octahedron PtNi/C-AT	690 ± 5	0.97 ± 0.2	275 ± 53	10

Figure 5.26 shows the relationship between the ORR specific activity and both the electrochemical ($Q_{CO}/2Q_H$) and physical (SD) markers of surface defectiveness. It can clearly be seen that the previously established trends are robust enough to cover the chemical ageing of the 'single crystal inspired' catalysts. Moreover, both plots in **Figure 5.26a** and **Figure 5.26b** suggest that the supposed 'perfect" surfaces are catalytically highly unstable, as the two markers testify that the acidic treatment and the corresponding Ni leaching induce surface defectiveness. Actually, even if mitigated in the case of the Octahedron and Cube PtNi/C catalysts, the formation of these structural defects combined with the Ni depletion from the surface, inhibit the strain, ligand and ensemble effects, based on uniformly strained and highly coordinated atoms. This results in a dramatic decline of the ORR specific activity along the 'perfect surface' branches of the 'reverse volcano' plot. It is noteworthy that, after similar acidic treatment, the defects-induced activity of the Sponge PtNi/C outweighs the one of the Octahedron PtNi/C (**Figure 5.26**). Also, by changing its strategy from 'perfect' to 'defective' surface *via* apparition of porosity, the Sphere PtNi/C retains most of its initial activity, becoming catalytically more active than the preferentially shaped Cube PtNi/C after acidic treatment, suggesting more sustainable ORR activity enhancement for the 'defects-do-catalysis' approach.
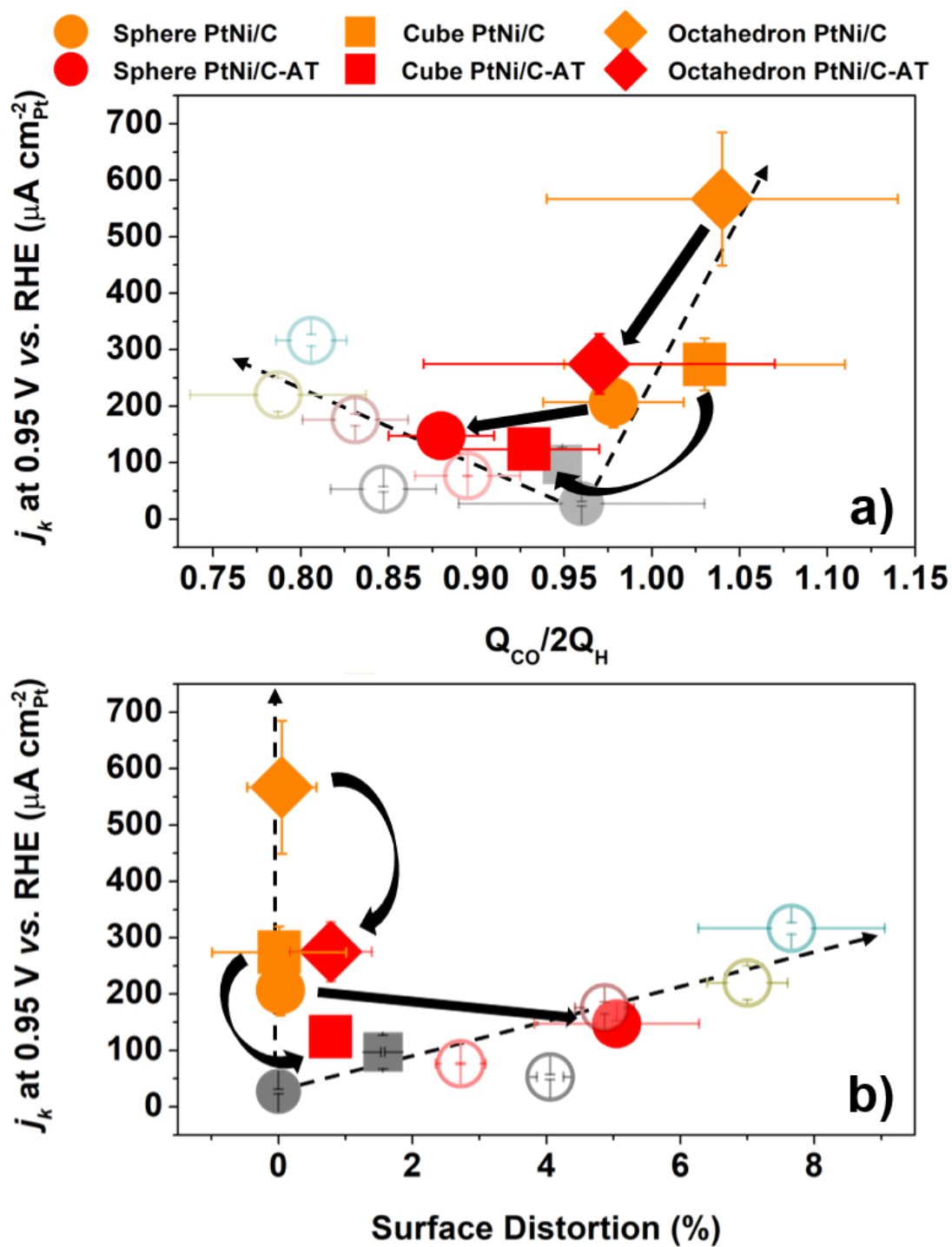
Figure 5.26: Relationship between the ORR specific activity measured at *E*= 0.95 V *vs*. RHE and both electrochemical (a) and physical (b) markers for the electrocatalysts evaluated in this section. The initial trend introduced in **Figure 5.18** is superposed for the sake of comparison. Transparent data points correspond to **Figure 5.18** while opaque symbols are related to the 'single crystal inspired' catalysts before (orange) and after (red) acidic treatment.

5.4.2 Accelerated Stress Tests

In this section, we tackle the issue of the long-term stability of the ORR electrocatalysts. Because degradation mechanisms under accelerated stress tests are already largely discussed in literature [136,182,208,209,215,234–236] and following the ideas developed in the previous section, we will describe the ageing of two selected electrocatalysts (Octahedron PtNi/C and Sponge PtNi/C). These two catalysts were selected because they show the best initial performance in their respective class of catalyst (shape-controlled *vs.* defective). The catalysts were aged using a 'load cycle' protocol consisting in 20,000 (20 k) potential cycles at 50 mV s^{-1} between 0.6 and 1.0 V *vs.* RHE in Ar-saturated 0.1 M HClO$_4$ at $T= 80$ °C. To gain further insights into the changes of the different structural and chemical parameters, individual experiments were performed for each electrocatalyst after 0, 100, 5,000 and 20,000 potential cycles. Note that 'zero potential cycle' experiment was performed to investigate the impact of the two ORR characterizations (before and after potential cycling).

Table 5.11: *iR* + mass transport corrected ORR specific activity (*SA*$_{0.95}$) and mass activity (*MA*$_{0.95}$) measured at *E*=0.95 V *vs.* RHE and average CO$_{ads}$ oxidation potential (μ_1^{CO}), Surface Distortion (SD), lattice parameter and crystallite size for the fresh and aged catalysts evaluated in this section. For the aged catalysts, the *MA*$_{0.95}$ values were calculated by normalizing the kinetic current for the ORR by the Pt mass initially loaded on the electrode.

Catalysts	SA$_{0.95}$ (μA cm$_{Pt}^{-2}$)	MA$_{0.95}$ (A g$_{Pt}^{-1}$)	μ_1^{CO} vs. RHE (mV)	SD (%)	Lattice parameter (Å)	Cryst. Size (nm)
Octahedron PtNi/C	567 ± 118	157 ± 19	678 ± 5	0.0 ± 0.5	3.822	9.2 ± 0.3
Octahedron PtNi/C-ORR	294	81	677	-1.2	3.826	7.1
Octahedron PtNi/C-100	231	64	688	-0.6	3.826	7.7
Octahedron PtNi/C-5k	130	36	691	1.5	3.824	9.4
Octahedron PtNi/C-20k	217	60	778	1.7	3.832	9.5
Sponge PtNi/C	317 ± 11	146 ± 4	644 ± 18	7.6 ± 1.4	3.820	4.5 ± 0.9
Sponge PtNi/C-ORR	277	127	656	5.1	3.884	8.5
Sponge PtNi/C-100	253	116	665	4.2	3.884	8.3
Sponge PtNi/C-5k	216	100	698	3.6	3.893	6.9
Sponge PtNi/C-20k	210	97	715	3.3	3.895	7.3

Table 5.11 lists the ORR activity (both SA and MA values) measured at *E*= 0.95 V *vs.* RHE for the two electrocatalysts after different numbers of potential cycles. As plotted in **Figure 5.27a**, the gap in initial specific activity between the Sponge PtNi/C and the Octahedron PtNi/C is compensated after two consecutive electrochemical ORR

measurements (see materials and methods section). The Sponge PtNi/C becomes more electrocatalytically active with increasing number of potential cycles between the two characterizations (100 and 5,000 potential cycles). It must be noticed that, between 5,000 and 20,000 potential cycles, an ORR activity gain is observed for the Octahedron PtNi/C. Finally, similar specific activity was measured for both catalysts after 20,000 potential cycles, corresponding to a 62 % and 34 % loss for Octahedron PtNi/C and Sponge PtNi/C, respectively. Moreover, due to the smaller crystallite size and highly porous structure, a higher Pt specific surface area was obtained for the Sponge PtNi/C than for the Octahedron PtNi/C catalyst (see **Table 5.5**). Combined with the nearly-identical ORR specific activity, a real advantage in terms of mass activity quickly appears for the defective catalyst as shown in **Figure 5.27b**. In the following, we will try to rationalize these variations in ORR activity.
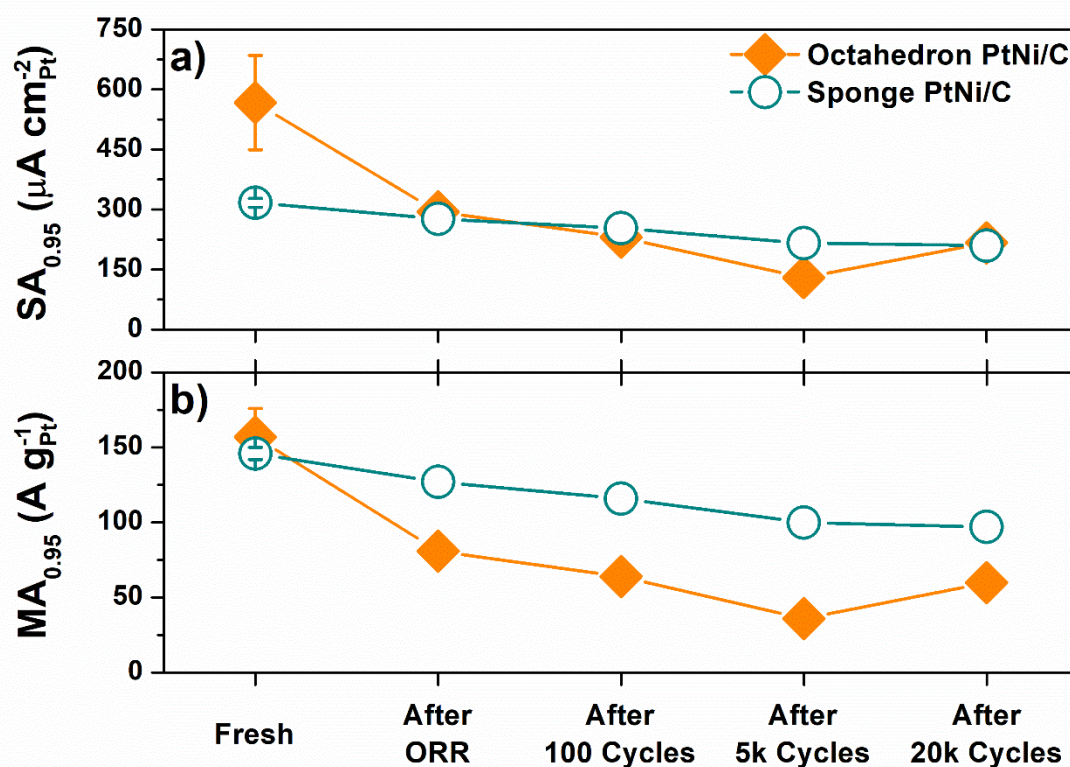
Figure 5.27: Variations of the specific (a) and the mass (b) activity for the ORR measured at E= 0.95 V *vs.* RHE for both Octahedron and Sponge PtNi/C electrocatalysts, before and after potential cycling between 0.6 and 1.0 V *vs.* RHE at T = 80 °C. The ORR activities were determined after correction for Ohmic losses and mass-transport in O_2-saturated 0.1 M $HClO_4$ at a potential sweep rate of 5 mV s^{-1} and a revolution rate of ω = 1600 rpm

CO_{ads} stripping voltammograms were also recorded before and after different numbers of potential cycles (**Figure 5.28**). Surprisingly, the surface reactivity toward CO_{ads} electrooxidation of the Octahedron PtNi/C was maintained during the first 5,000 potential

cycles, and then drastically lowered during the last 15,000 last potential cycles (see the variation of μ_1^{CO} as a function of the number of cycles plotted in **Figure 5.29**). This is in contrast with the ORR activity that gradually decreases during the first 5,000 potential cycles and then improved during the last 15,000 cycles, suggesting that the active sites for CO_{ads} electrooxidation and ORR are somehow independent from each other on Octahedron PtNi/C.
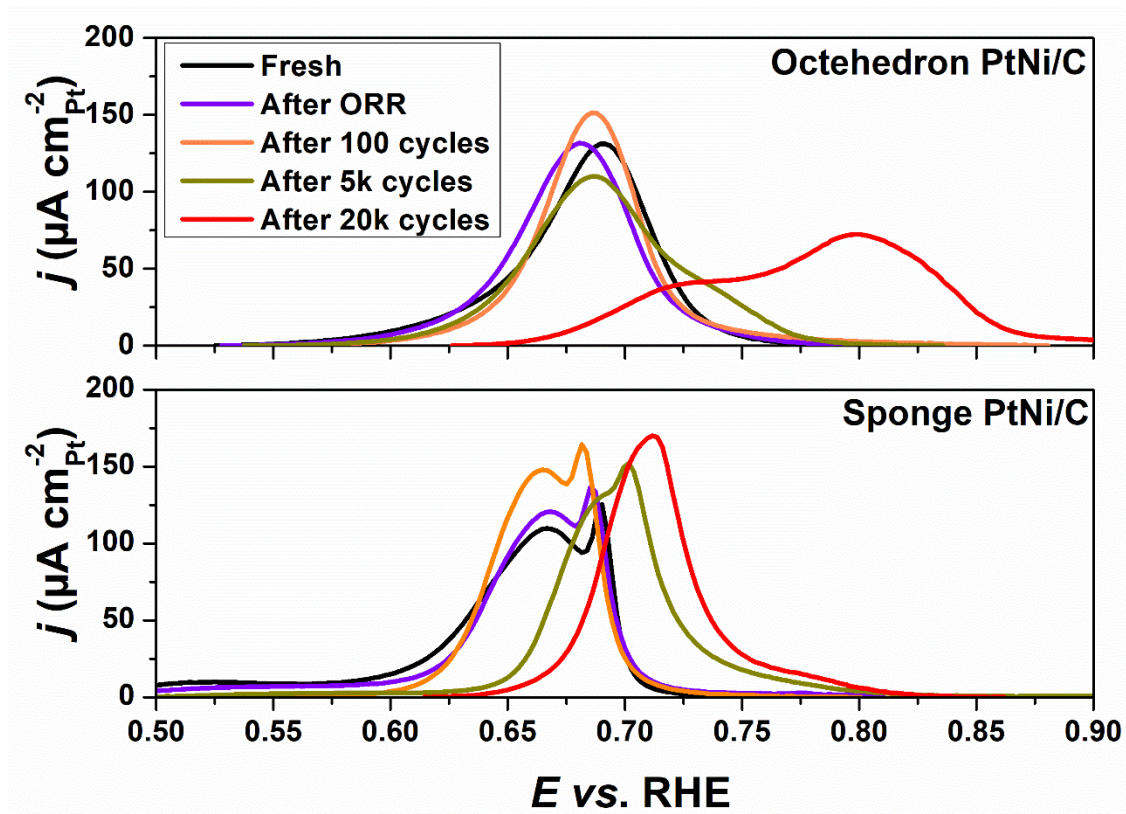
Figure 5.28: CO_{ads} stripping voltammograms recorded under Ar-saturated 0.1 M $HClO_4$ electrolyte at $v = 20$ mV s^{-1} for the Octahedron and Sponge PtNi/C before and after two consecutive ORR electrochemical characterizations and a different number of potential cycles.

Figure 5.28 and **Figure 5.29a** however show a more progressive decrease of the activity towards CO_{ads} electrooxidation in case of the Sponge PtNi/C catalyst. This is in line with the theory presented in **Chapter 4** of this manuscript showing the co-existence of oxophilic and oxophobic sites on structurally-disordered electrocatalysts. This more sustainable electrocatalytic activity for oxidation and reduction reactions is indirect evidence of the better durability of (at least some) structural defects.
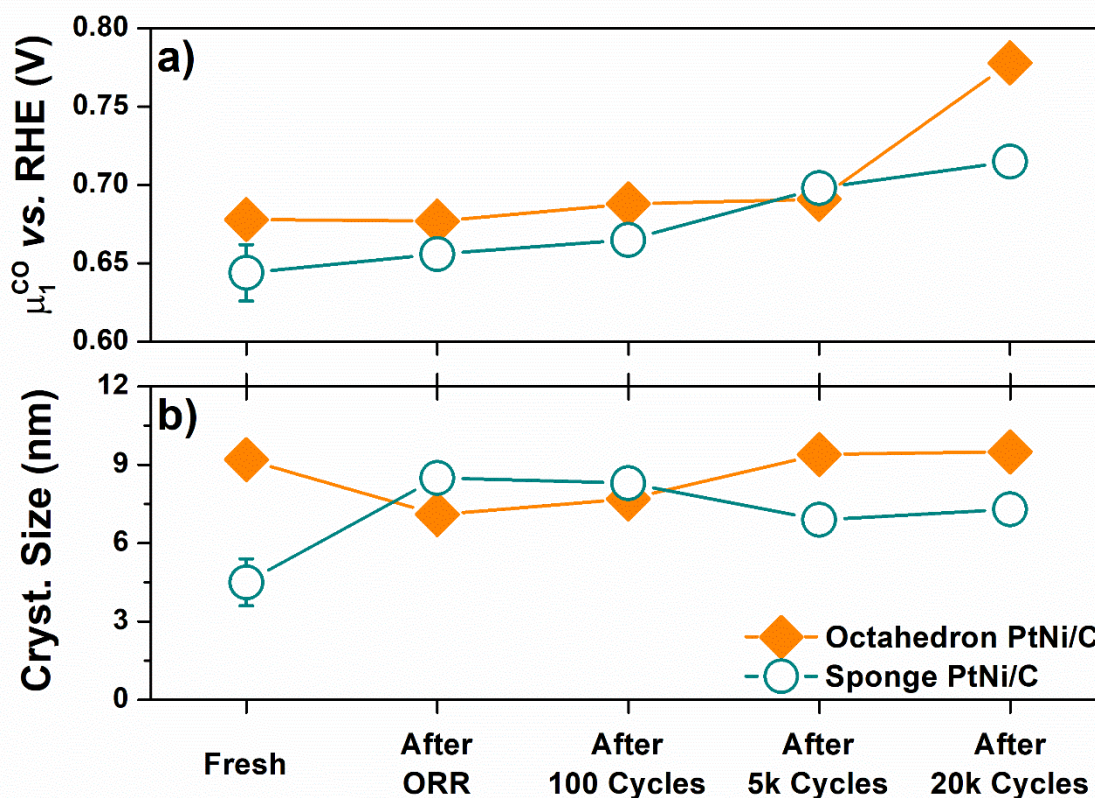
Figure 5.29: Variation of both μ_1^{CO} (a) and crystallite sze (b) for both Octahedron and Sponge PtNi/C electrocatalysts, before and after potential cycling between 0.6 and 1.0 V *vs.* RHE at $T = 80\ °C$.

Since the lattice parameter is key to ORR activity (strain effect), the evolution of the lattice parameter is plotted as a function of the number of potential cycles (**Figure 5.30a**). It is striking that in the case of the Sponge PtNi/C, more than 60 % of the lattice contraction was lost right after the first electrochemical characterization, this parameter remaining relatively constant later on. We explain this inability of the Sponge PtNi/C electrocatalysts to maintain the lattice strained (*i.e.* to protect Ni atoms from dissolution) due to its low crystallite size (< 5 nm). Indeed, as *ca.* 28 % of the atoms are located at the surface, removing the Ni atoms from the first 2-3 atomic layers during acid leaching [142] is here tantamount to the almost entire particle. Even more striking is the ability of the Octahedron PtNi/C to maintain its lattice strain while losing ORR activity (the latter being explained by the progressive loss of surface Ni and crystallographic orientation). It is noteworthy that the Sponge PtNi/C outweighs both the specific and the mass activity for the ORR of twice more strained (and close to the corresponding optimal value of 25 at. % Ni) Octahedral PtNi/C particles.

Finally, as presented in **Table 5.5** and **Figure 5.30b**, the depreciated electrocatalytic properties of the Sponge PtNi/C catalyst for electrooxidation and electroreduction reactions during potential cycling goes along with a diminution of the Surface Distortion value, the latter reaching a stable value.
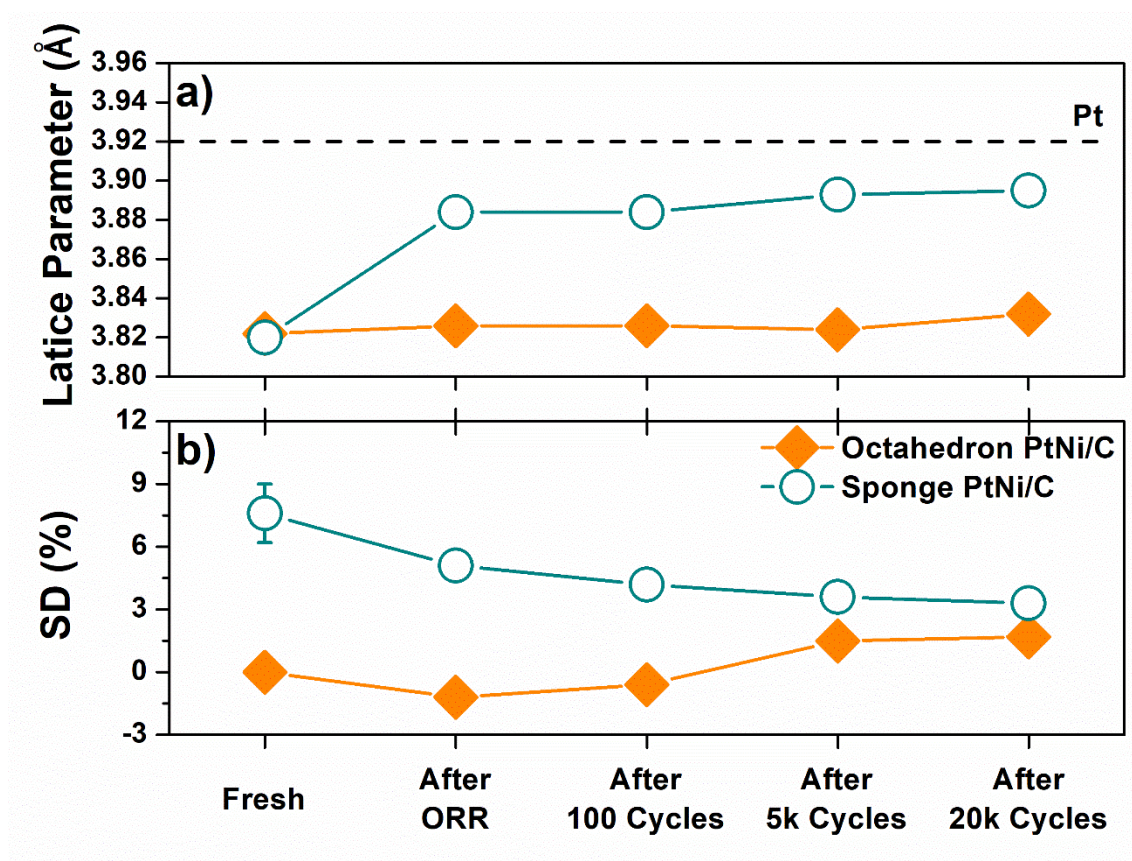
Figure 5.30: Evolution of the lattice parameter (a) and Surface Distortion (b) for both Octahedron and Sponge PtNi/C electrocatalysts, before and after a various amount of 50 mV s^{-1} potential cycles between 0.6 and 1.0 V *vs.* RHE at $T=$ 80 °C.

On the contrary, the progressive loss of electrocatalytic activity for the ORR of the Octahedron PtNi/C is marked by an almost null variation of the Surface Distortion (note that a negative value of the SD does not have physical sense, but is a consequence of the imperfection of the experimental microstrain-Ni relationship). However, the late increase of this parameter after 5,000 potential cycles somehow corresponds to the specific activity gain manifested by this catalyst. As suggested both by **Figure 5.30b** and **Figure 5.31**, whatever the initial surface state, the stable surface after 20,000 potential cycles seems to feature a positive Surface Distortion, halfway on the 'defective' branch of the 'reverse volcano'. Getting more insights about the possible various kinds of structural defects and both their stability and electrocatalytic activity properties would be a route to further improve this original and promising defects-based approach described in this work.
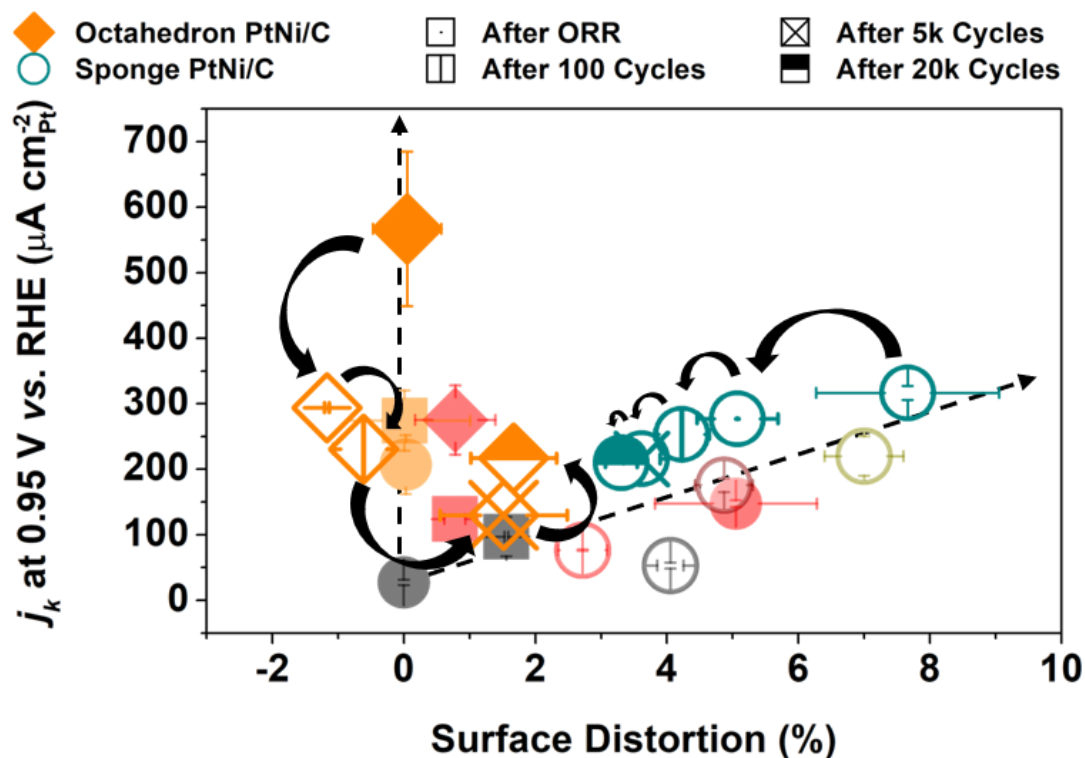
Figure 5.31: Relationship between the ORR specific activity measured at E= 0.95 V *vs*. RHE and the Surface Distortion for the electrocatalysts evaluated in this section. The initial trend introduced in **Figure 5.18** is superposed for the sake of comparison. Transparent data points correspond to **Figure 5.18** and **Figure 5.26b** while opaque symbols are related to Octahedron and Sponge PtNi/C catalysts before and after potential cycling between 0.6 and 1.0 V *vs*. RHE at T= 80 °C.

5.5 Conclusions

In this Chapter, physical and electrochemical markers of structural disorder were used to study the ORR activity of some of the best-performing nanocatalysts from the ORR electrocatalysis landscape. By exchanging knowledge and electrocatalytic materials with other European laboratories, global investigations were conducted on PtNi/C nanoparticles featuring various chemical composition, shape and morphology: from highly defective unsupported PtNi Aerogel to shape-controlled Pt$_3$Ni/C octahedra. Structural disorder manifested itself in any alloyed PtNi catalyst, the microstrain value being almost proportional to its Ni content: this translates that it is hardly possible to achieve perfect solid solutions from conventional synthesis methods operating at T < 300 °C. A simple model allowing to translate a 'bulk' property (microstrain) to a 'surface' property (Surface Distortion) was proposed. Complementary to microstrain, the Surface Distortion can help to disentangle the synergetic contributions of chemical composition,

crystallographic orientation and defectiveness for the CO_{ads} electrooxidation reaction. The μ_1^{CO} parameter could no longer be considered as a marker of structural defectiveness for catalysts featuring various Ni content and crystallographic orientation. Examining the ORR activity of one of the World's best performing nanocatalyst (Pt_3Ni/C nanooctahedra) has revealed the importance of the electrochemical protocol employed for the ORR activity measurement and the nonsense of an implicit 'record activity' race if a single unified measurement protocol is not used to determine the ORR activity worldwide. Finally, a closer look at the adsorption properties of the different PtNi/C electrocatalysts has unambiguously confirmed the limitations of the standard 'extended surfaces' approach to nanomaterials. In particular, the existence of co-adsorbed under-potentially H and OH species in the potential region comprised between 0.35 and 0.40 V *vs*. RHE is postulated for highly active and defective PtNi catalysts, a result that is in total contrast with the common beliefs. These unprecedented chemisorption properties were bridged to the physical Surface Distortion parameter, which provides a simple and versatile tool to quantify surface defectiveness. The comparison of the ORR activity of PtNi/C electrocatalysts synthesized from 'defects-do-catalysis' to that of 'extended surface' approach indicates superior initial ORR performance for the second. However, acidic treatment and accelerated stress tests revealed the superiority of the 'defects-do-catalysis' approach thereby opening a route for highly active and more durable ORR electrocatalysts.

6 GENERAL CONCLUSION AND OUTLOOK

This Ph.D. thesis was focused on the development of highly active and durable electrocatalysts for the ORR. In an alarming climatic and energetic context, where energy production and transportation sectors need breakthroughs, the PEMFC technology is likely to play a key role as it is a clean alternative to combustion engines. Because high loadings of Pt (an expensive and scarce metal) are needed to electrocatalyse the sluggish cathodic oxygen reduction reaction, hollow and/or porous nanocatalysts represent a promising approach to decrease the overall PEMFC cost and facilitate the massive market penetration of this technology. We investigated the detailed synthesis mechanism of this novel class of catalysts, rationalized their surface reactivity and discovered that the hollow structure is a lever to improve the electrocatalytic activity of Pt for both electrooxidation and electroreduction reactions. This statement was the starting point of a thrilling research project that has been rhythmed by pleasant collaborations briefly summarized below.

Through the collaboration with Dr. Jakub Drnec from the beamline ID31 at the ESRF, Dr. Jaysen Nelayah of MPQ laboratory and Dr. Pierre Bordet from Louis Néel Institute, a methodology based on powerful and cutting-edge techniques (including HRTEM, STEM-X-EDS, WAXS, SAXS, Rietveld refinement and PDF analysis of WAXS data) was developed to unveil the mechanism of formation and growth of hollow PtNi/C nanoparticles at the atomic scale. We showed that:

(i) The facile, surfactant-free and 'one pot' synthesis of the hollow PtNi/C nanoparticles proceeds via sequential steps. Because $Pt(NH_3)_4Cl_2.(H_2O)$ salt precursor slowly decomposes in water, the initial reduction of Ni^{2+} ions by $NaBH_4$ is kinetically promoted. The Ni/C nanoparticles act as sacrificial template for the sequential reduction of Pt^{2+} cations *via* galvanic displacement and/or chemical reduction with $NaBH_4$, resulting in an intermediate Ni-rich core@Pt-rich shell structure. The Pt-rich shell features a 'dome' shape with nanopores and is composed of ~3 nm large crystallites interconnected by grain boundaries. The hollow morphology is finally obtained by dissolution of the Ni-rich core, directly through the Pt-rich shell pores or *via* the nanoscale Kirkendall effect.

(ii) The hollow PtNi/C nanoparticles feature better ORR activity than solid PtNi/C nanoparticles of similar composition and crystallite size. A collapse of the

PtNi shell and the associated sintering of the crystallites (decrease of the density of grain boundaries) during thermal annealing leads to a dramatic loss of ORR performance.

(iii) The ORR activity of hollow PtNi/C nanoparticles varies non-linearly with the values of microstrain (also referred to as *local lattice strain*) extracted from the Rietveld refinement of WAXS patterns. The microstrain values are representative of the local deviations of the atom from their ideal position in the crystal cell (local structural defects).

This structure-activity relationship was further explored by synthesizing a library of nanocatalysts featuring various morphologies (solid, core@shell, or sponge-like), fixed low Ni content (~15 at. %) and crystallite sizes (< 5 nm). The results showed that:

(i) Nanocatalysts containing grain boundaries feature higher value of microstrain. However, the as-measured microstrain (raw microstrain) is influenced by the crystallite size (being overestimated for small crystallites) and needs to be corrected. We introduced a new parameter (the corrected microstrain) which takes into account the effect of dispersion, *i.e.* the fact that the structural disorder created by a grain boundary joining two crystallites is more or less compensated depending on the crystallite size.

(ii) Because the CO_{ads} stripping voltammograms depend on the crystallite size, the surface composition and the crystallographic orientation (all these parameters were fixed) but also on the density of structural defects, a new electrochemical marker (the average CO_{ads} oxidation potential, μ_1^{CO}) was introduced to quantify the structural disorder.

(iii) A near linear relationship was observed when the specific activity for the ORR was plotted as a function of the corrected microstrain or as a function of μ_1^{CO}, showing by two different approaches the positive impact of structural disorder on the ORR kinetics for various PtNi/C nanostructures.

(iv) Microstrained surfaces feature adjacent contracted (oxophobic) and relaxed (oxophilic) lattice regions, as showed by DFT calculations. These peculiar properties explain why an increase of the density of structural defects (microstrain) simultaneously enhance the electrocatalytic activity for the oxygen reduction reaction, but also for the electrooxidation of a monolayer of CO_{ads}, or the electrooxidation of methanol/ethanol.

Next, through a fruitful collaboration with the Electrochemistry Laboratory from the Paul Scherrer Institute (PSI), Switzerland, the Physical Chemistry group from TU Dresden, Germany and the Electrochemical Catalysis, Energy and Material Science group from TU Berlin, Germany, we extended our findings to advanced PtNi/C electrocatalysts from the ORR electrocatalysis landscape (spherical, cubic, octahedral, aerogel). Our results showed that:

(i) Alloying Pt with Ni induces microstrain, the value of which is nearly proportional to the Ni content. This structural disorder is mainly located in the bulk of the nanoparticle and so mildly influences its electrocatalytic properties. The former model was then refined and a new parameter (the 'Surface Distortion') was introduced to quantify the surface defectiveness independently from the Ni content.

(ii) For nanocatalysts featuring different Ni content and preferential orientation of the facets, the μ_1^{CO} value could no longer be used to quantify the density of structural defects. However, their benefitial effect on the CO_{ads} monolayer electrooxidation kinetics can be disentangled using the microstrain and the Surface Distortion.

(iii) A closer look at the adsorption properties of the different electrocatalysts has unambiguously confirmed that nanomaterials cannot fully reproduce the reactivity of extended surfaces. Especially, we provide evidence of co-adsorption of H and OH species in the H_{upd} region for highly defective catalysts. This was experimentally translating by $Q_{CO}/2Q_H$ ratios below 1, in total contrast with the trends usually expected for bimetallic surfaces.

(iv) These unprecedented adsorption properties can be predicted from the previously introduced Surface Distortion, showing the unambiguous link between catalyst structure and surface reactivity and revealing a new class of electrocatalysts.

(v) Comparison of ORR activity and structural disorder degree (through both the physical Surface Distortion and/or electrochemical $Q_{CO}/2Q_H$ ratio) for the different electrocatalysts before and after both acidic treatment and

accelerated stress tests presented the 'defects-do-catalysis' approach as a viable and sustainable alternative to the classical 'extended-surface' approach.

We would like to emphasize that the values of μ_1^{CO}, Surface Distortion and $Q_{CO}/2Q_H$ used in this manuscript to quantify structural disorder rest on numerous hypothesis, and their relevance are debatable and must be discussed. However, we believe this work finds robustness in the combination of both these new and indirect physical and electrochemical markers with classical and direct physical, chemical and electrochemical markers toward converging conclusions.

Finally, this manuscript ends with some perspectives that we would have liked to tackle. Some questions also remain unanswered:

(i) Structural defects, implemented *via* dealloying and/or grain boundaries have a positive impact on electrocatalytic properties, however the exact nature of these defects remains to a large extent unknown. Is structural disorder induced by the 'place exchange' mechanism comparable? Does it lead to quantifiable microstrain values?

(ii) More generally speaking, can we introduce a given structural defect in a reproducible manner on an extended surface and quantify its effect on the kinetics of a given reaction?

(iii) Is the gain in ORR activity a mean to access the density of microstrained catalytic sites?

(iv) Based on our experimental data and reports from literature, the electronic structure of defective sites modifies their affinity with oxygenated species (O, HO, HOO) and leads to a mix of oxophilic and oxophobic sites: is this approach a way to break the scaling relations?

APPENDIX 1: MATERIALS AND METHODS

Materials Synthesis

Reference Electrocatalyst

A Pt/Vulcan XC72® catalyst with a Pt weight fraction (wt. %) of 20% (TEC10V20E) was purchased from Tanaka Kinkinzoku Kogyo (TKK) and used as reference material without any treatment.

Synthesis of Monodisperse Solid PtNi/C Nanoparticles

To synthesize solid PtNi/C nanoparticles, 53 mg of $H_2PtCl_6.6H_2O$ (99.9 % metals basis, Alfa Aesar), 24 mg $NiCl_2.6H_2O$ metal salts (Putratronic® 99.9995 %, Alfa Aesar) and 118 mg of monosodium citrate (≥99 %, Roth) were first dissolved in a vial containing a 20 mL mixture of deionized water and ethylene glycol (EG) (Rotipuran® ≥ 99.9 %, Roth) (vol. ratio 1:1). Then, 74 mg of carbon black (Vulcan XC72®, Cabot) were dispersed by sonication in a separated vial containing also 20 mL of 1:1 EG:water mixture. The contents of each vial were then mixed in 20 mL of pure EG, leading to a 2:1 EG:water volumic ratio. The pH of the obtained mixture was the adjusted to 10 using a 0.5 M NaOH (Suprapur® 99.99 %, Merck) solution (diluted in 1:1 EG:water mixture). The resulting suspension was afterwards kept under vigorous stirring for 1 hour under argon atmosphere before being refluxed at $T = 160\ °C$ for 3 hours. The solution was allowed to cool down to room temperature under open air atmosphere for 12 hours with continuous stirring [237]. The pH of the mixture was then adjusted to 3 using a 0.5 M H_2SO_4 (Suprapur® 96 %, Merck) aqueous solution and left for 24 extra hours. Finally, the solution was filtered and copiously washed with deionized water before being dried at $T = 110\ °C$ for 1 hour.

Synthesis of Agglomerated Solid PtNi/C Nanoparticles

Agglomerated solid PtNi/C nanoparticles were obtained by using the same protocol as for the synthesis of monodisperse PtNi/C nanoparticle but without the addition of monosodium citrate. First, 53 mg of $H_2PtCl_6.6H_2O$ (99.9 % metals basis, Alfa Aesar) and 4.3 mg of $NiCl_2.6H_2O$ metal salts (Putratronic® 99.9995 %, Alfa Aesar) were dissolved in a vial containing a 20 mL mixture of deionized water and ethylene glycol (EG) (Rotipuran® ≥ 99.9 %, Roth) (volume ratio 1:1). 79 mg of carbon black support particles

(Vulcan XC72®, Cabot) were dispersed by sonication in a separated vial containing also 20 mL of 1:1 EG:water mixture targeting 20 wt. % Pt loading. Then, the contents of each vial were mixed in 20 mL of pure EG, leading to a 2:1 EG:water volume ratio. The pH of the obtained mixture was then adjusted to 10 using a 0.5 M NaOH (Suprapur® 99.99 %, Merck) solution (diluted in 1:1 EG:water mixture). The resulting suspension was kept under vigorous stirring for 1 hour under argon atmosphere before being refluxed at $T =$ 160 °C for 3 hours. The solution was then allowed to cool down to room temperature under open air atmosphere for 12 hours with continuous stirring [237]. The pH of the mixture was then adjusted to 3 using a 0.5 M H_2SO_4 (Suprapur® 96 %, Merck) aqueous solution and left for 24 extra hours. Finally, the solution was filtered and copiously washed with deionized water before being dried at $T =$ 110 °C for 1 hour.

Synthesis of Ni/C Nanoparticles

Ni/C nanoparticles were synthetized according to a protocol adapted from Ref. [165]. Briefly, 236 mg of sodium citrate (≥ 99 %, Roth), 171 mg of carbon Vulcan XC72® (Cabot) and 174 mg of $NiCl_2.6H_2O$ metal salts (99.9 % metals basis, Alfa Aesar) were mixed to 20 mL ethylene glycol (EG) (Rotipuran® ≥ 99.9 %, Roth). A 5 wt. % solution of KOH (99.99 % trace metals basis, Sigma Aldrich) in EG was then added dropwise to reach a pH ~ 9-10. The solution was then heated at $T =$ 160 °C for 20 hours in open atmosphere. After natural cooling, the final product was collected by filtration and dried at $T =$ 110 °C for 45 minutes. This protocol targeted a Ni weight fraction of 20 %, but AAS and TEM analysis revealed that the resulting powder featured only 7 wt. % of Ni and high surface area carbon support was fully covered with ~2 nm Ni nanoparticles.

Synthesis of Ni@Pt/C Nanoparticles

Ni@Pt/C nanoparticles were synthetized according to a protocol adapted from Ref. [165]. Briefly, 1.66 mL of a 20 mg mL^{-1} $H_2PtCl_6.6H_2O$ (99.9 % metals basis, Alfa Aesar) aqueous solution was mixed to 15 mL EG (Rotipuran® ≥ 99.9 %, Roth). A 5 wt. % solution of KOH (99.99 % trace metals basis, Sigma Aldrich) in EG was then added dropwise to reach a pH ~9-10. Then, 50 mg of 7 wt. % Ni/C nanoparticles synthetized according to the previously described protocol were added to the mixture. The solution was heated at $T =$ 160 °C for 6 hours in open atmosphere. After cooling at room temperature, the final product was collected by filtration and dried at $T =$ 110 °C for 45

minutes. This protocol targets 5.6 wt. % Ni in the final product, but AAS revealed a final Ni weight fraction of 1 wt. % indicating a loss in Ni content during the deposition of Pt, due to a combination of chemical reduction and galvanic displacement.

Synthesis of Hollow PtNi/C Nanoparticles

154 mg of $Pt(NH_3)_4Cl_2$ (Alfa Aesar, Specpure) and 180 mg of $NiCl_2$ (Fluka, > 98.0 %) were first mixed with 300 mg Vulcan XC72® (Cabot), 10 mL of ethanol and 140 mL of de-ionized water (Millipore). An aqueous solution of $NaBH_4$ (Aldrich 99.99 % - 5.5 mmol, 0.22 M) was then added at a rate of 5 ml min^{-1} and stirred for 1 h under magnetic stirring at room temperature ($T = 25 \pm 2$ °C). The resulting mixture was filtered, thoroughly washed by de-ionized water and dried for 45 minutes at $T = 110$ °C. The catalysts powder was then acid-treated for $t = 22$ h in a stirred 1 M H_2SO_4 (Suprapur® 96 %, Merck) solution at $T = 20$ °C and then filtered, washed and dried again following the same procedure.

Synthesis of Sponge PtNi/C Nanoparticles

Sponge PtNi/C nanoparticles were synthetized via an 'in-house' polyol method. 120 mg of Vulcan XC72® (Cabot), 54mg of $Pt(NH_3)_4Cl_2$ (Premion® 99.995% metals basis, Alfa Aesar) and 37 mg $NiCl_2.6H_2O$ metal salts (99.9 % metals basis, Alfa Aesar) were mixed in 20 mL ethylene glycol. After setting the pH to 9-10 by dropwise addition of a 5 wt. % solution of KOH in EG (Rotipuran® ≥ 99.9 %, Roth), the solution was heated in reflux at $T = 200$ °C for 20 hours. The final product was allowed to cool in open atmosphere and was then collected by filtration and dried at $T = 110$ °C for 45 minutes. The catalysts powder was then acid-treated for $t = 22$ h in a stirred 1 M H_2SO_4 (Suprapur® 96 %, Merck) solution at $T = 20$ °C and then filtered, washed and dried again following the same procedure.

Synthesis of PtNi/C Octahedra

To prepare PtNi/C octahedra, we used the method originally introduced by *Zhang et al.* [75]. Briefly, $Pt(acac)_2$ (160 mg, Alfa Aesar, Pt 48.0 % min) and $Ni(acac)_2$ (240 mg, Alfa Aesar, 95 %) salts precursors were dissolved in oleylamine (48 mL, Sigma-Aldrich, ≥ 98 %) and oleic acid (32 mL, Alfa Aesar, tech. 90%). The solution was then deaerated with N_2 and heated at 60 °C for 20 min. Afterwards, the solution was further heated to 130 °C at ~5 °C per minute and $W(CO)_6$ reducing agent powder (560 mg, Alfa Aesar, 97 %) was

quickly introduced and N_2 flow stopped. The solution was further heated to 230 °C and stirred for 45 min. The as produced octahedra were collected by centrifugation: basically, after the solution has cooled down, 60 mL ethanol and 20 mL toluene (Roth, $\geq$ 99.8 %) were added to the solution which was further divided in 4 centrifugation tubes, and centrifuged at 8000 rpm for 15 min. The as-separated NPs were re-dispersed in 20 mL toluene, while 160 mg XC-72R was ultrasonically dispersed in 20 mL toluene in a separated vial. The carbon and NPs were then mixed and dispersed with an ultrasonic horn for 30 min. The final product was finally centrifuged again (same conditions). To wash the NP the supernatant was replaced with ethanol and then centrifuged 3 consecutive times and finally freeze-dried.

Synthesis of PtNi/C Cube

To prepare PtNi/C cubes, we used the method originally introduced by Zhang *et al.* [75]. Briefly, Pt(acac)$_2$ (80 mg, Alfa Aesar, Pt 48.0 % min) salt precursor was dissolved in oleylamine (36 mL, Sigma-Aldrich, $\geq$ 98 %) and oleic acid (4 mL, Alfa Aesar, tech. 90%). The solution was then deaerated with N_2 and heated at 80 °C for 15 min. Afterwards the solution was further heated to 130 °C and $W(CO)_6$ reducing agent powder (200 mg, Alfa Aesar, 97 %) was quickly introduced and N_2 flow stopped. The solution was then heated from 130 °C to 200 °C, at a rate of ~ 4 °C min^{-1}. During the heating process a dropwise addition (107 µL min^{-1}) from a stock solution of 238 mg NiCl$_2$.6H$_2$O (Alfa Aesar, 99.9 % metals basis) dissolved in 10 mL Oleylamine (Sigma-Aldrich, $\geq$ 98) and 10 mL Oleic acid (Alfa Aesar, tech. 90%). The temperature was then further increased to 240 °C and maintained during 15 mins. The process to collect, support and wash the NPs was the same that for the PtNi octahedra.

Synthesis of Pt/C Cube

Cubes Pt/C were obtained by the exact same protocol that for the PtNi octahedra, but without the addition of a Ni salt precursor.

Synthesis of Sphere PtNi/C

Sphere PtNi/C were prepared using a protocol adapted from Gan *et al.* [213], also referred at the 'hot injection' method. In brief, Ni(acac)$_2$ metal precursor (77 mg, Alfa Aesar, 95 %) and 92 mg of 1, 2-tetradecanediol (TDD) reducing agent (Sigma-Aldrich 90 %) were dissolved in dibenzylether (30 mL, Sigma-Aldrich, $\geq$ 98.0 %) in the presence of

oleylamine (0.3 mL, Sigma-Aldrich, ≥ 98) and oleic acid (0.3 mL, Alfa Aesar, tech. 90%). After the solution was heated at 80 °C under N_2 flow for 30 min, the temperature was further increased to 200 °C. At this temperature, a preparation of Pt(acac)$_2$ (40 mg, Alfa Aesar, Pt 48.0 %) in 1, 2-dichlorobenzene (1.4 mL, Alfa Aesar, 99 %) was quickly introduced in the reactor. The solution was kept under continuous stirring at 200 °C for 1 hour. The process to collect, support and wash the NPs was the same that for the PtNi octahedra.

XRD Measurements

We used XRD to investigate the structural properties of the synthesized electrocatalysts. Depending on the technique used (WAXS, SAXS) and refinement (Rietveld, PDF) different crystallographic properties were extracted such as Pt lattice parameter, the crystallite size, the degree of microstrain or the distribution of inter-atomic distances. In a standard XRD measurement, the X-ray scattering arises from a crystal and produces Bragg peaks (diffraction peaks) as a function of the scattering angle (or spots or rings in 2D patterns) according to the Bragg's law:

$$n\lambda = 2dsin(\theta) \tag{A1.1}$$

Where n is an integer, λ is the wavelength of the radiation, d the interplanar distance between atomic planes and θ the angle between the incoming wave and the lattice plane.

The basic difference between WAXS and SAXS is the length scale investigated by each technique: WAXS detects order at the near atomic scale through the measurement of high angle reflexions (high θ) from inelastic scattering with the crystal lattice while SAXS probes larger structures based on electron density differences and elastic scattering within the crystal, and can consequently provide information about the size and shape of the nanoparticles and the eventual presence of pores.

Various experimental setups have been used along this Ph.D. thesis, depending on the problem investigated. They are described below.

Synchrotron WAXS Measurements (*Ex-Situ*)

The *ex-situ* synchrotron WAXS (and SAXS) measurements were used to characterize catalyst powders and were performed by Dr. Jakub Drnec at ID31 beamline of European Synchrotron Radiation facility (ESRF) in Grenoble, France. The high energy X-ray radiation (61 keV or 0.20 Å) was focused on the powder sample contained in a 1 mm diameter Kapton capillary, and the scattered signal was collected with a Dectris Pilatus CdTe 2M detector positioned 300 mm behind the sample. The size of the beam at the sample position was 4 × 30 μm (vertical × horizontal). The energy, detector distance and tilts were calibrated using a standard CeO_2 powder and the 2D diffraction patterns were reduced to the presented 1D curves using pyFAI software package [238] (an example is provided **Figure A1.1** for the reference Pt/C TKK catalyst).
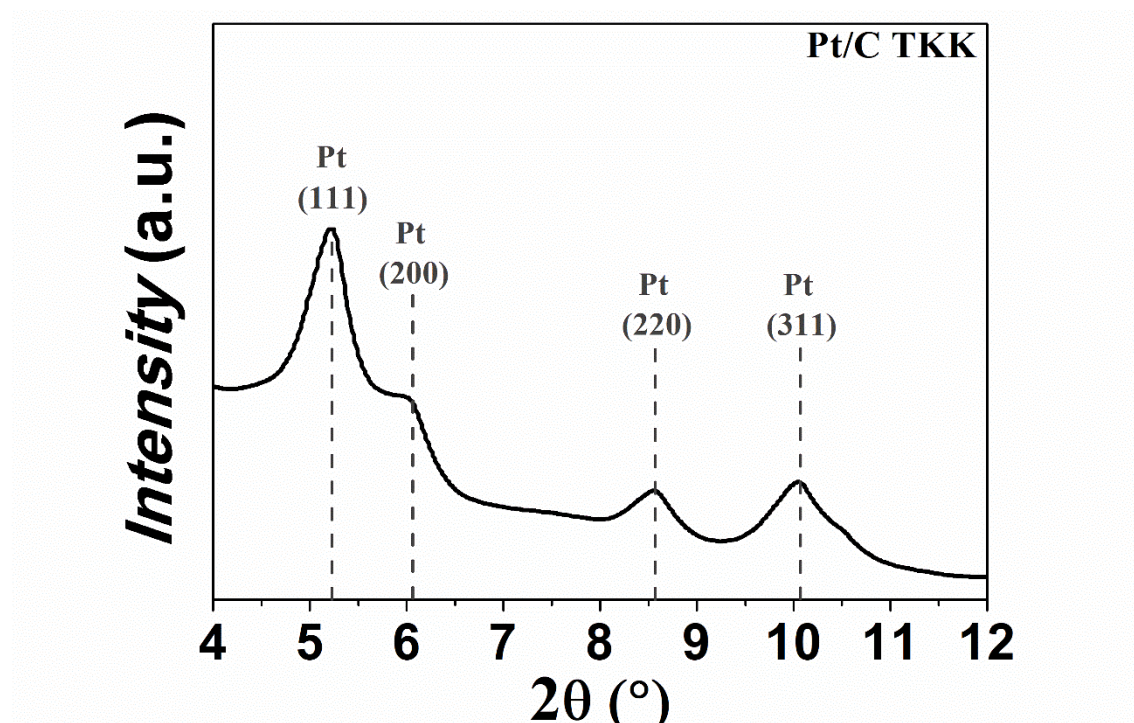
Figure A1.1: Synchrotron WAXS pattern of the reference Pt/C TKK in *ex-situ* configuration.

Synchrotron WAXS Measurements (*Operando*)

For the monitoring of the Hollow PtNi/C synthesis discussed in Chapter 3, the synthesis was performed in a poly(methyl methacrylate) cuvette of 4.5 × 1.25 × 1.25 cm (Plastibrand) placed perpendicularly to the X-ray beam, and used as a synthesis reactor. The metal and solution quantities (see Synthesis of Hollow PtNi/C catalyst above) were adapted to the reduced volume of the reactor. Magnetic stirring was maintained

throughout the whole duration of the syntheses and the dropwise NaBH₄ addition performed using a remote-controlled syringe (see **Figure A1.2**). The radiation from one undulator was monochromatized with a multilayer monochromator (bandwidth 0.3 %) to an energy of 60.0 keV ($\lambda = 0.207$ Å). The X-ray beam was focused with two transfocators to a size of 5 μm x 20 μm (vertical x horizontal relative to the plane of the accelerator ring) and the flux was 5×10^{12} photons s^{-1} at the sample position. The data were collected using a PerkinElmer 2D detector and azimuthally integrated using the pyFAI software package [238].
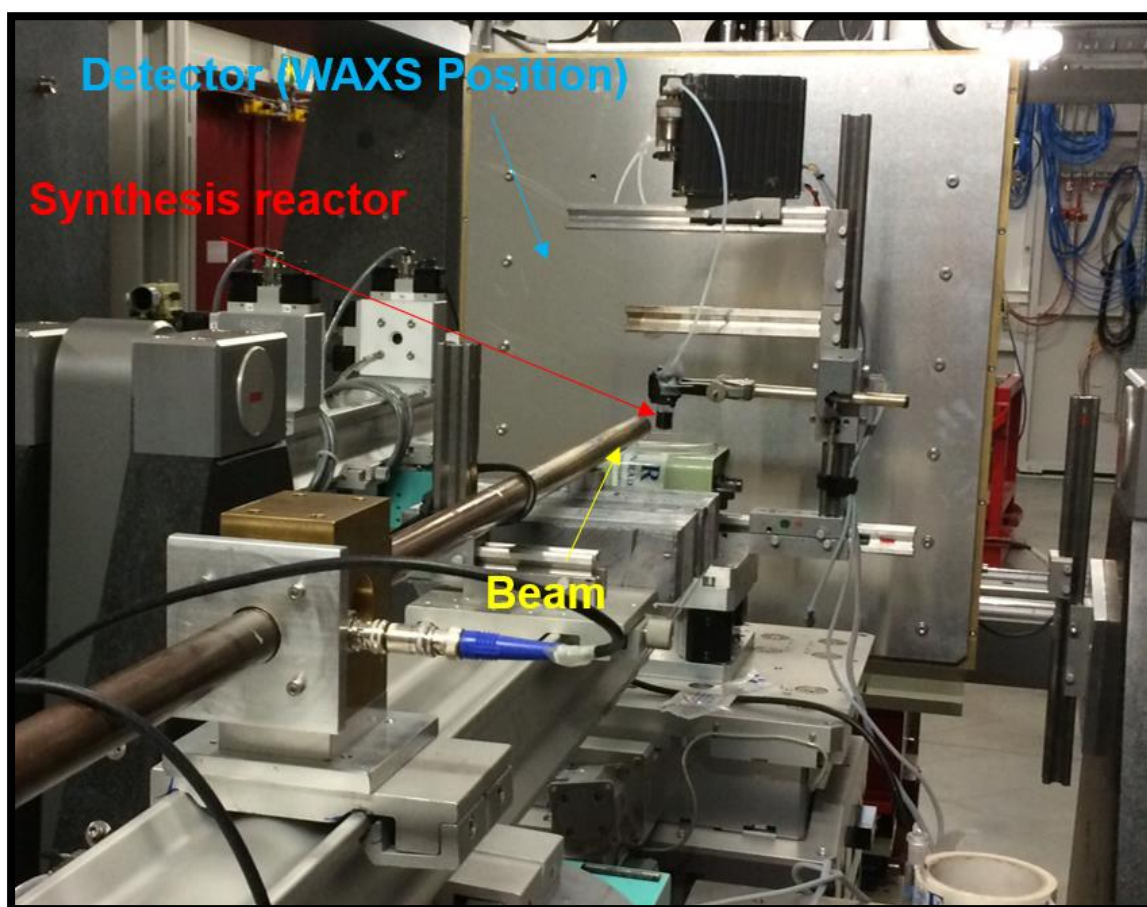
Figure A1.2: Picture of the *Operando* Synchrotron WAXS setup at the ID31 beamline, ESRF (November 2015).

SAXS Measurements (*Operando*)

In SAXS measurements, the experimental setup was similar that for WAXS, except that the detector was moved to a higher distance from the sample and a flight tube (inner part

under vacuum) between the sample and the detector was inserted to limit further air-induced scattering of the diffracted light (see **Figure A1.3**).
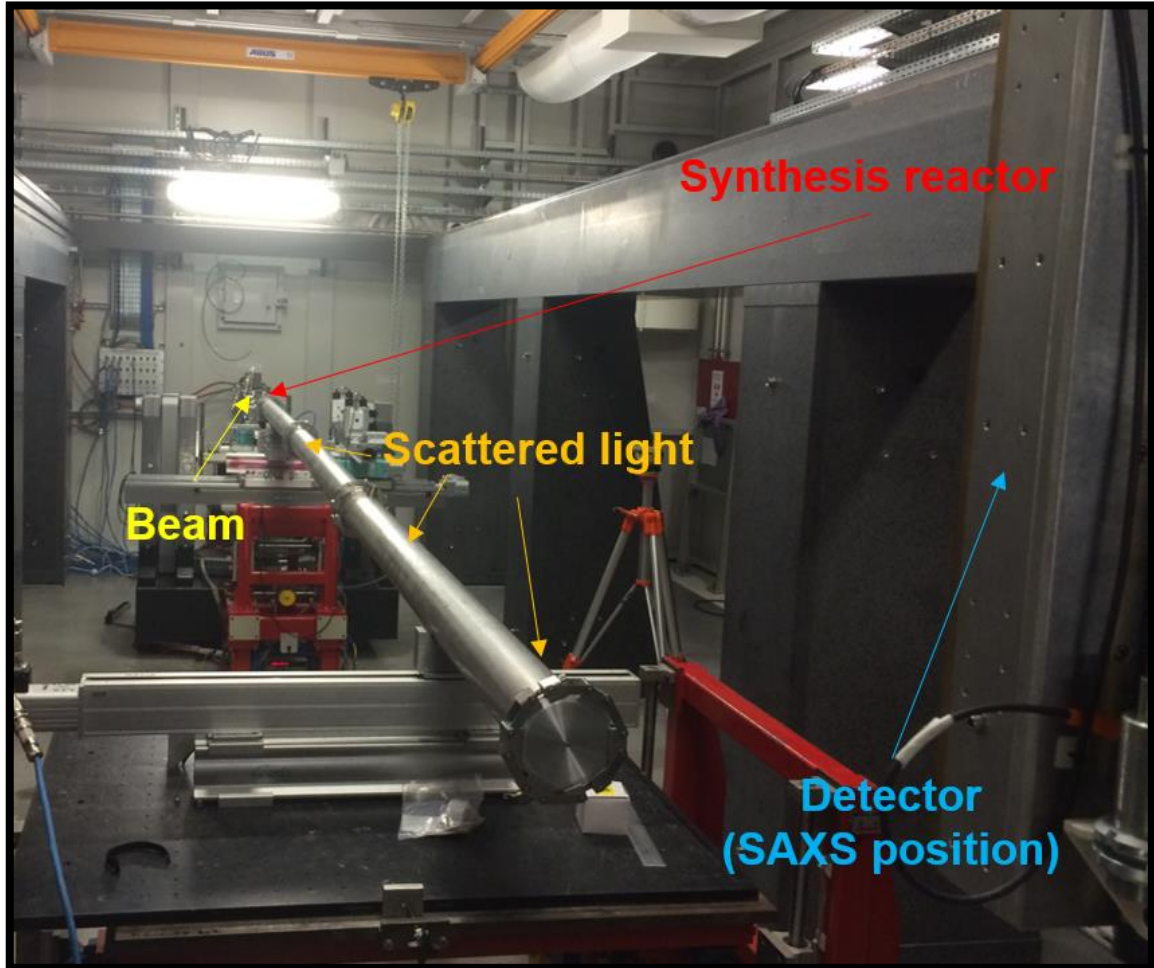
Figure A1.3: Picture of the *Operando* Synchrotron SAXS setup at the ID31 beamline, ESRF (November 2015).

The scattering intensity, I(p), at small angles can be described as:

$$I(q) \sim P(q) \cdot S(q) \tag{A1.2}$$

Where P(q) is the form factor that describes the shape of the individual NPs and S(q) is the structure factor of the nanoparticle assembly. For diluted solutions and particles with spherical symmetry (which is fair assumption in the case of this study), S(q) = 1 and **Equation (A1.2)** reduces to $I(q) \sim P(q)$. Hence, $I(q)$ provides direct information about the shape and the scattering length density distribution of the growing nanoparticles [239].

In this study, the form factor was a Fourier transform of the autocorrelation function (square of the form factor amplitudes):

$$P(q) = \langle |F(\vec{q})|^2 \rangle = \left\langle \left| \int_V \Delta \rho e^{(-i\vec{q}\vec{r})} d\vec{r} \right|^2 \right\rangle \tag{A1.3}$$

Where $\Delta\rho$ is a scattering length density difference between the nanoparticles and the solvent. Since the studied nanomaterials featured an inhomogeneous scattering length density distribution, we considered a model based on monodisperse spherical NP with a core-shell structure and $P(q)$ was substituted by an analytical expression [240]. This idealized model was then used to fit the SAXS data, and the scattering length density of the core and the shell, the core radius, the shell thickness and scaling were used as fitting parameters.
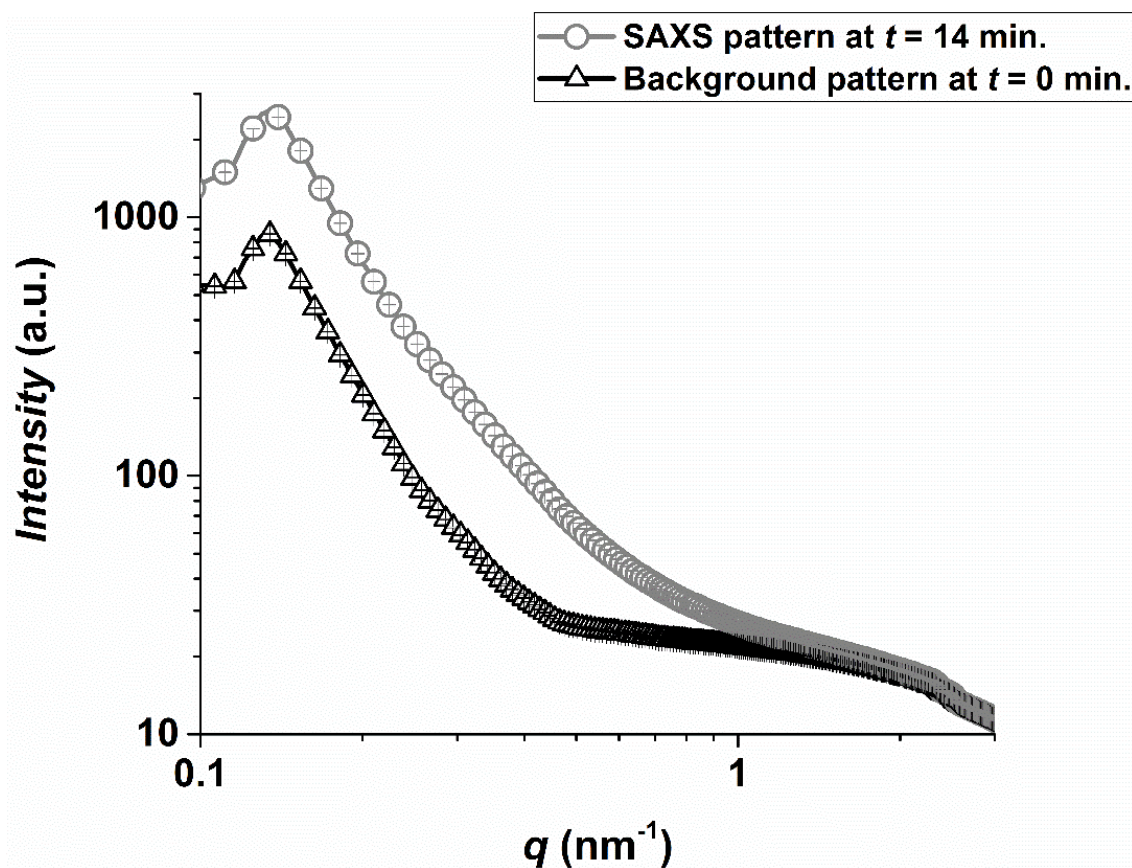
Figure A1.4: Measured SAXS pattern at $t = 0$ min and $t = 14$ min. Black curve: the last SAXS pattern taken before the beginning of the synthesis, which was used as a background. Grey curve: the SAXS curve measured at $t = 14$ min before the background subtraction. The error bar is the standard deviation

The *operando* SAXS data were analysed using a SAXS utilities package. The raw images were radially integrated with the PyFAI software package. The last SAXS pattern

measured before the adjunction of the $NaBH_4$ reducing agent solution (start of the synthesis) was subtracted from the subsequent patterns (**Figure A1.4**).

This subtraction did not completely eliminate the signal from the carbon support ($q = 0.13$ nm^{-1}), thereby suggesting that the structure of the carbon support changed during the first minutes of the synthesis, and stabilized later on.

The background corrected patterns were fitted using the same SAXS utilities package and a core/shell NP model (**Figure A1.5**). To avoid considering the peak at $q = 0.13$ nm^{-1} resulting from the carbon support, only the region shown in **Figure A1.5** was used to fit the form factor. Other models, such as solid nanoparticle, were also tested but resulted in unrealistic parameters.

Figure A1.5: Example of a fit of SAXS pattern. Grey squares: the background-corrected SAXS pattern at $t = 14$ min. Dark yellow curve: the fit using the core/shell NP model described in the main text.

Rietveld Refinements

Rietveld refinements were conducted by Dr. Pierre Bordet at Louis Néel Institute in Grenoble, France and were used to extract the crystallite size, lattice parameter and microstrain from the WAXS patterns *via* the Fullprof software [241] for 2θ values comprised between 3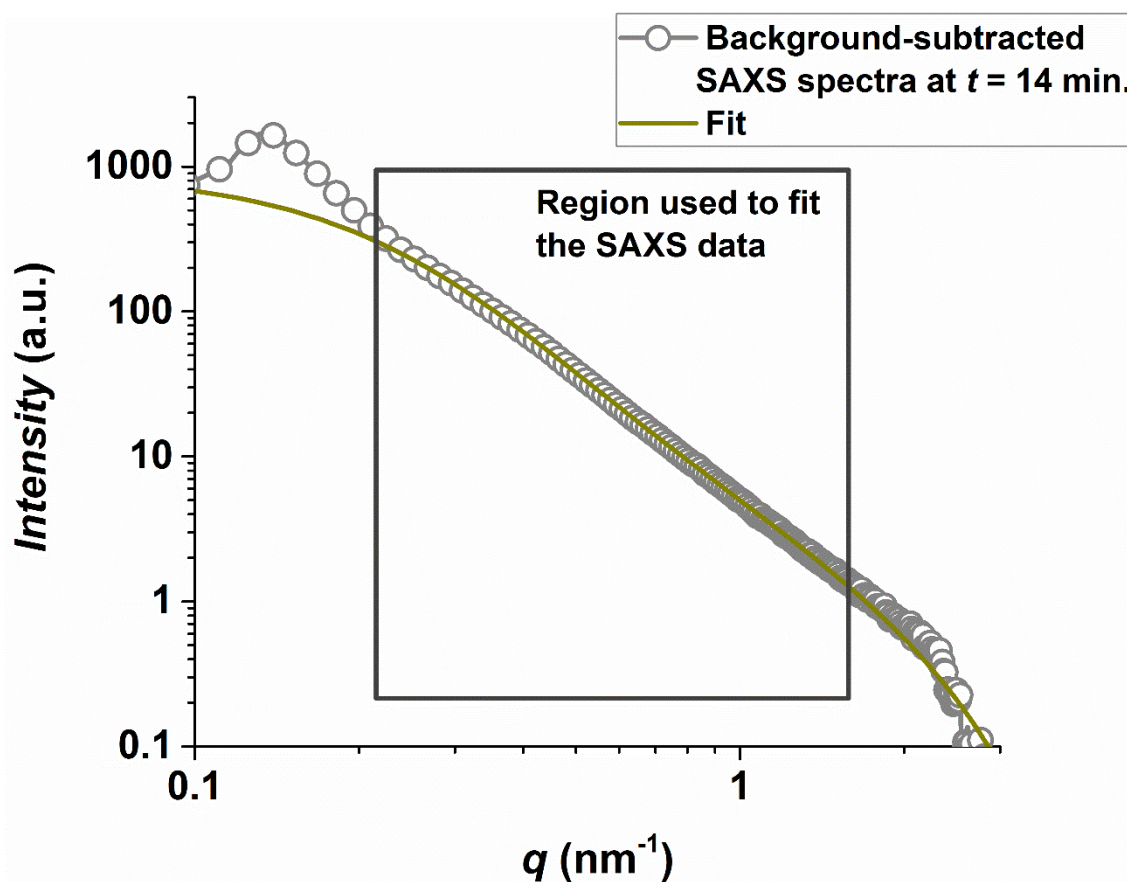.5 and 30°, using the *Fm3m* structure of Pt metal. The instrumental resolution function was determined by the refinement of a CeO_2 standard sample. After several trials, the Thomson-Cox-Hastings profile function was adopted with possibility for uniaxial anisotropic broadening from size origin [242].

The background was described by an interpolated set of points with refinable intensities (this procedure allowed a more accurate description of the background leading to improved diffraction peak profiles).

Pair Distribution Function Analysis

The PDF G(r) is based on the Fourier transform to direct space of total scattering powder diffraction data. It yields the probability of finding two atoms separated by a distance r in a sample [243] and thus provides a multiscale information about the atomic arrangement. Here, the PDF is defined as [244]:

$$G(r) = 4\pi r[\rho(r) - \rho_0] = \frac{2}{\pi} \int_{Q_{min}}^{Q_{max}} Q[S(Q) - 1] sinQr \, dQ \qquad (A1.4)$$

where ρ(r) is the microscopic pair density, ρ_0 the average pair density, S(Q) the structure function and $Q = (4\pi.\sin\theta)/\lambda$. Due to the subtraction of the average pair density, the G(r) function oscillates around 0, reflecting the excess presence or absence of interatomic distances at the corresponding r value. At distances above the size of the crystallite (coherent structural domain), the microscopic pair density becomes equal to the average pair density and the PDF vanishes. PDFs were obtained from the powder patterns using the PDFGetX3 software [245]. Final refinement cycles included the scale factor, an overall atomic displacement parameter (*a.d.p.*), the cubic cell parameter and the nanoparticle diameter, or isotropic coherent structural domain size [246].

Electrochemical Measurements

Characterizations

All the glassware accessories used in this study were first cleaned by soaking in a H_2SO_4:H_2O_2 mixture for at least 12 hours and thoroughly washing with boiling Mill-Q water. The electrochemical measurements were conducted using an Autolab PGSTAT302N in a custom-made four-electrode electrochemical cell thermostated at $T = 25 \pm 1$ °C. Fresh electrolyte solution (0.1 M $HClO_4$) was daily prepared with Milli-Q water (Millipore, 18.2 MΩ cm, total organic compounds < 3 ppb) and $HClO_4$ 96 wt. % (Suprapur®, Merck). The counter-electrode was a Pt grid and the reference electrode a commercial RHE (Hydroflex, Gaskatel GmbH) connected to the cell via a Luggin capillary. A Pt wire connected to the reference electrode was used to filter the high frequency electrical noise. Pictures of the experimental electrochemical four-electrode setup are shown **Figure A1.6**.
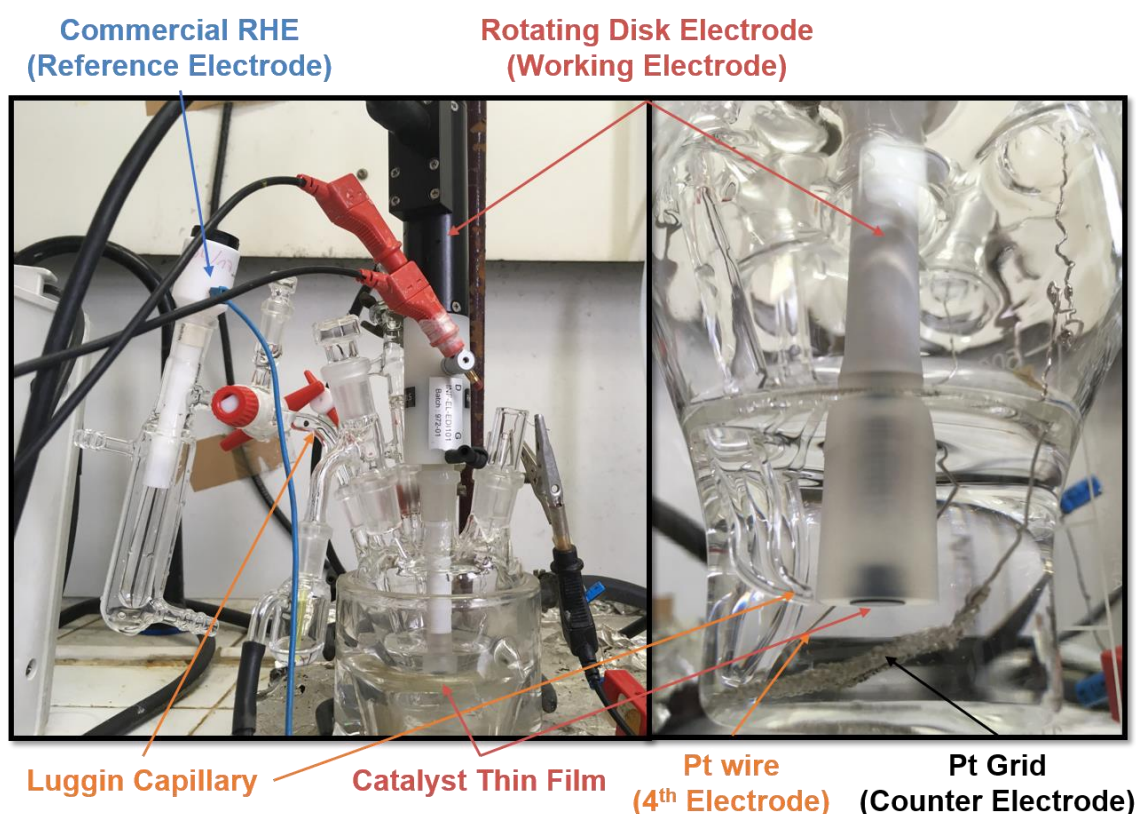

Figure A1.6: Pictures of the electrochemical four-electrode setup used in this manuscript.

To prepare the working electrodes, a suspension containing 10 mg of the targeted ~20 wt. % Pt(Ni) catalyst powder, 54 µL of 5 wt. % Nafion® solution (Electrochem. Inc.), 1446 µL of isopropanol and 3.6 mL (18.2 MΩ cm) of deionized water (MQ-grade, Millipore) was made. After sonication for 15 minutes, 10 µL of the suspension was pipetted onto a 0.196 cm^2 glassy carbon disk under rotation at 700 rpm and dried gently with a heat gun while the rotation was maintained (spin coating technique [186]) to ensure evaporation of the Nafion® solvents yielding a loading of *ca* 20 µg$_{Pt}$ cm^{-2}$_{geo}$.

Cyclic Voltammograms (CVs) were performed under different conditions to get insights on the surface properties and reactivity for the different electrocatalysts. A CV consists in recording the current flowing through the working electrode while sweeping its potential *vs*. the reference electrode, at a controlled sweep rate. Depending on the gaseous species saturation within the electrolyte (Ar, CO or O_2), and rotation speed of the electrode, the adsorption/desorption processes occurring at the electrode can be controlled. More details about the experimental protocols are given below.

Protocol 1 (standard LEPMI protocol, used all along this manuscript):

Prior to any electrochemical experiment, the working electrode was immersed into the deaerated electrolyte at E = 0.40 V *vs*. RHE (Ar >99.999 %, Messer). The following electrochemical techniques were then sequentially performed:

(i) Impedance Electrochemical Spectroscopy (EIS) measurements (E= 0.4 V *vs*. RHE, ΔE= 10 mV, 20 frequencies between 20 Hz and 100 kHz) were performed to determine the ohmic resistance of the cell. 90% of the resistance value was then dynamically compensated by the potentiostat software (Nova 2.1).

(ii) The base cyclic voltammograms were recorded in Ar-saturated electrolyte between 0.05 V and 1.23 V *vs*. RHE with a potential sweep rate of 500 (50 cycles, activation) and 20 mV s^{-1} (3 cycles, base voltammograms). The adsorption/desorption of H and surface oxides (OH) species strongly depend on the structure and the chemistry of the surface and near-surface layers. **Figure A1.7** displays a classical CV interpretation on Pt/C TKK as it is reported in literature. A more complex scenario for the highly defective electrocatalysts is discussed in Chapter 5.

Figure A1.7: Base cyclic voltammogram recorded in Ar-saturated 0.1 M HClO₄ electrolyte of the Sponge PtNi/C nanoparticles at a sweep rate of 20 mV s^{-1}. The different regions of interest are highlighted in colored squares and labelled.

(iii) The electrochemically active surface area (ECSA) was estimated using CO$_{ad}$ stripping coulometry: basically, a monolayer of CO$_{ads}$ is formed on the electrocatalyst surface by bubbling CO gas (> 99.997 %, Messer) in the electrolyte before being oxidized during a cyclic voltammetry after having purged the electrolyte from CO. The amount of oxidized CO species provides access to the Pt ECSA assuming that the electrooxidation of a CO$_{ads}$ monolayer requires 420 µC per cm^2 of Pt. The CO saturation coverage was established by bubbling CO for 6 min and purging with Ar for 34 min, while keeping the electrode potential at $E = 0.1$ V *vs.* RHE, then 3 cyclic voltammograms between 0.05 V and 1.23 V *vs.* RHE are recorded at 20 mV s^{-1}. During the first scan, the so-called H$_{upd}$ region is blocked due to the adsorption of CO$_{ads}$ species on the surface (see **Figure A1.8**, orange curve). Upon reaching a more positive potential, the CO$_{ads}$ species are oxidized according to **Equation (1.14)** presented in Chapter 1. The following scans are similar to the base voltammograms.
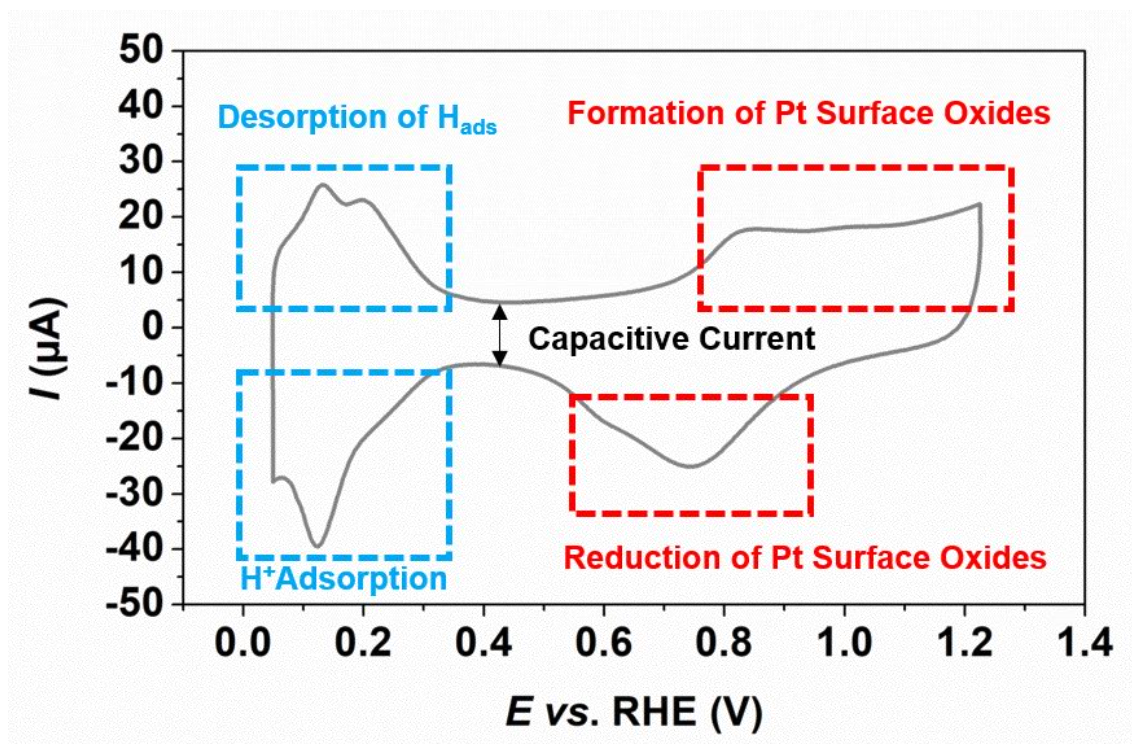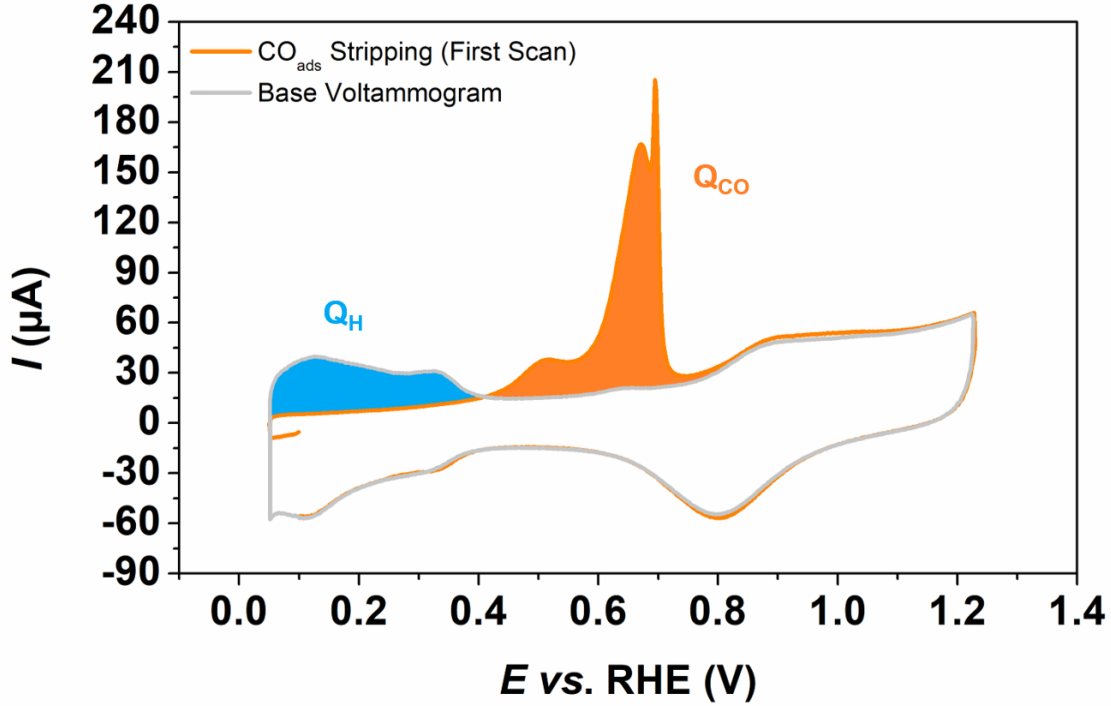
Figure A1.7: CO_{ads} stripping cyclic voltammograms recorded in Ar-saturated 0.1 M $HClO_4$ electrolyte of the Sponge PtNi/C nanoparticles at a sweep rate of 20 mV s^{-1}. The different regions of interest are highlighted and labelled.

(iv) The electrocatalytic activity for the ORR was measured in O_2-saturated 0.1 M $HClO_4$ solution (20 minutes of purging by oxygen > 99.99 %, Messer, while the electrode is still immerged at a potential of 0.4 V *vs.* RHE) using cyclic voltammetry between 0.20 and 1.05 V *vs.* RHE at a potential sweep rate of 5 mV s^{-1} and at different rotational speeds in the order: 400, 400, 900, 1600, 2500 and 400 rpm again. **Figure A1.8** shows the Ohmic drop corrected voltammograms recorded for the different electrode rotational speeds, the positive-going scan recorded at $\omega = 1600$ rpm scan after correction of the O_2 diffusion in solution, which is classically used for the determination of the ORR activity is also plotted in **Figure A1.8**. The correction of O_2 diffusion in solution is calculated *via* the Koutecky-Levich equation:

$$I_k = \frac{I x\, I_{lim}}{I_{lim} - I} \tag{A1.4}$$

Where I is the measured current, I_k is the kinetic current and I_{lim} is the diffusion-limited current (plateau observed at low potential in **Figure A1.8**).
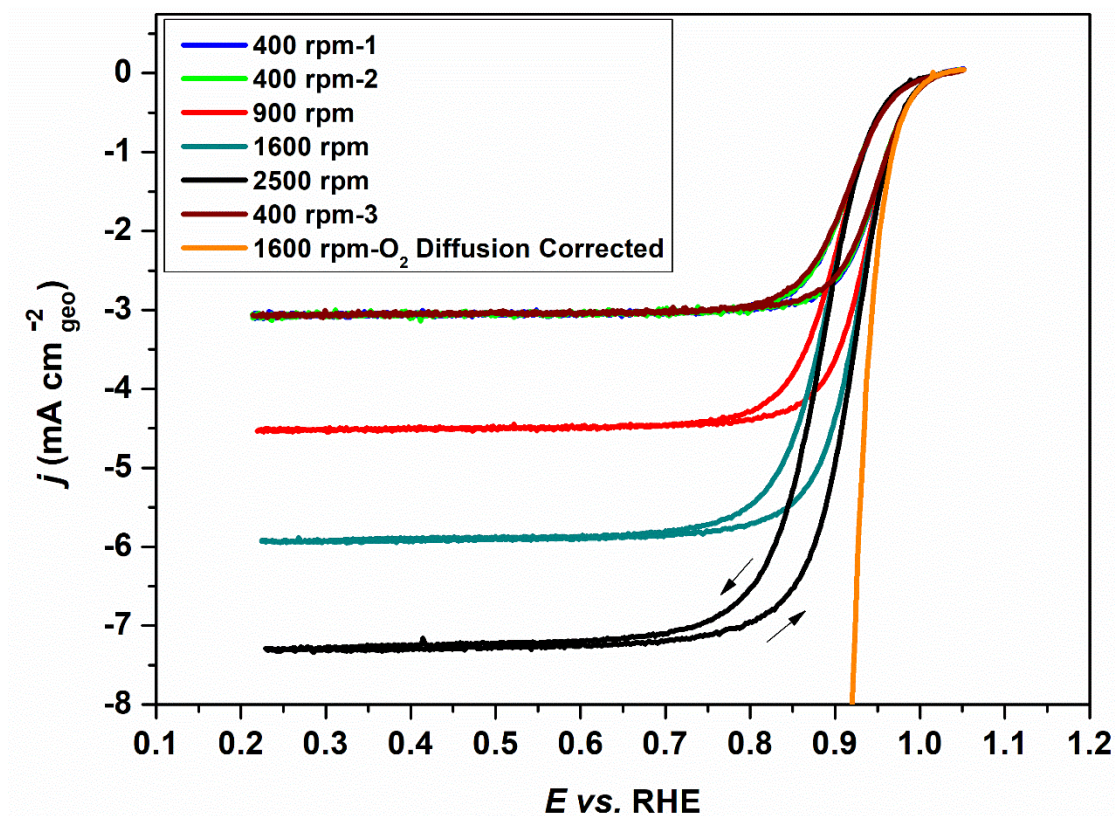
Figure A1.8: Ohmic drop corrected cyclic voltammograms recorded in O_2-saturated 0.1 M $HClO_4$ on Sponge PtNi/C nanoparticles at different electrode rotational speeds. Orange curve shows the positive-going 1600 rpm scan after correction of the O_2 diffusion in solution used for the determination of the ORR activity. The current is normalized by the geometric surface of the electrode (0.196 cm^2). Other conditions: $v= 5mV\ s^{-1}$, $T= 25 \pm 1\ °C$

The ORR specific/mass activity was determined by normalizing the current measured at $E = 0.95$ V *vs*. RHE from the 1600 rpm positive-going scan, after correction from the oxygen diffusion in the solution and the Ohmic drop (the Ohmic drop is compensated manually after the experiment as the dynamic compensation is disabled for this measurement), to the real surface area/mass of deposited Pt determined by CO_{ad} stripping voltammetry or AAS respectively.

Protocol 2 (used for comparison in chapter five)

The 'soft' protocol is rather identical than protocol 1 except that:

(i) The electrode is initially inserted at $E = 0.1$ V *vs*. RHE (so the EIS is performed at this potential)

(ii) The activation and base CVs consist in 25 potential cycles between 0.05 V and 1 V *vs*. RHE at 100 mV s^{-1} and 3 cycles between 0.05 V and 1 V *vs*. RHE at 20 mV s^{-1} respectively.

(iii) The CO_{ads} stripping experiment was similar except that the CVs were recorded between 0.05 V and 1 V *vs.* RHE at 20 mV s^{-1}.

(iv) The 20 minute saturation of the electrolyte with O_2 was performed with the electrode outside from the electrolyte under potential control (0.05 V *vs.* RHE)

(v) The ORR kinetics were measured using a single linear sweep voltammetry from 0.05 V to 1 V *vs.* RHE at 5 mV s^{-1} at 1600 rpm.

Accelerated Stress Tests

The accelerated stress tests were performed in the same glass cell that the one used for electrochemical characterizations, except that in order to avoid dissolution/deposition phenomena between the Pt grid at the counter electrode and the Pt-based catalyst at the working electrode, the Pt grid was replaced by a glassy carbon plate. Also, in order to prevent the rotating disk electrode engine from degradation due to acidic vapor during the long-term potential cycling at T= 80 °C, the rotating electrode was replaced by a static glass electrode holder.

Electron Microscopy

Principle

The interaction of an electron beam with a material produces a wide range of measurable signals as presented in **Figure A1.9**.

Various techniques were used along this manuscript depending on the sample property investigated. Generally, microscopy images were obtained using the transmitted and scattered electrons *via* Transmission Electron Microscopy (TEM) or Scanning Transmission Electron Microscopy (STEM) techniques, which give information on the nanoparticles morphology and structure. Also, when coupled with Energy Dispersive X-ray Spectroscopy (X-EDS or EDX, which uses the re-emitted X-rays), STEM can be used to build elemental map, giving insights on the sample chemical properties. Also, the emitted secondary electrons were used in Scanning Electron Microscopy (SEM) for imaging the Sponge PtNi/C catalyst in Chapter 4. Depending on the detector type and

position, various images can be built as shown **Figure A1.10.** Consequently, different microscopes were used depending on the technique, as detailed below.

electron beam

Auger Electrons (AE)
surface atomic composition

Secondary Electrons (SE)
topographical information (SEM)

Characteristic X-ray (EDX)
thickness atomic composition

Backscattered Electrons (SE)
atomic number and phase differences

Cathodoluminescence (CL)
electronic states information

Continuum X-ray (Bremsstrahlung)

SAMPLE

Inelastic Scattering
composition and bond states (EELS)

Incoherent Elastic Scattering

Elastic Scattering
structural analysis and HR imaging (diffraction)

Transmitted Electrons
morphological information (TEM)

Figure A1.9: Diagram illustrating the phenomena resulting from the interaction of highly energy electrons with matter. From Ref [247].

TEM Measurements

Standard TEM images were acquired using a JEOL 2010 TEM operated at 200 kV with a point to point resolution of 0.19 nm.

HRTEM Measurements

Aberration-corrected HRTEM images were acquired by Dr. Jaysen Nelayah at the University Paris Diderot, France, using a JEOL-ARM 200F transmission electron microscope operated at 200 kV and equipped with a cold-field emission gun and a CEOS aberration corrector of the objective lens. The PtNi/C NPs were first dispersed in dry

conditions on holey film copper TEM grids (Agar Scientific ltd). The HR-TEM investigations were undertaken on NPs lying over the holes of the thin holey carbon films to circumvent the contribution of the latter to the HR-TEM contrast.
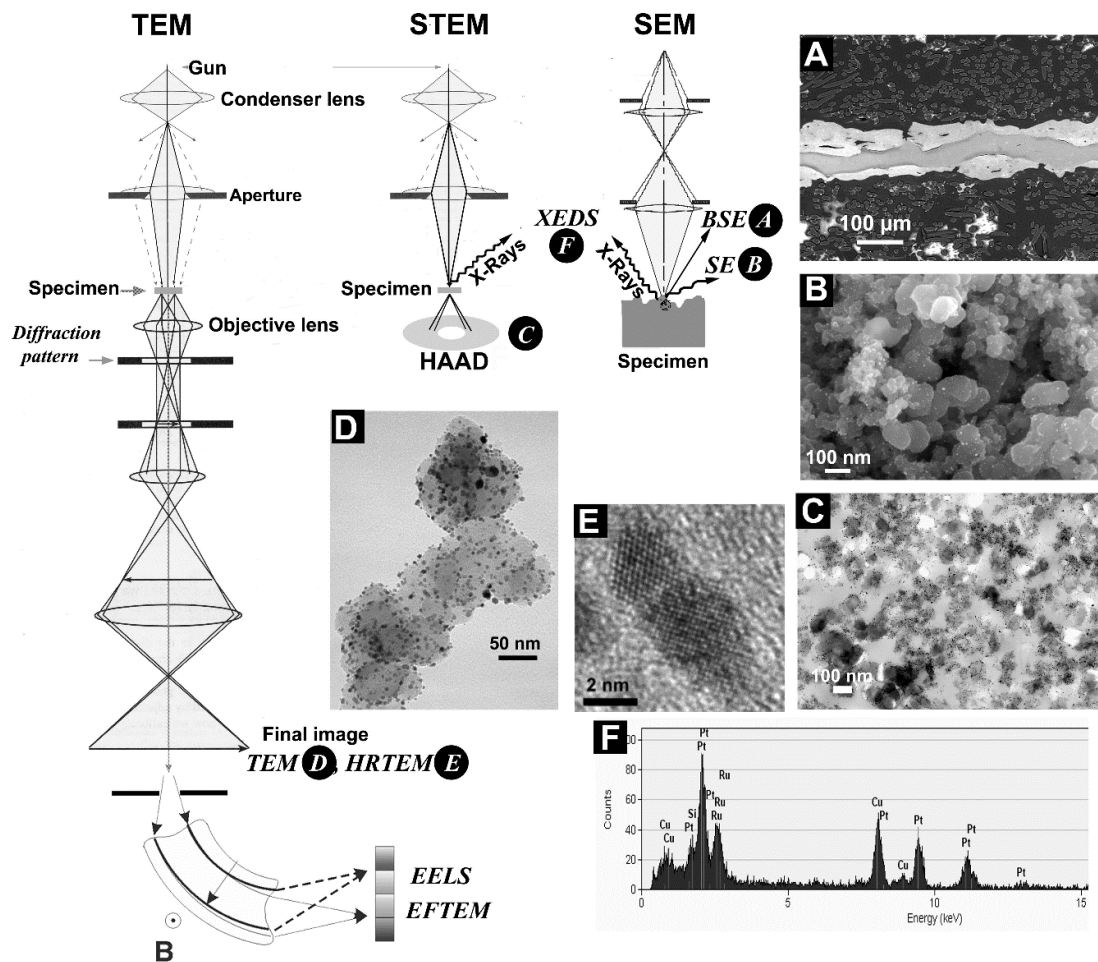
Figure A1.10: Scheme of SEM and TEM with examples of images of MEA in (a) SEM in BSE mode, (b) FEG-SEM in SE mode, (c) FEG-SEM-STEM of an ultramicrotomed MEA cross-section, (d) TEM and (e) HRTEM; (f) X-EDS microanalyses. From Ref. [248].

STEM Images and X-EDS Mapping

The STEM-X-EDS elemental maps were acquired with the help of Gilles Renou from SIMAP, Grenoble, France, using a JEOL 2100F microscope operated at 200 kV and equipped with a retractable large angle Silicon Drift Detector (SDD) Centurio detector. The X-EDS spectra were recorded on different magnifications, from hundreds to individual nanoparticles by scanning the beam in a square region of various sizes. The quantitative analyses were performed on Pt L and Ni K lines using the K-factor provide by the JEOL software.

HRSTEM Images and X-EDS Mapping

The HRSTEM-X-EDS were acquired by Dr. Laure Guetaz in CEA Grenoble, France, using a FEI–Titan Ultimate microscope. This microscope is equipped with two aberration correctors allowing a < 0.1 nm spatial resolution in STEM mode. Images showed in this manuscript were collected on a High Angle Annular Dark Field (HAADF) detector.

Other Characterization Technique

AAS Measurements

Atomic Absorption Spectroscopy (AAS) was used to quantify the Pt weight fraction (wt. %) in the catalysts. The measurements were performed using a AAS-PinAACle 900F from PerkinElmer. 5 mg of the electrocatalysts were first dissolved in aqua regia (HCl: HNO_3 3:1 volume ratio) made from high purity acids (37 vol. % ACS Reagent, Sigma - Aldrich and 65 vol. % Sigma-Aldrich for HCl and HNO_3 respectively) for 72 h at $T=$ 25°C. The solution was then diluted sevenfold to reach a range around 50-200 ppm Pt. The metal contents were then determined using three series of three measurements. The wavelength considered for Pt was $\lambda=$ 240.7 nm and a 37 mm hollow cathode lamp (Heraeus) was used.

APPENDIX 2: MODELLING ALLOYING AND DISORDER

Our experimental observations detailed in Chapter 5 suggested that structural disorder is more important when Ni atoms are alloyed to Pt atoms. The relation between the microstrain and the Ni content was nearly linear, but a polynomial fit suggested a possible inflexion point around 50 at. % Ni, the latter sounds rather physically correct, as introducing more than 50 % of a foreign element A in phase B is equivalent of less than 50 % of B into phase A. This was verified as detailed below:

As shown in F**igure A2.1**, using, Matlab, we simulated a 2-dimensional square crystal (grid), composed of $(lxd)^2$ atoms (initially Pt, white in the figure). The crystal can be sub-divided in 'local regions' containing l^2 atoms. For a given Pt:Ni crystal composition, l and d, the corresponding amount of Ni atoms are randomly (without repetition) introduced to replace Pt all over the crystal.

We can then define the local Ni composition (LC, in %) in position $(\boldsymbol{i}, \boldsymbol{j})$ where $(\boldsymbol{i}, \boldsymbol{j})$ are the coordinates of the upper left atom forming the region:

$$LC(i,j) = \frac{100}{l^2} \sum_{k=i}^{i+l} \sum_{n=j}^{j+l} \delta_{(i,j)} \tag{A2.1}$$

Where $\delta_{(i,j)}$ represents the nature of the atom, being 0 for Pt and 1 for Ni.

Also, as we want the local regions to be independent and to cover all the crystal, this equation must be used for all (i,j) verifying $i \ or \ j = kxl$ with the integer $k \leq d-1$. This way, the mean of all the LCs population corresponds to the whole crystal composition, and its deviation around the mean to the composition heterogeneity within the crystal.
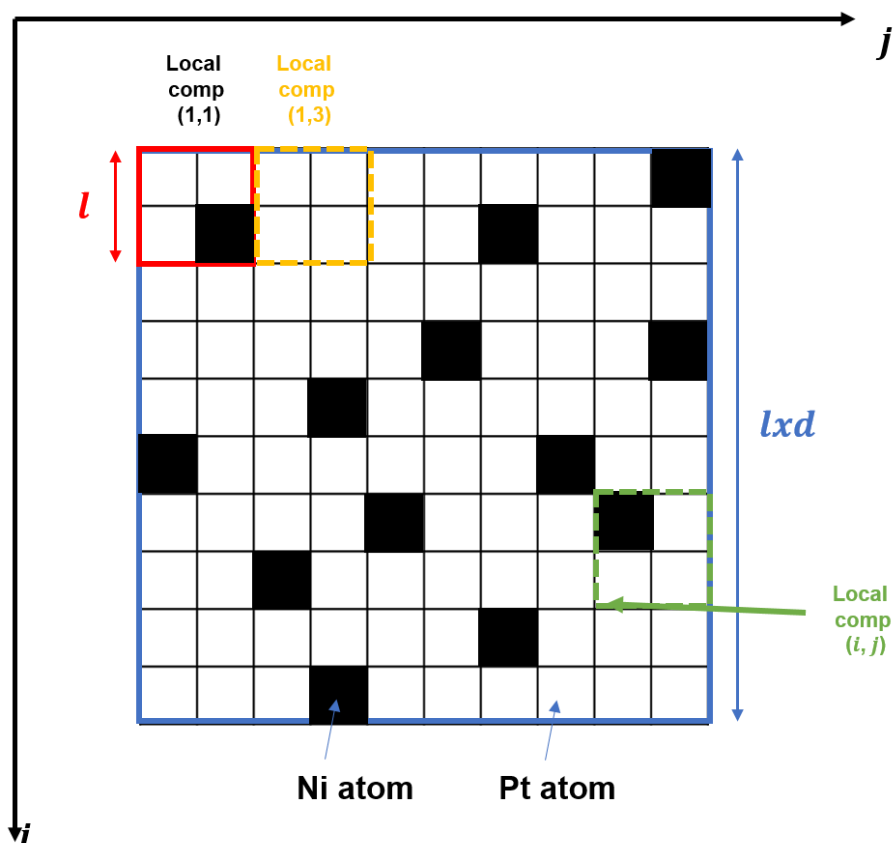
Figure A2.1: The theoretical 2D square crystal used in the model. It is composed of $(lxd)^2$ atoms (initially Pt, white), where l is the size of a local square region and lxd the size of the crystal. For a given crystal composition, a defined number of Ni atoms is randomly introduced in replacement of Pt atoms. Then, the local chemical compositions are calculated. All the crystal is explored so that the mean of the local compositions corresponds to the global crystal composition. The relative error between all these measurements is representative of the heterogeneity of the crystal. In the schematics, l=2 meaning a local region is composed of 4 atoms, the crystal is composed 100 atoms.

We tested this model for various values of l and d with $(lxd)^2 = 40,000$ (which approximatively corresponds to the number of Pt atoms composing a ~10 nm Pt cuboctahedron). The local composition was also converted into a lattice parameter, by applying the Vegard's law in each region. **Figure A2.2** shows the simulated results. For any pair of parameters tested, the microstrain shows a non-linear evolution with the Ni composition, featuring a maximum at 50 at. %. Depending on the set of parameters, the local region is composed of 4, 16 or 64 atoms and the crystal features 10,000, 2,500 or 625 regions, which strongly impacts on the microstrain value. For example, for l=2, the number of atoms is so small that the composition in a region values can only take discrete values (0, 25, 50, 75 or 100 % at. Ni), which are responsible of the peculiar shape of the simulated microstrain in that case. However, when increasing the size of the region, the predicted microstrain-composition trend is in the same order of value that the experimental data points considered in the chapter 5 of this manuscript.
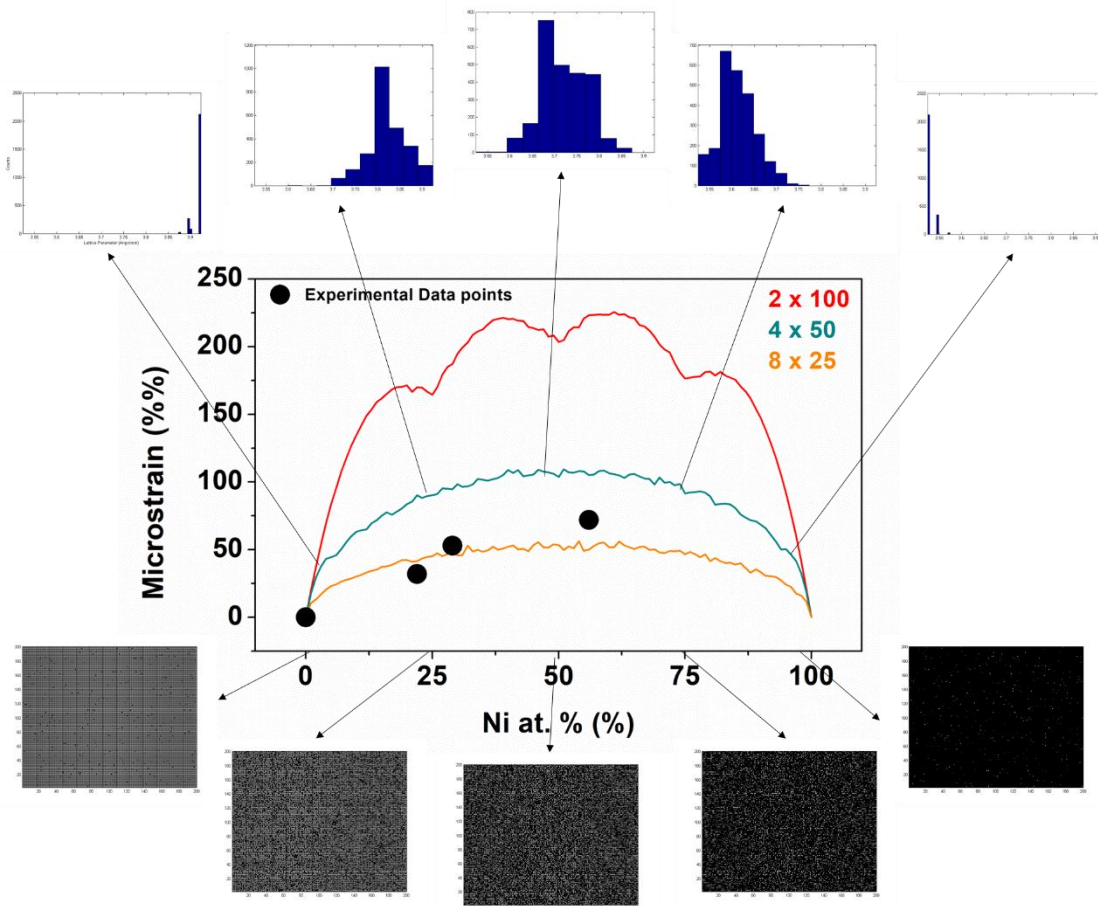
Figure A2.2: Simulated microstrain (mean of $\Delta a/a$ from all the regions) *vs.* the Ni global composition, for three pairs of l and d verifying $(lxd)^2 = 40,000$ (which approximatively corresponds to the number of Pt atoms composing a ~10 nm Pt cuboctahedron). The experimental data points are those used to estimate the microstrain-Ni content relationship in the chapter 5 of the manuscript. Histograms showing the distribution of the lattice parameter (top) and representation of the simulated crystal (bottom) for 4 x 50 pair.

Note that this model does not pretend to be perfect as too many parameters are neglected (3D structure, fcc structure, atoms size, Ni diffusion etc.) but rather should be regarded as a mathematical mean to provide evidences of structural disorder induced by the non-perfect mixing of two elements.

REFERENCES

1. Hansen, J., Ruedy, R., Sato, M. & Lo, K. Global surface temperature change. *Rev. Geophys.* **48,** RG4004 (2010).

2. Francey, R. J. *et al.* Atmospheric verification of anthropogenic CO2 emission trends. *Nat. Clim. Chang.* **3,** 520–524 (2013).

3. MacFarling Meure, C. *et al.* Law Dome CO2, CH4 and N2O ice core records extended to 2000 years BP. *Geophys. Res. Lett.* **33,** 2000–2003 (2006).

4. Keeling, C. D. *et al.* Atmospheric carbon dioxide variations at Mauna Loa Observatory, Hawaii. *Tellus A* **28,** 538–551 (1976).

5. Andres, R. J. *et al.* A synthesis of carbon dioxide emissions from fossil-fuel combustion. *Biogeosciences* **9,** 1845–1871 (2012).

6. Böhm, F., Joachimski, M, M., Lehnert, H., Retiner, J. Evidence for preindustrial variations in the marine surface water carbonate system from coralline sponges. *Geochemistry Geophys. Geosystems* **3,** 1–13 (2002).

7. Hansen, J. *et al.* Dangerous human-made interference with climate: a GISS modelE study. *Atmos. Chem. Phys.* **7,** 2287–2312 (2007).

8. International Energy Agency. Key world energy statistics. *Statistics (Ber).* 80 (2016). doi:10.1787/key_energ_stat-2016-en

9. International Energy Agency. *Key Coal Trends*. (2016).

10. International Energy Agengy. *Key Renewable Trends 2016*. (2016).

11. International Energy Agengy. *Global EV Outlook 2015 key takeaways*. (2015).

12. International Energy Agency. *Global EV Outlook 2016 Electric Vehicles Initiative*. (2016).

13. Becherif, M. *et al.* Hydrogen Energy Storage: New Techno-Economic Emergence Solution Analysis. *Energy Procedia* **74,** 371–380 (2015).

14. Turner, J. A. Sustainable hydrogen production. *Science* **305,** 972–4 (2004).

15. Besancon, B. M. *et al.* Hydrogen quality from decarbonized fossil fuels to fuel cells. *Int. J. Hydrogen Energy* **34,** 2350–2360 (2009).

16. Zuttel, A., Remhof, A., Borgschulte, A. & Friedrichs, O. Hydrogen: the future energy carrier. *Philos. Trans. R. Soc. A Math. Phys. Eng. Sci.* **368,** 3329–3342 (2010).

17. Peighambardoust, S. J., Rowshanzamir, S. & Amjadi, M. Review of the proton exchange membranes for fuel cell applications. *Int. J. Hydrogen Energy* **35,** 9349–9384 (2010).

18. Kreitmeier, S., Schuler, G. a., Wokaun, A. & Büchi, F. N. Investigation of membrane degradation in polymer electrolyte fuel cells using local gas permeation analysis. *J. Power Sources* **212,** 139–147 (2012).

19. Gubler, L., Dockheer, S. M. & Koppenol, W. H. Radical (HO●, H● and HOO●) Formation and Ionomer Degradation in Polymer Electrolyte Fuel Cells. *J. Electrochem. Soc.* **158,** B755 (2011).

20. Kocha, S. S., Yang, J. D. & Yi, J. S. Characterization of Gas Crossover and Its Implications in PEM Fuel Cells. **52,** (2006).

21. Kreitmeier, S., Michiardi, M., Wokaun, A. & Büchi, F. N. Factors determining the gas crossover through pinholes in polymer electrolyte fuel cell membranes. *Electrochim. Acta* **80,** 240–247 (2012).

22. de Bruijn, F. a., Dam, V. a. T. & Janssen, G. J. M. Review: Durability and Degradation Issues of PEM Fuel Cell Components. *Fuel Cells* **8,** 3–22 (2008).

23. Liu, W., Ruth, K. & Rusch, G. Membrane Durability in PEM Fuel Cells. **231,** 227–231 (2001).

24. Pozio, A., Silva, R. F., De Francesco, M. & Giorgi, L. Nafion degradation in PEFCs from end plate iron contamination. *Electrochim. Acta* **48,** 1543–1549 (2003).

25. Healy, J. *et al.* Aspects of the Chemical Degradation of PFSA Ionomers used in PEM Fuel Cells. *Fuel Cells* **5,** 302–308 (2005).

26. Xie, J. *et al.* Durability of PEFCs at High Humidity Conditions. *J. Electrochem.*

Soc. **152,** A104 (2005).

27.   Teranishi, K., Kawata, K., Tsushima, S. & Hirai, S. Degradation Mechanism of PEMFC under Open Circuit Operation. *Electrochem. Solid-State Lett.* **9,** A475 (2006).

28.   Inaba, M. *et al.* Impacts of air bleeding on membrane degradation in polymer electrolyte fuel cells. *J. Power Sources* **178,** 699–705 (2008).

29.   Curtin, D. E., Lousenberg, R. D., Henry, T. J., Tangeman, P. C. & Tisack, M. E. Advanced materials for improved PEMFC performance and life. *J. Power Sources* **131,** 41–48 (2004).

30.   (U.S. Department of Energy). Fuel Cell Technical Team Roadmap. *U. S. Drive Partnersh.* 9 (2013). doi:10.2172/1220127

31.   Zamel, N. & Li, X. Effect of contaminants on polymer electrolyte membrane fuel cells. *Prog. Energy Combust. Sci.* **37,** 292–329 (2011).

32.   Vogel, W., Lundquist, J. & Ross, P. Reaction patways and poison II. The rate controlling step for electrochemical oxidation of hydrogen on Pt in acid and poisoning of the reaction by CO. *Electrochim. Acta* **20,** 79–93 (1975).

33.   Gilman, S. The Mechanism of Electrochemical Oxidation of Carbon Monoxide and Methanol on Platinum . 11 , The (' Reactant-Pair ” Mechanism for Electrochemical Oxidation of Carbon Monoxide and Methanol '. *J. Phys. Chem.* **68,** 70–80 (1964).

34.   Gasteiger, H. A., Markovic, N., Ross, P. N. & Cairns, E. J. CO Electrooxidation on Well-Characterized Pt-Ru Alloys. 617–625 (1994).

35.   Iannielo, R., Schmidt, V. M., Stimming, U., Stumper, J. & Wallau, A. CO adsorption and oxydation on Pt and Pt-Ru alloys: dependance on substrate composition. *Electrochim. Acta* **39,** 1863 (1994).

36.   Iwasita, T. Electrocatalysis of methanol oxidation. *Electrochim. Acta* **47,** 3663–3674 (2002).

37.   Wasmus, S. & Ku, A. Methanol oxidation and direct methanol fuel cells : a selective review 1. **461,** 14–31 (1999).

38. Markovic, M. & Gasteiger, H. A. Electro-oxydation mechanism of methanol and formic acid on Pt-Ru alloy surface. *Electrochem. commun.* **40,** 91–98 (1995).

39. Gojković, S. L., Vidaković, T. R. & Đurović, D. R. Kinetic study of methanol oxidation on carbon-supported PtRu electrocatalyst. *Electrochim. Acta* **48,** 3607–3614 (2003).

40. Ishikawa, Y., Liao, M. S. & Cabrera, C. R. Oxidation of methanol on platinum, ruthenium and mixed Pt-M metals (M = Ru, Sn): A theoretical study. *Surf. Sci.* **463,** 66–80 (2000).

41. Yeager, E. Electrocatalysts for O2 reduction. *Electrochim. Acta* **29,** 1527–1537 (1984).

42. Damjanovic, A. & Brusic, V. Electrode kinetics of oxygen reduction on oxide-free platinium electrodes. **12,** 615–628 (1966).

43. Chen, S. & Kucernak, A. Electrocatalysis under Conditions of High Mass Transport Rate: Oxygen Reduction on Single Submicrometer-Sized Pt Particles Supported on Carbon. *J. Phys. Chem. B* **108,** 3262–3276 (2004).

44. Paulus, U. A., Wokaun, A., Scherer, G. G., Schmidt, T. J. & Stamenko, V. Oxygen reduction on high surface area Pt-based alloy catalysts in comparison to well defined smooth bulk alloy electrodes. **47,** (2002).

45. Nørskov, J. K. *et al.* Origin of the overpotential for oxygen reduction at a fuel-cell cathode. *J. Phys. Chem. B* **108,** 17886–17892 (2004).

46. Rossmeisl, J., Karlberg, G. S., Jaramillo, T. & Norskov, J. K. Steady state oxygen reduction and cyclic voltammetry. *Faraday Discuss.* **140,** 337–346 (2008).

47. Yu, X. & Ye, S. Recent advances in activity and durability enhancement of Pt/C catalytic cathode in PEMFC. *J. Power Sources* **172,** 145–154 (2007).

48. Passalacqua, E. & Antonucci, P. L. The influence of Pt on the electrooxidation behaviour of carbon in phosphoric acid. *Electrochim. Acta* **37,** 2725–2730 (1992).

49. Roen, L. M., Paik, C. H. & Jarvi, T. D. Electrocatalytic Corrosion of Carbon Support in PEMFC Cathodes. *Electrochem. Solid-State Lett.* **7,** A19 (2004).

50. Antolini, E. Carbon supports for low-temperature fuel cell catalysts. *Appl. Catal. B Environ.* **88,** 1–24 (2009).

51. Antolini, E. Graphene as a new carbon support for low-temperature fuel cell catalysts. *Appl. Catal. B Environ.* **123–124,** 52–68 (2012).

52. Castanheira, L. *et al.* Carbon corrosion in proton-exchange membrane fuel cells: Effect of the carbon structure, the degradation protocol, and the gas atmosphere. *ACS Catal.* **5,** 2184–2194 (2015).

53. Castanheira, L. *et al.* Carbon corrosion in proton-exchange membrane fuel cells: From model experiments to real-life operation in membrane electrode assemblies. *ACS Catal.* **4,** 2258–2267 (2014).

54. Virkar, A. V. & Zhou, Y. Mechanism of Catalyst Degradation in Proton Exchange Membrane Fuel Cells. *J. Electrochem. Soc.* **154,** B540 (2007).

55. Guilminot, E. *et al.* Membrane and Active Layer Degradation upon PEMFC Steady-State Operation. *J. Electrochem. Soc.* **154,** B1106 (2007).

56. Dubau, L. *et al.* A review of PEM fuel cell durability: Materials degradation, local heterogeneities of aging and possible mitigation strategies. *Wiley Interdiscip. Rev. Energy Environ.* **3,** 540–560 (2014).

57. Stonehart, P., Box, P. O. & Road, C. 'Development of Advanced Noble Metal-Alloy Electrocatalysts for Phosphoric Acid Fuel Cells (PAFC)'. *Berichte der Bunsengesellschaft für Phys. Chemie* 913–921 (1990). doi:10.1002/bbpc.19900940907

58. Hammer, B. & Nørskov, J. K. Electronic factors determining the reactivity of metal surfaces. *Surf. Sci.* **343,** 211–220 (1995).

59. Stamenkovic, V. *et al.* Changing the activity of electrocatalysts for oxygen reduction by tuning the surface electronic structure. *Angew. Chemie - Int. Ed.* **45,** 2897–2901 (2006).

60. Jalan, V. & Taylor, E. J. Importance of interatomic spacing in catalytic reduction of oxygen in phosphoric acid. 2299–2302 (1983). doi:10.1149/1.2119574

61. Frelink, T., Visscher, W. & van Veen, J. a. R. Particle size effect of carbon-

supported platinum catalysts for the electrooxidation of methanol. *J. Electroanal. Chem.* **382,** 65–72 (1995).

62. Mukerjee, S. Role of Structural and Electronic Properties of Pt and Pt Alloys on Electrocatalysis of Oxygen Reduction. *J. Electrochem. Soc.* **142,** 1409 (1995).

63. Stamenkovic, V. R. *et al.* Improved oxygen reduction activity on Pt3Ni(111) via increased surface site availability. *Science* **315,** 493–497 (2007).

64. Greeley, J. *et al.* Alloys of platinum and early transition metals as oxygen reduction electrocatalysts. *Nat. Chem.* **1,** 552–556 (2009).

65. Maillard, F. *et al.* Durability of Pt3Co/C nanoparticles in a proton-exchange membrane fuel cell: Direct evidence of bulk Co segregation to the surface. *Electrochem. commun.* **12,** 1161–1164 (2010).

66. Dubau, L. *et al.* Durability of Pt[sub 3]Co/C Cathodes in a 16 Cell PEMFC Stack: Macro/Microstructural Changes and Degradation Mechanisms. *J. Electrochem. Soc.* **157,** B1887 (2010).

67. Dubau, L. *et al.* Further insights into the durability of Pt3Co/C electrocatalysts: Formation of 'hollow' Pt nanoparticles induced by the Kirkendall effect. *Electrochim. Acta* **56,** 10658–10667 (2011).

68. Vej-Hansen, U. G., Rossmeisl, J., Stephens, I. E. L. & Schiøtz, J. Correlation between diffusion barriers and alloying energy in binary alloys. *Phys. Chem. Chem. Phys.* **18,** 3302–3307 (2016).

69. Stephens, I. E. L., Bondarenko, A. S., Grønbjerg, U., Rossmeisl, J. & Chorkendorff, I. Understanding the electrocatalysis of oxygen reduction on platinum and its alloys. *Energy Environ. Sci.* **5,** 6744 (2012).

70. Stephens, I. E. L., Bondarenko, A. S., Bech, L. & Chorkendorff, I. Oxygen Electroreduction Activity and X-Ray Photoelectron Spectroscopy of Platinum and Early Transition Metal Alloys. *ChemCatChem* **4,** 341–349 (2012).

71. Escudero-Escribano, M. *et al.* Pt5Gd as a highly active and stable catalyst for oxygen electroreduction. *J. Am. Chem. Soc.* **134,** 16476–9 (2012).

72. Escudero-Escribano, M. *et al.* Tuning the Activity of Pt alloy Electrocatalysts be

Means of the Lanthanide Contraction. *Science (80-.).* **352,** 73–76 (2016).

73. Kelsall, R. W., Hamley, I. W. & Geoghegan, M. *Nanoscale Science and Technology.* (2005). doi:10.1002/0470020873.fmatter

74. Roduner, E. Size matters: why nanomaterials are different. *Chem. Soc. Rev.* **35,** 583 (2006).

75. Zhang, J., Yang, H., Fang, J. & Zou, S. Synthesis and oxygen reduction activity of shape-controlled Pt(3)Ni nanopolyhedra. *Nano Lett.* **10,** 638–644 (2010).

76. Carpenter, M. K., Moylan, T. E., Kukreja, R. S., Atwan, M. H. & Tessema, M. M. Solvothermal synthesis of platinum alloy nanoparticles for oxygen reduction electrocatalysis. *J. Am. Chem. Soc.* **134,** 8535–8542 (2012).

77. Cui, C. *et al.* Octahedral PtNi nanoparticle catalysts: Exceptional oxygen reduction activity by tuning the alloy particle surface composition. *Nano Lett.* **12,** 5885–5889 (2012).

78. Cui, C., Gan, L., Heggen, M., Rudi, S. & Strasser, P. Compositional segregation in shaped Pt alloy nanoparticles and their structural behaviour during electrocatalysis. *Nat. Mater.* **12,** 765–71 (2013).

79. Gan, L. *et al.* Element-specific anisotropic growth of shaped platinum alloy nanocrystals. *Science* **346,** 1502–1506 (2014).

80. Choi, S. Il *et al.* Synthesis and characterization of 9 nm Pt-Ni octahedra with a record high activity of 3.3 A/mgPt for the oxygen reduction reaction. *Nano Lett.* **13,** 3420–3425 (2013).

81. Beermann, V. *et al.* Rh-Doped Pt-Ni Octahedral Nanoparticles: Understanding the Correlation between Elemental Distribution, Oxygen Reduction Reaction, and Shape Stability. *Nano Lett.* **16,** 1719–1725 (2016).

82. Oezaslan, M., Hasché, F. & Strasser, P. Pt-Based Core–Shell Catalyst Architectures for Oxygen Fuel Cell Electrodes. *J. Phys. Chem. Lett.* **4,** 3273–3291 (2013).

83. Snyder, J., McCue, I., Livi, K. & Erlebacher, J. Structure/processing/properties relationships in nanoporous nanoparticles as applied to catalysis of the cathodic

oxygen reduction reaction. *J. Am. Chem. Soc.* **134,** 8633–45 (2012).

84. Stamenkovic, V. R. *et al.* Trends in electrocatalysis on extended and nanoscale Pt-bimetallic alloy surfaces. *Nat. Mater.* **6,** 241–247 (2007).

85. Mayrhofer, K. J. J., Juhart, V., Hartl, K., Hanzlik, M. & Arenz, M. Adsorbate-Induced surface Segregation for core-shell nanocatalysts. *Angew. Chemie - Int. Ed.* **48,** 3529–3531 (2009).

86. Wang, C. *et al.* Monodisperse Pt(3)Co nanoparticles as electrocatalyst: the effects of particle size and pretreatment on electrocatalytic reduction of oxygen. *Phys. Chem. Chem. Phys.* **12,** 6933–6939 (2010).

87. Peng, Z. & Yang, H. Designer platinum nanoparticles: Control of shape, composition in alloy, nanostructure and electrocatalytic property. *Nano Today* **4,** 143–164 (2009).

88. Adzic, R. R. *et al.* Platinum monolayer fuel cell electrocatalysts. *Top. Catal.* **46,** 249–262 (2007).

89. Strasser, P. & Kühl, S. Dealloyed Pt-based core-shell oxygen reduction electrocatalysts. *Nano Energy* http: //dx.doi.org/10.1016/j.nanoen.2016.04.047 (2016). doi:10.1016/j.nanoen.2016.04.047

90. Gan, L., Yu, R., Luo, J., Cheng, Z. & Zhu, J. Lattice strain distributions in individual dealloyed Pt-Fe catalyst nanoparticles. *J. Phys. Chem. Lett.* **3,** 934–938 (2012).

91. Gan, L., Heggen, M., Rudi, S. & Strasser, P. Core−Shell Compositional Fine Structures of Dealloyed PtxNi1−x Nanoparticles and Their Impact on Oxygen Reduction Catalysis. *Nano Lett.* **12,** 5423–5430 (2012).

92. Kuttiyiel, K. a. *et al.* Bimetallic IrNi core platinum monolayer shell electrocatalysts for the oxygen reduction reaction. *Energy Environ. Sci.* **5,** 5297 (2012).

93. Kuttiyiel, K. a *et al.* Nitride Stabilized PtNi Core − Shell Nanocatalyst for high Oxygen Reduction Activity. (2012).

94. Gan, L., Cui, C., Rudi, S. & Strasser, P. Core–Shell and Nanoporous Particle Architectures and Their Effect on the Activity and Stability of Pt ORR

Electrocatalysts. *Top. Catal.* **57,** 236–244 (2013).

95. Han, B. *et al.* Record activity and stability of dealloyed bimetallic catalysts for proton exchange membrane fuel cells. *Energy Environ. Sci.* **8,** 258–266 (2015).

96. Oezaslan, M., Heggen, M. & Strasser, P. Size-Dependent morphology of dealloyed bimetallic catalysts: Linking the nano to the macro scale. *J. Am. Chem. Soc.* **134,** 514–524 (2012).

97. Gan, L., Heggen, M., O'Malley, R., Theobald, B. & Strasser, P. Understanding and controlling nanoporosity formation for improving the stability of bimetallic fuel cell catalysts. *Nano Lett.* **13,** 1131–1138 (2013).

98. Erlebacher, J. An Atomistic Description of Dealloying. *J. Electrochem. Soc.* **151,** C614 (2004).

99. Erlebacher, J. & Margetis, D. Mechanism of Hollow Nanoparticle Formation Due to Shape Fluctuations. *Phys. Rev. Lett.* **112,** 155505 (2014).

100. Sieradzki, K. *et al.* The Dealloying Critical Potential. *J. Electrochem. Soc.* **149,** B370 (2002).

101. Erlebacher, J., Aziz, M. J., Karma, a, Dimitrov, N. & Sieradzki, K. Evolution of nanoporosity in dealloying. *Nature* **410,** 450–453 (2001).

102. Strasser, P. *et al.* Lattice-strain control of the activity in dealloyed core–shell fuel cell catalysts. *Nat. Chem.* **2,** 454–460 (2010).

103. Yin, Y. *et al.* Formation of hollow nanocrystals through the nanoscale Kirkendall effect. *Science* **304,** 711–4 (2004).

104. Xia, X., Wang, Y., Ruditskiy, A. & Xia, Y. 25Th Anniversary Article: Galvanic Replacement: a Simple and Versatile Route To Hollow Nanostructures With Tunable and Well-Controlled Properties. *Adv. Mater.* **25,** 6313–33 (2013).

105. Skrabalak, S. E. *et al.* Applications. **41,** 1587–1595 (2008).

106. Cobley, C. M. & Xia, Y. Engineering the properties of metal nanostructures via galvanic replacement reactions. *Mater. Sci. Eng. R Reports* **70,** 44–62 (2010).

107. Wang, Z. L., Ahmad, T. S. & E1-Sayed, M. A. Steps, ledges and kinks on the

surfaces of platinum nanoparticles of different shapes. *Surf. Sci.* **380,** 302–310 (1997).

108. Wang, Z. L. Transmission Electron Microscopy of Shape-Controlled Nanocrystals and Their Assemblies. *J. Phys. Chem. B* **104,** 1153–1175 (2000).

109. Xia, X., Zeng, J., Oetjen, L. K., Li, Q. & Xia, Y. Quantitative Analysis of the Role Played by Poly (vinylpyrrolidone) in Seed-Mediated Growth of Ag Nanocrystals. *J. Am. Chem. Soc.* **134,** 1793–1801 (2012).

110. Xia, X. & Xia, Y. Symmetry Breaking during Seeded Growth of Nanocrystals. *Nano Lett.* **12,** 6038–6042 (2012).

111. Wu, Y., Cai, S., Wang, D., He, W. & Li, Y. Syntheses of water-soluble octahedral, truncated octahedral, and cubic Pt-Ni nanocrystals and their structure-activity study in model hydrogenation reactions. *J. Am. Chem. Soc.* **134,** 8975–8981 (2012).

112. Zhang, H. *et al.* Synthesis of Pd-Pt bimetallic nanocrystals with a concave structure through a bromide-induced galvanic replacement reaction. *J. Am. Chem. Soc.* **133,** 6078–6089 (2011).

113. González, E., Arbiol, J. & Puntes, V. F. Carving at the Nanoscale : Sequential Galvanic Exchange and Kirkendall Growth at Room Temperature. (2011).

114. Liang, H.-P. *et al.* Pt hollow nanospheres: facile synthesis and enhanced electrocatalysts. *Angew. Chem. Int. Ed. Engl.* **43,** 1540–3 (2004).

115. Zhao, J., Chen, W., Zheng, Y. & Li, X. Novel carbon supported hollow Pt nanospheres for methanol electrooxidation. *J. Power Sources* **162,** 168–172 (2006).

116. Snyder, J., Livi, K. & Erlebacher, J. Oxygen Reduction Reaction Performance of [MTBD][beti]-Encapsulated Nanoporous NiPt Alloy Nanoparticles. *Adv. Funct. Mater.* **23,** 5494–5501 (2013).

117. Fan, H., Cheng, M., Wang, Z. & Wang, R. Layer-controlled Pt-Ni porous nanobowls with enhanced electrocatalytic performance. *Nano Res.* **2,** 1–12 (2016).

118. Shan, A., Chen, Z., Li, B., Chen, C. & Wang, R. Monodispersed, ultrathin NiPt

hollow nanospheres with tunable diameter and composition via a green chemical synthesis. *J. Mater. Chem. A* **3,** 1031–1036 (2015).

119. Li, Z. *et al.* A simple strategy to form hollow Pt3Co alloy nanosphere with ultrathin Pt shell with significant enhanced oxygen reduction reaction activity. *Int. J. Hydrogen Energy* 1–10 (2016). doi:10.1016/j.ijhydene.2016.08.124

120. Peng, Z., Wu, J. & Yang, H. Synthesis and Oxygen Reduction Electrocatalytic Property of Platinum Hollow and Platinum-on-Silver Nanoparticles †. *Chem. Mater.* **22,** 1098–1106 (2010).

121. Chen, H. M. *et al.* Hollow Platinum Spheres with Nano-Channels : Synthesis and Enhanced Catalysis for Oxygen Reduction. *J. Phys. Chem. C* 7522–7526 (2008).

122. Jong Wook, H. & Shin Wook, K. Controlled Synthesis of Pd À Pt Alloy Hollow Nanostructures with Enhanced Catalytic Activities for Oxygen. *ACS Nano* **6,** 2410–2419 (2012).

123. Bae, S. J., Yoo, S. J., Lim, Y., Kim, S. & Lim, Y. Facile Preparation of Carbon-Supported PtNi Hollow Nanoparticles with High Electrochemical Performance. (2012).

124. Dubau, L. *et al.* Beyond conventional electrocatalysts: hollow nanoparticles for improved and sustainable oxygen reduction reaction activity. *J. Mater. Chem. A* **2,** 18497–18507 (2014).

125. Chen, C. *et al.* Highly crystalline multimetallic nanoframes with three-dimensional electrocatalytic surfaces. *Science* **343,** 1339–43 (2014).

126. Stamenkovic, V. R. & Markovic, N. M. *V . A . 2 Nanosegregated Cathode Alloy Catalysts with Ultra-Low Platinum Loading*. *DoE Annual Progress Report* (2015).

127. Stephens, I. E. L. *et al.* Tuning the activity of Pt(111) for oxygen electroreduction by subsurface alloying. *J. Am. Chem. Soc.* **133,** 5485–5491 (2011).

128. Sun, Q., Ren, Z., Wang, R., Wang, N. & Cao, X. Platinum catalyzed growth of NiPt hollow spheres with an ultrathin shell. *J. Mater. Chem.* **21,** 1925 (2011).

129. Wang, J. X. *et al.* Kirkendall effect and lattice contraction in nanocatalysts: a new strategy to enhance sustainable activity. *J. Am. Chem. Soc.* **133,** 13551–7 (2011).

130. Sun, Y. & Xia, Y. Shape-controlled synthesis of gold and silver nanoparticles. *Science* **298,** 2176–9 (2002).

131. Chen, J. *et al.* Optical Properties of Pd- Ag and Pt- Ag Nanoboxes Synthesized via Galvanic Replacement Reactions. *Nano Lett.* **5,** 2058 (2005).

132. Sun, Y. & Xia, Y. Mechanistic study on the replacement reaction between silver nanostructures and chloroauric acid in aqueous medium. *J. Am. Chem. Soc.* **126,** 3892–901 (2004).

133. Renaud, G. *et al.* Real-Time Monitoring of Growing Nanoparticles. *Science (80-.).* **300,** 1416–1419 (2003).

134. Leroy, F. *et al.* Self-organized growth of nanoparticles on a surface patterned by a buried dislocation network. *Phys. Rev. Lett.* **95,** 1–15 (2005).

135. Lazzari, R., Renaud, G., Jupille, J. & Leroy, F. Self-similarity during growth of the Au Ti O2 (110) model catalyst as seen by the scattering of x-rays at grazing-angle incidence. *Phys. Rev. B - Condens. Matter Mater. Phys.* **76,** (2007).

136. Dubau, L. *et al.* Tuning the Performance and the Stability of Porous Hollow PtNi/C Nanostructures for the Oxygen Reduction Reaction. *ACS Catal.* **5,** 5333–5341 (2015).

137. Bard, A. J., Parsons, R. & Jordan, J. *Standard Potentials in Aqueous Solution.* (1985).

138. Bae, S. J. *et al.* Facile preparation of carbon-supported PtNi hollow nanoparticles with high electrochemical performance. *J. Mater. Chem.* **22,** 8820 (2012).

139. Carenco, S., Portehault, D., Boissière, C., Mézailles, N. & Sanchez, C. Nanoscaled metal borides and phosphides: Recent developments and perspectives. *Chem. Rev.* **113,** 7981–8065 (2013).

140. Caputo, R., Guzzetta, F. & Angerhofer, A. Room-temperature synthesis of nickel borides via decomposition of NaBH 4 promoted by nickel bromide. *Inorg. Chem.* **49,** 8756–8762 (2010).

141. Jia, Q. *et al.* Circumventing Metal Dissolution-Induced Degradation of Pt-alloy Catalysts in Proton Exchange Membrane Fuel Cells: Revealing the Asymmetric

Volcano Nature of Redox Catalysis. *ACS Catal.* acscatal.5b02750 (2015). doi:10.1021/acscatal.5b02750

142. Durst, J. *et al.* Reversibility of Pt-skin and Pt-skeleton nanostructures in acidic media. *J. Phys. Chem. Lett.* **5,** 434–439 (2014).

143. Dubau, L. *et al.* Defects do Catalysis: CO Monolayer Oxidation and Oxygen Reduction Reaction on Hollow PtNi/C Nanoparticles. *ACS Catal.* **6,** 4673−4684 (2016).

144. Li, G., Boerio-goates, J., Woodfield, B. F. & Li, L. Evidence of linear lattice expansion and covalency enhancement in rutile TiO2 nanocrystals Evidence of linear lattice expansion and covalency enhancement in rutile TiO2 nanocrystals. *Appl. Phys. Lett.* **85,** 259–261 (2010).

145. Qin, W. & Szpunar, J. a. Origin of lattice strain in nanocrystalline materials. *Philos. Mag. Lett.* **85,** 649–656 (2005).

146. Maniammal, K., Madhu, G. & Biju, V. X-ray diffraction line profile analysis of nanostructured nickel oxide: Shape factor and convolution of crystallite size and microstrain contributions. *Phys. E Low-dimensional Syst. Nanostructures* **85,** 214–222 (2017).

147. Mezzavilla, S. *et al.* Experimental Methodologies to Understand Degradation of Nanostructured Electrocatalysts for PEM Fuel Cells: Advances and Opportunities. (2016). doi:10.1002/celc.201600170

148. Paffett, M. T., Daube, K. A., Gottesfeld, S. & Campbell, C. T. Electrochemical and surface science investigations of PtCr alloy electrodes. *J. Electroanal. Chem.* **220,** 269–285 (1987).

149. Bardi, U., Beard, B. C. & Ross, P. N. Surface oxidation of a Pt80Co20 alloy - An X-Ray photoelectron spectroscopy and low energy electron diffraction study on the [100] and [111] oriented single crystal surfaces. *J. Vac. Sci. Technol. A* **6,** 665–670 (1988).

150. Chem, D. P. & Soc, A. C. Oxygen Reduction at Pt(0.65)Cr(0.3)s, Pt(0.2)Cr(0.8) and Roughened Platinum. *J. Electrochem. Soc.* **135,** 1431–1436 (1988).

151. Gauthier, Y. *et al.* PtxNi1-x(111) alloy surfaces: structure and composition in relation to some catalytic properties. *Surf. Sci.* **162,** 342–347 (1985).

152. Bligaard, T. & Nørskov, J. K. Ligand effects in heterogeneous catalysis and electrochemistry. *Electrochim. Acta* **52,** 5512–5516 (2007).

153. Gasteiger, H. A. & Marković, N. M. Just a Dream -- or Future Reality? *Science (80-.).* **324,** 48–49 (2009).

154. Durst, J. *et al.* Reversibility of Pt-skin and Pt-skeleton Nanostructures in Acidic Media. *J. Phys. Chem. Lett.* **5,** 434–439 (2014).

155. Greeley, J. & Nørskov, J. K. A general scheme for the estimation of oxygen binding energies on binary transition metal surface alloys. *Surf. Sci.* **592,** 104–111 (2005).

156. Shao, M., Chang, Q., Dodelet, J.-P. & Chenitz, R. Recent Advances in Electrocatalysts for Oxygen Reduction Reaction. *Chem. Rev.* **116,** 3594−3657 (2016).

157. Price, S. W. T., Rhodes, J. M., Calvillo, L. & Russell, A. E. Revealing the details of the surface composition of electrochemically prepared Au@Pd Core@Shell nanoparticles with in situ EXAFS. *J. Phys. Chem. C* **117,** 24858–24865 (2013).

158. Zhang, Y. *et al.* Hollow core supported Pt monolayer catalysts for oxygen reduction. *Catal. Today* **202,** 50–54 (2013).

159. Kertis, F. *et al.* Structure / Processing Relationships in the Fabrication of Nanoporous. *J. Miner. Met. Mater. Soc.* **62,** 50–56 (2010).

160. Fievet, F., Lagier, J. P. & Figlarz, M. Preparing Monodisperse Metal Powders in Micrometer and Submicrometer Sizes by the Polyol Process. *MRS Bull.* **14,** 29–34 (1989).

161. Oh, H. S., Oh, J. G. & Kim, H. Modification of polyol process for synthesis of highly platinum loaded platinum-carbon catalysts for fuel cells. *J. Power Sources* **183,** 600–603 (2008).

162. Schrader, I. *et al.* Surface Chemistry of 'Unprotected' Nanoparticles: A Spectroscopic Investigation on Colloidal Particles. *J. Phys. Chem. C* **119,** 17655–

17661 (2015).

163. Kharisov, B. I. *et al.* Solubilization, dispersion and stabilization of magnetic nanoparticles in water and non-aqueous solvents: recent trends. *RSC Adv.* **4,** 45354–45381 (2014).

164. Bae, S. J. *et al.* Facile preparation of carbon-supported PtNi hollow nanoparticles with high electrochemical performance. *J. Mater. Chem.* **22,** 8820 (2012).

165. Kang, J. *et al.* Effect of Ni core structure on the electrocatalytic activity of Pt-Ni/C in methanol oxidation. *Materials (Basel).* **6,** 2789–2818 (2013).

166. Westsson, E. & Koper, G. How to Determine the Core-Shell Nature in Bimetallic Catalyst Particles? *Catalysts* **4,** 375–396 (2014).

167. Montejano-Carrizales, J. M. & Morán-López, J. L. Geometrical characteristics of compact nanoclusters. *Nanostructured Mater.* **1,** 397–409 (1992).

168. Montejano-Carrizales, J. M., Aguilera-Granja, F. & Morán-López, J. L. Direct enumeration of the geometrical characteristics of clusters. *Nanostructured Mater.* **8,** 269–287 (1997).

169. Qin, W., Nagase, T., Umakoshi, Y. & Szpunar, J. a. Relationship between microstrain and lattice parameter change in nanocrystalline materials. *Philos. Mag. Lett.* **88,** 169–179 (2008).

170. Mocherla, P. S. V, Karthik, C., Ubic, R., Ramachandra Rao, M. S. & Sudakar, C. Tunable bandgap in BiFeO3 nanoparticles: The role of microstrain and oxygen defects. *Appl. Phys. Lett.* **103,** 1–6 (2013).

171. Feng, X., Jiang, K., Fan, S. & Kanan, M. W. A Direct Grain-Boundary-Activity Correlation for CO Electroreduction on Cu Nanoparticles. *ACS Cent. Sci.* **2,** 169–174 (2016).

172. Shinozaki, K., Zack, J. W., Richards, R. M., Pivovar, B. S. & Kocha, S. S. Oxygen Reduction Reaction Measurements on Platinum Electrocatalysts Utilizing Rotating Disk Electrode Technique. *J. Electrochem. Soc.* **162,** F1144–F1158 (2015).

173. Markovic, N. M., Sarraf, S. T., Gasteigert, H. a & Ross, P. N. (Jr. . Surfaces in Alkaline Solution. *J. Chem. Soc. Faraday Trans.* **92,** 3719–3725 (1996).

174. Jayasayee, K. *et al.* Oxygen reduction reaction (ORR) activity and durability of carbon supported PtM (Co, Ni, Cu) alloys: Influence of particle size and non-noble metals. *Appl. Catal. B Environ.* **111–112,** 515–526 (2012).

175. Samjeské, G., Xiao, X. Y. & Baltruschat, H. Ru decoration of stepped Pt single crystals and the role of the terrace width on the electrocatalytic CO oxidation. *Langmuir* **18,** 4659–4666 (2002).

176. Lin, W. F., Iwasita, T. & Vielstich, W. Catalysis of CO Electrooxidation at Pt, Ru, and PtRu Alloy. An in Situ FTIR Study. *J. Phys. Chem. B* **103,** 3250–3257 (1999).

177. Maillard, F. *et al.* Size effects on reactivity of Pt nanoparticles in CO monolayer oxidation: the role of surface mobility. *Faraday Discuss.* **125,** 357-377-407 (2004).

178. Maillard, F. *et al.* Influence of particle agglomeration on the catalytic activity of carbon-supported Pt nanoparticles in CO monolayer oxidation. *Phys. Chem. Chem. Phys.* **7,** 385–393 (2005).

179. Maillard, F., Savinova, E. R. & Stimming, U. CO monolayer oxidation on Pt nanoparticles: Further insights into the particle size effects. *J. Electroanal. Chem.* **599,** 221–232 (2007).

180. Urchaga, P., Baranton, S., Coutanceau, C. & Jerkiewicz, G. Electro-oxidation of CO chem on Pt nanosurfaces: Solution of the peak multiplicity puzzle. *Langmuir* **28,** 3658–3663 (2012).

181. Cui, C. *et al.* Shape-selected bimetallic nanoparticle electrocatalysts: evolution of their atomic-scale structure, chemical composition, and electrochemical reactivity under various chemical environments. *Faraday Discuss.* **162,** 91 (2013).

182. Zhao, Z., Dubau, L. & Maillard, F. Evidences of the migration of Pt crystallites on high surface area carbon supports in the presence of reducing molecules. *J. Power Sources* **217,** 449–458 (2012).

183. Zhao, Z. *et al.* Carbon corrosion and platinum nanoparticles ripening under open circuit potential conditions. *J. Power Sources* **230,** 236–243 (2013).

184. Lopez-Cudero, A., Solla-Gullòn, J., Herrero, E., Aldaz, A. & Feliu, J. M. CO electrooxidation on carbon supported platinum nanoparticles: Effect of

aggregation. *J. Electroanal. Chem.* **644,** 117–126 (2010).

185. Garsany, Y., Baturina, O. a, Swider-Lyons, K. E. & Kocha, S. S. Experimental methods for quantifying the activity of platinum electrocatalysts for the oxygen reduction reaction. *Anal. Chem.* **82,** 6321–8 (2010).

186. Garsany, Y., Singer, I. L. & Swider-Lyons, K. E. Impact of film drying procedures on RDE characterization of Pt/VC electrocatalysts. *J. Electroanal. Chem.* **662,** 396–406 (2011).

187. Takahashi, I. & Kocha, S. S. Examination of the activity and durability of PEMFC catalysts in liquid electrolytes. *J. Power Sources* **195,** 6312–6322 (2010).

188. Gasteiger, H. A., Kocha, S. S., Sompalli, B. & Wagner, F. T. Activity benchmarks and requirements for Pt, Pt-alloy, and non-Pt oxygen reduction catalysts for PEMFCs. *Appl. Catal. B Environ.* **56,** 9–35 (2005).

189. Kriston, A., Xie, T., Ganesan, P. & Popov, B. N. Analysis of the Effect of Pt Loading on Mass and Specific Activity in PEM Fuel Cells. *J. Electrochem. Soc.* **160,** F406–F412 (2013).

190. Calle-Vallejo, F. *et al.* Finding optimal surface sites on heterogeneous catalysts by counting nearest neighbors. *Science (80-.).* **350,** 185–189 (2015).

191. Alia, S. M., Pylypenko, S., Neyerlin, K. C., Kocha, S. S. & Pivovar, B. S. Nickel Nanowire Oxidation and Its Effect on Platinum Galvanic Displacement and Methanol Oxidation. *ECS Trans.* **64,** 89–95 (2014).

192. Alia, S. M. *et al.* Oxidation of Platinum Nickel Nanowires to Improve Durability of Oxygen-Reducing Electrocatalysts. *J. Electrochem. Soc.* **163,** F296–F301 (2016).

193. Koenigsmann, C., Zhou, W. P., Adzic, R. R., Sutter, E. & Wong, S. S. Size-dependent enhancement of electrocatalytic performance in relatively defect-free, processed ultrathin platinum nanowires. *Nano Lett.* **10,** 2806–2811 (2010).

194. Henning, S. *et al.* Pt-Ni Aerogels as Unsupported Electrocatalysts for the Oxygen Reduction Reaction. *J. Electrochem. Soc.* **163,** F998–F1003 (2016).

195. Liu, W. *et al.* Bimetallic aerogels: High-performance electrocatalysts for the

oxygen reduction reaction. *Angew. Chemie - Int. Ed.* **52,** 9849–9852 (2013).

196. Li, M. *et al.* Ultrafine jagged platinum nanowires enable ultrahigh mass activity for the oxygen reduction reaction. *Science (80-.).* **354,** 1414–1419 (2016).

197. Le Bacq, O. *et al.* Effect of Atomic Vacancies on the Structure and the Electrocatalytic Activity of Pt-rich/C Nanoparticles: A Combined Experimental and Density Functional Theory Study. *ChemCatChem* **9,** 2324–2338 (2017).

198. Jusys, Z. & Behm, R. J. Methanol Oxidation on a Carbon-Supported Pt Fuel Cell CatalystsA Kinetic and Mechanistic Study by Differential Electrochemical Mass Spectrometry. *J. Phys. Chem. B* **105,** 10874–10883 (2001).

199. Lai, C. S. S. & Koper, M. T. M. Electro-oxidation of ethanol and acetaldehyde on platinum single-crystal electrodes. *Faraday Discuss.* **140,** 399–416 (2008).

200. Ross, P. N. & Soc, J. E. Structure Sensitivity in the Electrocatalytic Properties of Pt : I . Hydrogen Adsorption on Low Index Single Crystals and the Role of Steps Structure Sensitivity in the Electrocatalytic Properties of Pt I . Hydrogen Adsorption on Low Index Single Crystals. **126,** 67–77 (1979).

201. Van Der Niet, M. J. T. C., Garcia-Araez, N., Hernández, J., Feliu, J. M. & Koper, M. T. M. Water dissociation on well-defined platinum surfaces: The electrochemical perspective. *Catal. Today* **202,** 105–113 (2013).

202. Farias, M. J. S., Herrero, E. & Feliu, J. M. Site selectivity for CO adsorption and stripping on stepped and kinked platinum surfaces in alkaline medium. *J. Phys. Chem. C* **117,** 2903–2913 (2013).

203. Farias, M. J. S., Camara, G. A. & Feliu, J. M. Understanding the CO Preoxidation and the Intrinsic Catalytic Activity of Step Sites in Stepped Pt Surfaces in Acidic Medium. *J. Phys. Chem. C* **119,** 20272–20282 (2015).

204. Gómez-Marín, A. M. & Feliu, J. M. Oxygen reduction on nanostructured platinum surfaces in acidic media: Promoting effect of surface steps and ideal response of Pt(1 1 1). *Catal. Today* **244,** 172–176 (2015).

205. Sugimura, F., Nakamura, M. & Hoshi, N. The Oxygen Reduction Reaction on Kinked Stepped Surfaces of Pt. *Electrocatalysis* **8,** 46–50 (2017).

206. Chattot, R., Asset, T., Bordet, P., Drnec, J. & Dubau, L. Beyond Strain and Ligand Effects: Microstrain-Induced Enhancement of the Oxygen Reduction Reaction Kinetics on Various PtNi/C Nanostructures. *ACS Catal.* **7,** 398–408 (2017).

207. Asset, T. *et al.* Structure-Activity Relationships for the Oxygen Reduction Reaction in Porous Hollow PtNi/C Nanoparticles. *ChemElectroChem* **3,** 1591–1600 (2016).

208. Dubau, L., Nelayah, J., Asset, T., Chattot, R. & Maillard, F. Implementing Structural Disorder as a New Direction to Improve the Stability of PtNi/C Nanoparticles. *ACS Catal.* **7,** 3072–3081 (2017).

209. Asset, T. *et al.* Elucidating the Mechanisms Driving the Aging of Porous Hollow PtNi/C Nanoparticles by Means of COads Stripping. *ACS Appl. Mater. Interfaces* DOI: 10.1021/acsami.7b05782 (2017). doi:10.1021/acsami.7b05782

210. Watanabe, M. & Tsurumi, K. Activity and Stability of Ordered and Disordered Co-Pt Alloys for Phosphoric Acid Fuel Cells. *J. ...* **141,** 6–15 (1994).

211. Calle-Vallejo, F. *et al.* Why conclusions from platinum model surfaces do not necessarily lead to enhanced nanoparticle catalysts for the oxygen reduction reaction. *Chem. Sci.* 2283–2289 (2016). doi:10.1039/C6SC04788B

212. Cui, C. *et al.* Carbon Monoxide-Assisted Size-Confinement of Bimetallic Alloy Nanoparticles. *Jacs* 1–11 (2013).

213. Gan, L., Rudi, S., Cui, C., Heggen, M. & Strasser, P. Size-Controlled Synthesis of Sub-10 nm PtNi3 Alloy Nanoparticles and their Unusual Volcano-Shaped Size Effect on ORR Electrocatalysis. *Small* 3189–3196 (2016). doi:10.1002/smll.201600027

214. LaMer, V. K. & Dinegar, R. H. Theory, Production and Mechanism of Formation of Monodispersed Hydrosols. *J. Am. Chem. Soc.* **72,** 4847–4854 (1950).

215. Beermann, V. *et al.* Rh-doped Pt-Ni octahedral nanoparticles: understanding the correlation between elemental distribution, ORR and shape stability. *Nano Lett.* acs.nanolett.5b04636 (2016). doi:10.1021/acs.nanolett.5b04636

216. Henning, S. *et al.* Unsupported Pt-Ni Aerogels with Enhanced High Current

Performance and Durability in Fuel Cell Cathodes. *Angew. Chemie Int. Ed.* (2017). doi:10.1002/anie.201704253

217. Kimmel, G. & Dayan, D. X-ray diffraction characterization of microstrain in some uranium alloys. *Powder Diffr.* **13,** 89–95 (1998).

218. Arenz, M. *et al.* The Effect of the Particle Size on the Kinetics of CO Electrooxidation on High Surface Area Pt Catalysts. *J. Am. Chem. Soc.* **127,** 6819–6829 (2005).

219. Feibelman, P. J. *et al.* The CO/Pt(111) Puzzle. *J. Phys. Chem. B* **105,** 4018–4025 (2001).

220. Farias, M. J. S. *et al.* Mobility and oxidation of adsorbed CO on shape-controlled Pt nanoparticles in acidic medium. *Langmuir* **33,** 865–871 (2017).

221. Love, B. & Lipkowski, J. in *Electrochemical Surface Science* 485–496 (1988).

222. Coutanceau, C., Urchaga, P. & Baranton, S. Diffusion of adsorbed CO on platinum (100) and (111) oriented nanosurfaces. *Electrochem. commun.* **22,** 109–112 (2012).

223. Lebedeva, N. P., Rodes, A., Feliu, J. M., Koper, M. T. M. & Van Santen, R. A. Role of crystalline defects in electrocatalysis: CO adsorption and oxidation on stepped platinum electrodes as studied by in situ infrared spectroscopy. *J. Phys. Chem. B* **106,** 9863–9872 (2002).

224. Calle-Vallejo, F., Pohl, M. D. & Bandarenka, A. S. Quantitative Coordination-Activity Relations for the Design of Enhanced Pt catalysts for CO Electro-Oxidation. (2017). at <http://pubs.acs.org.ezproxy.lib.purdue.edu/doi/pdf/10.1021/acscatal.7b01105>

225. Van Der Vliet, D. F. *et al.* Unique electrochemical adsorption properties of Pt-skin surfaces. *Angew. Chemie - Int. Ed.* **51,** 3139–3142 (2012).

226. Bandarenka, A. S. *et al.* Design of an active site towards optimal electrocatalysis: Overlayers, surface alloys and near-surface alloys of Cu/Pt(111). *Angew. Chemie - Int. Ed.* **51,** 11845–11848 (2012).

227. Ruvinskiy, P. S., Bonnefont, A. & Savinova, E. R. Further Insight into the Oxygen

Reduction Reaction on Pt Nanoparticles Supported on Spatially Structured Catalytic Layers. 123–133 (2011). doi:10.1007/s12678-011-0046-1

228. Corcoran, C. J., Tavassol, H., Rigsby, M. A., Bagus, P. S. & Wieckowski, A. Application of XPS to study electrocatalysts for fuel cells. *J. Power Sources* **195,** 7856–7879 (2010).

229. Panchenko, a., Koper, M. T. M., Shubina, T. E., Mitchell, S. J. & Roduner, E. Ab Initio Calculations of Intermediates of Oxygen Reduction on Low-Index Platinum Surfaces. *J. Electrochem. Soc.* **151,** A2016 (2004).

230. Shao, M., Peles, A. & Shoemaker, K. Electrocatalysis on Platinum Nanoparticles : Particle Size Effect on. *Nano Lett.* **11,** 3714–3719 (2011).

231. Perez-Alonso, F. J. *et al.* The effect of size on the oxygen electroreduction activity of mass-selected platinum nanoparticles. *Angew. Chemie - Int. Ed.* **51,** 4641–4643 (2012).

232. Schulenburg, H., Durst, J., M??ller, E., Wokaun, A. & Scherer, G. G. Real surface area measurements of Pt3Co/C catalysts. *J. Electroanal. Chem.* **642,** 52–60 (2010).

233. Marichev, V. A. Reversibility of platinum voltammograms in aqueous electrolytes and ionic product of water. *Electrochim. Acta* **53,** 7952–7960 (2008).

234. Baldizzone, C. *et al.* Stability of Dealloyed Porous Pt/Ni Nanoparticles. *ACS Catal.* **5,** 5000–5007 (2015).

235. Neyerlin, K. C., Srivastava, R., Yu, C. & Strasser, P. Electrochemical activity and stability of dealloyed Pt–Cu and Pt–Cu–Co electrocatalysts for the oxygen reduction reaction (ORR). *J. Power Sources* **186,** 261–267 (2009).

236. Hasché, F., Oezaslan, M. & Strasser, P. Activity, Structure and Degradation of Dealloyed PtNi3 Nanoparticle Electrocatalyst for the Oxygen Reduction Reaction in PEMFC. *J. Electrochem. Soc.* **159,** B25 (2012).

237. Oh, H. S., Oh, J. G., Hong, Y. G. & Kim, H. Investigation of carbon-supported Pt nanocatalyst preparation by the polyol process for fuel cell applications. *Electrochim. Acta* **52,** 7278–7285 (2007).

238. Ashiotis, G. *et al.* The fast azimuthal integration Python library: PyFAI. *J. Appl.*

Crystallogr. **48,** 510–519 (2015).

239. Li, T., Senesi, A. J. & Lee, B. Small Angle X-ray Scattering for Nanoparticle Research. *Chem. Rev.* **116,** 11128–11180 (2016).

240. Bartlett, P. & Ottewill, R. H. A neutron scattering study of the structure of a bimodal colloidal crystal. *J. Chem. Phys.* **96,** 3306–3318 (1992).

241. Rodríguez-Carvajal, J. Recent advances in magnetic structure determination by neutron powder diffraction. *Phys. B Condens. Matter* **192,** 55–69 (1993).

242. Thompson, P., Cox, D. E. & Hastings, J. B. Rietveld Refinement of Debye-Scherrer Synchrotron X-ray Data from A1203. *J. Appl. Crystallogr.* **20,** 79–83 (1987).

243. Proffen, T., Billinge, S. J. L., Egami, T. & Louca, D. Structural analysis of complex materials using the atomic pair distribution function – a practical guide. *Zeitschrift für Krist.* **218,** 132–143 (2003).

244. Egami, T. & Billinge, S. J. L. *Underneath The Bragg Peaks: Structural Analysis of Complex Materials - Second Edition.* (Elsevier, 2012).

245. Farrow, C. L. *et al.* PDFfit2 and PDFgui: computer programs for studying nanostructure in crystals. *J. Phys. Condens. Matter* **19,** 335219 (2007).

246. Howell, R. C., Proffen, T. & Conradson, S. D. Pair distribution function and structure factor of spherical particles. *Phys. Rev. B - Condens. Matter Mater. Phys.* **73,** (2006).

247. Wikimedia Commons. at <https://commons.wikimedia.org/wiki/File:Electron_Interaction_with_Matter.svg >

248. Chatenet, M., Guétaz, L. & Maillard, F. in *vol. 5* (eds. Vielstich, W., Gasteiger, H. A. & Yokokawa, H.) 844–860 (John Wiley & Sons, 2009).

Abstract

This PhD thesis was initially motivated by the understanding of the peculiar electrocatalytic activity of hollow PtNi/C nanoparticles for the oxygen reduction reaction (ORR). Investigations on the formation and growth mechanism of this novel class of nanocatalysts using *operando* X-ray and electron-based techniques revealed that, beyond alloying effects, structural disorder is a lever to boost the ORR kinetics on bimetallic nanomaterials. The 'defects do catalysis' concept was progressively extended to various PtNi catalyst nanostructures, namely to advanced shape-controlled nanocatalysts from the ORR electrocatalysis landscape thanks to fruitful collaborations with European laboratories. This work shows that, through their distorted surface, microstrained nanomaterials feature unprecedented adsorption properties and represent a viable approach to sustainably enhance the ORR activity.

Key words: Proton-Exchange Membrane Fuel Cell, Electrocatalysis, Nanoparticles, Structural Defects, Microstrain, Oxygen Reduction Reaction.

Résumé

Cette thèse a été initialement motivée par la compréhension de l'activité électrocatalytique particulière de particules PtNi/C creuses pour l'electroréduction du dioxygène (ORR). L'étude des mécanismes de formation et croissance de ces particules creuses, grâce à des techniques *operando* basées sur l'interaction rayons X- et/ou électrons-matière, a permis de montrer que les défauts cristallins améliorent les propriétés électrocatalytiques de nanomatériaux bimétalliques pour l'ORR. Le concept de « catalyseur défectueux » a pu être progressivement étendu à d'autres nanostructures PtNi, notamment des nanocatalyseurs à forme contrôlée, grâce à de fructueuses collaborations avec d'autres laboratoires européens. Ce travail montre, qu'en raison de la distorsion de leur surface, les nanomatériaux défectueux présentent des propriétés d'adsorption uniques, définissant ainsi une nouvelle classe de catalyseurs prometteurs et stables.

Mots clefs : Pile à Combustible à Membrane Echangeuse de Protons, Electrocatalyseurs, Nanoparticules, Défauts Structuraux, Micro-Déformation, Réduction de l'Oxygène.